Optical Study of Shear and Longitudinal Acoustic Waves and Complex Relaxation Dynamics of Glass Forming Liquids

by

Darius H Torchinsky

B.S. Physics, Indiana University (1999)
B.S. Mathematics, Indiana University (1999)

Submitted to the Department of Physics
in partial fulfillment of the requirements for the degree of

Doctor of Philosophy

at the

MASSACHUSETTS INSTITUTE OF TECHNOLOGY

June 2008

Author ....
Department of Physics
April 29, 2008

Certified by ....
Keith A. Nelson
Professor
Thesis Supervisor

Certified by ....
Erich P. Ippen
Professor
Thesis Supervisor

Accepted by ....
Thomas J. Greytak
Associate Department Head for Education

Optical Study of Shear and Longitudinal Acoustic Waves and Complex Relaxation Dynamics of Glass Forming Liquids

by

Darius H Torchinsky

Submitted to the Department of Physics
on April 29, 2008, in partial fulfillment of the
requirements for the degree of
Doctor of Philosophy

Abstract

The spectroscopic technique Impulsive Stimulated Scattering (ISS) was refined and used to study the complex structural relaxation dynamics of glass forming liquids, allowing both empirical modeling and testing of the predictions of the mode-coupling theory (MCT). Longitudinal and shear acoustic waves throughout much of the MHz frequency range, time-dependent thermal expansion on nanosecond and microsecond scales, and slower thermal diffusion were all monitored in real time. The data were used to construct complex longitudinal modulus spectra spanning from $\sim$ 30 kHZ to 3 GHz, and complex shear modulus spectra from $\sim$ 10 MHz to 1 GHz.

In the liquid tetramethyl tetraphenyl trisiloxane, experiments which verified time-temperature superposition of its relaxation dynamics permitted construction of a master plot of scaled relaxation spectra in the entire temperature range studied. MCT predictions of power-law frequency dependencies of the high and low frequency wings of the loss modulus yielded a high-frequency exponent parameter in good agreement with the width of the non-exponential relaxation kinetics. The low-frequency exponent did not agree with the predicted value.

In triphenyl phosphite, measurements of the measured shear relaxation spectrum over two decades in frequency revealed that it does not match the previously measured longitudinal spectrum, suggesting that different underlying degrees of freedom contribute to shear and compressional relaxation.

Measurement of shear wave propagation as a function of temperature lent credence to the dominance of the temperature dependence of the transport by the instantaneous shear modulus. These measurements also call into question other relationships drawn between glass mechanical behavior and the supercooled liquid fragility.

In work conducted collaboratively, the ISS technique was employed in single-shot measurements of liquid benzene under conditions of shock loading. The results indicate that benzene remains in a liquid state for at least 200 ns after the shock's arrival. ISS was also used to characterize both the thermal transport and mechanical properties of nanofluids. Finally, results of ISS acoustic measurements of thin films and their relationship with the study of glass forming liquids are briefly discussed.

Thesis Supervisor: Keith A. Nelson
Title: Professor

Thesis Supervisor: Erich P. Ippen
Title: Professor

Acknowledgments

First, I would like to thank my advisor, Keith Nelson, for his support, guidance, and many words of wisdom. During all my years at MIT, I haven't met a mind like his in its keenness and originality; when I was able to leave his office after a meeting and feel that I actually understood everything he said, I knew I was finally ready to graduate. I will always aspire to his level of knowledge and creativity, boundless enthusiasm and energy for science, and his ability to just get things.

Thinking back to my undergrad days, I have to acknowledge the mentors whose insights shaped me in lasting ways: Alex Dzierba taught my first college level physics class and inspired me to ditch biology and become a physicist. Brian Serot was an amazing quantum mechanics professor and certainly the best physics teacher I have ever had. David Baxter gave me a first taste of research in his lab, complete with the experience of dealing with non-functioning experiment.

My close college friends Amanda Chambliss, Terry Durkin, Lisa Martin, and Jane Soung supported me from before day one of grad school, and I feel privileged that they have not let me fall out of touch. The deepest thanks go to Reed Arnos (aka "Freddie Magoun"), Deborah Boggs, Joel Eaves (aka "Patty O'Brien"), Aidan Foley, Ian Gavalakis, Dan Greenbaum, Lynn Johnson, Phoebe Kwan, Shiqi Kwei, Andy Linshaw, Predrag Nikolic, Juan Pedraza, David Strozzi, and Mukund Thattai. I could write volumes on my appreciation to them as they each affected my life in very meaningful ways.

I spent many long months in the lentil fields of Pullman, WA for the ISTS shock work, and several people helped ease the homesickness. Otto Berg, Radu Custealcean, Oleg Fatyanov, Brandon Lalone, Kevin Mattern, Seth Root, and Hari Simha made all the difference, be it through drinking at Rico's, fishing in the Snake river, or sharing my deep appreciation for the œuvre of Borat. On the scientific side, I would like to thank Prof. Yogendra Gupta, Zbigniew Dreger and Naoki Hemmi for their support and for all they have taught me. I would also like to thank Zbigniew for his lasting friendship.

There have been a multitude of Nelson group members since I joined, and I have enjoyed working with, and hanging out with, every one. Again, each deserve their own words of thanks that would fill pages. Jaime Choi (née Beers), Tina Hecksher, Thomas Hornung, Maria Kandyla, Kenji Katayama, Ben Paxton, Emmanuel Perronne, Thomas Pezeril, Peter Poulin, Rebecca Slayton, Nikolai Stoyanov, Josh Vaughan, David Ward, and Masashi Yamaguchi are among the old guard, and I remember them with much fondness. I would also like to separately thank former group members Thomas Feurer and Christ Glorieux for their continued friendship and support. Dylan Arias, Cindy Bolme, Zhao Chen, Kenan Gundogdu, Janos Hebling, Harold Hwang, Jeremy Johnson, Christoph Klieber, Kung-Hsuan Lin, Kara Manke, Gagan Saini, Taeho Shin, Eric Statz, Kathy Stone, Duffy Turner, Johanna Wendlandt, Patrick Wen, Kit Werley, and Ka-Lo Yeh are the present Nelson group, and I wish them the happiness and success that they helped bring me. Jeremy Johnson, in particular, deserves special thanks for his heroic efforts, as much of the work in chapters 5 and 6 was done collaboratively with him. Finally, the most sincerest thanks go to Gloria Pless who, in many ways, kept the group together.

Lauren Deflores, Josh Lessing, Joseph Loparo, were all friends and members of the Tokmakoff group who made no small impact on my experience here in very positive ways. Matteo Chiesa and Aaron Schmidt from the Gang Chen group were the best collaborators one could hope for, making the process of science both productive and fun.

Last of all, I would like to thank my loving parents Alberto and Massi, my brother Cyrus, and my wife Jae Hee Kang. They supported me through dark times of Judo injuries, qualifying exam anxieties, broken lasers, non-functional experiments, and in all-too-fresh retrospect, thesis-writing. It is no exaggeration to say that without any of them, I wouldn't have been able to make it to the end, and it is to them that I dedicate this thesis.

To my loving parents, my brother Cyrus, and to my wife Jae Hee Kang.

Contents

List of Figures

List of Tables

Chapter 1

Introduction

Despite being one of the first genuinely human made and engineered materials [1], in many regards glass remains an enigma. While solid and thus mechanically rigid, it is nearly identical structurally to its corresponding melted liquid state; nevertheless, it continues to flow on millennial time scales [2]. More troubling is that the transition from liquid to glass is marked by an increase of the viscosity by seventeen orders of magnitude, all the while preserving the same structure. Indeed, even drawing the boundaries between the viscous liquid state and the glassy state is accepted as arbitrary.

So, how best to understand a phenomenon so veiled in ambiguities? Attempts to cast the glass transition into the same mould as conventional phase transitions [3, 4, 5] have met with failure [6]. Neither experiments nor numerical simulations show divergences of the static correlation functions which are a hallmark of the cooperative behavior as understood in the theory of phase transitions. Thus, the transition must be viewed from a kinetic and dynamical perspective. To this end, it has been broadly recognized that the key to understanding the dynamics of the glass transition lies in the often broad relaxation spectra apparent from mechanical and dielectric linear response measurements.

This thesis presents an advancement of the study of glass forming, as well as simple, liquids in a number of directions which expand our ability to characterize mechanical relaxation. My tool of choice has been the nonlinear optical technique known as Impulsive Stimulated Scattering, a spectroscopy whose ability to both generate and probe coherent acoustic waves makes it an ideal candidate for the study of mechanical relaxation. This technique has been applied in a number of different situations as described below.

In Chapter 2, I present a background of the liquid-glass transition, starting with basic phenomenology. The prevailing first-principles theory of the transition, the mode coupling theory, is covered here, and the predictions most relevant to mechanical spectroscopy are described. I also review some recent advances in the theory, as well as the view of the existence of a growing dynamical length scale in the glass transition.

These results set the stage for chapter 3, in which I give a brief overview of the Impulsive Stimulated Scattering (ISS) technique, as well as a motivation for its use in supercooled liquid studies. I begin by reviewing prior derived results of the ISS VVVV signal [7] and I discuss the different contributions to the signal in terms of their physical origins. I then present original results of the analogous derivation in the VHVH configuration in supercooled liquids, highlighting the effects of structural relaxation on the shear degrees of freedom on the system. For both longitudinal and shear waves, I provide experimental results that illustrate the effects of structural relaxation on the acoustic measurements.

Chapter 3 continues with a discussion of the experimental apparatus I have built to perform measurements of longitudinal and shear waves in supercooled liquids. After the data acquisition and analysis are described in detail, the chapter concludes with important notes on sample preparation.

The above provides the background for the experimental results of this thesis, which begin with chapter 4. Here, results are presented on the mapping of the longitudinal relaxation spectrum in a prototypical glass-forming liquid, tetramethyl tetraphenyl trisiloxane (DC704) over 7 orders of magnitude in time. While this work is similar to prior experiments conducted on other liquids, the acoustic frequency range achieved here is a first for Impulsive Stimulated Scattering, or other mechanical spectroscopy studies of supercooled liquids. I describe the analysis I have performed, which examines the growing time scale characteristic of the transition and quantifies the Debye-Waller factor – a measure of the system's non-ergodicity, or "falling out of equilibrium." I have also shown evidence of an experimentally measured time-temperature-superposition, which conforms with both theoretical predictions and other measurements performed on this liquid in different frequency and temperature regimes.

Probing the longitudinal spectrum is a useful albeit incomplete method of studying glass formers, as a more complete picture of mechanical relaxation also encompasses the evolution of the shear acoustic spectrum. In light of this, chapter 4 presents preliminary results of an attempt to measure the shear relaxation spectrum of DC704; only partial results are presented due to the small shear ISS signal from this liquid.

Nevertheless, this provides motivation for chapter 5 where I have extended the technique of depolarized Impulsive Stimulated Brillouin Scattering to encompass a larger frequency range. With a coworker apprentice, I have set out to probe the broadest spectral information possible in the glass forming liquid triphenyl phosphite. The results presented therein constitute the broadest bandwidth shear acoustic measurements performed optically on this or any glass forming system. As before, the objective is to test assertions regarding the evolution of the slower components of relaxation, in this case from the point of view of the transverse current correlations. This is made possible by building upon prior work on this liquid [8, 9]; I have also added an analysis of the shear spectrum in relation to the longitudinal one, where we find that, in contrast with the mode-coupling theory, the two degrees of freedom do not have consistent relaxation behavior.

As a theoretical understanding of the glass transition is still elusive, alternatives to the mode-coupling theory, based on the samples' elastic parameters, have sprung up to fill the void. One of these is the "shoving" model [10], which proposes that the non-Arrhenius evolution of relaxation time with temperature finds its origin in the instantaneous shear elastic modulus G_∞ – as the molecules collectively rearrange in response to a perturbation, they do non-compressive physical work on their neighbors. This work sets the activation energy of the overall flow event whose gradual arrest is at the root of increasing viscosity. Other authors have built upon this work by taking a more phenomenological approach where they seek to draw correlations between the supercooled liquid's fragility (or departure from Arrhenius kinetics) and the corresponding glassy state's elastic parameters.

These assertions may also be tested by the Impulsive Stimulated Scattering technique, and chapter 6 describes a direct test of these notions. With a coworker, I have measured depolarized Brillouin scattering responses from ten glass forming liquids, rivalling the sum total of the depolarized Brillouin scattering literature. Our results provide evidence for a correspondence between the average relaxation time and the shear modulus. We also conclude that the ratio of bulk to shear moduli of the glassy state and the evolution of the relaxation time of the liquid state of a given system cannot be correlated in the way that other authors have proposed.

Chapter 7 describes how the spectroscopic techniques utilized in this thesis are extended to interrogate simple liquid systems out of equilibrium, with a view towards understanding glass forming liquids under similar conditions. With collaborators, we have designed, built, and then implemented an experimental apparatus to conduct the first single-shot, ISS studies of a sample under shock loading. We find a marked difference between the elastic parameters of shocked liquid benzene when contrasted with benzene under the corresponding static high pressure. We can conclude directly from its mechanical behavior that benzene is not able to crystallize under shock at the pressures achieved, nor is it likely to be in a vitrified state, after at least 200 ns.

Recent developments in the theory of liquids have centered on the study of colloids, which share much in terms of phenomenology with glass forming liquids. Working with collaborators, we have demonstrated the flexibility of the ISS technique in determining the mechanical and thermal transport properties of "nanofluids" – liquids with an immersion of alumina nanoparticles. These transport measurements provide a consistency check of previous measurements conducted with different methods, and also lay the groundwork for future studies on these systems.

The chapter ends with mention of work that I have done with collaborators involving acoustic measurements on thin-film multilayers. How these results may impact the study of glass forming liquids is discussed therein.

Chapter 8 presents a conclusion of this thesis where results are summarized and future directions of research are provided, as well as ideas by which to improve the experimental methods used above.

Chapter 2

Phenomenology and Theory of the Glass Transition

2.1 Introduction

Despite the widespread prevalence of glass in our everyday lives, the phenomenon of vitrification is not yet fully understood. Further than the marked difference in viscosity between the liquid and glassy states, the transition is rife with a rich phenomenology ranging from distinct changes in heat capacities to evidence for growing dynamic length scales. This behavior is made more remarkable by its apparent universality; materials ranging from associated and van der Waals liquids to ionic liquids, polymers and colloids display many of the same characteristics upon cooling, indicating that a common theory should underly their understanding. Explaining these characteristics is the goal of present-day glass forming liquid theory.

Below, we present a broad introduction to the basic phenomenology of the glass transition, as well as review some of the theoretical attempts that have been proposed to describe it. In the interest of motivating the measurements made in this thesis, we will restrict ourselves to a discussion focussed on changes in mechanical properties upon cooling.

2.2 Basic Phenomenology

Owing to the quite vast difference in mechanical behavior between a liquid and its corresponding glass, it would be reasonable to assume that these two states should be structurally distinguishable on a microscopic level. To the contrary, measurements of the static structure factor $S(q)$ by x-ray diffraction show no differences between them [11], except for a modest change in density associated with thermal contraction upon cooling. Indeed, structural transitions between different amorphous states are only found in a paucity of materials, and usually under the rather exotic circumstances of confinement [12] or static high pressure [13]. One example of recent interest is water, whose already rich pressure-temperature phase diagram has recently been shown to also encompass three distinct amorphous glassy phases [14]. Another example, quite relevant for the work presented here, is the case of triphenyl phosphite (TPP), a van der Waals bonded organic molecular glass forming liquid. Within a given temperature range, TPP apparently exhibits the ability to undergo a shift from a "regular" liquid phase to a "glacial" liquid phase [15]. It is worth emphasizing that, as far as can be discerned from any measurements, the mechanical properties of the distinct states of the liquids described here are little different from one another, despite the apparent change in liquid structure; for sure, their small mechanical differences certainly do not rival the scale spanned by liquid and glass.

2.2.1 The Susceptibility Spectrum and Growing Time Scales

In light of the preceding discussion, a different physical marker than microscopic structure is needed, and so we adopt the view that the transition should be considered kinetically in terms of relaxation times or transport quantities. An understanding in terms of transport quantities is conceptually straightforward. When flow becomes arrested, or if electrical conductivity of an ionic glass former is greatly decreased, we may use this as our measuring stick for the transition. In terms of the shear viscosity η, the simple liquid state is arbitrarily defined at $\eta = 10^{-4}$ P [16]. The glass transition temperature T_g is then (also arbitrarily) assigned to the temperature at which the system has reached a viscosity of $\eta = 10^{13}$ P.

An interpretation in terms of relaxation times is not as transparent. To understand what is meant by this, we consider linear response measurements of various susceptibilities of liquids taken over broad frequency regimes. In more precise terms, we are examining the change of a property δA of a system in response to an external driving field a at frequency ω:

$$\delta A = \hat{\chi}(\omega)a(\omega). \tag{2.1}$$

Here, $\hat{\chi}$ represents the frequency dependent susceptibility of interest. Since the viscosity increases by 17 orders of magnitude going from the liquid to glass state, it is reasonable to assume that the characteristic relaxation time should follow suit. Thus, we require for complete characterization, a metrology capable of spanning such a large frequency range. A good example is provided by dielectric spectroscopy [17], popular for its exceptional dynamic range of over 17 decades in frequency. This technique probes the orientational-orientational correlation function

$$\chi(t) = \langle \delta\theta(0)\delta\theta(t) \rangle, \tag{2.2}$$

where $\delta\theta(t)$ represents the angular displacement of a molecular glass-former's dipole from its original equilibrium orientation at time t. Thus, $a = E$ is the electric field, $A = P$ is the polarization and $\chi = \epsilon$ is the liquid's time dependent permittivity.

Due to the disorder of the liquid state beyond any length scale greater than a given molecule's first two solvation shells, the naïve experimentalist may assume that the frequency-dependent susceptibility would be featureless save some signature of the short range order at very high frequencies. Experimental data provided by the reactive part ϵ' in figure 2-1(a) and dissipative part ϵ'', shown in figure 2-1(b) immediately put this notion to rest. ϵ'' clearly shows a broad, yet distinct peak spanning many decades in frequency, whose progression as a function of temperature is clearly towards lower frequencies, while ϵ' exhibits dispersive character that matches ϵ''. Taken together, we may assign them as two pieces (related by the Kramers-Kronig transformation) of a complex susceptibility $\epsilon^* = \epsilon' + i\epsilon''$, where the imaginary part ϵ'' is referred to as the dielectric relaxation spectrum.

Another clear feature of the spectra in figure 2-1(b) is the separation of time scales. On the slower end is the broad peak which shifts over many orders magnitude in time with a change in temperature. This feature is known as the α relaxation, and is representative of the collective reorganization that takes place on large scales, such as during a flow event. The part of the spectrum contained at higher frequencies around 1 THz is known as the β relaxation, and as we can see in figure 2-1(b) it is generally independent of the temperature. These designations will be of utmost importance in the remaining discussion of the glass transition throughout this thesis.

To date, it is impossible to fit the spectra shown in figure 2-1 by a form that is justifiable from first principles, and so many authors extend the arguments of Debye in analyzing a relaxation spectrum. In the Debye model, relaxation is given as the response of a system with one characteristic time scale τ_R. When probed in the frequency domain, the Debye form of the complex susceptibility is given as

$$\chi(\omega) = \frac{1}{1 - i\omega\tau_R}. \tag{2.3}$$

Experimentally measured susceptibility curves of glass forming liquids are generally much broader and more asymmetric than what is realized by equation 2.3. A more general fitting function given by the Havriliak-Negami form [19]

$$\chi \propto \frac{1}{(1 - (i\omega\tau_R)^\alpha)^\beta} \qquad 0 < \alpha, \beta \leq 1 \tag{2.4}$$

is able to fit almost any separately varying relaxation spectrum feature over several decades in frequency. Here, the exponent α serves as a variance parameter by broadening the Debye distribution, and β acts as a skew parameter. τ_R is interpreted a characteristic relaxation time. In the glass-forming community T_g is (somewhat arbitrarily) defined as the temperature at which $\tau_R = 100$ s.

We also note that equation 2.4 is known as the Havriliak-Negami relaxation function, and is not the only generalization of a Debye spectrum. The Cole-Davidson

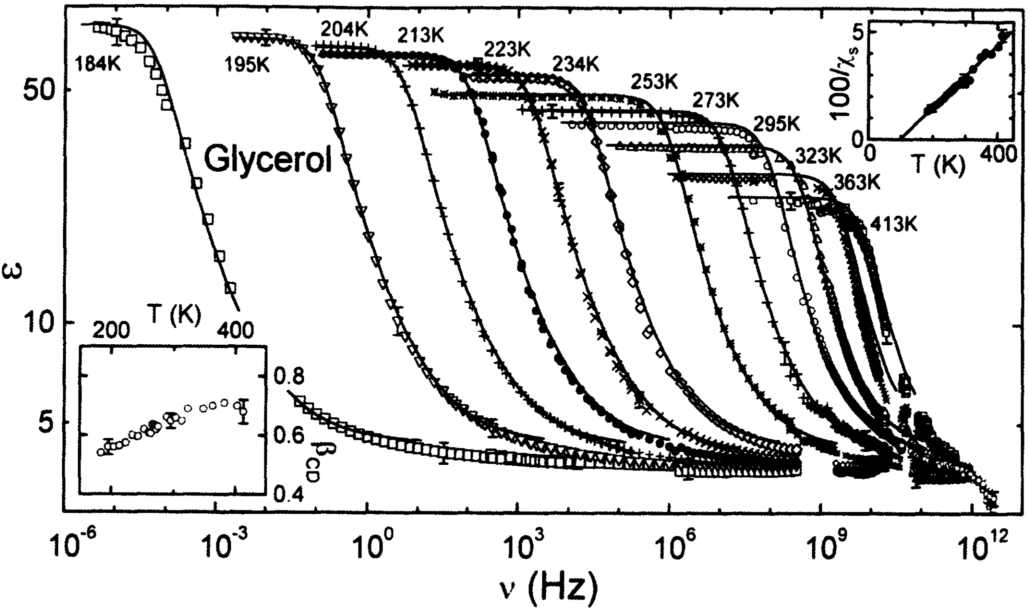

(a) Reactive part of dielectric relaxation spectrum. From [18].

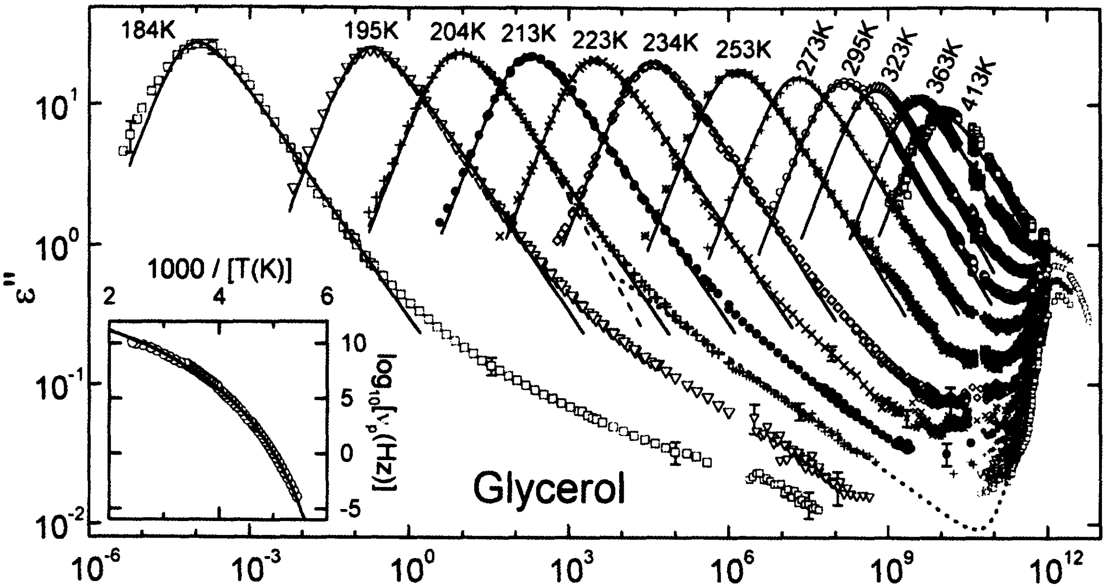

(b) Dissipative part of dielectric relaxation spectrum.

Figure 2-1: Dielectric relaxation in glycerol where (a) shows the reactive part of the permittivity as a function of frequency ν, and (b) the dissipative part. Note the structure in the imaginary part. Figure taken from [18].

function takes $\alpha = 1$, β variable, and expresses a distribution with skew but typical width. The Cole-Cole relaxation function assumes $\beta = 1$, α variable, implying a wide, but symmetric distribution. Selection between these three functions has no theoretical basis, and is considered to be at the discretion of the researcher.

Relaxation dynamics may be measured in the frequency or time domain. In such a case, we may imagine a perturbing field which is turned on adiabatically from time $t = -\infty$ and abruptly shut off at $t = 0$. The change in the observable $\delta A(t)$ is thus given by

$$\delta A(t) = \Phi(t) A(0), \tag{2.5}$$

where $\Phi(t)$ is the relaxation function. In terms of experimentally measurable parameters of the glass transition, $\Phi(t)$ may fit the decay of two-point correlation functions measured in the time domain, such as equation 2.2.

Equivalently, such a material response could also be measured by the sudden imposition of a static perturbing field at time $t = 0$, and observing the relaxation of the material towards its new equilibrium state

$$\delta A(t) = \Psi(t) \delta A(t \to \infty). \tag{2.6}$$

$\Psi(t)$ and $\Phi(t)$ are simply related by the equality $\Phi(t) = 1 - \Psi(t)$. This framework will be of importance in our experiments.

From our experience with the frequency domain susceptibility curves, where there are two well-separated time scales for relaxation, we expect that the evolution of $\Phi(t)$ should progress in two distinct steps. The fast β relaxation should occur at very short times, and its character should vary little as the liquid is cooled. At the longer times of the α relaxation, we should witness the full decay of $\Phi(t)$. This expectation is borne out by both experimental data and computer simulations of glass forming liquids, an example of the latter being provided for amorphous selenium in figure 2-2(a). We also notice from figure 2-2(a) that, as the system is cooled, the β and α relaxation separate in time, their separation marked by a plateau that grows in length with the decrease in temperature. Much theoretical effort has been spent

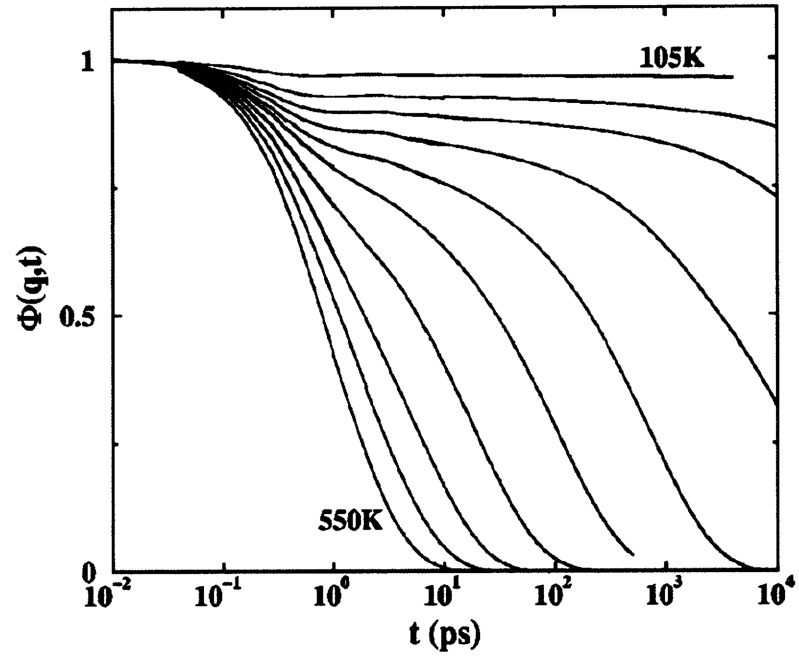

(a) Unscaled decay of two-point correlator.

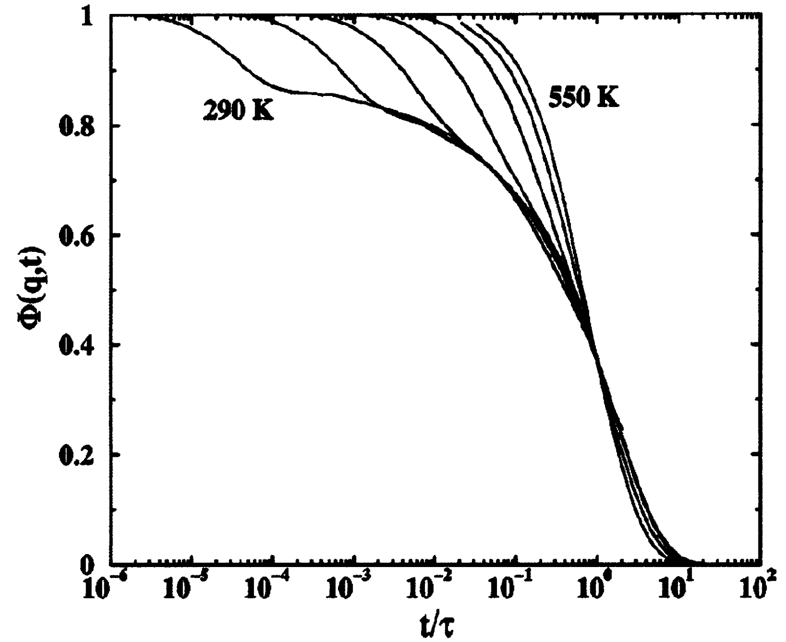

(b) Scaled decay of two-point correlator.

Figure 2-2: Decay of the two point correlator in amorphous selenium as determined from molecular dynamics simulations. (a) depicts an unscaled two-point correlator. Of note is that, with decreasing temperature, a plateau develops between the fast, β decay and the slow α decay. In (b), all of the plots have been scaled to nearly collapse to a common α decay. Figure taken from [20].

trying to understand the characteristics of this plateau, and the relaxation dynamics that precede and follow it, and we will defer this discussion until we have developed the mode-coupling theory.

It then falls on how to describe the time-dependent behavior which constitutes the α relaxation, as was done above for the frequency domain. If we are to assume a single relaxation time, we recover the simple exponential decay of the Debye model

$$\Phi(t) \propto \exp(-t/\tau_R), \tag{2.7}$$

which, in analogy to its Fourier domain companion equation 2.3, does a poor job of fitting experimental data. Better fits for the average relaxation time are obtained using the stretched exponential or Kohlrausch-Williams-Watts (KWW) relaxation function

$$\Phi(t) = \exp\left(-(t/\tau_R)^{\beta}\right) \qquad 0 < \beta \leq 1, \tag{2.8}$$

where the β parameter is used to account for the stretching in time that the relaxation displays when contrasted with pure exponential decay. This equation lacks a first-principles explanation but nevertheless provides excellent fits of time-domain α relaxation data for glass forming liquids.

While equations 2.4 and 2.8 are both representative of similar (and admittedly heuristic) generalizations of Debye relaxation, neither has a closed-form Fourier transform which may be related to the other[1], and thus the exponents and relaxation times τ_R are not common between the two functions. Mathematical comparisons between these two different approaches to relaxation in glass forming liquids can only be approached in a rather complex manner covered by Hilfer [21, 22] where an asymptotic series is used to produce one function in the other's domain. This numerically determined transformed spectrum can then itself be fit by the corresponding function in the transformed domain to recover the relevant parameters. This analysis is described in depth in chapter 4 where it is used.

---

[1] An analytical form for the Fourier transform of equation 2.4 only exists for $\alpha = 1/2, 1$, $\beta = 1$, while in equation 2.8, only for $\beta = 1/2, 1$.

2.2.2 Dynamical Heterogeneity, Non-Arrhenius Relaxation

The inability to model the susceptibility peak or, equivalently, the decay of a two-point correlator by Debye relaxation with a single relaxation time is a subject of long-standing interest. Two scenarios have been proposed [11, 23] as most spectroscopies, which interrogate a large collection of relaxing regions, are not be able to distinguish between a single non-exponential decay manifest in all probed regions, or a collection of exponential decays with different, locally varying values of τ_R. The latter interpretation is referred to as "dynamical heterogeneity."

When the evolution of the relaxation time is probed as in the dielectric experiments described above, or when the viscosity is measured in a rheology experiment, its dependence on temperature is not simply exponential. Rather, systems display strongly non-Arrhenius kinetics, as can be seen in figure 2-3. Numerous fitting functions have been posited in order to fit the dependence of $\tau_R(T)$ or $\eta(T)$ [24], the most popular being the Volger-Fulcher-Tammann (VFT) equation written for the average, or characteristic, relaxation time as

$$\tau_R = \tau_0 \exp\left(\frac{B}{T - T_0}\right) \tag{2.9}$$

where τ_0 and B are fitting parameters with units of seconds and temperature, respectively, and T_0 is a characteristic temperature. A formally identical equation is used for the temperature dependence of the viscosity. Despite much effort, there is still little insight as to the physical significance of the parameter T_0. Further, a single set of VFT parameters generally does not fit the entire curve $\eta(T)$ or $\tau_R(T)$, and so authors generally take care to fit different temperature regimes with different parameters.

2.2.3 Fragility and the Angell Plot

Earlier, it was mentioned that the several different classes of glass-forming liquid behave in nearly identical fashions under cooling. This alludes to ideas of universality based on the theory of phase transitions. Despite much effort on the part of theorists, there remains to be identified any static correlator whose critical divergence at a set temperature can be identified with a liquid-glass transition. Nevertheless, significant efforts have been made to classify different liquids' behavior in a meaningful way which seeks to highlight their similarities.

Of great use in describing a glass is its so-called "fragility," which is a measurement of the departure of the glass-former's relaxation behavior from Arrhenius-activated kinetics. In determining a glass-former's fragility, a plot is made of viscosity η or relaxation time τ_R, versus a normalized inverse temperature, T_g/T; the normalization in temperature serves to bring the behavior of all liquids to the same domain and range of a common plot, known after its originator as the "Angell" plot [25, 26]. The fragility m is defined as the slope of this curve at T_g

$$m = \left(\frac{\partial \log(\tau)}{\partial(T_g/T)}\right)_{T=T_g} . \tag{2.10}$$

Perfectly Arrhenius kinetics will have a fragility value of $m = 17$, and those materials close to this limit are referred to as "strong" liquids, while those with a larger value of m are deemed "fragile" liquids; note that this nomenclature does not refer to the actual resistance of the vitrified material to breakage.

There are a few trends that separate strong and fragile glass formers. Strong glasses are generally metallic or covalently bonded network glass formers, such as common silicate-based window glass. Their intermolecular interactions tend to be very strong and highly directional. Fragile glasses are usually hydrogen-bonded and van der Waals bonded organical molecular liquids whose intermolecular attractions are typically very non-directional and fall off faster than r^{-2}, where r is the intermolecular separation. All of these materials share the phenomenology described above.

2.2.4 Evidence of Growing Dynamic Length Scales

The concept of a diverging length scale, as is associated with typical phase transitions and critical behavior, may not be altogether lost in the glass transition, and the transition may yet be viewed through the lens of critical phenomena. Biroli and

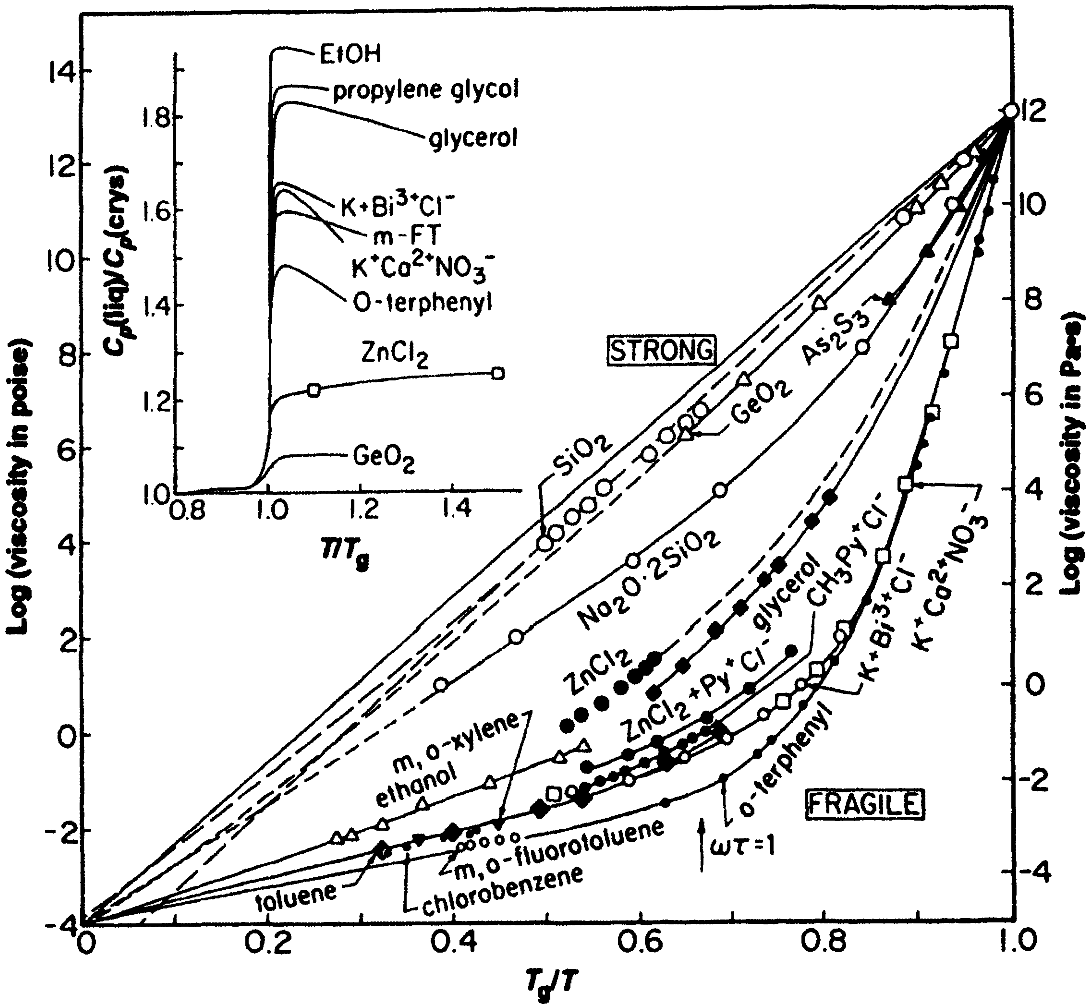

Figure 2-3: Angell plot for various glass forming liquids. For all liquids, the temperature has been scaled so that they fall in a common domain and range. The most noticeable trend is that most liquids do not obey simple Arrhenius kinetics (the straight line). This leads to the classification of "strong" versus "fragile", where the former is closer to Arrhenius activated kinetics, and the latter further away. Figure taken from [26].

coworkers have taken steps toward a renormalization group formulation for a dynamic order parameter in terms of the the density-density correlation function, given as

$$\Phi(t) = \langle \delta\rho_q(0)\delta\rho_q(t)\rangle. \tag{2.11}$$

The dependence on wavevector indicates that we must seek diverging behavior in the four point density correlation function, represented in real space by

$$\chi_4(t) = \frac{1}{V}\int d\mathbf{r}\langle \delta\rho(0,0)\delta\rho(0,t)\delta\rho(\mathbf{r},0)\delta\rho(\mathbf{r},t)\rangle. \tag{2.12}$$

Equation 2.12 measures the cooperativity of dynamical events located at the origin and those at another location **r**. Divergence would reflect growth of cooperatively rearranging regions as the glass transition temperature is approached. In contrast to conventional critical phenomena, no static divergences are present.

Direct measurement of a four-point correlation function such as that represented by relation 2.12 requires resolution in both space and time. The few measurements made to date have been performed on macroscopic colloidal systems [27] for which it is possible to directly tag constituent particles and track their behavior as the packing fraction is increased. Berthier and coworkers have been able to construct a lower bound on χ_4 which provides direct evidence of growing length scales in bulk supercooled liquids without the need for difficult spectroscopies. This is done by considering the derivative of a two-point correlator $F(t)$ with respect to a control parameter x

$$\chi_x(t) = \frac{\partial F(t)}{\partial x}. \tag{2.13}$$

In this thesis, we take $F(t)$ as the two point density correlator 2.11 and choose the derivative with respect to temperature, i.e. $x = T$. The result in the NPT ensemble, relevant for the experiments described below, is given by the fluctuation-dissipation theorem as [28]

$$k_B T^2 \chi_T(t) = N\langle \delta C(t)\delta H(0)\rangle \tag{2.14}$$

where $C(t) = \delta\rho(t)\delta\rho(0)$ in the case of density fluctuations. Here, N is the number of particles, k_B is the Boltzmann constant, and $\delta H(t)$ is the fluctuating enthalpy per unit particle. It now just remains to relate 2.14 to the four-point correlator of interest. This is done by noting that $\chi_4(t)$ in the NPH ensemble of constant enthalpy is related to the constant temperature NPT ensemble through [29]

$$\chi_4(t) = \chi_4^{NPH}(t) + k_B T^2 \chi_T^2(t)/c_P. \tag{2.15}$$

Since $\chi_4^{NPH}(t) > 0$, we can then obtain a lower bound for $\chi_4(t)$ as

$$\chi_4(t) \geq \frac{k_B}{c_P} T^2 \chi_T^2(t), \tag{2.16}$$

where an analogous equation holds for $\hat{\chi_4}(\omega)$ [30]. Hence, a determination of the frequency-dependent susceptibility spectrum as a function of temperature can be used to directly determine a lower bound for dynamic length-scale correlations. Figure 2-4 shows an example of this analysis performed for dielectric relaxation data, where a clear increase of this lower bound with an increase of relaxation time is observed via the peak of the quantity $\chi_T(\omega)$. The abscissa indicates the time scale of relaxation as it occurs in the liquid, while the ordinate is a measure of the dynamic length scale of this relaxation. As the temperature is reduced, the relaxation spectrum moves to longer times and, accordingly, the dynamic length scale associated with this relaxation increases.

2.3 The Mode-Coupling Theory of the Glass Transition

2.3.1 Introduction

The mode coupling theory refers to a truly microscopic, non-phenomenological approach to describing glass transition phenomena. The basis of the theory lies upon the Mori-Zwanzig projection operator formalism [16, 31, 32, 33, 34, 35], a method developed in the 1960s for the treatment of generalized relaxation. This method also

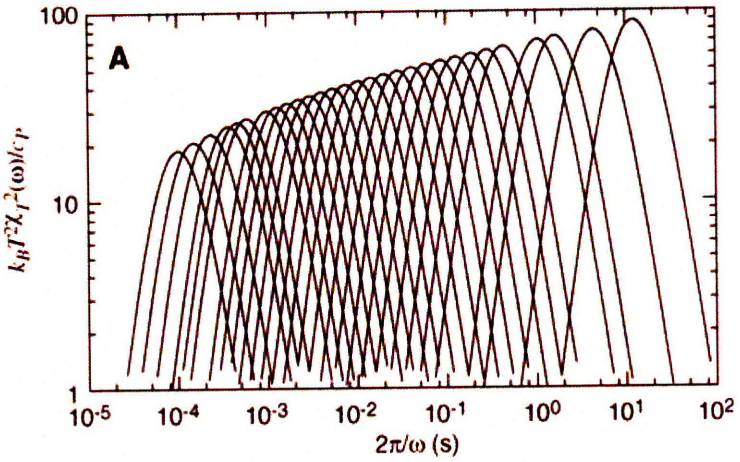

Figure 2-4: Evidence of growing length scales in supercooled glycerol. On the vertical axis is the lower bound variable χ_T and on the horizontal axis is the inverse frequency. As the temperature is decreased, the characteristic relaxation time increases, as well as the peak of the susceptibility χ_T, indicating a large lower bound for cooperative dynamics. Figure taken from [28].

finds great use in the description of light scattering spectra [34, 35]. Here we will essentially replicate the derivation of the equations of motion as provided in [16]; what follows differs little from this reference, although we will provide further depth and insight on certain steps.

In the Mori-Zwanzig formulation, the procedure is the attempt to separate the evolution of a vector of slow variables **A** in which we have physical interest, from those fast variables whose time dependence is too rapid to be relevant to the dynamics being studied. This partitioning of slow variables from fast variables must be made partly by hand, thus requiring physical intuition and motivation.

2.3.2 Derivation of the Equations of Motion

We consider a liquid comprised of N constituent particles obeying a classical Hamiltonian $H(x,p)$. Hamilton's equation of motion for any function g of the coordinates x and the canonical momentum p is given by

$$\dot{g} = \{H, g\} = i\mathcal{L}g, \tag{2.17}$$

where $\{\cdot,\cdot\}$ expresses the usual Poisson brackets. Equation 2.17 thus defines the action of the Liouville operator $\mathcal{L}$ whose role is to provide the time dependence of g. A formal solution of 2.17 is given by $g(t) = exp(i\mathcal{L}t)g(0)$, where the right-hand-side may be evaluated via a power series expansion in $i\mathcal{L}$.

The next step in approaching workable equations of motion for glass forming liquids is to define an inner product of two generally complex variables $(g|h) = \langle \delta g^* \delta h \rangle$ as the canonical average of fluctuations of g and h, i.e. $\delta g = g - \langle g \rangle$. With this inner product, we may then define a normalized projection operator $\mathcal{P}$ which projects the fluctuating content of any arbitrary function, say g, onto the slow variables $\mathbf{A}$ by

$$\mathcal{P}g = (\mathbf{A}|g)(\mathbf{A}|\mathbf{A})^{-1}\mathbf{A}, \tag{2.18}$$

where again, the inner-product operates on the fluctuating portions of its arguments only. Note that $\mathcal{P}$ is also a projection operator in the mathematical sense, i.e. that $\mathcal{P}^2 = \mathcal{P}$. This implies that the operator $(1-\mathcal{P})$ is orthogonal to $\mathcal{P}$: $(1-\mathcal{P})\mathcal{P} = \mathcal{P} - \mathcal{P}^2 = 0$, and projects the content of any function into a subspace orthogonal to that of $\mathbf{A}$.

Using 2.17 for $\mathbf{A}$ allows us to produce its time dependence $d\mathbf{A}/dt = \exp(i\mathcal{L}t)\mathbf{A}$. Inserting the identity operator $1 = \mathcal{P} + (1-\mathcal{P})$ after the propagator in this time-dependent expression allows us to write

$$\begin{aligned} d\mathbf{A}/dt &= \exp(i\mathcal{L}t)[\mathcal{P} + (1-\mathcal{P})]i\mathcal{L}\mathbf{A} && (2.19)\\ &= i\boldsymbol{\Omega}\cdot\mathbf{A} + \exp(i\mathcal{L}t)(1-\mathcal{P})i\mathcal{L}\mathbf{A}. && (2.20) \end{aligned}$$

$\boldsymbol{\Omega} = \exp(i\mathcal{L}t)\mathcal{P}\mathcal{L}\mathbf{A}$ is called the "frequency," as will become evident later on when a time-domain expression for the density autocorrelation function $\phi_q(t) = \langle \delta\rho_q(t)\delta\rho_q(0)\rangle$ is derived. The task is now to rewrite eq. 2.19 in a form which provides more physical insight. To that end, we take the second term on the right-hand-side of eq. 2.20 and add and subtract the propagator of the orthogonal variables $\exp(i(1-\mathcal{P})\mathcal{L}t)$:

$$\exp(i\mathcal{L}t) = \exp(i\mathcal{L}t) - \exp(i(1-\mathcal{P})\mathcal{L}t) + \exp(i(1-\mathcal{P})\mathcal{L}t)$$

$$
\begin{aligned}
&= \exp(i\mathcal{L}t)[1-\exp(-i\mathcal{L}t)\exp(i(1-\mathcal{P})\mathcal{L}t)] + \exp(i(1-\mathcal{P})\mathcal{L}t) && (2.21)\\
&= \exp(i\mathcal{L}t)S(t) + \exp(i(1-\mathcal{P})\mathcal{L}t). && (2.22)
\end{aligned}
$$

$S(t)$ is just the grouping of the bracketed terms in equation 2.21, and a more useful expression is retrieved by taking its derivative with respect to, and subsequently integrating in, time

$$
S(t) = \int_0^t d\tau \exp(-i\mathcal{L}\tau) i\mathcal{P}\mathcal{L} \exp(i(1-\mathcal{P})\mathcal{L}\tau) \tag{2.23}
$$

where $S(0) = 0$ as can be seen by setting $t = 0$ in the bracketed quantity of 2.21.

Substitution of equation 2.23 into equation 2.20 yields

$$
\begin{aligned}
\frac{d\mathbf{A}}{dt} &= i\mathbf{\Omega}\cdot\mathbf{A} + \int_0^t d\tau \exp(i\mathcal{L}(t-\tau)) i\mathcal{P}\mathcal{L}\exp(i(1-\mathcal{P})\mathcal{L}\tau)(1-\mathcal{P})i\mathcal{L}\mathbf{A}\\
&\quad + \exp(i(1-\mathcal{P})\mathcal{L}t)(1-\mathcal{P})i\mathcal{L}\mathbf{A}. && (2.24)
\end{aligned}
$$

We can now group terms of the second line into

$$
\mathbf{f}(t) = \exp(i(1-\mathcal{P})\mathcal{L}t)(1-\mathcal{P})i\mathcal{L}\mathbf{A}, \tag{2.25}
$$

whose form demands some comment. As mentioned above, the operator $1-\mathcal{P}$ is orthogonal to $\mathcal{P}$, which implies that it projects out the part of a function which is orthogonal to the slow variables $\mathbf{A}$. Additionally, evolution in time is given by a propagator whose argument $(1-\mathcal{P})\mathcal{L}t$ is orthogonal to the other variables' propagators.

Hence, we deduce that $\mathbf{f}(t)$ is orthogonal to $\mathbf{A}$, i.e. $(\mathbf{f}(t)|\mathbf{A}) = 0$. In terms of $\mathbf{f}(t)$, 2.24 becomes

$$
\frac{d\mathbf{A}}{dt} = i\mathbf{\Omega}\cdot\mathbf{A} + \int_0^t d\tau \exp(i\mathcal{L}(t-\tau)) i\mathcal{P}\mathcal{L}\mathbf{f}(\tau) + \mathbf{f}(t), \tag{2.26}
$$

where now it simply remains to find a more convenient representation of the convolution integral. To this end, we consider the product $i\mathcal{P}\mathcal{L}\mathbf{f}(\tau) = (i\mathbf{A}|\mathcal{L}f(\tau))(\mathbf{A}|\mathbf{A})^{-1}\mathbf{A}$. Due to the Hermiticity of $\mathcal{L}$, $(i\mathbf{A}|\mathcal{L}\mathbf{f}(\tau)) = (i\mathcal{L}\mathbf{A}|\mathbf{f}(\tau))$. We can then insert the identity operator and use the linear property of the inner product to obtain

$$\begin{aligned}(i\mathcal{L}\mathbf{A}|\mathbf{f}) &= (i(1-\mathcal{P}+\mathcal{P}\mathcal{L})\mathbf{A}|\mathbf{f}) \\ &= (i(1-\mathcal{P})\mathcal{L}\mathbf{A}|\mathbf{f}) + (i\mathcal{P}\mathcal{L}\mathbf{A}|\mathbf{f}). \end{aligned} \tag{2.27}$$

Operation of $\mathcal{P}$ on the quantity $\mathcal{L}\mathbf{A}$ will yield a function proportional to $\mathbf{A}$. Hence, the second term in 2.27 is equal to zero due to the orthogonality of $\mathbf{A}$ and $\mathbf{f}$. Closer examination of the first term reveals that the left-hand term of the inner-product is equal to $-\mathbf{f}(0)$, i.e. the complex conjugate of equation 2.25 when $t = 0$. Hence, $(\mathbf{A}|\mathcal{L}\mathbf{f}(\tau)) = -(\mathbf{f}(0)|\mathbf{f}(\tau))$ and the convolution integral may be rewritten

$$-\int_0^t d\tau(\mathbf{f}(0)|\mathbf{f}(\tau))(\mathbf{A}|\mathbf{A})^{-1}\exp(i\mathcal{L}(t-\tau))\mathbf{A}. \tag{2.28}$$

Defining $(\mathbf{f}(0)|\mathbf{f}(t))(\mathbf{A}|\mathbf{A})^{-1} = \mathbf{M}(t)$ and applying the propagator in the preceding equation, the equation of motion for $\mathbf{A}$ can finally be written as

$$\frac{d\mathbf{A}}{dt} = i\boldsymbol{\Omega}\cdot\mathbf{A} - \int_0^t d\tau\mathbf{M}(\tau)\mathbf{A}(t-\tau) + \mathbf{f}(t). \tag{2.29}$$

Examination of equation 2.29 should make it evident where the names of the various terms have come from – this equation has the form of a generalized Langevin equation where $\boldsymbol{\Omega}$ plays the role of the frequency and $\mathbf{f}$ functions as the random force[2]. $\mathbf{M}$ is considered as a memory function – its effects are felt on the variable $\mathbf{A}$ after a delay t.

At this point, it becomes necessary to make a connection with relevant observables. As mentioned above, the slow parameter of the glass transition may be taken as (although not restricted to) the fluctuations in density; the density-density correlation function is observable through light scattering experiments [34], neutron scattering experiments [36], and inelastic x-ray scattering [37]. Thus, the easiest means to make contact with experiment is in the form of a dynamic correlation function of the form

---

[2] Equation 2.29 is *not* the generalized Langevin equation. Further discussion of this point is provided on page 150 of [33].

$\mathbf{C}(t) = \langle \mathbf{A}^*(0)\mathbf{A}(t)\rangle$. Thus, we multiply 2.29 from the left with $\mathbf{A}^*(0)$ and take the canonical average to arrive at

$$\dot{\mathbf{C}}(t) = i\mathbf{\Omega} \cdot \mathbf{C}(t) - \int_0^t d\tau \mathbf{M}(\tau) \cdot \mathbf{C}(t-\tau). \tag{2.30}$$

Equation 2.30 can be solved by a Laplace transformation in time, yielding

$$\tilde{\mathbf{C}}(s) = \frac{-\mathbf{C}(0)}{s\mathbf{I} + \mathbf{\Omega} - i\tilde{\mathbf{M}}(s)} \tag{2.31}$$

If an explicit form for $\tilde{\mathbf{M}}(s)$ is known, a complete solution of the equations of motion is trivial. Usually, this is not the case and $\tilde{\mathbf{M}}(s)$ must be approximated. Recalling the memory kernel's definition as the autocorrelation of the random force $\mathbf{f}$, we can use the relation given by 2.25 to obtain an equation of motion for $\mathbf{f}$

$$\frac{d\mathbf{f}(t)}{dt} = i(1-\mathcal{P})\mathcal{L}\mathbf{f}(t) \tag{2.32}$$

and then follow all of the same arguments that led up to equation 2.30 to produce an analogous equation for $\mathbf{f}$

$$\frac{d\mathbf{f}}{dt} = i\mathbf{\Omega}_1 \cdot \mathbf{f}(t) - \int_0^t \mathbf{M}_1(\tau) \cdot \mathbf{f}(t-\tau)d\tau + \mathbf{f}_1(t). \tag{2.33}$$

where now the new Liouville operator is $\mathcal{L}_1 = (1-\mathcal{P})\mathcal{L}$ and the new projector $\mathcal{P}_1$ is given by $\mathcal{P}_1 g = (\mathbf{f}|g)(\mathbf{f}|\mathbf{f})^{-1}\mathbf{f}$. This provides a frequency, fluctuating force, and memory function as

$$i\mathbf{\Omega}_1 = (\mathbf{f}|i\mathcal{L}_1\mathbf{f}) \cdot (\mathbf{f}|\mathbf{f})^{-1} \tag{2.34}$$

$$\mathbf{f}_1(t) = \exp[i(1-\mathcal{P}_1)\mathcal{L}_1 t]i(1-\mathcal{P}_1)\mathcal{L}_1\mathbf{f} \tag{2.35}$$

$$\mathbf{M}_1(t) = (\mathbf{f}_1|\mathbf{f}_1(t)) \cdot (\mathbf{f}|\mathbf{f})^{-1} \tag{2.36}$$

Taking the inner product of 2.33 with $\mathbf{f}^*(0)$ yields

$$\frac{d\mathbf{M}(t)}{dt} = i\mathbf{\Omega}_1 \cdot \mathbf{M}(t) - \int_0^t d\tau \mathbf{M}_1(\tau) \cdot \mathbf{M}(t-\tau) \tag{2.37}$$

whose Laplace transform is

$$\tilde{\mathbf{M}}(s) = -\frac{\mathbf{M}(0)}{s\mathbf{I} + \mathbf{\Omega}_1 - i\tilde{\mathbf{M}}_1(s)^{-1}}. \tag{2.38}$$

The preceding arguments leading up to equation 2.38 can be repeated recursively leading to the n^{th} order expansion

$$\frac{d\mathbf{M}_n(t)}{dt} = i\mathbf{\Omega}_{n+1} \cdot \mathbf{M}_n(t) - \int_0^t d\tau \mathbf{M}_{n+1}(\tau) \cdot \mathbf{M}_n(t-\tau) \tag{2.39}$$

which finally leads to a repeated fraction for the expression of $\tilde{\mathbf{C}}(s)$

$$\tilde{\mathbf{C}}(s) = \cfrac{-1}{s\mathbf{I} + \mathbf{\Omega} + \cfrac{1}{s\mathbf{I} + \mathbf{\Omega}_1 + \cfrac{1}{s\mathbf{I} + \mathbf{\Omega}_2 + \cdots} \cdot i\mathbf{M}_1(0)} \cdot i\mathbf{M}(0)} \cdot \mathbf{C}(0). \tag{2.40}$$

To this point, no approximations have been made, entailing that equation 2.40 is exact; in fact, equation 2.40 is nothing more than a restatement of equation 2.17 [33]. The physics a particular system can then be recovered by an appropriate choice of slow variables in the vector $\mathbf{A}$ and making appropriate approximations to the memory function $\mathbf{M}$ [35]. Since the glass transition is marked by an increase in viscosity upon cooling, it is natural to choose those variables associated with flow to be the slow, relevant variables of the theory. The traditional choice for $\mathbf{A}$ is a single-element column vector consisting of the density fluctuations of wavevector q, ρ_q [16], while other theorists extend the theory to incorporate transverse current fluctuations, j_q [38], as well as their coupling with each other. Once the selection of the slow variables has been made, the remaining issue is how to truncate the hierarchy described by the continued fraction in equation 2.40. Working to high order is difficult mathematically, and so the fraction is typically closed after second order. The final issue is how to approximate the memory function $\mathbf{M}$.

The crux of the mode-coupling approximation is that the different fluctuations of the slow variables $\mathbf{A}$ can decay into either other modes of the same type (say, a density fluctuation into another density fluctuation), or into other conserved hydrodynamic modes (e.g. a density fluctuation may decay into a transverse current fluctuation). This idea was originally proposed by Kawasaki in his study of the critical slowing-down of density fluctuations near the liquid-gas critical point [35, 39], and finds inspiration in the observations presented in section 2.2.1 regarding the growing time scale of density fluctuations in liquids cooled to their glass transition temperature.

Mathematically, this mode coupling is represented by products of the fluctuations of the slow variable, of the form $\mathbf{AA}$. Here the two copies of $\mathbf{A}$ represent the fluctuations of the two modes under consideration; since this quantity is the product of two slow variables, it is, itself, a slow variable. Furthermore, the product $\mathbf{AA}$ is generally *not* orthogonal to the fluctuating force $\mathbf{f}$, so that the memory function $\mathbf{M}(t) = (\mathbf{f}|\mathbf{f}(t)) \cdot (\mathbf{A}|\mathbf{A})^{-1}$ may also have a nonzero overlap with the product $\mathbf{AA}$.

This is the fundamental launching point for the mode-coupling theory of Bengtzelius and coworkers [40], who assumed that the random force may simply be replaced by its projection onto the set of all coupled terms $\mathbf{AA}$; coupling to higher order is considered too small to impact the dynamics. This is equivalent to stating that the slow part of $\mathbf{M}$ is fully contained by the set of these pair products.

For the rest of the discussion, we shall consider $\mathbf{A} = A$, a scalar quantity which may be the density fluctuations $\delta\rho$. The memory function can then be split into a fast piece and a slow, mode coupling piece M_{MC}, yielding

$$M_{MC}(t) = |(AA|f)|^2(AA|AA)^{-1} \cdot (AA|AA)^{-1} \cdot (AA|\exp[i(1 - \mathcal{P}\mathcal{L}t]AA) \cdot (A|A)^{-1}. \tag{2.41}$$

The physical implication of this approach is that the slow dynamics are contained in the coupling of the modes with each other (represented by the pair product (AA)), and it is this which creates the mechanism for structural arrest. As the liquid is cooled, this non-linear feedback of coupled modes inhibits the relaxation of the slow variables, causing the liquid to solidify while also inhibiting the motion necessary for crystallization.

Further physical insight is needed to connect the mode-coupling theory with the real-life glass transition. This can only be approached mathematically with further simplification of 2.41, which contains static four-point correlation functions and a propagator whose impact on the time evolution is not straightforward. Concerning the four-point correlators, the factorization approximation is made, which states that the four-point correlator can be replaced by the product of two-point correlators

$$(AA|AA) \approx (A|A)^2 \tag{2.42}$$

and that the propagator of the projected dynamics can be replaced by the original one

$$\exp[i(1-\mathcal{P})\mathcal{L}t] \approx \exp i\mathcal{L}t. \tag{2.43}$$

The result is that the memory function $M_{MC}(t)$ can be written as

$$M_{MC}(t) = |V(AA,f)|^2 (A|A(t)) \cdot (A|A(T)) \tag{2.44}$$

where the "vertex" $|V(AA,f)|^2$ can be obtained from equations 2.42 and 2.43.

This is the final step toward producing the equations of motion of the mode-coupling theory as it applies to the glass transition. Picking the slow variable as the normalized density-density correlator

$$\begin{aligned} \mathbf{A} &= \frac{1}{N}\frac{\langle \delta\rho(\mathbf{q},t)\delta\rho^*(\mathbf{q},t)\rangle}{\langle \delta\rho(\mathbf{q},0)\delta\rho^*(\mathbf{q},0)\rangle} \\ &= \frac{F(q,t)}{S(q)}, \end{aligned} \tag{2.45}$$

relation 2.40 can be closed to second order to yield

$$\Phi(q,z) = \frac{-1}{s - \dfrac{\Omega_q^2}{s + \Omega_q^2\left(\tilde{M}^{reg}(q,z) + \tilde{M}(q,z)\right)}}. \tag{2.46}$$

Here, $S(q)$ is the static structure factor and $\Omega_q^2 = q^2 k_B T/(mS(q))$, where k_B is the Boltzmann constant and m is the particle mass. In relation 2.46, the memory function has been explicitly split between its fast, "regular" part, $\tilde{M}^{reg}(q,z)$, and the slow part $\tilde{M}(q,z)$. Transforming this equation to the time domain produces

$$\ddot{\Phi}(t) + \Omega_q^2 \Phi(t) + \Omega_q^2 \int_0^t dt' [M^{reg}(q, t-t') + M(q, t-t')] \dot{\Phi}(q, t') = 0 \tag{2.47}$$

where the slow part of the memory function is given by

$$M(q,t) = \frac{1}{2(2\pi)^2} \int d\mathbf{k} V^{(2)}(q, k, |\mathbf{q}-\mathbf{k}|) \Phi(k,t) \Phi(|\mathbf{q}-\mathbf{k}|, t). \tag{2.48}$$

In this expression, the vertex $V^{(2)}$ is given by

$$V^{(2)}(q, k, |\mathbf{q}-\mathbf{k}|) = \frac{n}{q^2} S(q) S(k) S(|\mathbf{q}-\mathbf{k}|) \left(\frac{\mathbf{q}}{q} [\mathbf{k} c(k) + (\mathbf{q}-\mathbf{k}) c(|\mathbf{q}-\mathbf{k}|)] \right)^2, \tag{2.49}$$

n being the particle density, and $c(k) = n(1 - 1/S(q))$.

Equations 2.47-2.49 constitute the mode-coupling equations. The hallmark of the mode-coupling theory derives from the products of density autocorrelations in equation 2.48, which constitute the nonlinear feedback mechanism. The strength of this feedback is controlled by the strength of the vertex $V^{(2)}$, equation 2.49, whose amplitude is set by the values of the static structure factor contained therein.

Thus, the mode-coupling theory gives us the physical picture of how structural arrest occurs. Cooling or compression of the system results in a change of the static structure factor $S(q)$, which become more sharply peaked. This, in turn, serves to increase the degree of coupling between the density fluctuations. The increase in this coupling results in an increase in the retarded viscosity which controls relaxation of the system back to its unperturbed state. In a real-space picture, the interpretation is in terms of a "caging" effect. Molecules are trapped in a cage formed by their neighbors, which are in turn trapped in their own cages, etc. As the system is cooled or compressed, the amount of cooperative motion required to rearrange in response to a perturbation increases and the dynamics slow down accordingly, all the way until complete arrest.

2.3.3 Predictions of the Mode-Coupling Theory

Now that the complete equations have been derived, it is possible to form both qualitative and quantitative predictions on the glass transition through the study of their solutions. What follows are results that are obtained from the so-called "idealized mode-coupling theory," which takes only the density fluctuations as the slow variable.

Time-Temperature Superposition, criticality and non-ergodicity

In the process of vitrification, the alpha relaxation peak is shifted out to progressively lower frequency with the reduction of temperature. Fits to the alpha relaxation spectrum are made and a relaxation time τ is deduced, either through the time-domain fit of the decay of the two-point correlator $\Phi(q, t)$, or by a frequency domain relaxation function. In the mode-coupling theory, the spectrum itself is predicted to not change in shape. Rather, the dependence of the two-point correlator is given by

$$\Phi(t, T) = \Phi(t/\tau(T)). \tag{2.50}$$

This result is known as time-temperature-scaling or time-temperature-superposition (TTS). In the idealized mode-coupling theory, the function $\tau(T)$ is predicted to increase with a decrease in the temperature as

$$\tau_x(T) = C_x(T - T_c)^{-\gamma}, \tag{2.51}$$

where T_c is a critical temperature approached from the liquid side. With the average relaxation time infinite, the system cannot relax in response to an external perturbation, implying the "falling out of equilibrium" commonly used for describing the glass transition. Now unable to relax, the liquid ceases to be ergodic, i.e. it is not able to visit all allowable parts of phase space, specifically those associated with crystallization.

The mode-coupling theory provides a numerical estimate of the so-called non-ergodicity, or Debye-Waller factor, and we will closely review the arguments presented in Hansen and MacDonald which provide this through the so-called F_2 model, which assumes that the largest contribution to the static structure factor is given by its first, largest peak, i.e. $S(q) \approx 1 + a\delta(q - q_{max})$. We also approximate that the fast dynamics of the memory function given by M_{reg} are quick relative to the other dynamics in the problem, i.e. $M_{reg}(t) = \nu\delta(t)$. This leaves the mode-coupling equation as

$$\ddot{\Phi}(t) + \Omega_q^2 \nu \dot{\Phi}(t) + \Omega_q^2 \Phi(t) + \lambda \Omega_q^2 \int_0^\infty \left[\Phi(t-t')\right]^2 \dot{\Phi}(t')dt'. \tag{2.52}$$

Where λ is a control parameter which sets the magnitude of the mode coupling and may represent the effect of density or temperature.

When equation 2.52 is written in the Laplace domain it becomes

$$\tilde{\Phi}(s) = \frac{-1}{s - \dfrac{\Omega_q^2}{s + \nu + \Omega_q^2 \tilde{M}(s)}}, \tag{2.53}$$

where the memory function is identified as

$$\tilde{M}(s) = \lambda \int_0^\infty \left[\Phi(t)\right]^2 \exp(-st)dt. \tag{2.54}$$

We are interested in the finite, final value f that the two-point correlator reaches in the long time limit, i.e $\lim_{t\to\infty} \Phi(t) = f$; or, using the final value theorem of Laplace transforms

$$\lim_{s\to 0} \tilde{\Phi}(s) = f/s. \tag{2.55}$$

Using equation 2.55 in equation 2.52 and solving for the memory function gives

$$\lim_{s\to 0} \tilde{M}(s) = \frac{f}{s(1-f)}. \tag{2.56}$$

Equivalently, solving for $\tilde{M}(s)$ in the $s \longrightarrow 0$ limit produces

$$\lim_{s \to 0} \tilde{M}(s) = \frac{\lambda f^2}{s} \tag{2.57}$$

which, combined with the previous expression gives

$$\frac{f}{1-f} = \lambda f^2. \tag{2.58}$$

There are two solutions. The first is $f = 0$, implying that the correlator has fully relaxed and the system is in the ergodic state. In the non-ergodic state, the two-point correlator remains at a finite value for long times, given by

$$f = \frac{1}{2}\left[1 \pm (1 - 4/\lambda)^{1/2}\right]. \tag{2.59}$$

As f refers to the physically observable two-point density correlator, it must be a real number. Hence, only the root $f = 0$ is acceptable for $\lambda < 4$. In the limit of $\lambda \longrightarrow \infty$, $\frac{1}{2}\left[1 - (1 - 4/\lambda)^{1/2}\right] \longrightarrow 0$, implying that the system comes closer to ergodicity with increase in the controlling parameter. This, too, is unphysical. Thus, we pick the root $\frac{1}{2}\left[1 + (1 - 4/\lambda)^{1/2}\right]$, which states that the larger the controlling parameter, the closer $\Phi(t)$ is to 1 and the more out of equilibrium the system becomes. Conventionally, the non-ergodicity parameter is given in terms of the distance from the transition by $\epsilon = \sigma(\lambda - \lambda_C)/\lambda_C$, where $\sigma = -1$ for an ergodic system and $\sigma = +1$ for the arrested one. The expression for f then reveals a square-root cusp as ϵ tends to zero

$$\lim_{\epsilon \to 0} f = \frac{1}{2}(1 + \epsilon^{1/2}). \tag{2.60}$$

An alternative definition of the non-ergodicity parameter in terms of elastic parameters is given by [41]

$$\lim_{q \to 0} f = 1 - \left(\frac{c_0}{c_\infty}\right)^2, \tag{2.61}$$

where c_0 is the zero-frequency longitudinal speed of sound and c_∞ is the instantaneous speed of sound. The identification of equation 2.61 as the non-ergodicity parameter comes about by integrating the $q \rightarrow 0$ limit of the dynamical structure factor for elastic light scattering

$$S_q(\omega) \propto \frac{M''(\omega)/\omega}{[(\omega/q)^2\rho - M'(\omega)]^2 + [M''(\omega)]^2}. \tag{2.62}$$

This integral defines the Debye-Waller factor; taking its low-wavevector limit yields equation 2.61.

From the previous discussion, it should be obvious what non-ergodicity refers to mathematically: that the two-point correlator does not decay back to zero at long times. In other words, the system remains out of equilibrium for all times, not just on the time-scales relevant for observation. In contrast to the case of diverging length scales in order-disorder transitions, this mathematical divergence is unphysical. The standard physical argument theorists have devised to address this issue is that thermally activated processes, such as coupling to transverse current modes, step in to relax the system back to equilibrium at long times. The "extended" mode coupling theory explicitly incorporates these extra modes into the vector of slow variables, and when many of the above computations are performed with them in place, ergodicity is mathematically restored.

Recent work by Mayer, Miyazaki, and Reichman [43] points to the factorization of the four-point correlators and replacement of the propagator $\exp(i(1-\mathcal{P})\mathcal{L}t)$ by $\exp(i\mathcal{P}\mathcal{L}t)$ as being the mathematical sources of these woes. These steps represent the two significant, uncontrolled approximations of the Mode Coupling Theory – they are utilized simply as mathematical conveniences whose only justification comes from the ability of the subsequent theory to make predictions that match computer simulation and experiment. In [43], Mayer et al. delay this factorization entirely by directly incorporating the higher order correlations and building a coupled hierarchy independent of mode wavevector. In the recursive relationship, however, they derive exact relationships between the hierarchy of frequencies Ω_n. The mode coupling equations are as before with the coupling vertex V (referred to as Λ in [43]) approximated as pairs of the static structure factor. When evaluating the hierarchy numerically to

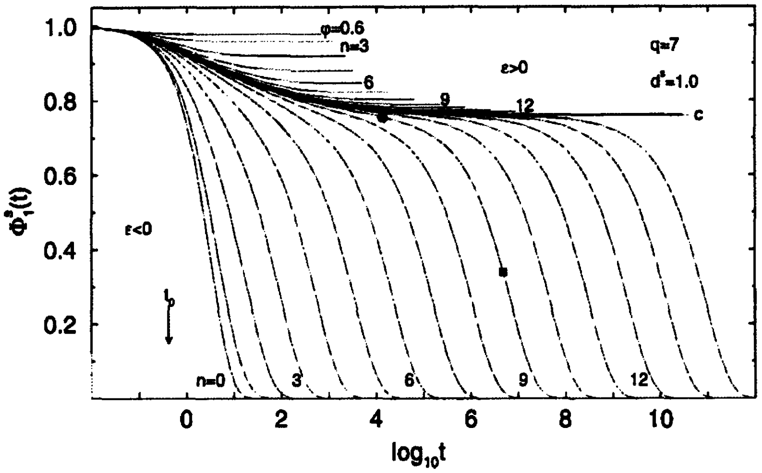

Figure 2-5: Behavior of the two-point correlator for a hard-sphere system for various packing fractions. We note that at and above a critical packing fraction, denoted in the figure by c, the correlator does not relax back to equilibrium at long times, and in fact persists out to $t \to \infty$, illustrating the concept of non-ergodicity. Figure taken from [42].

finite order, the density-density correlator is still observed to level off to a plateau for a critical value V_c of the vertex parameter, i.e. for specific values of the static structure factor. This value of V_c grows monotonically with an increase in the evaluated order. When the hierarchy is taken to infinite order, ergodicity is restored for all values of the coupling vertex without the need to incorporate any more variables than the original density fluctuations. Equally remarkable is the fact that this approach to the mode-coupling theory still produces many of the other predictions, specifically those surrounding factorization of the two-point correlator, as discussed below.

Behavior of the two-point correlator

The biggest successes of the mode-coupling theory are centered around the behavior of the two-point correlator in the β relaxation regime and how it relates to the α regime. The first of these is the so-called "factorization property," which states that the time dependence of any correlator of the variable x in the β regime is given by

$$\Phi_x(t) = \Phi_x^c + h_x G(t), \tag{2.63}$$

the sole caveat being that x must have a non-zero projection onto density fluctuations. Φ^c_x is the magnitude of the non-ergodicity parameter, h_x is a critical amplitude, and $G(t)$ is a universal function in common with all considered relaxing variables. Substituting 2.63 into 2.47 and using the approximation that the system is close to the critical point defined by 2.51 gives

$$\sigma + \lambda G(t)^2 = \frac{d}{dt}\int_0^t G(t-t')G(t')dt', \tag{2.64}$$

where $\sigma = C(T_c - T)/T_c$ denotes the distance from the critical temperature T_c, and λ is the so-called "exponent parameter," a quantity which may be calculated from the vertices $V^{(2)}$. The expression for $G(t)$ can only be determined asymptotically, allowing us to investigate four distinct regimes of interest. We may consider the system to be either in the nonergodic state, i.e. $T < T_c$, or in the liquid state $T > T_c$. Then, we make a division in time either much earlier or later relative to the occurrence of the plateau at t_σ. Within the mode-coupling theory, the location of the plateau is shown to obey a power-law divergence in temperature of the form

$$t_\sigma = t_0/|\sigma|^{1/2a}, \tag{2.65}$$

where t_0 is a microscopic time, and the exponent a will be determined below.

For early times, i.e. when $t \ll t_\sigma$,

$$G(t) = \sqrt{|\sigma|}(t_\sigma/t)^a \tag{2.66}$$

on either side of the critical temperature T_c. The exponent a is related to the parameter λ by

$$\frac{\Gamma(1-a)^2}{\Gamma(1-2a)} = \lambda, \tag{2.67}$$

Γ being the standard Γ-function and $0 < a < 0.5$.

For times $t \gg t_\sigma$ but still much shorter than the α relaxation regime,

$$G(t) = \begin{cases} \sqrt{|\sigma|\,(1-\lambda)} & T < T_c \\ -\sqrt{|\sigma|}\,(t/t_\sigma)^b & T > T_c \end{cases} \tag{2.68}$$

where the exponent $0 < b < 1$ of the critical, liquid state dynamics is given in terms of λ by

$$\frac{\Gamma(1+b)^2}{\Gamma(1+2b)} = \lambda. \tag{2.69}$$

The expressions 2.66 and 2.68 for $G(t)$ in the different limits may now be resubstituted into the original factorized equation 2.63 to recover the behavior of the correlator for all times and temperatures. Below T_c,

$$\Phi_x(t) = \begin{cases} \Phi_x^c + h_x\sqrt{|\sigma|}(t_\sigma/t)^a & t_0 \ll t \ll t_\sigma \\ \Phi_x^c - h_x\sqrt{|\sigma|}/\sqrt{1-\lambda} & t_0 \ll t_\sigma \ll t \end{cases} \tag{2.70}$$

while above the critical temperature,

$$\Phi_x(t) = \begin{cases} \Phi_x^c + h_x\sqrt{|\sigma|}(t_\sigma/t)^a & t_0 \ll t \ll t_\sigma \\ \Phi_x^c - h_x\sqrt{|\sigma|}(t/t_\sigma)^b & t_0 \ll t_\sigma \ll t. \end{cases} \tag{2.71}$$

Of note in equation 2.70 is the fact the universal function $G(t)$ is constant for all values of time when the system is cooled below T_c. This expresses that the system is not allowed to return to equilibrium, reflecting the non-ergodicity described above. Above T_c, as described in 2.71, we can obtain insight on the decay of the two-point correlator in the α regime, which decays as $(t/\tau)^b$, where

$$\tau = t_0/|\sigma|^\gamma. \tag{2.72}$$

γ is thus given in terms of the other exponents by

$$\gamma = \frac{1}{2a} + \frac{1}{2b}, \tag{2.73}$$

a result which states that the fast β dynamics measurable by the exponent a are inherently tied to the slow α dynamics governed by b.

2.3.4 Recent Theoretical Developments and Improvements

Das and coworkers have studied the physics of shear waves in supercooled liquids from the mode-coupling perspective in a number of recent publications [44, 45, 46, 47]. In this case, one must add the transverse currents (and their coupling to density fluctuations) to the collection of slow variables and examine the transverse autocorrelation function, the physically relevant correlator for shear waves. The system studied is a collection of hard spheres in the Percus-Yevick approximation, and thus the packing fraction Δ is the relevant control parameter. When a critical packing fraction $\Delta_c = 0.525$ is reached, the system jams and the density autocorrelators do not relax to equilibrium at long times, indicating the onset of the ideal glassy phase.

The onset of shear waves is observed when the transverse autocorrelation function exhibits an oscillatory decay, which does not necessarily occur only for values of $\Delta > \Delta_c$. Instead, the relevant parameter is a characteristic wavevector q_0 below which the correlator is simply diffusive and shear wave propagation is not observed to occur. The model predicts a power law divergence of the length scale $L_0 = 2\pi/q_0$ as

$$L_0 = \frac{1}{(\Delta - \Delta_c)^{1.2}} \tag{2.74}$$

when the critical packing fraction is approached. Treatment with an extended theory that properly accounts for all couplings of the various transverse modes to the density shows that a complete divergence is cut off, leaving a weaker enhancement. Further results in [45] include the behavior of the transverse acoustic velocity which, below critical packing fraction, is shown to go to zero at finite wavevector.

This approach differs slightly from that taken in [46], which is motivated by the supposed connection between the elastic parameters of the glass and the transport quantities of the liquid state. Briefly, in this treatment, the mode-coupling theory is generalized to include in its collection of slow modes the displacements $\mathbf{u}_\alpha$ from their equilibrium positions $\mathbf{R}_\alpha^0$ of the disordered state (here α indicates the particle index). Since the supercooled liquid is considered solid on the timescales of the simulation, the positions $\mathbf{R}_\alpha^0$ are considered stationary, and as particle displacements in a solid medium are considered, the resulting generalized Langevin equation explicitly includes terms containing the shear and bulk elastic moduli G and K, respectively.

The authors pick the control parameter Δ_0 to represent the scaled temperature of an Angell plot T/T_g, and study the evolution of the average relaxation time in the α regime versus Δ_0 in order to determine a fragility parameter. The upper wavevector cutoff of the density fluctuations considered in the numerical evaluation of the integrals computed in this study (denoted in [46] by Λ) provides a second control parameter, $\lambda_0 = (\Lambda^3/6\pi^2 n_0)(v/c_L)$. Here n_0 is the equilibrium density, c_L is the longitudinal sound speed, and $v = 1/\sqrt{\beta \overline{m}}$ is an average thermal velocity for a particle of mass $\overline{m}$ at a temperature given by $\beta = 1/k_B T$. The results of performing this analysis as a function of parameters K/G is shown in figure 2-6, where good agreement between experiment and theory can be recovered for $\lambda_0 = 0.4$.

Other theoretical predictions from this model include a derived dependence of the stretching parameter of the KWW law, β, as a function of the Poisson ratio, σ. Further analysis of the dependence of the power law exponent a of equation 2.70 versus K/G in the long-time limit is also discussed therein.

2.3.5 Tests and Failures of the Mode-Coupling Theory

The results of the mode-coupling theory discussed above have been been tested repeatedly since the first predictions were formulated in the mid to late 80's. The literature abounds with light scattering measurements [49, 50], dielectric relaxation studies [51], x-ray [52] and neutron scattering [53] experiments, and nuclear magnetic resonance measurements [54]. Computer simulation is also an indispensable tool in the study of the theory [55], as it is able to give insight to response on small length and time scales that are difficult to examine in the lab.

Arguably, the biggest success of the mode-coupling theory has been the relationships between the exponents of the β and α relaxation regime, specifically equations

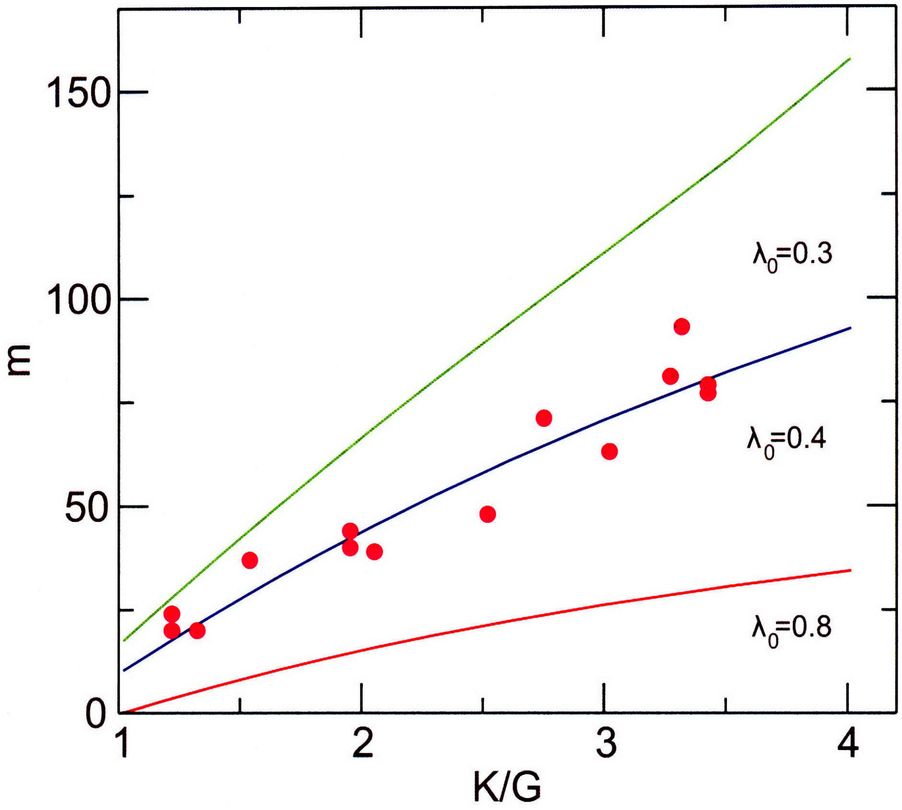

Figure 2-6: Fragility versus K/G in MCT elastic model for three different values of the wavevector cutoff λ_0, with Δ_0 fixed at 1.7. The points are experimental data taken from [48]. For the value $\lambda_0 = 0.4$, the model matches the observation of a correlation between fragility and ratio of bulk and shear elastic moduli. Figure taken from [46].

2.67 and 2.69. These have been confirmed by both molecular dynamics simulations and experiments [56]. Further, many of the predictions concerning the square-root cusp of the non-ergodicity parameter, described above, have been confirmed by both light scattering measurements [57], as well as by inelastic x-ray [58] and neutron scattering [59].

Despite these successes, the mode-coupling theory suffers from a collection of shortcomings which preclude its acceptance as the overarching theory of the glass transition. The most famous of these is the prediction of completely frozen-out dynamics at the critical temperature T_c. Experimentally, T_c has been determined to be well above T_g through non-ergodicity measurements. As the system is still in the supercooled liquid state at these temperatures, it is certain that the two-point correlator is not inhibited from coming back to equilibrium at long times. This is the issue addressed by Mayer et al. [43] and discussed above.

Another problem is that the aforementioned predictions for a power law divergence in the relaxation times, and thus for transport coefficients, are only valid for a small temperature range and do not fully encapsulate the experimentally observed dynamics as well as the VFT equation. A proper theory of the glass transition would be able to account for the evolution of relaxation in *all* temperature and frequency regimes. To date, that has yet to be accomplished.

An imperfect theory it may be at present, but as demonstrated in [43], it is a changing one and thus worthy of continued attention and experimental scrutiny. As the natural variable of the mode-coupling theory is fluctuations in density, any metrology which directly couples into these is well suited to test its predictions and guide theorists towards overcoming its shortcomings. This motivates the extensions of light scattering techniques which directly probe these fluctuations and whose use will form the experimental foundation of this thesis.

Chapter 3

Experimental Methods

3.1 Introduction

In the previous chapter, we saw the need to interrogate the density fluctuations of the liquid state, as they can provide a direct window upon the relaxation dynamics intrinsic to the glass transition. These density fluctuations comprise the longitudinal acoustic phonon spectrum whose most common method of measurement has been Brillouin Scattering spectroscopy. In this technique, depicted schematically by figure 3-1, a single CW laser beam is incident upon the sample and this light is scattered from thermally present phonons. By measuring the frequency shift at a selected angle for the scattered light, energy and momentum conservation can be used to recover the phonon frequency and wavevector. Measurements conducted at various scattering angles can thus build an acoustic phonon spectrum.

Typically the signal levels in Brillouin Spectroscopy are very low, and each data point generally requires hours of signal averaging. To overcome this significant experimental disadvantage, we have chosen a technique, Impulsive Stimulated Scattering (ISS), by which a large, coherent population of acoustic phonons at a user-selected wavevector can be created and subsequently probed. The presence of this large coherent phonon amplitude boosts signal levels significantly, and the beating of the Stokes and Anti-Stokes contributions to the scattered light can become large enough that the scattering may even be recorded in the time domain on a single-shot basis, as

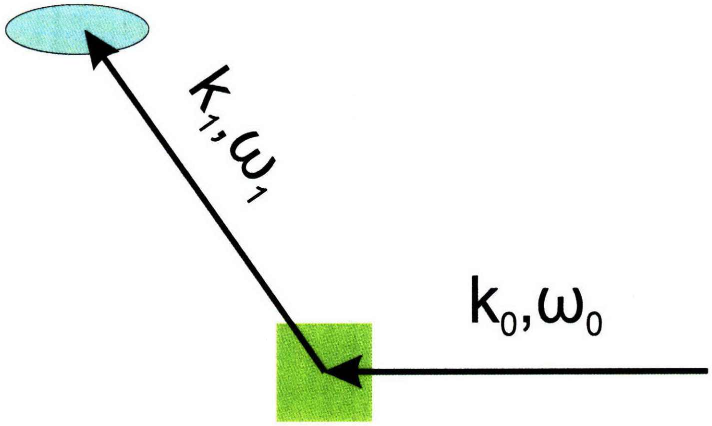

Figure 3-1: Schematic description of Brillouin scattering. A beam of frequency ω_0 and wavevector k_0 is scattered off of the sample by thermally present phonons with frequency ω_{ph} and wavevector k_{ph}. The scattered light comes out frequency shifted as $\omega_1 = \omega_0 \pm \omega_{ph}$ and wavevector $k_1 = |k_0 \pm k_{ph}|$.

opposed to integrated over several hours in the frequency domain.

The methodology of an ISS experiment is simple, in principle. As depicted in figure 3-2, a single pulse from a short-pulse laser system is selected, split into two parts, and the two pulses intersected within the sample at an experimentalist-defined angle. Depending upon the relative polarizations of the two intersected beams, the result is an interference pattern - or grating - of either laser intensity or polarization inside the sample. This optical grating lasts for only the duration of the laser pulse, and given the short nature of the exciting pulses compared to any acoustic oscillation period, the material is driven impulsively. The excitation so generated shares the grating character of the optical excitation pattern. It is this quality of the metrology which is the source of its more common name, "transient grating."

Once driven, the evolution of this excitation in time is probed by coherent scattering of a separate beam. For optimal scattering to occur, this beam must be introduced at the Bragg diffraction angle set by the wavelength of the imprinted grating. In practical terms, this beam may be a piece of the original driving laser that has been mechanically and incrementally stepped at regular delayed intervals to build up a time-dependent signal trace of diffracted light. With the advent of fast digitizing electronics, it may also be a CW laser whose diffraction off the time-evolving transient

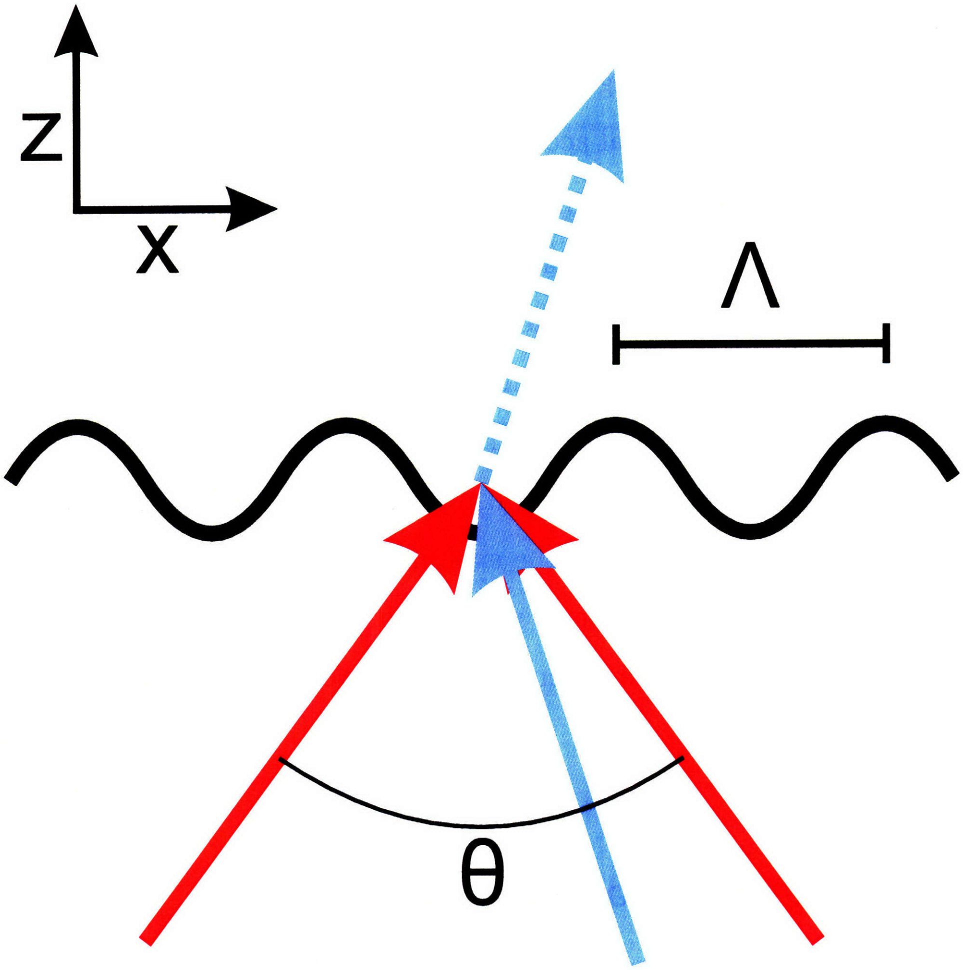

Figure 3-2: Schematic description of Impulsive Stimulated Scattering. Two ultrashort pump pulses, shown here in red, are incident on the sample with relative angle θ to generate a grating pattern of wavelength $\Lambda = \lambda/2\sin(\theta/2)$, where λ is the wavelength of the light. A probe beam, designated in blue, is incident upon the grating at the Bragg angle, and exchanges energy and momentum with material excitations of the grating wavevector. The coherently scattered probe light, shown here by the dashed line, is recorded in the time-domain by an amplified photodetector.

material grating is recorded on a digitizing scope.

Transient grating methods have found their use in studying a variety of systems: in superconductors to probe quasiparticle lifetimes [60], as a probe of electronic excited state dynamics [61], and to generate narrowband terahertz responses via Raman active modes in ferroelectric crystals [62], to name a few. For the experiments on glass-forming liquids, we take advantage of their ability to thermally and electrostrictively drive both shear and longitudinal acoustic waves.

In what follows, we shall first introduce the transient grating technique from a theoretical point of view. Both longitudinal and shear components of the signal will be computed from generalized hydrodynamics, and their characteristics as a function of temperature examined. Other consequences of laser excitation, such as the torque on the constituent molecules which results in a decaying orientational response (Optical Kerr Effect), will be briefly discussed within the context of the derivation of shear waves. From there, we will describe the experimental apparatus that has been built and used to perform the measurements made in this thesis. We proceed with detailed information on how the data has been processed. We conclude with the procedures used in sample purification.

3.2 Theoretical Considerations

Before attempting to derive signal, we first concern ourselves with which variables' time dependencies are interrogated in a transient grating experiment on supercooled liquids. To this end, we consider the i^{th} component of the probe electric field E^i_{inc} incident on an excited portion of the medium. In the linear response regime, the j^{th} component of the scattered electric field E^j_{sc} of the probing laser is proportional to the change in refractive index δn. As changes in the magnetic permeability $\delta\mu^{ij}$ in such experiments are negligible, the relevant part of the refractive index is the material's permittivity and so $\delta n \propto \delta\epsilon^{ij}$. Mathematically, the scattered field is proportional to

$$E^j_{sc}(\vec{k} \pm \vec{q}, t) \propto \delta\epsilon^{ij}(\vec{q}, t) E^i_{inc}(\vec{k}, t) \tag{3.1}$$

where $\vec{k}$ is the incident wavevector, $\vec{k}+\vec{q}$ is the scattered wavevector, and $\vec{q}$ is the transient grating wavevector.

Equation 3.1 states that in order to compute the signal embedded in the time-dependence of E^j_{sc}, we need to compute the time-dependence of the material's permittivity, or equivalently its polarizability, induced by the pump laser. This quantity couples to many of the intensive variables of the system. For longitudinal waves, which are fluctuations in density, the variables that concern us are the density ρ and temperature T. The importance of the former is obvious whereas the latter is relevant mainly for the reason that changes in temperature are usually strongly coupled to changes in density. We also note that in some materials, fluctuations in density and temperature couple to the diagonal components of ϵ^{ij}, and hence in the longitudinal case, the polarization states of the incident and scattered waves are the same. This gives rise to the name polarized scattering. Since both incident pump fields, the incident probe field, and the scattered signal field share the same polarization, this configuration is denoted VVVV.

In the case of shear waves, the change in the permittivity $\delta\epsilon^{ij}$ is not the result of changes in either density or temperature. Rather, it is the induced polarization anisotropy Q^{ij} which is the relevant variable [63]. This quantity couples into the off-diagonal components of ϵ^{ij}, and it is these components which are responsible for the scattered field. Here, the incident and scattered electric fields have different polarizations, hence the phrase "depolarized scattering" is used to describe the process by which shear waves are observed. In this case, the two pump beams are perpendicularly polarized to each other, and the incident probe field has an orthogonal polarization to the scattered signal field. We denote this configuration VHVH.

The theory for Impulsive Stimulated Scattering in supercooled liquids has been developed elsewhere for the case of longitudinal waves [7] and we will review the derivation below. The corresponding derivation for shear waves is similar in practice, but offers enough subtlety to be treated separately and in detail.

3.2.1 VVVV Signal

The transient grating experiment, as depicted in figure 3-2, results from the action of two coherent, polarized pulses of field strength $E_0/2$ incident upon the sample at an angle θ. Each beam has a wavevector given by $\mathbf{k} = \pm k_x\hat{x} + k_z\hat{z}$, using the coordinate system of figure 3-2. For fields polarized in the $\hat{y}$ direction

$$\mathbf{E}(\mathbf{r}) = E_0 e^{i(\omega t - k_z z)}\cos(k_x x)\hat{y}. \tag{3.2}$$

where $\omega = ck$ is the frequency of the light field. Equation 3.2 shows us that the intersection of the two beams has resulted in a modulation of the overall field with wavelength $\Lambda = 2\pi/k_x$.The field may interact with the sample in a variety of ways, and we describe the two processes relevant for longitudinal wave generation.

In a process known as electrostriction the field first instantaneously induces electric dipole moments in the material, whose magnitude is given by $\mathbf{p} = \alpha\mathbf{E}$, where α is the liquid's polarizability. These dipoles now have an electrostatic interaction with the field that generated them. The energy of this interaction is given by $U = -\mathbf{p}\cdot\mathbf{E} = -\alpha|E|^2$, where E is given by 3.2. The compressional force in the grating dimension is thus given by

$$\begin{aligned} F &= -\nabla U \\ &= \alpha k_x E_0^2 \sin(2k_x x). \end{aligned} \tag{3.3}$$

Since the duration of the electric field is short with respect to the period of an acoustic wave, this force is impulsive, and the excitation process goes by the name Impulsive Stimulated Brillouin Scattering (ISBS). We note that the electrostrictive excitation force scales linearly with the wavevector, the polarizability, and the light intensity.

The second mechanism of longitudinal-wave excitation is by the absorption of the excitation light into the sample, either into electronic or vibrational degrees of freedom. The former are usually the result of pumping with an ultraviolet source. The latter can be achieved with infrared wavelengths; in the cases of direct importance here (organic molecular liquids), the laser wavelength $\lambda \sim 1$ µm matches the third overtone of the O-H stretching mode. In either the electronic or vibrational route, the absorbed energy is rapidly thermalized, and the result is a grating in temperature. The absorption and the temperature grating are proportional to the intensity I of the incident light as

$$\begin{aligned} \delta T \propto I \propto |E^2| &= E_0^2 \cos^2(k_x x) \\ &= \frac{E_0^2}{2}(1 - \cos(2k_x x)). \end{aligned} \tag{3.4}$$

Regions of higher temperature have a lower equilibrium density, and so the resulting step-function compressional stress launches longitudinal acoustic waves with force $F \propto \delta T$. This process of launching acoustic waves via sudden heating is known as Impulsive Stimulated Thermal Scattering (ISTS). It shares in common with ISBS the linear dependence upon light intensity and the same grating spacing Λ, although its force magnitude is independent of grating wavevector and is 90 degrees out of phase with the electrostrictive case.

With this information, we are ready to derive the signal. The starting point is the set of linearized hydrodynamic equations of motion written in the time domain and Fourier transformed from real space to the wavevector domain according to

$$\mathcal{F}\{f(\mathbf{r})\} = \int_{-\infty}^{\infty} d\mathbf{r} f(\mathbf{r}) e^{i\mathbf{q}\cdot\mathbf{r}}. \tag{3.5}$$

The first equation is the conservation of mass

$$\frac{\partial}{\partial t}\delta\rho(q,t) - \rho_0 i q v_{\|}(q,t) = 0; \tag{3.6}$$

which expresses that the local change in density, $\delta\rho$ of a region under consideration is due to particles flowing into and out of it. Here, v is the velocity and q is the wavevector. The subscript on v denotes that the choice has been made here to only consider the part of the velocity parallel to the propagation of the wave, as the interest is in the derivation of longitudinal waves.

Second is the Navier-Stokes equation

$$\rho_0 \frac{\partial v_{\|}(q,t)}{\partial t} - iq\frac{k_B T_0}{S(q)}\delta\rho(q,t) - iq\frac{k_B T_0}{S(q)}\rho_0 \kappa \delta T(q,t) + \rho_0 q^2 \int_0^t dt \phi_L(q,t-t')v_{\|}(q,t') = iqF(q,t) \tag{3.7}$$

which is an expression of the conservation of momentum. Here, $S(q)$ is the static structure factor, T_0 is the local temperature, κ the thermal expansion coefficient, and F the force due to the laser. The first term is the usual mass times acceleration term, the second term expresses the force due to a change in density, and the third term describes the force due to a change in temperature. In the damping term, the convolution integral involving ϕ_L is a generalization of the viscosity term in the original Navier-Stokes equation and accounts for the complex structural relaxation dynamics of glass forming liquids. This term recalls the memory function term in the mode-coupling equations of motion, equations 2.47-2.49.

Finally, the last equation needed to derive longitudinal signal expresses the conservation of energy,

$$\rho_0 c_v \frac{\partial \delta T(q,t)}{\partial t} - c_v \frac{\gamma - 1}{\kappa}\frac{\partial \delta\rho(q,t)}{\partial t} + \zeta q^2 \delta T(q,t) = Q(q,t) \tag{3.8}$$

c_v is the specific heat at constant volume, γ is the ratio of the specific heats c_p/c_v, ζ is the thermal conductivity, and Q is the thermal energy coupled in by the absorption of the pump laser light. Here, the first term represents the time dependence of the temperature, the second describes the change in temperature due to a change in density, and the third term the diffusion of heat.

As mentioned above, we are interested in the fluctuating part of the density which couples into the permittivity. Thus we seek a solution of equations 3.6 - 3.8 by taking the Laplace transform defined by

$$\mathcal{L}\{g(t)\} = \int_0^\infty dt g(t) e^{-st} \tag{3.9}$$

and eliminating the variable $v_{\parallel}$ between equations 3.6 and 3.7. The result is

$$\left\{ \frac{s^2}{q^2} + s\phi_L(q,s) + \frac{k_B T_0}{S(q)} \right\} + \left\{ \rho_0 \kappa \frac{k_B T_0}{S(q)} \right\} \delta T(q,s)$$

$$= -F(q,s) + \delta\rho(q) \left\{ \frac{s}{q^2} + \phi_L(q,s) \right\} \tag{3.10}$$

and

$$\left\{ -\frac{s(\gamma-1)c_v}{\kappa} \right\} \delta\rho(q,s) + \left\{ \rho_0 c_v s + \zeta q^2 \right\} \delta T(q,s)$$

$$= Q(q,s) - \delta\rho(q) \frac{(\gamma-1)c_v}{\kappa} + \delta T(q) \rho_0 c_v. \tag{3.11}$$

The quantities $\delta\rho(q)$ and $\delta T(q)$ in the above equations correspond to the spontaneous fluctuations in density and temperature already present in the liquid and may be set to zero; they are several orders of magnitude smaller than the stimulated fluctuations we are interested in. With this, we can cast these equations into matrix form as

$$\begin{pmatrix} \frac{s^2}{q^2} + s\phi_L(q,s) + \frac{k_B T_0}{S(q)} & \rho_0 \kappa \frac{k_B T_0}{S(q)} \\ -\frac{s(\gamma-1)c_v}{\kappa} & \rho c_v s + \zeta q^2 \end{pmatrix} \begin{pmatrix} \delta\rho(q,s) \\ \delta T(q,s) \end{pmatrix} \tag{3.12}$$

$$= \begin{pmatrix} -F(q,s) + \delta\rho(q) \left\{ s/q^2 + \phi_L(q,s) \right\} \\ Q(q,s) - \delta\rho(q) \frac{(\gamma-1)c_v}{\kappa} + \delta T(q) \rho_0 c_v \end{pmatrix}. \tag{3.13}$$

This can be solved for the four response functions of the system.

$$G_{\rho\rho}(q,s) = \frac{1}{\Delta} \left\{ s q^2 + \frac{\zeta q^4}{\rho_0 c_v} \right\} \tag{3.14}$$

$$G_{\rho T}(q,s) = \frac{1}{\Delta} \left\{ -\frac{\kappa q^2}{c_v} \frac{k_B T_0}{S(q)} \right\} \tag{3.15}$$

$$G_{T\rho}(q,s) = \frac{1}{\Delta} \left\{ -\frac{(\gamma-1) s q^2}{\rho_0 \kappa} \right\} \tag{3.16}$$

$$G_{TT}(q,s) = \frac{1}{\Delta}\left\{\frac{s^2}{\rho_0 c_v} + \frac{q^2}{\rho_0 c_v}\phi_L(q,s)s + \frac{q^2}{\rho_0 c_v}\frac{k_B T_0}{S(q)}\right\} \tag{3.17}$$

Where Δ is given by

$$\begin{aligned} \Delta &= s^3 + s^2 q^2 \left\{\phi_L(q,s) + \zeta/(\rho_0 c_v)\right\} \\ &\quad + s\left\{\frac{\zeta q^4}{\rho_0 c_v}\phi_L(q,s) + \gamma q^2 \frac{k_B T_0}{S(q)}\right\} + \frac{\zeta q^4}{\rho_0 c_v}\frac{k_B T_0}{S(q)}. \end{aligned} \tag{3.18}$$

Δ is the dispersion relation – its roots determine the nature of the excitations observed in the system. Complex roots indicate propagating excitations, and real roots relate to diffusive ones.

$G_{\rho\rho}$ and $G_{\rho T}$ are the ISBS and ISTS response functions, respectively, and are discussed at length below. The terms $G_{T\rho}$ and G_{TT} describe the temperature changes due to either a change in density or the direct heating via the laser. Since the refractive index is far less sensitive to T than to ρ, these terms do not give rise to significant signals, and will be neglected for the rest of the analysis of our results.

In the modelling of the observed signal, we have generalized the viscosity term to include memory. For the benefit of understanding the salient points of our measurements, here we use the Debye model which is characterized by a single relaxation time τ_R. We separate the term ϕ_L into a relaxing part and a background part. The Laplace transform of the Debye relaxation function can be expressed as

$$\lim_{q\to 0}\phi_L(q,s) = \nu_L + \frac{c_\infty^2 - c_0^2}{1 + s\tau_R}\tau_R = \nu_L + \phi_L^R(q,s) \tag{3.19}$$

where we have added a background viscous damping term, $\nu_L = (\eta_B + \frac{4}{3}\eta_S)/\rho$ to the equation, and c_∞ and c_0 are the infinite frequency and zero-frequency longitudinal acoustic speeds, respectively.

When equation 3.19 is substituted into equation 3.18, a proper factorization is neither straightforward nor instructive. Instead, the preferred method of solution is to make the approximations $\nu_L q^2 \ll c_0 q$ and $\Gamma_H \ll c_0 q$ (here, $\Gamma_H = \chi q^2$, where $\chi = \zeta/\rho_0 c_p$ is the thermal diffusivity), which enable easy factorization of Δ, and then proceed via a perturbation expansion in these small parameters. The result of this procedure is

$$\Delta = (s + \Gamma_H)(s + i\omega_A + \Gamma_A)(s - i\omega_A + \Gamma_A)\left[s + \frac{c_0^2}{c_A^2 \tau_R}\right] = 0 \tag{3.20}$$

The four roots of equation 3.20 detail the three different excitations present in the excited liquid[1]. The first root is purely real, and provides the thermal diffusion time Γ_H. This represents the decay of the induced grating response via the transport of heat from the grating peaks to nulls. The other real root in the the fourth term denotes another dissipative mode. In this case it has a time scale related to the relaxation time τ_R, which implies a time-dependent transient grating response due to structural relaxation in the liquid.

The second and third terms in 3.20 represent left and right going acoustic waves of frequency ω_A and damping rate Γ_A. The acoustic frequency is given by

$$\omega_A = c_A q = c_0 q \left[D + \sqrt{D^2 + (c_0 q \tau_R)^{-2}}\right]^{1/2} \tag{3.21}$$

where

$$D = \frac{1}{2}\left[c_\infty^2 c_0^{-2} - (c_0 q \tau_R)^{-2}\right]. \tag{3.22}$$

The damping rate is given by

$$\Gamma_A = \frac{1}{2} q^2 \left\{(\nu_L + (\gamma - 1)\chi) + \chi(1 - c_0^2/c_A^2)\right\} \tag{3.23}$$

$$+ \frac{1}{2} q^2 \frac{c_\infty^2 - c_0^2}{1 + (\omega_A \tau_R)^2} \tau_R, \tag{3.24}$$

assuming $\Gamma_H \tau_R \ll 1$.

The damping rate is itself comprised of four terms. The first is simply due to the background viscous damping, and scales as q^2. This term becomes important when ISS is used to measure the longitudinal viscosity of a liquid.

The second and third terms are related to thermal diffusion. As the longitudinal

---

[1] Note that the last factor is given by $(s + \frac{c_0^2}{c_A^2 \tau_R})$ – the expression in [7] has a misprint. The solution as printed is correct, however.

wave passes through the liquid, the periodic compression of the wave slightly increases the local temperature. The heat generated can then move to the uncompressed region before the rarefaction occurs. In practice, the compression and rarefaction in the MHz range of ISS occur far too quickly for thermal diffusoin across this distance to occur, as Γ_H is much less than any of the other terms in Γ_A. In other words, the influence of thermal diffusion on acoustic damping could only be important in the regime where the thermal diffusion is on the order of an acoustic period. Therefore, we may neglect the second and third terms for all of the analysis conducted in the rest of this thesis.

The fourth term is due to the structural relaxation dynamics, and has the form of the imaginary part of the Debye relaxation function. This term shows how the relaxation dynamics give rise to acoustic damping. As remarked in [7], it may be necessary to separate the effects of the structural relaxation dynamics from the background viscous damping in order to characterize the former from measured acoustic damping rates.

After a partial fraction expansion of the dispersion relation 3.18, the expressions for $G_{\rho\rho}$ and $G_{\rho T}$ may then be Laplace transformed back into the time domain. The signal in an ISBS experiment is thus given by

$$\begin{aligned} G_{\rho\rho}(q,t) &= \frac{c_A^2 q^2 \tau_R^2 + c_0^2 c_A^{-2}}{c_A^2 q^2 \tau_R^2 + c_0^4 c_A^{-4}} \frac{q}{c_A} e^{-\Gamma_A t} \sin(\omega_A t) \\ &+ \frac{(1 - c_0^2 c_A^{-2}) q^2 \tau_R}{c_A^2 q^2 \tau_R^2 + c_0^4 c_A^{-4}} [-e^{-\Gamma_A t} \cos(\omega_A t) + e^{-c_0^2 t / c_A^2 \tau_R}] \end{aligned} \tag{3.25}$$

while that of an ISTS experiment is

$$G_{\rho T} = A \left[e^{-\Gamma_H t} - e^{-\Gamma_A t} \cos(\omega_A t) \right] + B \left[e^{-\Gamma_H t} - e^{-c_0^2 c_A^{-2} t / \tau_R} \right] \tag{3.26}$$

where

$$A = -\frac{\kappa}{c_p} \frac{c_0^2}{c_A^2} \frac{c_A^2 q^2 \tau_R^2 + c_0^2 c_A^{-2}}{c_A^2 q^2 \tau_R^2 + c_0^4 c_A^{-4}} \tag{3.27}$$

and

$$B = -\frac{\kappa}{c_p} \frac{q^2 \tau_R^2 (c_A^2 - c_0^2)}{c_A^2 q^2 \tau_R^2 + c_0^4 c_A^{-4}}. \tag{3.28}$$

In both equations 3.25 and 3.26, we see the modes that were alluded to in the dispersion relation 3.20 and we shall analyze each one in turn.

Equation 3.25 is comprised of two oscillatory terms from the acoustic response, and the diffusive term from to the structural relaxation dynamics. The thermal mode is missing due to the fact that this response function only probes changes in density due to electrostriction. It can be shown that the last term in equation 3.25 only becomes relevant when $1/\omega_A$ is on the order of τ_R. In practice, however, it is still small compared with the first term and thus it can be neglected. This implies that the signal in a VVVV ISBS experiment is dominated by the acoustic modes.

The structure of the solution to equation 3.26 is richer, where all modes of equation 3.20 are manifest. Here, the signal is split into contributions due to simple driven acoustic and thermal responses (proportional to A) and contributions from the structural relaxation dynamics (proportional to B). In contrast to the ISBS case, the coefficient B in ISTS may become on the same order as A, and the effects of structural relaxation dynamics are plainly evident in the time domain. Physically, this behavior results from the step-function stress imposed on heated regions of the liquid which induces thermal expansion towards its new, spatially modulated equilibrium state. As we have seen in chapter 2, the change in density occurs in two steps: a quick one due to the β relaxation dynamics, and a slow one due to the α relaxation dynamics. When the α relaxation dynamics are slowed down, the thermal expansion is correspondingly slowed. For mathematical simplicity we have assumed Debye relaxation dynamics, but in fact highly non-exponential thermal expansion given by the structural relaxation function $\Phi(t)$ from equation 2.5 can be observed. In practice, in ISTS, we are able to use this to recover relaxation dynamics from $\sim 10^{-7}$ s to $\sim 10^{-3}$ s, limited on the shorter time-scales by the acoustic response and on longer time scales by thermal diffusion or the repetition rate of the measurement.

To further analyze this signal, we examine its features in four regimes of interest as illustrated in figure 3-3. First, when the sample is in the liquid state (a,a'), the acoustic velocity $c_A \approx c_0$ and $B \approx 0$. At short times we see the counterpropagating acoustic waves represented by the cosine term, and at long times thermal diffusion is observed.

In the low-T glassy state (d,d'), the acoustic speed $c_A \approx c_\infty$, and $\omega_A \tau_R \gg 1$. Again, we see acoustic waves and thermal diffusion at short and long times, respectively, and the amplitude of B is reduced with respect to A.

At intermediate temperatures where $\omega_A \tau_R \sim 1$ (b,b'), the structural relaxation contribution to acoustic damping, as represented by the last term in equation 3.23, becomes important. This provides us a method by which to map the relaxation spectrum in the frequency domain: measurements at as broad a distribution of wavevectors as possible are taken, and the frequencies ω_A and damping rates Γ_A are determined. These can then be used to reconstruct the relaxation spectrum by relating it to the mechanical susceptibility, the complex longitudinal elastic modulus $M^*(\omega) = M'(\omega) + iM''(\omega)$, using the relations

$$M'(\omega_A) = \rho \frac{\omega_A^2 - \Gamma_A^2}{q^2} \tag{3.29}$$

$$M''(\omega_A) = \rho \frac{2\omega_A \Gamma_A}{q^2}. \tag{3.30}$$

The modulus can then be related back to the original relaxation spectrum ϕ_L by [7]

$$\frac{M'(\omega_A)}{\rho} = -\omega_A \mathrm{Im}\left[\phi_L(q, \omega_A)\right] + c_0^2 \tag{3.31}$$

$$\frac{M''(\omega_A)}{\rho} = \omega_A \mathrm{Re}\left[\phi_L(q, \omega_A)\right] + \omega_A \left[\nu_L + \chi(\gamma - 1)\right]. \tag{3.32}$$

The above equations have been derived in the Debye model, where an analytic solution can be found in the time domain. The more realistic case of non-exponential relaxation has been typically treated by a phenomenological KWW stretched exponential relaxation function $\exp(-(t/\tau_R)^\beta)$, as mentioned earlier. As we have done in the description of time-domain relaxation in chapter 2, we may heuristically substitute this form instead of the exponential in equation 3.26. This does not change how the values for ω_A and Γ_A relate to the modulus.

At somewhat lower T (c,c'), $\omega_A \tau_R > 1$, the acoustic damping rate is reduced, and structural relaxation dynamics can be observed directly in the form of a gradual time-dependent thermal expansion, as discussed above.

The information provided by ISTS is not limited to mapping of the structural relaxation spectrum through the measured acoustic parameters and thermal expansion dynamics, although this is already of great significance and will be exploited amply in this thesis. It is also possible to test one of the more significant predictions of the mode-coupling theory, the existence and evolution of the non-ergodicity parameter, directly from the time-domain data. In the limit that the three time scales are well separated (i.e. $\omega_A \ll \tau_R^1 \ll \Gamma_H$), we may take the ratio of the coefficient B to the total signal $A + B$ and obtain

$$\frac{B}{A+B} = 1 - \frac{c_0^2}{c_\infty^2} \tag{3.33}$$

which we recognize from chapter 2 as being the non-ergodicity parameter. This information can also be obtained directly from the determination of the frequency-dependent longitudinal modulus, provided there is a wide enough frequency range to clearly observe c_∞ and c_0.

3.2.2 VHVH Signal

In order to compute the VHVH signal, we must first determine how the laser excites the sample. In the VHVH geometry, the driving fields are given by

$$\vec{E}(t,x,y,z) = E_0 \cos(\omega t - k_x x - k_z z)\hat{x} + E_0 \cos(\omega t + k_x x - k_z z)\hat{y}. \tag{3.34}$$

As the interest is in driving shear waves, the liquid's polarizability α_{ij} must be used in its full tensor form to account for the fact that the dipole moment does not necessarily lie along the direction of the electric field:

$$\begin{pmatrix} p_x \\ p_y \end{pmatrix} = \begin{pmatrix} \alpha_{11} & \alpha_{12} \\ \alpha_{21} & \alpha_{22} \end{pmatrix} \begin{pmatrix} E_x \\ E_y \end{pmatrix}. \tag{3.35}$$

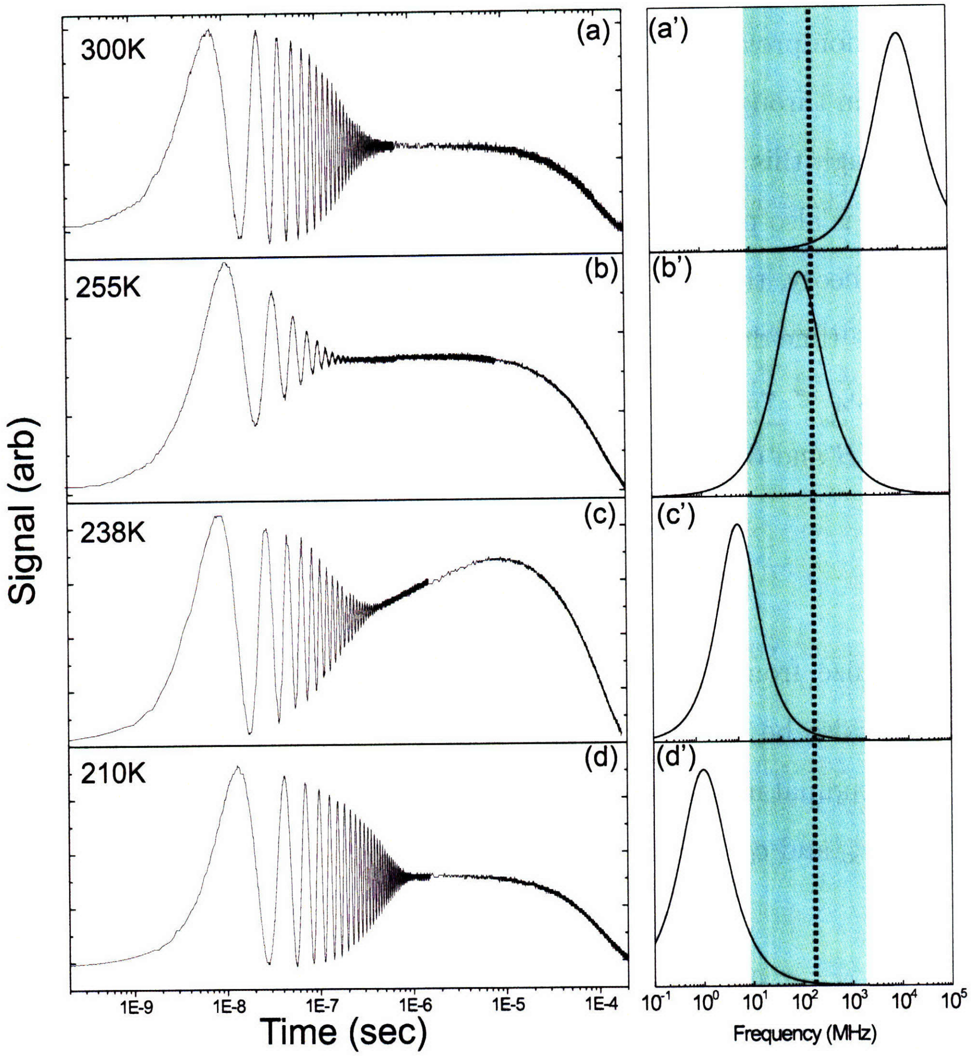

Figure 3-3: Representative longitudinal signal taken in DC704 with $\lambda = 40$ µm and at the specified temperatures. To the right are representative loss modulus spectra, not the actual spectra of DC704. The acoustic frequency regime accessible by ISTS is represented by the shaded area. When the relaxation spectrum is at higher frequencies than the measured acoustic frequency (a,a'), the acoustic wave is underdamped as in a simple liquid. When the relaxation spectrum overlaps with the acoustic frequency, acoustic energy is dissipated into the coincident structural relaxation dynamics, resulting in strong acoustic damping as shown in (b,b'). At colder temperatures (c,c') when the relaxation spectrum is centered somewhat lower than the acoustic frequency, the liquid becomes highly viscous and the thermal expansion dynamics reveal complex structural relaxation. At still lower temperatures (d,d'), the relaxation dynamics are far slower than any of the responses probed by ISTS, and the acoustic waves is underdamped as in an ordinary solid. No slow structural relaxation is observed since thermal diffusion ends the measurement on a faster time scale.

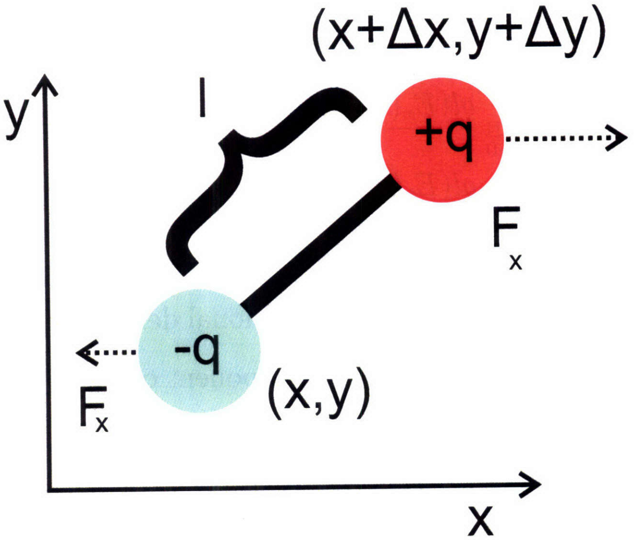

Figure 3-4: Force on aligned dipole in electric field gradient. There is a different amount of force on the positive charge located at $(x+\Delta x, y+\Delta y)$, and the negative charge located at (x, y). The result is a net translational force on the center of mass of the dipole. We also note that the dipole is not parallel to the electric field (not depicted).

The resulting dipole moment of a molecule in the liquid is given by

$$\overrightarrow{p} = E_0 \begin{pmatrix} \alpha_{11}\cos(\omega t - k_x x - k_z z) + \alpha_{12}\cos(\omega t + k_x x - k_z z) \\ \alpha_{21}\cos(\omega t - k_x x - k_z z) + \alpha_{22}\cos(\omega t + k_x x - k_z z) \end{pmatrix}. \tag{3.36}$$

At this point, we are able to compute the force in the VHVH geometry. In order to do so, we consider a dipole comprised of two distinct charges of strength q and separated by a distance $l = \sqrt{(\Delta x)^2 + (\Delta y)^2}$, as depicted in figure 3-4. The negative charge is located at (x, y) and the positive one at $(x+\Delta x, y+\Delta y)$. Due to the electric field gradients in equation 3.34, there is a net force in both the x and y directions given by

$$F_x = q(E_x(x+\Delta x, y+\Delta y) - E_x(x, y)) \tag{3.37}$$

$$F_y = q(E_y(x+\Delta x, y+\Delta y) - E_y(x, y)). \tag{3.38}$$

We multiply and divide the right hand sides of both 3.37 and 3.38 by the charge separation l and take the limit $l \to 0$ in order to recover the point dipole p of the molecule as

$$F_x = \lim_{l \to 0} \frac{ql(E_x(x+\Delta x, y+\Delta y) - E_x(x,y))}{l} \tag{3.39}$$

$$F_y = \lim_{l \to 0} \frac{ql(E_y(x+\Delta x, y+\Delta y) - E_y(x,y))}{l}. \tag{3.40}$$

We recognize in equations 3.39 and 3.40 a directional derivative taken along the orientation of the dipole moment. Thus, the i^{th} component of the force can be represented as

$$F_i = \overrightarrow{p} \cdot (\nabla E_i). \tag{3.41}$$

In the preceding derivation, we neglected the portion of the H-polarized field that lies in the $\hat{z}$ direction. Only the projection of this field along the $\hat{x}$ direction can contribute to driving the shear wave. The result is that the excitation efficiency is also proportional to the projection of the H-polarized beam onto the x-axis, and so the force must also scale as $\cos(\theta/2)$, where θ is the angle between beams.

We compute the force by substituting the fields from equation 3.34 and the induced dipole moment from equation 3.36 into equation 3.41. Ignoring constants and terms that oscillate at twice the optical frequency since they do not contribute to acoustic signal [64], we are left with

$$\overrightarrow{F} = -\cos(\theta/2)\frac{E_0^2 k_x}{2}[\alpha_{12}\sin(2k_x x)\hat{x} + \alpha_{11}\sin(2k_x x)\hat{y}]. \tag{3.42}$$

This expression shows that the driving strength of the shear wave is proportional to both the diagonal and off-diagonal polarizabilities α_{11} and α_{12}, the laser intensity E_0^2, the wavevector $q = 2k_x$ of the acoustic wave, in addition to the geometrical scattering factor $\cos(\theta/2)$. The minus sign also shows that the sense of the force is opposite that of the polarized ISBS case above.

The situation described above mathematically is presented graphically in figure 3-5. The polarization grating that results from the crossed V- and H-polarized pulses is shown in a). The force given by equation 3.42 deforms a given element of the liquid in a sheared fashion as shown in b), the sum total of which provides a shear wave

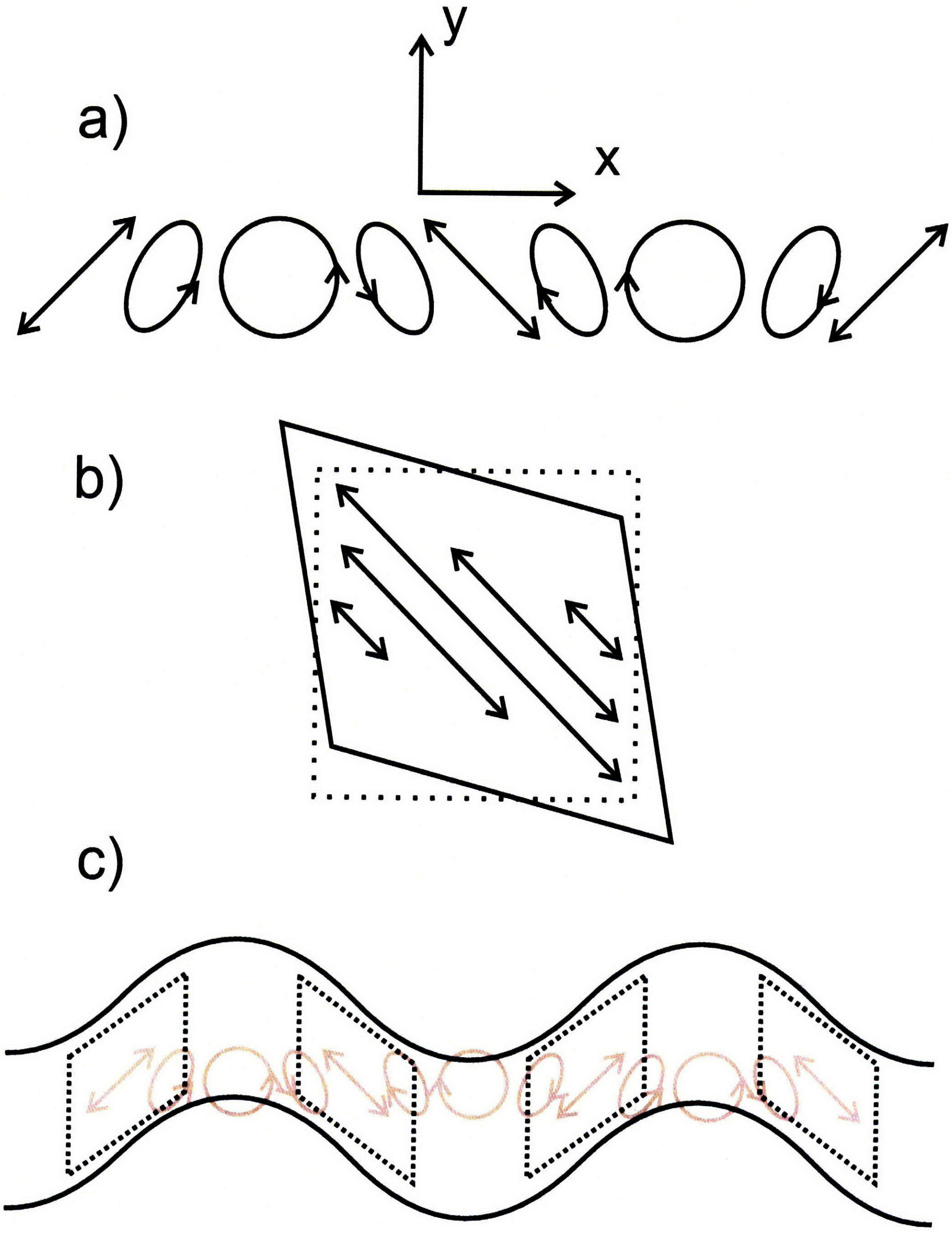

Figure 3-5: a) The intersection of the two pump beams results in a grating whose time-averaged polarization state is described as regions which blend from circular to elliptical to linear polarization, to elliptical and change to circular of the opposite helicity. b) Only the linear components of the polarization are able to exert a net force on the liquid. Considering a segment of the liquid of the size of the region between circular polarization states, the resulting electrostriction is a volume-preserving shearing force. Here, the initial cell is depicted as a dotted square and its sheared, equal-volume element is solid. c) The alternating regions of linear polarization induce similarly alternating sheared regions of the liquid, the result of which is a shear wave polarized in the y direction.

polarized in y, depicted in c).

Finally, we note that in addition to the force in equation 3.42, the laser torques the molecules about their centers of mass according to $\vec{\tau} = \vec{p} \times \vec{E}$. In the liquid case, where $\alpha_{11} = \alpha_{22} = \alpha_{\|}$ and $\alpha_{12} = \alpha_{21} = \alpha_{\perp}$, we recover

$$\vec{\tau} = E_0^2 \alpha_{\|} \sin(\omega t - k_z z) \sin(2k_x x)\hat{z} \tag{3.43}$$

Unlike the acoustic wave case, the torque only scales with the laser intensity and the diagonal polarizability – the signal strength does not depend upon the grating wavevector.

In computing the signal in an ISBS experiment, we assume that the measured scattered light is proportional to the time-dependent polarizability anisotropy $Q^{\alpha\beta}$. We start with the generalized, linearized hydrodynamic equations of motion. First is the momentum density conservation law,

$$\frac{\partial}{\partial t}\rho \mathbf{u}(\mathbf{r}, t) + \nabla \cdot \Pi(\mathbf{r}, t) = 0 \tag{3.44}$$

where ρ is the density, $\mathbf{u}(\mathbf{r}, t)$ the velocity, and $\Pi(\mathbf{r}, t)$ the stress tensor. The next relevant equation is the expression for the stress tensor

$$\begin{aligned} \Pi^{\alpha\beta}(\mathbf{r}, t) &= \delta_{\alpha\beta} P(\mathbf{r}, t) - \eta \tau_{\alpha\beta}(\mathbf{r}, t) \\ &\quad + \delta_{\alpha\beta}(\frac{2}{3}\eta - \zeta)\nabla \cdot \ \mathbf{u} \ (\mathbf{r}, t) - \mu Q_{\alpha\beta}(\mathbf{r}, t) + F_{\alpha\beta}(\mathbf{r}, t). \end{aligned} \tag{3.45}$$

$\delta_{\alpha\beta}$ is the Kronecker delta, $P(\mathbf{r}, t)$ is the pressure, η is the shear viscosity, ζ is the longitudinal viscosity, $Q_{\alpha\beta}(\mathbf{r}, t)$ is the orientational variable, μ expresses the coupling of translational force due to rotational motion, and $\mathbf{r}$ is the spatial coordinate. $F_{\alpha\beta}(\mathbf{r}, t)$ is the external shearing stress of the laser field, assumed to be a Dirac delta function in time and wavevector, and $\tau_{\alpha\beta}$ is the rate of strain, defined by

$$\tau_{\alpha\beta} = \frac{\partial u_\alpha(\mathbf{r}, t)}{\partial r_\beta} + \frac{\partial u_\beta(\mathbf{r}, t)}{\partial r_\alpha}. \tag{3.46}$$

The polarizability anisotropy obeys its own equation of motion, given by

$$\frac{\partial Q_{\alpha\beta}(\mathbf{r},t)}{\partial t} = -\Gamma_o Q_{\alpha\beta}(\mathbf{r},t) + \xi\tau_{\alpha\beta}(\mathbf{r},t) + Q_0(\mathbf{r},t) \tag{3.47}$$

where Γ_o is the orientational relaxation rate, ξ is the torque due to translational motion, and $Q_0(\mathbf{r},t)$ is the torque exerted by the laser. As with the laser-induced stress, the torque will also be modelled as a Dirac delta function in time and wavevector. We are also assuming Debye orientational relaxation.

We set the grating wavevector in the x direction and the transverse direction to be y. For notational convenience, we also omit the arguments of the variables. Since we are interested in shear waves, we select the transverse elements of the above equations, and after a Fourier-Laplace transform defined as above in equations 3.5 and 3.9 we are left with

$$\begin{aligned} \Pi^{xy} &= -\eta_s\tau^{xy} + F^{xy} + \mu Q && (3.48)\\ \rho s v_y &= -iq\Pi^{xy} && (3.49)\\ \tau^{xy} &= s\epsilon^{xy} && (3.50)\\ sQ &= -\Gamma_o Q + \xi\tau + Q_0. && (3.51) \end{aligned}$$

The above system can be solved for the orientational variable to yield

$$Q^{xy} = \frac{\xi q^2 F^{xy} + Q_0(s\rho + q^2\eta)}{(s+\Gamma_o)(s\rho + q^2\eta) - \xi\mu q^2}. \tag{3.52}$$

In order to arrive at an analytic solution, we make the approximation that $\xi\mu q^2$ is a coupling of higher order that can be ignored in the solution of the equations of motion. This is formally equivalent to omitting the term proportional to μ in equation 3.45 but keeping ξ in equation 3.47. Physically, we are making the approximation that the rotational motion of the molecules does not cause measurable translational motion, but that the translational motion does amount to a significant torque. In this approximation, the expression for Q^{xy} separates as

$$Q^{xy} = \frac{\xi q^2 F^{xy}}{(s+\Gamma_o)(s\rho + q^2\eta)} + \frac{Q_0}{s+\Gamma_o}. \tag{3.53}$$

In order to extract how the structural relaxation dynamics are manifest in our signals, we proceeded as in Boon and Yip [65] and model the α peak by Debye relaxation where the kinematic viscosity η/ρ is generalized to $\nu_0 + \frac{c_\infty^2 \tau_r}{1+s\tau_r}$. Here, ν_0 is the background kinematic shear viscosity η_0/ρ, c_∞ is the infinite frequency speed of sound, and τ_r is the characteristic relaxation time. In this model, the above equations can be solved for Q^{xy} to yield

$$Q^{xy} = \frac{\xi q^2 F^{xy}}{\rho} \frac{1}{(s+\Gamma_o)(s + \nu_0 q^2 + \frac{c_\infty \tau_r q^2}{1+s\tau_r})} + \frac{Q_0}{s+\Gamma_o}. \tag{3.54}$$

Equation (3.54) can be recast into the form:

$$Q^{xy} = \frac{\xi q^2 F^{xy}}{\rho} \frac{1+s\tau_r}{(s+\Gamma_o)(s+\Gamma_A+i\omega_A)(s+\Gamma_A-i\omega_A)} + \frac{Q_0}{s+\Gamma_o} \tag{3.55}$$

where the damping rate Γ_A is given by

$$\Gamma_A = \frac{1}{2\tau_r} + \frac{q^2\nu_0}{2} \tag{3.56}$$

and the frequency of oscillation ω_A by

$$\omega_A = \sqrt{c_\infty^2 q^2 - \left(\frac{1}{2\tau_r} - \frac{q^2\nu_0}{2}\right)^2}. \tag{3.57}$$

Γ_A is comprised of two terms, the first due to the structural relaxation dynamics, and the second due to the background damping. We also note that ω may go to zero for finite wavevector when

$$c_\infty q = \frac{1}{2\tau_r} - \frac{q^2\nu_0}{2}. \tag{3.58}$$

This condition may be met for finite q in the case where τ_r is comparable to the acoustic period.

Separation of equation 3.55 by partial fractions yields a time domain solution

$$\begin{aligned} Q^{xt}(q,t) &= \frac{\xi q^2 F^{xy}}{\rho}\left[A e^{-\Gamma_A t}\sin(\omega_A t) + B\left(e^{-\Gamma_o t} - e^{-\Gamma_A t}\cos(\omega_A t)\right)\right] \\ &\quad + Q_0 \exp(-\Gamma_o t) \end{aligned} \tag{3.59}$$

where

$$A = \frac{1}{\omega_A}\frac{\tau_R(\Gamma_A^2 + \omega_A^2 - \Gamma_A\Gamma_o) + (\Gamma_o - \Gamma_A)}{(\Gamma_o - \Gamma_A)^2 + \omega_A^2} \tag{3.60}$$

and

$$B = \frac{1 - \Gamma_o \tau_r}{(\Gamma_o - \Gamma_A)^2 + \omega_A^2}. \tag{3.61}$$

The solution represented by equation 3.59 is comprised of two pieces. The term proportional to $q^2 F^{xy}$ is due to the shear acoustic response, and the other term proportional Q_0 is a decaying exponential independent of q. This orientational response is the Optical Kerr Effect (OKE) signal. We also note the presence of OKE signal in the acoustic response, due to the rotational-translational coupling.

Analogously to the longitudinal case, we may examine the behavior of the solution represented by equation 3.59 in three regimes of interest. These three limits are represented by the data in figure 3-6. In all cases, we will neglect the background damping. Due to the rotational translational coupling, there is the additional complication that we must also consider the effect of Γ_o on the signal through its contribution to the factors A and B.

When the sample is in the glassy regime, $\omega_A \tau_r \gg 1$, which implies that $\Gamma_A \simeq 0$. We also note that the orientational relaxation is also in the regime where $\Gamma_o \simeq 0$. In this case, $A \propto \tau_r/\omega_A$ which is much larger than $B \propto \omega_A^{-2}$. Hence we observe underdamped oscillations about the zero baseline due to counterpropagating shear acoustic waves.

In the case where $\omega_A \tau_r \sim 1$, the analysis requires more care. If we assume that the orientational relaxation rate is on the order of τ_r^{-1}, the term proportional to A contributes as τ_r/ω_A and the term proportional to B contributes as $1/\omega_A^2$. The numerator of B carries the additional complication that its value may be close to

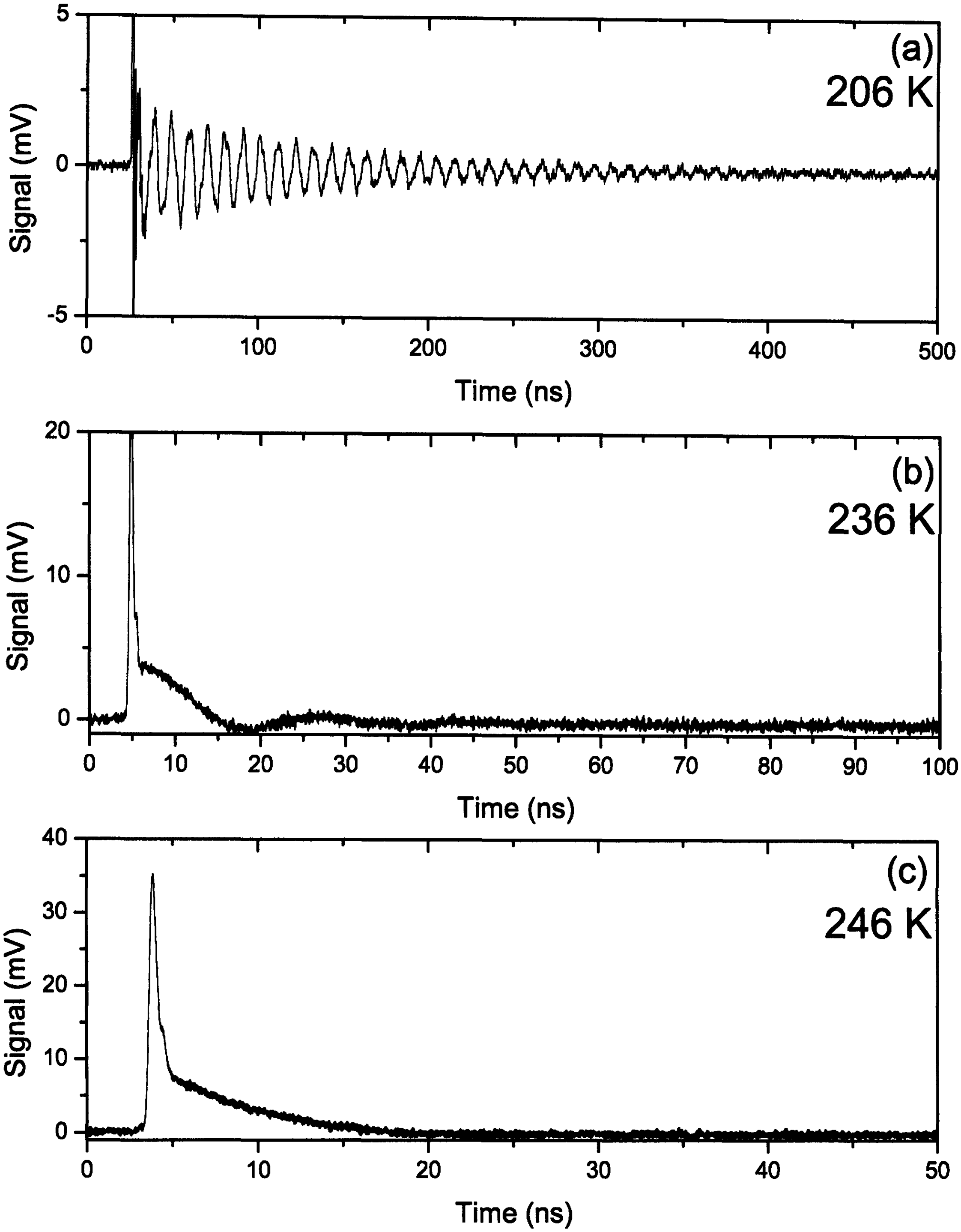

Figure 3-6: Representative shear signal taken in triphenyl phosphite with $\lambda = 10$ µm and at the specified temperatures. In (a) the material is in a vitreous state where $\omega_A \tau_r \gg 1$. Here the oscillations are underdamped and last for several cycles. When $\omega \tau_r \sim 1$ as in (b), the oscillations become heavily damped due to the exchange of the acoustic energy with the relaxation dynamics as well as the fact that the material is gaining the ability to flow. Also in this regime, the orientational relaxation is significant enough that the oscillations do not occur about zero. Finally, in (c) the acoustic waves are overdamped as the real part of the shear modulus has gone to zero – all that is left is the orientational response.

zero in this regime if, for instance, $\Gamma_o\tau_r \approx 1$. If it is not, then the two terms may contribute equally to the signal, i.e. if $\Gamma_o = \Gamma_A = 1/2\tau_r$ and $\omega_A\tau_r = 1$, then $B = A/2$. Since there is a subtraction of a cosine from a sine term with the same argument, this could manifest as an acoustic phase whose magnitude is related to the relative amplitudes of A and B. Finally, we note that in this case, the orientational response has contributions both from direct excitation of the OKE signal, as well as the term from the rotational-translational coupling.

At higher temperatures, the condition stated by equation 3.58 can be met for the wavevector regime reached by the ISBS experiment. In this case, equation 3.55 can be written

$$Q^{xy} = \frac{\xi q^2 F^{xy}}{\rho} \frac{1 + s\tau_r}{(s+\Gamma_o)(s+\Gamma_B)(s+\Gamma_C)} + \frac{Q_0}{s+\Gamma_o} \tag{3.62}$$

where

$$\Gamma_{B,C} = \frac{1}{2\tau_r} \pm \sqrt{\left(\frac{1}{2\tau_r} - \frac{q^2\nu_0}{2}\right)^2 - c_\infty^2 q^2} \tag{3.63}$$

In this case, the time domain signal separates as

$$Q^{xy} = \frac{\xi q^2 F^{xy}}{\rho}(\Gamma_B - \Gamma_C)\left(A' e^{-\Gamma_B t} - B' e^{-\Gamma_C t}\right) + C' e^{-\Gamma_o t} \tag{3.64}$$

with

$$A' = \frac{1 - \Gamma_B\tau_r}{\Gamma_B - \Gamma_o} \tag{3.65}$$

$$B' = \frac{1 - \Gamma_C\tau_r}{\Gamma_C - \Gamma_o} \tag{3.66}$$

$$C' = \frac{\xi q^2 F^{xy}}{\rho} \frac{1 - \Gamma_o\tau_r}{(\Gamma_B - \Gamma_o)(\Gamma_C - \Gamma_o)} + Q_0. \tag{3.67}$$

In equation 3.64, the time dependence of the signal derives from the sum of a q-dependent biexponential from the overdamped shear mechanical response and the q-independent OKE signal.

Analogous to the longitudinal case, we can consider a frequency dependent modulus $G^*(s) = G'(s) + iG''(s)$ which obeys the dispersion relationship [66]

$$\rho s^2 + G(s)q^2 = 0, \tag{3.68}$$

which yields the following expressions for the real and imaginary parts of the shear modulus from the acoustic frequency and damping rate

$$\begin{aligned} G'(\omega_A) &= \rho\frac{\omega_A^2 - \Gamma_A^2}{q^2} && (3.69) \\ G''(\omega_A) &= \rho\frac{2\omega_A\Gamma_a}{q^2}. && (3.70) \end{aligned}$$

As equation 3.68 has been derived considering the strain, in order to compare it with the results of the above analysis, we must solve for the strain from the original equations of motion. This gives the dispersion relation

$$\rho s^2 + \eta s q^2 = 0. \tag{3.71}$$

Comparison between equations 3.68 and 3.71 yields the connection between the elastic modulus and the relaxation spectrum

$$\begin{aligned} \frac{G'(\omega_A)}{\rho} &= -\omega_A \mathrm{Im}[\eta(q,\omega_A)] && (3.72) \\ \frac{G''(\omega_A)}{\rho} &= \omega_A \mathrm{Re}[\eta(q,\omega_A)] + \omega_A\nu_0. && (3.73) \end{aligned}$$

We conclude by noting that orientational responses of anisotropic molecules can be induced not only by the excitation pulses, as in the case of OKE, but also by flow that occurs due to the induced density changes [67]. Both of these sources lead to signals that can be suppressed by proper selection of probe and signal polarizations. Thus the excitation pulse polarizations (VV or VH) we used to select the material responses that are driven, and (where possible), the probe polarizations, were selected to suppress unwanted orientational contributions to signal. In general, this can be easily achieved while examining longitudinal signal due to its large amplitude. This step was impractical when measuring shear responses, as a choice of polarization which would suppress the orientational response often reduced the already weak shear signal beyond the limit of detection.

3.3 Experimental System[2]

The pump laser used for these experiments is a High Q FemtoRegen regeneratively amplified laser based on an Yb:KGW gain medium lasing from 1030 nm to 1040 nm. The repetition rate is adjustable from 500 Hz to 100 kHz, with an average power that falls from 400 mW at the lowest repetition rates to 200 mW at the highest ones. At 1 kHz, which was the most experimentally convenient rate, it has an output energy of 400 µJ per pulse. The pulse duration is adjustable upon recompression from anywhere from 250 fs to 10 ps.

Acoustic waves in the wavevector regime accessed by ISTS and ISBS are on the order of 10 MHz to 1 GHz in frequency, and so are still driven impulsively for pulse durations up to 100 ps or longer. With longer pulse durations, the peak powers of the pulses are not great enough to cause permanent chemical change, even when the integrated fluence is high. To this end, we often bypassed the compressor of the laser. This leaves a certain amount of temporal chirp in the output pulse which does not impact the acoustic measurements. The only other effect is a slightly larger output spot size with no reduction in spot quality.

The probe laser used for much of the data collected in this thesis is a CW Sanyo DL-8032-001 diode laser lasing at 830 nm with a maximum average power of 150 mW. The choice of this particular diode laser was motivated by its single transverse mode output at the maximum power for a wavelength that is sufficiently close to that of the pump laser that lenses can focus both beams to the same focal planes. The probe laser is housed in a Thorlabs model LDM21 unit and is powered by a Newport model 560 diode driver with a current limit set to 200 mA (operation of the diode above

---

[2] The pump laser system and all of its idiosyncracies are described in detail in Appendix A – here we provide the parameters of experimental interest.

this limit results in irreversible failure). This mount can also thermoelectrically cool the diode, but due to the low output power of the diode, this was unnecessary. The output was collimated into an elliptical spot by an aspheric lens which was screwed into the diode mount. The beam was then relayed to the experiment.

3.3.1 Optical Setup

Homodyne vs. Heterodyne Detection

The diffracted intensities of an ISS experiment can range anywhere from 10^{-5} at best to 10^{-8} depending upon the efficiency of the pumping as well as diffraction. As the probing field needs to be weak relative to the pump to avoid further exciting the sample, detection of small signal fields can present a significant challenge. To overcome this difficulty, without exception in this thesis, we have taken advantage of the principle of heterodyne detection to boost detectable signal levels. In this case, the time-dependent signal field $E_{sc}(t)$ is superposed upon a static, coherent local oscillator or "reference" field E_{LO} which is typically several orders of magnitude larger than $E_{sc}(t)$. The intensity registered by the detector is then given by

$$\begin{aligned} I &= |E_{sc}(t) + E_{LO}|^2 \\ &= |E_{sc}(t)|^2 + |E_{LO}|^2 + 2\cos(\varphi)E_{sc}(t)E_{LO}, \end{aligned} \tag{3.74}$$

where φ is the optical phase between the scattered and local oscillator (LO) fields. In equation 3.74, $E_{sc}(t)^2$ is the intensity of the original scattered field. It is called the homodyne contribution, and its quadratic dependence indicates that a sinusoidal signal will be detected at twice its frequency. The homodyne signal may be considered negligible if the LO field amplitude is adjusted properly.

E_{LO}^2 is a static quantity and provides a large DC offset; having no time-dependence, it can also be ignored. Thus, we see that amplification is provided by the cross term, or heterodyne contribution $2\cos(\varphi)E_{sc}E_{LO}$, which gives the time-dependence of the field $E_{sc}(t)$ itself. We note that the optical phase φ must be optimized to provide the

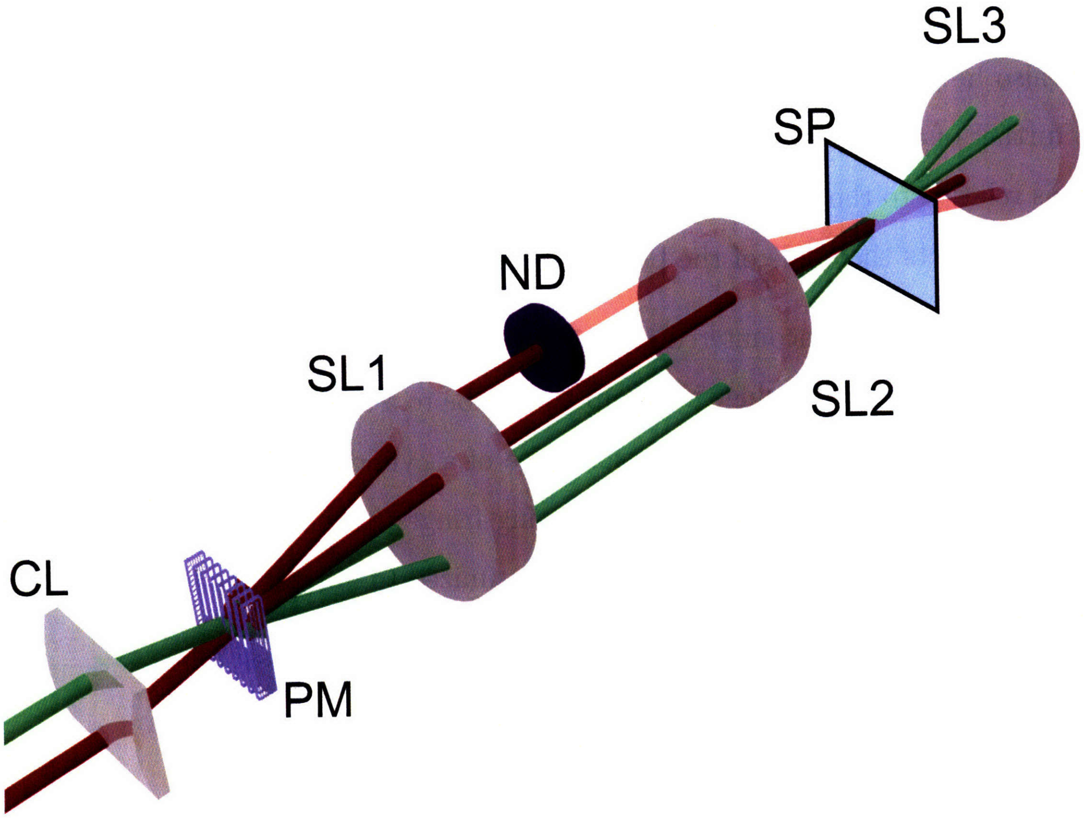

Figure 3-7: 3D perspective view of ISTS setup. The green beam is the pump and the red beam is the probe. The two beams encounter the cylindrical lens (CL) that brings them to an elliptical spot at a common point on the phase mask (PM). A two-lens telescope formed by lenses (SL1) and (SL2) images the phase mask grating pattern seen by the beams to the sample plane (SP). In between these two lenses is an ND filter (ND) which is placed in the path of the local oscillator to attenuate it. A third lens (SL3) recollimates the beams so that signal field, overlapped with the local oscillator, can be isolated and sent to the detector (not pictured). Also not pictured is a glass slide that is placed in the other, non-attenuated, half of the probe and is used for optical phase cycling as described in the text.

largest possible signal, and may be adjusted to provide a positive or negative signal relative to the baseline provided by E_{LO}^2.

Achromatic Lens Setup

Figure 3-7 shows the transient grating setup used in the experiments conducted in a majority of this thesis. The pump and probe beams are introduced to the experiment parallel to one another by two sets of turning mirrors, the first far from the experiment, the other nearby. Use of these two mirrors can achieve a level beam height and parallel travel in the far field, both of which are optimal for the experiment. These mirrors may also be used to "tweak" the experiment for greater signal. Small adjustment of the further of the two mirrors, due to its long lever arm, essentially translates one the beams relative to the other, while similarly small adjustment of the closer of the two mirrors impacts the angle of the beams more than it does the overlap.

The first element encountered is a 15 cm focal length cylindrical lens (CL) which serves the purpose of drawing the pump and probe to a common point while focussing them down in the transverse dimension. Use of a cylindrical optic preserves a large beam width that encompasses several grating fringes of the phase mask (PM). The phase mask's etch depths and features are optimized to diffract the light into the ±1 order of diffraction according to the equation

$$m\Lambda = \frac{\lambda}{2\sin\theta/2} \tag{3.75}$$

where m is the order of the diffracted light, Λ is the feature size of the grating, λ is the wavelength of the light, and θ is the angle between the diffracted beams. The etch depth of the phase mask can only be optimized to one wavelength of the incident light at a time. The result is that for all other wavelengths, there is a significant portion of the light that goes straight through the phase mask (zero order transmission) without diffraction. For this setup, we have chosen to optimize the etch depth for the probe wavelength, as the pump intensity already had to be routinely turned down in these experiments to avoid sample damage, while more probe light simply yielded more signal. A spatial filter had to be incorporated to block out the "0-order" pump light later in the setup.

The first optical element after the phase mask is a 15cm focal length Thorlabs model AC508-150-B near-IR, 2 inch spherical achromatic lens (SL1). This lens functions both to collimate the beams (if they are focussed into the grating) and bring them all parallel to one another. The use of achromatic lenses in the experiment not only serves to nearly eliminate chromatic abberations between pump and probe, but also greatly reduces geometrical abberations, as well. At small grating spacings

(1.75 µm, here), the pump beams nearly clip the edges of the lenses. This means that both the imaging defects from operating outside the paraxial limit, as well as chromatic abberations would render this experiment impossible with conventional plano-convex lenses.

The second lens used was a Thorlabs AC508-075-B near-IR, 7.5 cm focal length 2 inch achromat, which was selected for having the largest available numerical aperture, and thus able to produce the smallest grating spacings. The beams cross at its focal point, which is where the grating is formed and where the sample must sit. With the first lens, SL1 and SL2 constitute a two lens telescope that relays the image of the beams on the phase mask onto the sample with a factor of 2 demagnification. In this configuration, it is possible to access experimental wavelengths from $\Lambda = 1.75$ µm ($q = 3.59$ µm^{-1}) up until $\Lambda = 49.7$ µm ($q = 0.126$ µm^{-1}), though in practice, this setup was used from 1.75 µm to 6.56 µm.

A point worthy of mention in the alignment of these lenses: conventional wisdom dictates that the curved surfaces of both of these plano-convex lenses should face outwards of the beam path. In the case of the transient grating experiment this is exactly wrong, as the more relevant requirement for making a good grating pattern at the sample is more determined by the beam pointing than it is by the Rayleigh range; i.e., when ±1 order beams, diverging from the phase mask, first encounter a lens, it is far more effective that this face be flat. Likewise, when crossing the beams, it is best done with the parallel beams first encountering the curved faces of the final optic. Not doing so can lead to exaggerated abberation defects in the imaging and will greatly reduce signal levels.

In between SL1 and SL2 is depicted an ND filter which serves to attenuate the local oscillator field. In practice we have used an ND3 filter, although other values of attenuation may be more appropriate depending upon saturation effects in the detection electronics (see below). In the other arm of the probe beam, we have placed a glass slide (not pictured) whose adjustment can change φ, the optical phase between the signal field and local oscillator. The glass slide was glued to a mirror mount so that the phase could be changed by turning one of the mount's adjustment screws. In practice, the screw was replaced by a Thorlabs model Z612 motorized actuator and controlled by a Thorlabs model TDC001 Servo controller. This allowed measurement of positive and negative phase signals to be recorded back-to-back during overnight, temperature-dependant scans.

Besides the glass slide and ND filter, other modifications to the beam characteristics can be made. In particular half-waveplates may be introduced into any of the beams in order to rotate its polarization before it reaches the sample; this is the approach we took in making depolarized transient gratings such as depicted in figure 3-4a.

Finally, we note that the last focussing optic depicted in figure 3-7 is another Thorlabs AC508-075-B near-IR, 7.5 cm focal length 2 inch achromat which is used to recollimate the beams. The signal field and colinear local oscillator can then be spatially filtered away from the other three beams using a pinhole, and this light then focussed onto the detector.

Mirror-Based Setup

An alternate setup, depicted in figure 3-8 was used for transient grating spacings from $\Lambda = 6.70$ µm to $\Lambda = 100.9$ µm. In this configuration, two separate phase masks (PM) are used for the pump and probe. The two beams are recombined at a dichroic mirror after collimation. We have also chosen to use spherical reflectors (SM1, SM2, SM3) instead of lenses where SM1 and SM2 are 50 cm focal length, and SM3 is 25 cm focal length. In order to generate longer wavelength acoustic waves, the second focusing mirror (SM3) can be replaced by a 50 cm, or even 100 cm, achromatic lens.

Since this setup is based around focussing mirrors, this requires that there be a small departure from normal incidence (usually less than 10 degrees, as a rule of thumb) upon the mirrors to avoid large abberations. In order to meet this condition, the phase masks are oriented such that the diffraction occurs vertically, i.e. outside of the plane of figure 3-8.

This approach was motivated by a number of concerns. First was the need to be able to use the half-waveplates mounted in rotation stages in the paths of all the

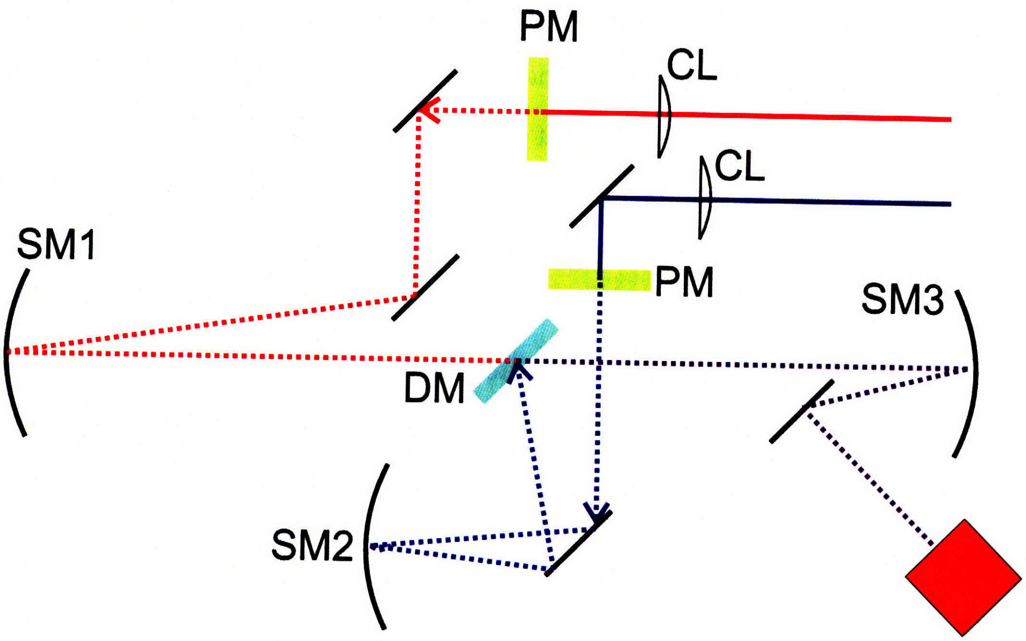

Figure 3-8: Mirror-based ISTS setup. The two collimating mirrors are physically separated, while the focussing mirror is common between the pump and probe. The orange box at the end of the beam path is used to denote the cryostat where the sample is located.

beams without occluding any of the other beams in the process. These were placed in between the collimating mirrors (SM1 for the probe and SM2 for the pump) and the dichroic mirror DM; with the four beams separated in such a manner into pairs, it was possible to use waveplates in the probe beam down to a grating spacing of 24.9 µm with the 2 : 1 imaging or 49.8 µm with 1 : 1 imaging. This set the limits on the largest grating spacing measured in the shear wave experiments.

Second, the complete separation of the pump and probe beams before the focussing mirror also allows for different focal-length cylindrical lenses (CL1 and CL2 for the probe and pump, respectively) to focus into the separate phase masks, and in fact, the relative spot sizes of pump and probe on the sample can be controlled entirely separately from one another.

Finally, this setup is completely achromatic. The use of mirrors will always result in the same imaging for any choice of pump and probe wavelengths. Additionally, the phase masks can be chosen to have an etch depth optimized for the wavelength of the beam that they are used in.

The main drawback of this method was that the use of non-common path optics introduced relative phase instability in heterodyne measurements due to air currents and vibrations on the table. The result is that the relative phase φ between local oscillator and probe picks up noise and turns this into an instability of the measurement. The vibrations become more important for smaller grating spacings, so the noise is exacerbated for shorter acoustic wavelength measurements. Interestingly, we found that turning on the HEPA filters above the optical table actually served to stabilize the setup. This problem does not exist for the homodyne measurement, where there is no optical phase information recorded and vibrations of either phase mask are immaterial.

3.3.2 Detection

Detectors and Probe Lasers

Detection of acoustic waves is performed by a Cummings Electronics Laboratory Model 3031-0003 amplified avalanche photodiode whose amplification has a bandwidth of approximately 10 kHz - 3 GHz. The AC coupling allows for measurement of induced gratings without a fluctuating background due to pointing instability and fluctuations in the quantity E_{LO}.

The detector used for slow responses was a New Focus model 1801-FS amplified photodiode detector with a bandwidth specified by the manufacturer to be between DC and 125MHz. We found it absolutely essential to use this detector for both thermal and structural responses, as it was not possible to reliably deconvolve the effects of the AC coupling from the slow response for the Cummings detector.

In either case, the detection limits the level set by the local oscillator field E_{LO}^2. For the New Focus detector, the output DC voltage saturates to a maximum value, completely disguising any signal behavior. We have also found that operating close to this limit can yield incorrect behavior and provide inconsistent fits of long-time signals such as thermal diffusion or structural relaxation dynamics.

For the Cummings detector, excessive levels of background light will cause saturation of the detector's gain for the amplified fast response, despite its AC coupling. The result is actually an attenuation of the response that can serve to disguise the dynamics of interest and also lead to spuriously high observed decay rates for acoustic waves. In practice, we have found that an upper level of background light is roughly 85 µW CW at 830 nm, although due to the responsivity of the diode as a function of wavelength, this number is relaxed somewhat when probing with shorter wavelengths.

This last point indicates that the choice of probe wavelength must be balanced between several factors: if lenses are preferred, it must match the pump wavelength closely enough for the phase mask to be properly imaged at the sample, or else special achromatic lenses with design wavelengths specifically for the pump and probe should be used. A second issue is that the photodiode must have ample sensitivity at the detection wavelength to be useful; most photodiodes have a peak in their sensitivity in the 800 nm range. Finally, we note that these two points should be balanced by the fact that Brillouin scattering, like Rayleigh scattering, has a cross-section that scales as $1/\lambda^4$ with probe wavelength.

Depolarized Scattering

The use of phase masks and heterodyne detection in depolarized measurements on glass forming liquids is a recent development and demands further comment. In order to create a polarization grating such as that in figure 3-5a, it is necessary to insert $\lambda/2$ plates in the paths of at least two of the beams to rotate their polarizations perpendicular to the other coincident pulse. Ensuring that the pump pulses are still coincident in time requires that a piece of glass of identical thickness to the waveplate be inserted in the part of the beam whose polarization is not rotated. In practice, this was accomplished by inserting another waveplate aligned so as to not influence the polarization of the beam in question.

Even though zero order waveplates were used, there is an inevitable extent to which the output polarization is not pure, resulting in a superposition of both an intensity grating and a polarization grating. In the past, this inconvenience has been dealt with by introducing Glan-Thompson polarizers into the paths of all the beams to clean up the incident polarizations. The main drawback is that this introduces further non common-path optics into the setup, and also tends to walk beams, implying that even greater care needs to be taken in the initial alignment of the experiment.

With the use of CW heterodyne detection, however, this becomes unnecessary. The beam which is diffracted by the shear wave is amplified by heterodyne detection as it now shares the same polarization as the local oscillator. The portion which is diffracted by the density grating now has a perpendicular polarization to the local oscillator and thus does not get amplified. As homodyne signals are typically quite small, the amount of parasitic longitudinal signal is typically very small, if at all measurable, entailing that the use of Glan-Thompson polarizers to clean up depolarized signal is an unnecessary complication.

A drawback of the use of phase masks in depolarized measurements is the close proximity of the beams for larger grating spacing measurements; in practical terms, there is a limited amount of space in which to insert the $\lambda/2$ waveplates, while such a limitation does not exist when using beamsplitters and mirrors. In practice, this may be overcome by using square waveplates whose fast axis is aligned with one of the optic's edges. A simple holder may be designed to hold these two waveplates in the path of the two laser beams.

Pump Laser Optimization

Some of the experiments performed below required chopping the output of the laser to a repetition rate slower than can safely be achieved electronically by turning down the laser repetition rate[3]. Due to this particular regenerative amplifier's construction, there exists a steady stream of oscillator pulses at 78 MHz that come out colinear with the amplified pulse. This static background is not sufficient to generate measurable acoustic signal on its own, but the cumulative effect of 60 mW of oscillator power incident on the sample causes a static thermal grating. Chopping of the amplified pulse also chops this static thermal grating, whose disappearance and reappearance are marked by thermal decays and rises, respectively. While this effect is small, it is

---

[3] This is for the laser's sake. See Appendix A for an important discussion of this point.

noticeable, and can be inconvenient for samples which provide little signal. Therefore, effective chopping requires the selection of a single pulse while rejecting the oscillator train. This can be most easily performed with the use of an electro-optic or acousto-optic modulator.

The second point is concerned with the gating of the amplified pulse in the amplifier cavity. We simply note that care must be taken that the timing is adjusted to minimize pre and post pulses, the existence of which can doubly excite the sample and wash out the acoustic signals of interest, as well as cause other troublesome signal artifacts.

3.4 Data Acquisition and Fitting

The detector was attached to a Tektronix model TDS-7404 digital oscilloscope which has a bandwidth from DC to 4 GHz. The oscilloscope was externally controlled via GPIB interface and the data traces recorded on a computer using a home-made Labview program. This program was also able to automate data acquisition by using an adaptive loop to help the temperature controller reach a set temperature and ensure that it was stabilized at this temperature for a given amount of time before acquiring the data. Neither laser was blocked during the process of changing temperature. The automation was also able to adjust the glass slide in order to cycle the optical phase φ of the heterodyne beam between two preset positions that were optimized for positive and negative phase signals. Most of the data acquired below did not use this scheme, however, as its development was fairly late in the course of data acquisition.

Data of both positive and negative optical phase were collected independently for every data point used in this thesis. This was defined by, in the longitudinal case, the offset of the signal from the baseline before $t = 0$ and, in the shear wave case, the direction of the non-resonant electronic response. Subtraction of the negative phase signal from positive phase signal allows for the removal of common-mode electronic noise (such as is emitted by the Pockels cell), and also generally boosts the signal to noise ratio of the measured signal, as can be seen in figure 3-9.

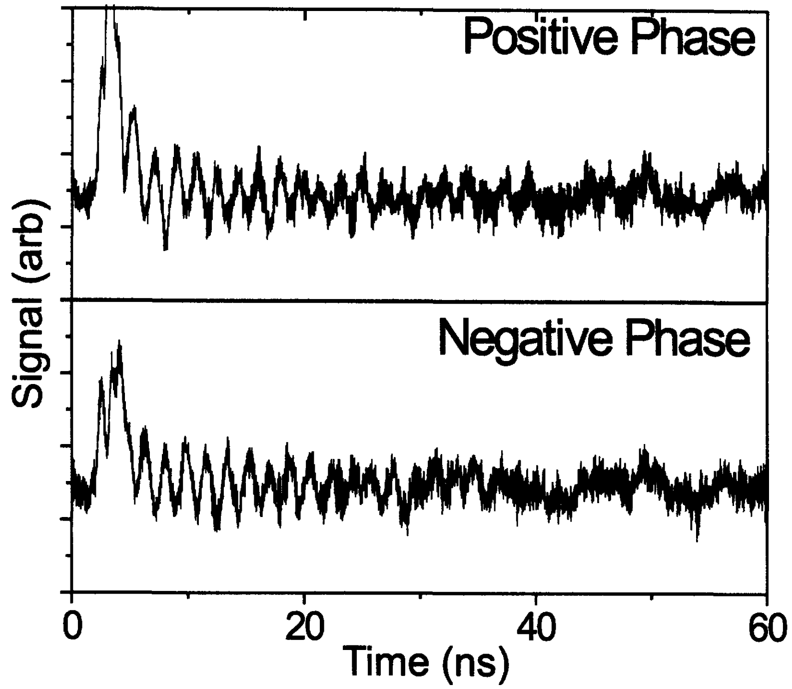

(a) Positive and negative phase shear wave signals in 5-phenyl 4-ether at 261 K.

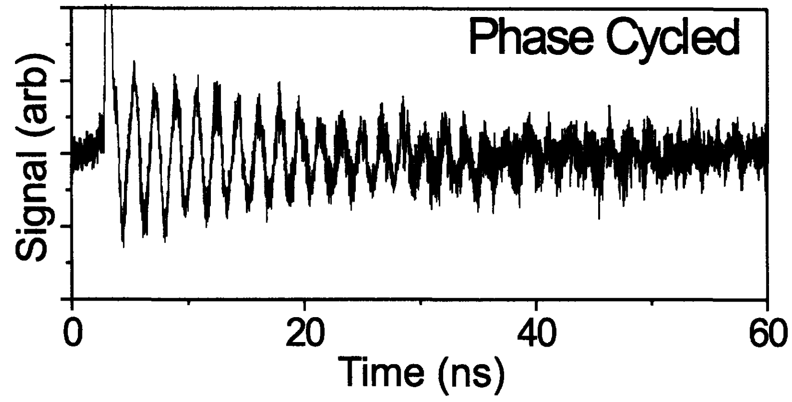

(b) Phase cycled shear wave signal in 5-phenyl 4-ether at 261 K.

Figure 3-9: Effect of phase cycling on signal. (a) shows the raw positive and negative data traces. At $t = 0$, some of the pump light has gotten into the detector amounting in the negative phase never reaching below zero. We also observe electronic noise in the second half of the data trace. Both of these artifacts are "common mode" forms of noise that drop out upon phase cycling, as seen in trace (b). The scales of all traces are identical.

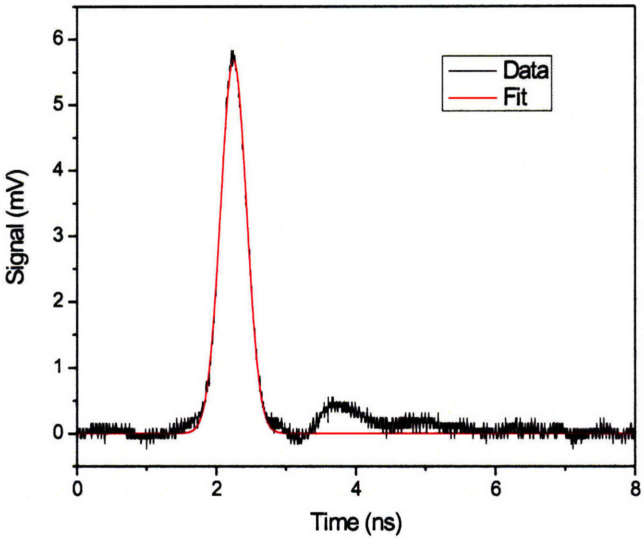

Figure 3-10: Example of instrument response function obtained by sending a small portion of the laser pulse into the detector. The Gaussian is able to fit almost all of the features of the detector's instrument response. There is a little bit of the response after the Gaussian that is not accounted for, but which we found to be insignificant.

The phase cycled signal was then fit in the time domain to the appropriate theoretical signal function given above. Effort was made to include the effect of the detector's instrument response function (IRF) on the signal, which was modelled by a Gaussian of the form

$$IRF(t) = A \exp\left(\frac{t - t_0}{\sigma}\right)^2, \tag{3.76}$$

where A is an amplitude parameter, t_0 is the fitted arrival time of the laser pulse and $t = 0$ for the experiment, and σ is a width parameter for the Gaussian. An example of an IRF is shown in figure 3-10 for fit parameters $A = 5.69$ ns, $t_0 = 2.24$ ns, and $\sigma = 0.262$ ns. In the case of shear waves, this IRF was fit to the hyperpolarizability spike separately for each individual data trace; we have found the σ parameter to vary little from fit to fit.

The measured signal is then given by the convolution of the IRF with the theoretical signal as, in practice, it is a lot easier to fit the convolved function than to deconvolve the instrument response from the frequency domain. The fits were performed with the nonlinear least squares method embedded in the prepackaged MATLAB "`fit`" function. Generally, proper judgment is involved in fitting the time-domain traces, and for ease of use, a GUI was developed for fitting the time-domain data. In the cases of poor signal to noise, the implementation of MATLAB's Butterworth filtering was used to find realistic starting parameters, but the fits ultimately used for subsequent analysis were always performed on the unfiltered data.

All of the data used for mapping relaxation spectra were acoustic traces taken at a single timescale on the oscilloscope. Due to their temporally broad characteristics, direct determination of the structural relaxation parameters τ_R and β requires pasting together several data sweeps taken at different oscilloscope time scales. Slight variations of signal intensity are likely between phase cycled sweeps, and to account for this, we subtracted any offset from before $t = 0$ to bring all traces to a common baseline, superposed the two traces at their common data points[4], and used MATLAB's "`fminsearch`" function to produce the multiplication factor of the longer-time signal which gave best overlap. The plots in figure 3-3 were generated in this manner.

3.5 Sample Preparation and Handling

Several authors vacuum distill the liquid under study into the dust-free cells, and then flame-seal the cells under vacuum. While preferred, this is not presently possible given the configuration of the cell being used [68]. In all of the studies performed for this thesis, the most sample preparation consisted of heating the liquids under vacuum to remove volatile impurities, using the drying agent $MgSO_4$, or a combination of both. This is quite important as impurities such as phenols, alcohols, and especially water, may either phase separate from the liquid under study, rendering it opaque and unusable, or they may even crystallize, causing the glass former to crystallize, too.

After outgassing, we removed dust (which may serve as nucleation sites for crys-

---

[4] Traces of differing time-scale also have different resolution, hence the need to pair up the different sweeps accordingly.

tals) by transferring the liquid to the cell through a teflon millipore filter. We have found it of great importance to use teflon as the filtering medium, as opposed to the several other options otherwise available – such as cellulose – which may be dissolved by the liquid and then either phase separate or crystallize on their own.

Liquids may contract significantly upon cooling. If the resulting stresses are not relieved after the liquid has lost the ability to flow, the glass may crack, rendering the sample opaque and unsuitable for study. To avoid this issue, a cell with movable windows, as described in [68], is used in the experiments. In practice, the cell did not work as well as hoped, likely due to the teflon o-rings holding in the windows being too tight to allow the window to move inwards upon cooling. In these cases, the liquid either had to be melted and recooled or, if there was a clear path, the sample moved so that light could still get through.

After the liquid was loaded inside, the cell was attached to the coldfinger of a Janis model ST-100-H cryostat which was evacuated in order to avoid condensation on the sample during cooling. The vacuum also lowered the thermal load of the coldfinger. We have used liquid nitrogen exclusively in this thesis, and the boil-off from the mini-dewar that it was contained in was enough back pressure to be able to force the cryogen into the cryostat. The sample temperature was regulated by a LakeShore Cryotronics, Inc model 331 temperature controller which was able to keep the temperature stable to within 0.01 K for each data point using the cryostat's heater located at the interface of the coldfinger and the sample.

Chapter 4

Impulsive Stimulated Thermal Scattering Study of DC704

4.1 Introduction

In the previous chapters, we described how Impulsive Stimulated Scattering may be used as an effective tool in characterizing the phenomenological aspects of the glass transition, as well as be a means of testing the predictions of the mode-coupling theory. In what follows, we present an ISS study of the glass forming liquid tetramethyl tetraphenyl trisiloxane, a diffusion pump oil developed by the Dow-Corning company and sold by the trade name DC704. Our choice of sample is motivated by the work of Dyre and Olsen, who have characterized both the bulk and shear mechanical, as well as dielectric relaxation of this liquid across several decades in frequency from 10^{-3} Hz up to $10^{4.5}$ Hz [69, 70]. Below, we employ ISS in order to map the longitudinal spectrum from 10^7 Hz to 10^{10} Hz through acoustic measurements, and 10^3 Hz to 10^7 Hz through direct determination of relaxation in the time-domain. Thus, among the many long-term goals of this study is a view towards extending the dynamic range of measured acoustic spectra.

Our broad dynamic range in time and frequency also allows for a comparison between our two methods for obtaining the modulus, and is presented below. We shall also use the acoustic spectra we obtain to look for evidence of growing dynamic

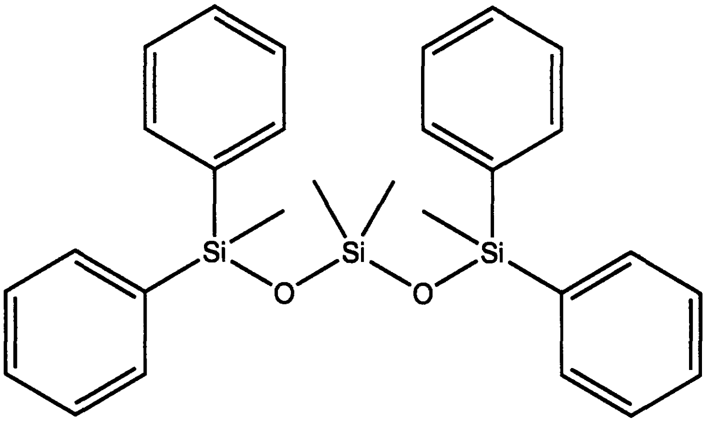

Figure 4-1: Chemical structure of tetramethyl tetraphenyl trisiloxane. The liquid is likely to be entirely van der Waals bonded due to the phenyl groups; as the oxygens are bonded silicon atoms, hydrogen bonding is likely prohibited.

length scales using the analysis of Berthier et al [28].

An analysis in terms of the mode-coupling theory is also presented. Here we look for a square-root cusp in the Debye-Waller factor, which is a quantitative measure of the non-ergodicity, or "falling out of equilibrium" of the liquid. The information we obtain on the evolution of the relaxation also allows us to test the notion of time-temperature superposition. Our mode-coupling analysis concludes with a measure, and comparison, of two of the three critical exponents of the theory.

Finally, we have been able to observe propagating shear waves in DC704 over a modest range of temperatures and wavevectors. Below we present preliminary results of an attempt to produce a shear spectrum, and form a comparison with the longitudinal spectrum.

4.2 Experimental Methods

The lasers and experimental configurations that were used for these measurements are described above in chapter 3; in order to span as broad a frequency range as possible, we have used both the lens-based and mirror-based setups. The acoustic wavelength for both setups was calibrated through ISTS measurements in ethylene glycol, for which the speed of sound is known to a high degree of accuracy [66]. This calibration was double-checked after all of the data collection was finished and the variation in acoustic wavelength ranged from approximately 0.1% at the smallest to 1.8% at the largest with an average value of 0.7%. This determined our uncertainties in the sound speeds, but did not affect the uncertainties in the damping rate.

In both setups, when acoustic spectra were measured, the signal was collected with a Cummings Electronics Labs Model 3031-0003 amplified photodiode with 10 kHz - 3 GHz bandwidth. When longer time signals were studied, we used a New Focus Model 1801-FS detector with a bandwidth of DC to 125 MHz. In all cases, the signal was processed by a Tektronix TDS-7404 digitizing oscilloscope with a 4 GHz bandwidth. Depending upon signal-to-noise ratios, signals from 2,000 to 4,000 repetitions of the measurement were averaged for each data trace, with total data acquisition times of less than a minute per trace.

When building acoustic spectra, data were taken for every available wavelength in the range from 1.75 µm to 101 µm by fixing the temperature and scanning the this wavelength. These grating spacings were 1.75 µm, 1.97 µm, 2.33 µm, 2.68 µm, 3.14 µm, 3.64 µm, 4.20 µm, 4.85 µm, 5.66 µm, 6.56 µm, 6.70 µm, 7.61 µm, 9.13 µm, 10.2 µm, 11.7 µm, 13.7 µm, 15.7 µm, 18.3 µm, 21.3 µm, 24.9 µm, 28.5 µm, 33.0 µm, 38.1 µm, 44.2 µm, 49.8 µm, 50.7 µm, 56.9 µm, 65.9 µm, 76.0 µm, 88.0 µm, and 101 µm. The raw data are provided in Appendix B. In order to have a baseline of comparison from setup to setup, we have taken one wavevector in common between different configurations of the optics.

Scans of the temperature at fixed wavevector were also done in order to provide access to the evolution of acoustic velocity and damping rate as a function of T. In these cases, the temperature was set to 330 K and decreased slowly over a period of many hours. Differences of 2K in temperature were typically given 30 minutes to equilibrate before the data were taken. This was also done in the regime where the structural relaxation is evident in the time domain (for 1.97 µm, 11.7 µm, 24.9 µm and 49.8 µm grating spacings), although for experimental convenience, here the data were taken upon warming.

DC704 was obtained from Sigma Aldrich and used without purification. The liquid was transferred into the cell through a 0.22 µm millipore filter; as the sample was observed to become slightly opaque upon cooling, the liquid was placed in a 5 mm fused quartz cuvette made by Starna Cells, which provided a small enough optical path length to not attenuate the signal beam, but was more than thick enough to permit the excitation of bulk acoustic gratings. It was discovered after the measurements were performed that the opacity was due to phase separation of water and other dissolved impurities from the base liquid, and this could be largely overcome by mixing the sample with a drying agent such as anhydrous $MgSO_4$, combined with heating under vacuum. This fact was discovered after this study was completed. Nevertheless, the DC704 never crystallized during the course of our experiments.

Once loaded, the cuvette was placed in a holder provided by Janis where it was ensured that good thermal contact was made between the two with indium foil. The holder was directly attached to the coldfinger of a Janis model ST-100 cryostat which was controlled by a Lakeshore model 331 temperature controller. Temperature sensing was provided by a factory calibrated Lakeshore model PT-102 platinum resistor which was immersed in the liquid a few millimeters away from where the beams were crossed for the experiment. Both temperatures were stable to within 0.01 K for the duration of each measurement.

4.3 Results and Discussion

Four separate traces of ISTS data recorded with 38.1 µm grating spacing, representing the four different signal regimes are shown in figure 4-2. In all traces at short times, there are oscillations due to the counterpropagating acoustic waves, and at long times, the signal decays to zero due to diffusion of the thermal grating. The trace in (a) shows data taken in the high-temperature liquid state, showing weak damping of the acoustic wave. In the regime where the α relaxation is on the time scale of an acoustic period, mechanical energy is quickly dissipated into structural relaxation and the acoustic signal is strongly damped, as shown in (b). At slightly lower temperatures as depicted in (c), α relaxation dynamics extend to time scales significantly longer

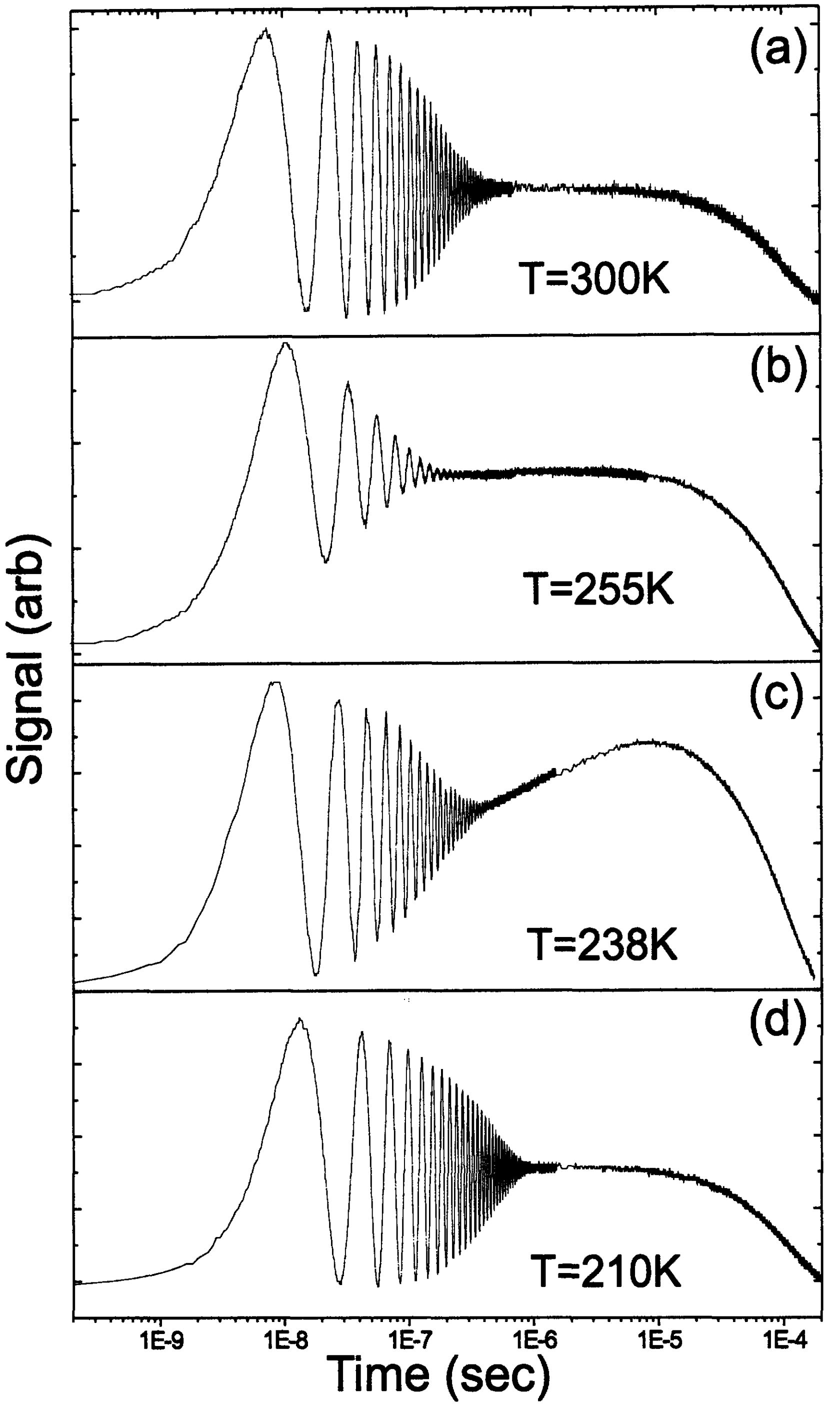

Figure 4-2: Longitudinal signal from DC704 at four temperatures. the grating fringe spacing was 38.1 µm. The different regimes are discussed in detail in the text.

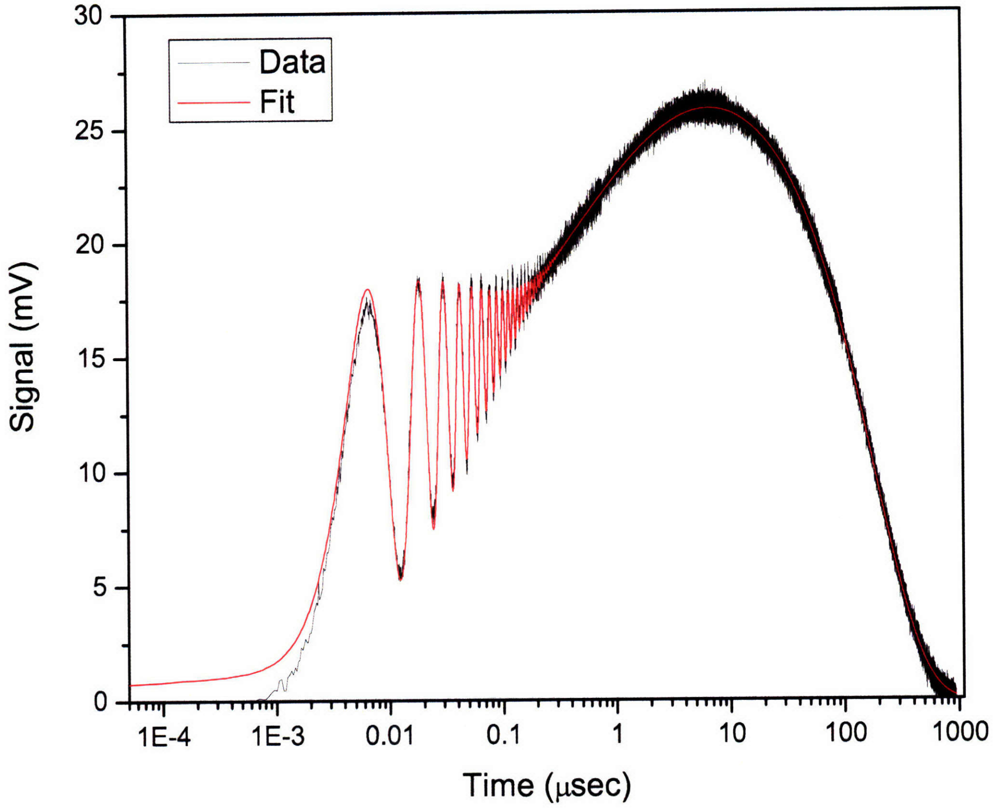

Figure 4-3: Longitudinal signal in DC704 at 242K, 24.9 μm grating spacing. The fit is able to account for all observed features of the data.

than that of the acoustic response, resulting in reduced acoustic damping and slow components of thermal expansion that are observed directly in the data. Finally, when the liquid is cooled into the glassy state as in (d), the damping is observed to decrease significantly, and the slow components of thermal expansion are no longer observed because thermal diffusion releases the stress on a faster time scale.

Figure 4-3 details one particular trace which shows excellent agreement with a fit to the model function

$$A(e^{-t/\tau_{th}} - e^{-\Gamma t}\cos(\omega_A t)) + B(e^{-t/\tau_{th}} - e^{-(t/\tau_s)^{\beta}}) + Ce^{-\Gamma t}\sin(\omega_A t) \tag{4.1}$$

which is identical to equation 3.26 in section 3.2.1, save for a sine term added to express contribution from ISBS signal. Here, A and B are ISTS amplitudes, while C is the amplitude for the ISBS signal. τ_{th} is the thermal decay time and τ_s is the characteristic structural relaxation time stretched by the exponent β. These two variables will be known as τ_{KWW} and β_{KWW} in all that follows. Finally, ω_A is the observed acoustic frequency, and Γ is the total acoustic damping rate, including the background viscous damping.

The fits were performed by first fitting the acoustic part of the response with freely varying parameters for all other quantities. After that, the time window was expanded to incorporate the full signal sweep and the other parameters were fit while the acoustic parameters were held fixed. When acoustic data were analyzed to form frequency domain spectra, data for each temperature were fit in succession from highest wavevector to smallest, and the results for the previous fit were used as the starting parameters in the next fit. In the cases where time domain relaxation was studied, data were fitted for all temperatures taken with a given wavevector. Randomly selecting a number of different experimental traces and fitting with random starting parameters always reproduced the same fitted values to within the stated 95% confidence interval provided by the fitting routine, as did reversing the fitting procedure (i.e. fitting long-time behavior before the acoustic response), indicating that there was no operator bias in the fits.

4.3.1 Phenomenological Analysis

Using the above fitting procedure allows access to the characteristics and evolution of the α relaxation spectrum, specifically the KWW function used to model the slow rise in our signals, $\exp(-(t/\tau_{KWW})^{\beta_{KWW}})$. Data were taken every 2 degrees in the temperature regime in which it was observed, specifically from 220 K to 248 K. Fits which yielded a value for τ_{KWW} which was longer than the time between laser pulses (here 1 ms) were cast out as being unrealistic. This restricted the temperature range from 230 K to 248 K for the wavevectors in which we could examine this feature.

A plot of the behavior of τ_{KWW} as a function of temperature is shown in figure 4-4. The data span several orders of magnitude in time, from 100 ns to 1 ms, over a range of 28 K. We note that there is quite good agreement between the data taken at 24.9 µm and 50.7 µm. Time-dependent thermal expansion signals were also recorded with grating wavelengths of 11.7 µm and 101 µm. At 101 µm, thermal diffusion was so

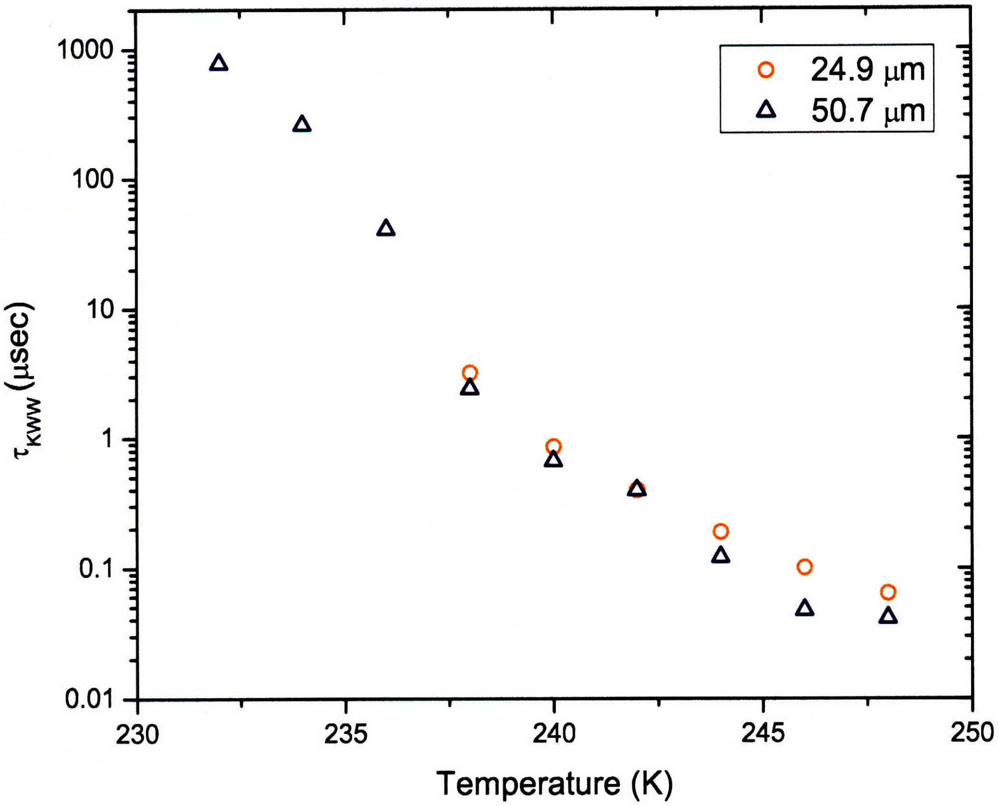

Figure 4-4: τ_{KWW} in DC704 as a function of temperature. The data from 24.9 µm and 50.7 µm show excellent agreement.

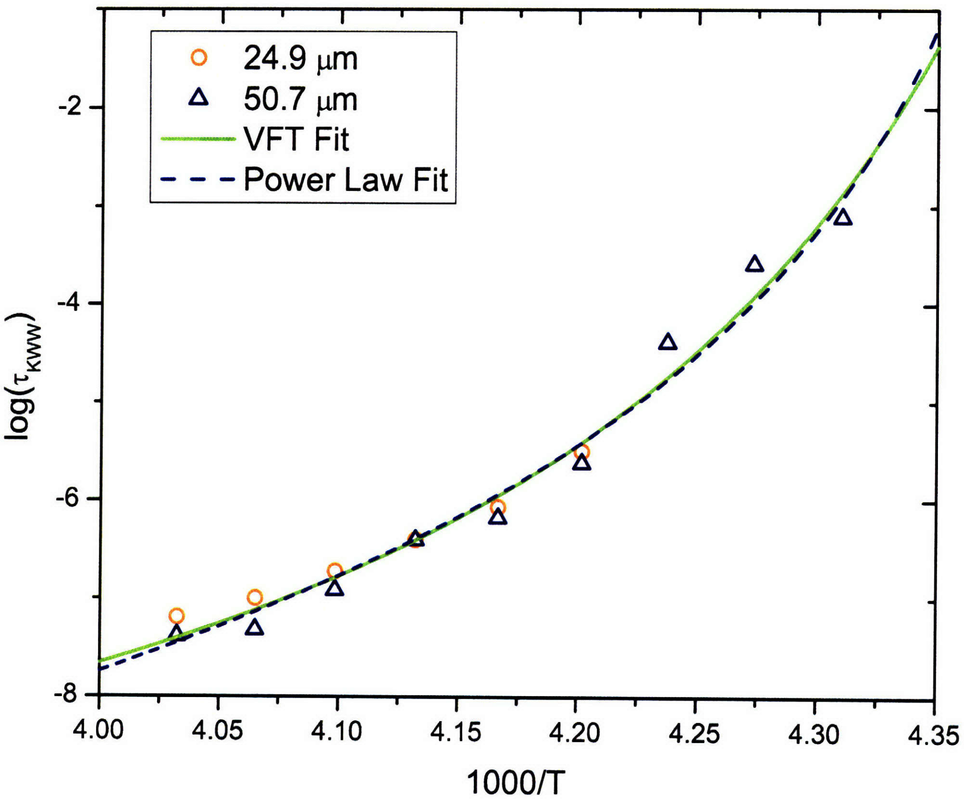

Figure 4-5: VFT and power law fits to relaxation time determined from KWW fits in DC704. Both give good agreement with the data. The VFT fit parameters we obtain here are $\tau_0 = 3 \pm 18$ ps, $B = 300 \pm 200$ K, and $T_0 = 218 \pm 8$ K, while the power law yields $\gamma = 7 \pm 3$ and $T_c = 227 \pm 5$ K. The power law fits are explained in more detail in the context of the mode-coupling theory below.

slow that it exceeded the time between repetitions of the measurement. The resulting buildup of the stead-state signal level from shot to shot had no significant effect on the observed acoustic frequency and damping rate, but likely led to significant distortions of the slower signals and the KWW fits to them. At 11.7 μm, the time-dependent thermal expansion was observed on time scales that extended across two regimes that were measured by two different photodetectors and that were difficult to connect reliably into a single time-dependent feature. The data at 24.9 μm and 50.7 μm were recorded with a single (low-bandwidth) photodetector, and at these wavelengths thermal diffusion from one measurement was complete well before the next measurement began.

A VFT fit to the data is also shown in figure 4-5 where a reasonably good fit is given to the 24.9 μm and 50.7 μm data for all values of the scaled inverse temperature

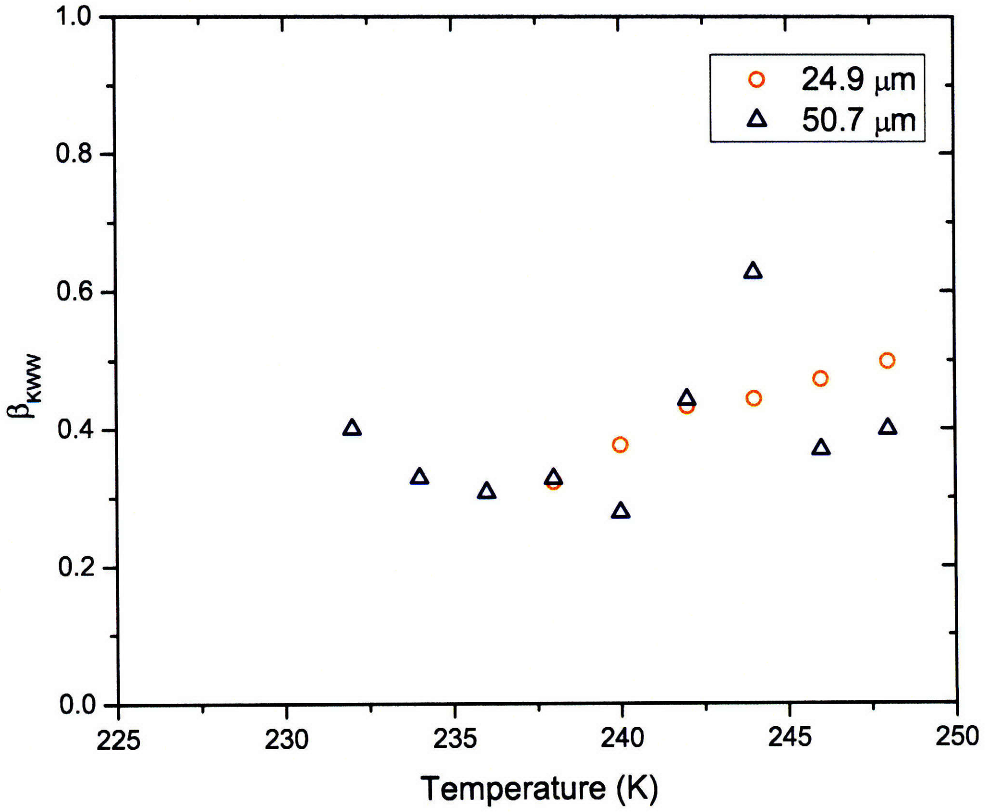

Figure 4-6: β_{KWW} in DC704 as a function of temperature. The relative invariance of β_{KWW} with temperature over the wide range of relaxation times indicates that DC704 obeys time-temperature superposition with $\beta_{KWW} = 0.4$.

1000/T. The fit parameters we obtain here are $\tau_0 = 3\ \pm 18$ ps, $B = 300\ \pm 200$ K, and $T_0 = 218\ \pm 8$ K. From this expression, we are able to deduce a glass transition temperature where T_g is defined as the temperature at which $\tau = 100$ s. The value of T_g that we obtain is 227 K, which is in contrast with other measurements of DC704 [70, 71] where a value of $T_g = 210$ K has been obtained. As VFT fits are not universal, this implies that the temperature region of this portion of the analysis, which only goes down to 230 K, is sufficiently far away from the slow dynamics to adopt VFT parameters that would provide the correct value for T_g.

Examining the fitted values of β_{KWW} shows a remarkably small amount of variation with temperature, where all values cluster around $\beta_{KWW} = 0.4 \pm 0.1$. Thus, we can conclude that, in the temperature regime examined here (230 K - 248 K), DC704 exhibits time-temperature superposition.

When only acoustic contributions to the signal appeared at short times, the data

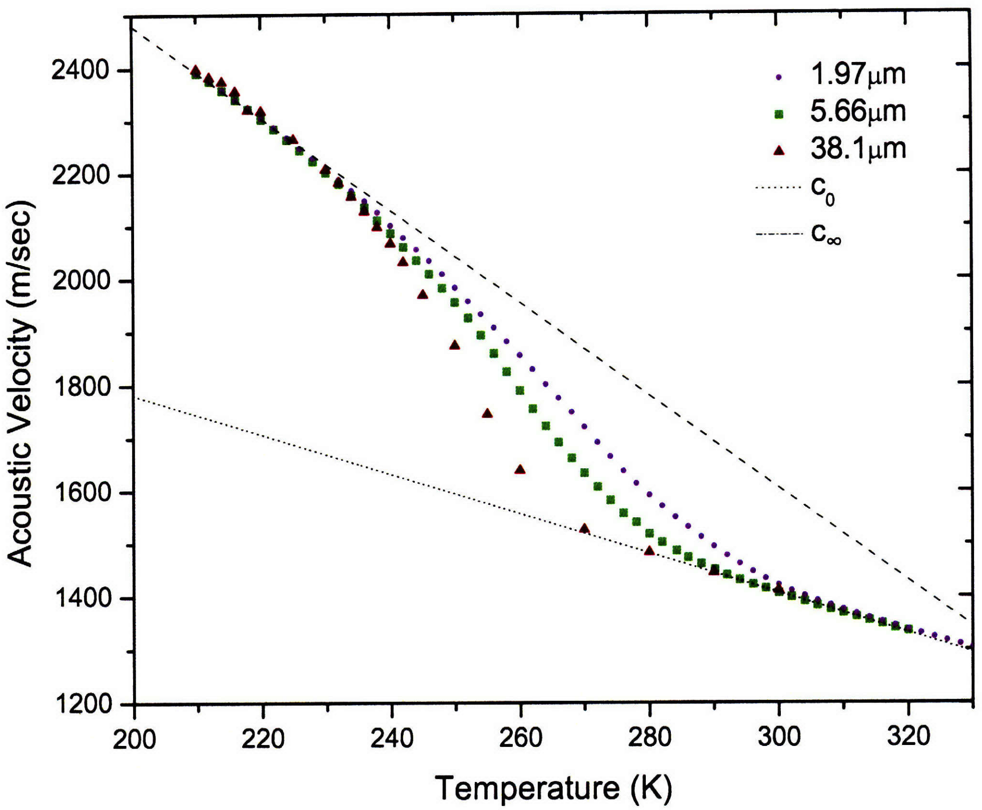

Figure 4-7: Acoustic velocity in DC704 as a function of temperature for three wavevectors. Also plotted are linear extrapolations for the values of c_0 and c_∞.

were fit to the full time domain form given in equation 4.1. For smaller grating spacings (smaller than 7.5 μm), we note that the ISBS contribution to the signal became significant because, as described in Chapter 3, the magnitude of contribution increases linearly wth wavevector. In cases where time-dependent thermal expansion overlapped with the acoustic response, we fit to the full form of equation 4.1 to account for the gradual rise, but we only used the acoustic parameters, as the KWW parameters could not be determined reliably.

In figures 4-7 and 4-8, the measured acoustic frequencies and damping rates, respectively, as a function of temperature are shown for a variety of grating spacings ranging from 1.97 μm to 38.1 μm. The data show all the features consistent with the material undergoing a transition from liquid to glass, as mentioned above in the description of the signal in various temperature regimes. First we examine the shift of the acoustic velocity in the two separate regimes. For high temperatures ($1/\tau_R \gg \omega_A$), the acoustic damping rate is low, and the velocity increases linearly with temperature.

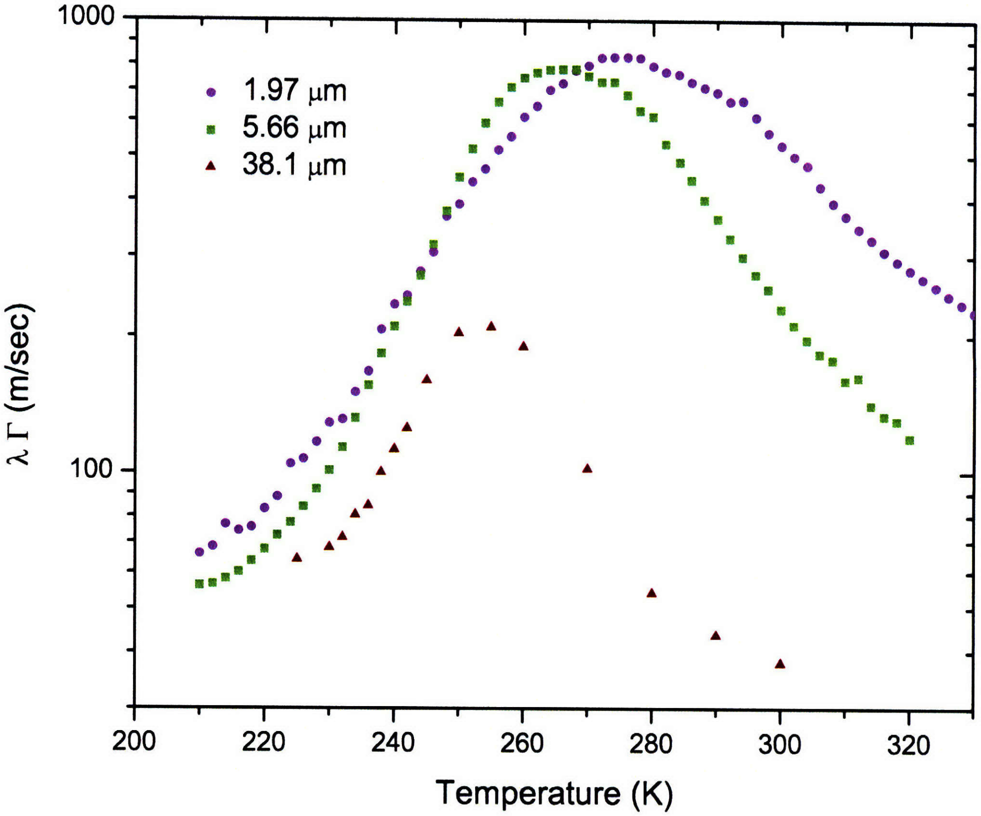

Figure 4-8: Scaled acoustic damping rate in DC704 for three wavevectors, where the scaling has been done by multiplying by the acoustic wavelength λ. The damping rates for higher wavevector are much larger due to the $\sim q^2$ background damping. The low-temperature damping rates at 38.1 μm wavelength were too low to measure reliably due to propagation of the acoustic waves away from the excitation and probing region.

Being on the slow side of the relaxation, this allows us to extrapolate a value for the zero frequency sound speed c_0. Here we have assumed linear dependence on temperature and fit points from several grating spacing in the region from 330 K to 310 K. This analysis yields

$$c_0 = 2530 \pm 10 \text{ [m/s]} - 3.53 \pm 0.05 \text{ [m/s} \cdot \text{K]}\ T \text{ [K]}, \tag{4.2}$$

as depicted in figure 4-7.

When $1/\tau_R \sim \omega_A$, there is a peak in the damping rate, and a significant change in the sound speed. For the wavevectors used, these features appear in the temperature range 240 K - 270 K. Finally, at low temperatures (210 K - 230 K), $1/\tau_R \ll \omega_A$, the damping comes back down to low values, and again the acoustic velocity increases approximately linearly with a decrease in temperature. A fit of the velocity vs. temperature in this range yields a phenomenological expression for the evolution of the instantaneous longitudinal sound speed c_∞

$$c_\infty = 4230 \pm 50 \text{ [m/s]} - 8.7 \pm 0.2 \text{ [m/s} \cdot \text{K]}\ T \text{ [K]}. \tag{4.3}$$

The expressions for low and high-frequency acoustic velocities cannot be extrapolated reliably into temperature ranges far from those measured directly. Additional measurements (including ultrasonics, Brillouin scattering, or picosecond ultrasonics [72]) are needed for this purpose.

The damping rate Γ may be used to get an estimate of the background viscous damping term $1/2\nu_l q^2$. This has been extracted by fitting the acoustic decay rate versus the wavevector squared for a series of data points taken at the two extremes of our acoustic scans for which time-domain fits yielded accurate results: namely at 320 K and 216 K. For temperatures warmer than 330 K or colder than 216 K, the damping rate relative to the frequency was low enough that the finite size of the probe and excitations spot impacted the shape of the signal. Once the damping coefficient was determined at each temperature extreme, we assumed a linear dependence upon the temperature, which produced the result

$$\nu_L(T) = (31 \pm 2\ [\mathrm{m}^2/\mathrm{s}] + 0.13 \pm 0.01\ [\mathrm{m}^2/\mathrm{s}\cdot\mathrm{K}](T[K] - 320\ [\mathrm{K}])). \tag{4.4}$$

Using the acoustic parameters determined at a common temperature, the complex frequency-dependent longitudinal modulus $M^*(\omega) = M'(\omega) + iM''(\omega)$ can be determined from

$$M'(\omega_A) = \rho\frac{\omega_A^2 - \Gamma_A^2}{q^2} \tag{4.5}$$

$$M''(\omega_A) = \rho\frac{2\omega_A\Gamma_A}{q^2} \tag{4.6}$$

where ρ is the density, and the background damping has been subtracted as $\Gamma_A = \Gamma - 1/2\nu_L q^2$. Thermal contraction of the sample was accounted for by using literature data of the temperature dependence of density [73, 74]

$$\rho(T) = 1.0679\ [\mathrm{kg/m^3}] + 7.2\times10^{-4}\ [\mathrm{kg/m^3}\cdot\mathrm{K}](298\ [\mathrm{K}] - T[\mathrm{K}]) \tag{4.7}$$

in order to extract the true moduli.

Modulus plots are shown in figures 4-9 and 4-10. Of note in our data is a small jog in the moduli around $\omega_A/2\pi = 40$ MHz, and another at $\omega_A/2\pi = 300$ MHz. These small jumps are the result of using three different optical configurations for the data that were taken at three different times and hence on three different cool-down cycles. We are confident that the small uncertainties in wavevector (± 1% or less) and temperature (typically ± 0.1 K or less) are not the source of the jog. We conclude that the jog may result from differences in the cooling rates, which ranged from approximately 1 K/min to 6 K/min.

Once data points for the modulus were obtained, they were fit to the relationship

$$M^*(\omega) = M_\infty - \frac{M_0 - M_\infty}{(1 + (i\omega\tau_{HN})^{\alpha_{HN}})^{\beta_{HN}}} \tag{4.8}$$

where M_∞ and M_0 are the infinite frequency and static longitudinal moduli, respec-

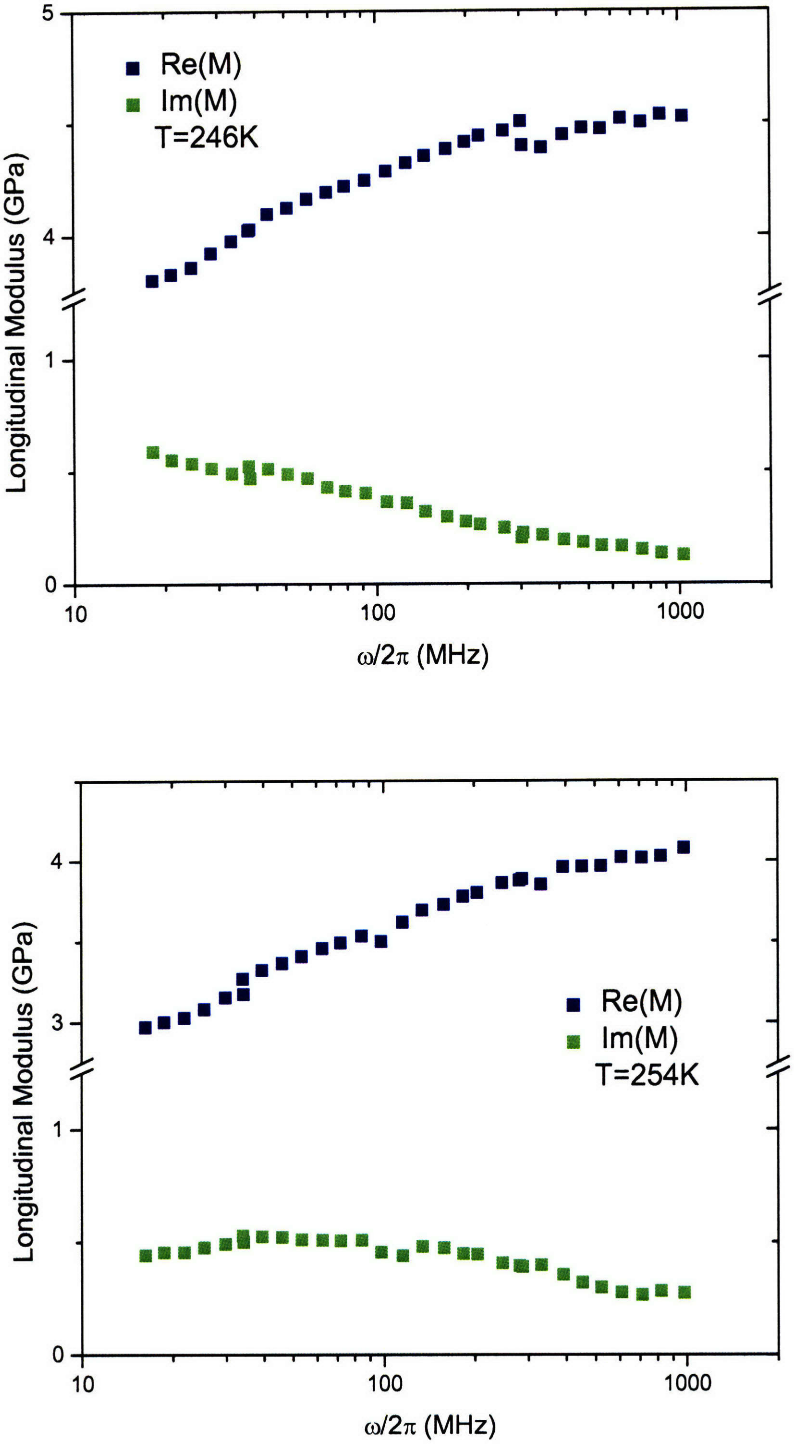

Figure 4-9: Longitudinal relaxation spectrum at 246K and 254K. The real part is in blue, imaginary in green.

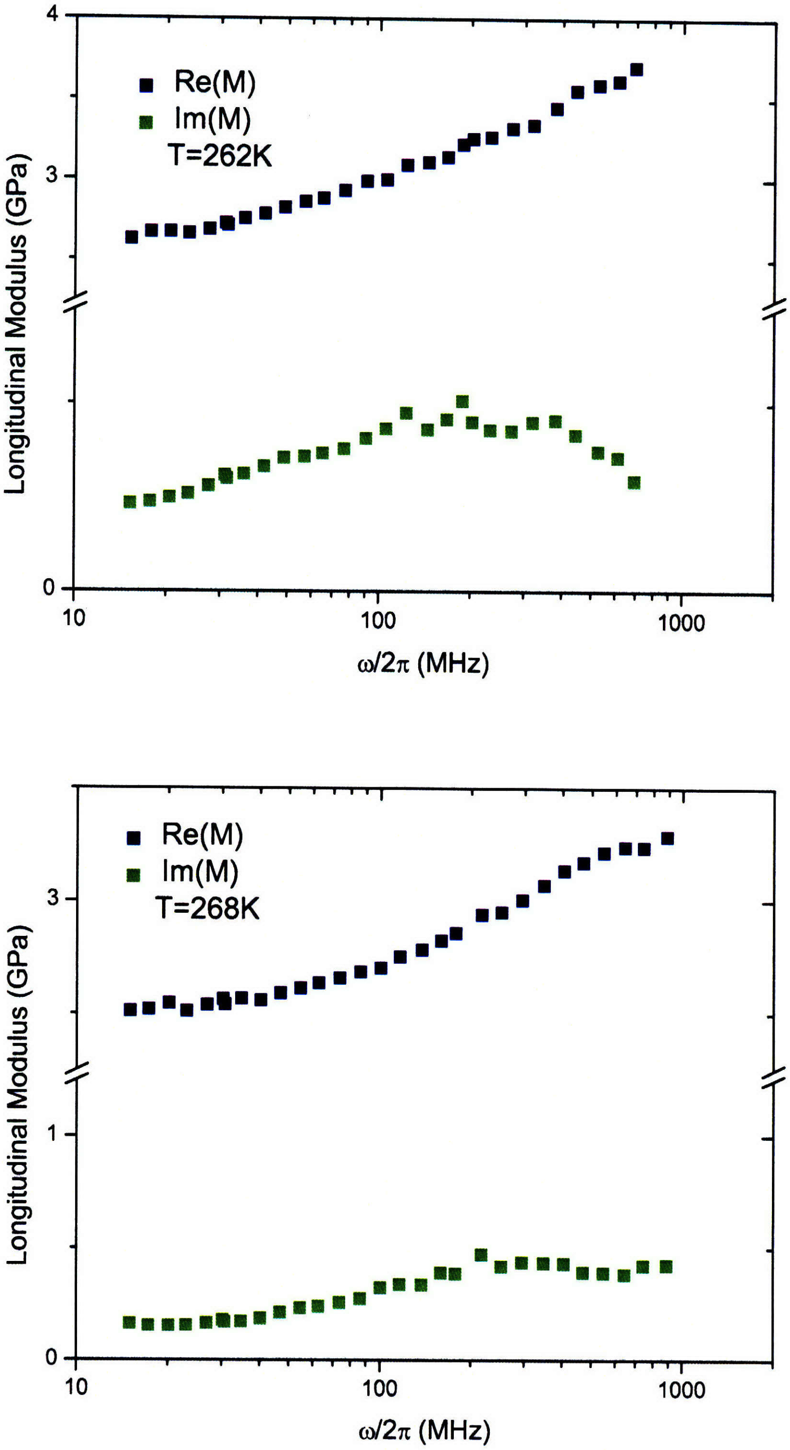

Figure 4-10: Longitudinal relaxation spectrum at 262K and 268K. The real part is in blue, imaginary in green.

tively. We have chosen to model the relaxation peak by a Havriliak-Negami distribution as its use of two separate exponent parameters better facilitates the transition between it and its time-domain analogue, the KWW function. This transition was accomplished using the recent work by Hilfer [21, 22] where a series expansion representation for the Fourier transform of the KWW function is given by

$$\mathcal{F}(\exp(-(t/\tau_\beta)^\beta)) = \begin{cases} 1 - \sum_{k=0}^{\infty} \frac{(-1)^k \Gamma((k+1)/\beta)}{\beta \Gamma(k+1)} (-i\omega\tau_\beta)^{k+1} & |i\omega\tau_\beta| \to 0 \\ 1 - \sum_{k=0}^{\infty} \frac{(-1)^k \Gamma(\beta k+1)}{\Gamma(k+1)} (-i\omega\tau_\beta)^{-\beta k} & |i\omega\tau_\beta| > 0. \end{cases} \tag{4.9}$$

where $\Gamma(x)$ is the complementary incomplete Gamma function

$$\Gamma(x) = \int_0^\infty e^{-t} t^{x-1} dt. \tag{4.10}$$

In both expressions of equation 4.9, τ represents τ_{KWW} and β is β_{KWW}. The upper expression in 4.9 is an asymptotic series that applies in the low frequency limit, and the lower is a convergent series for larger frequencies. In our analysis, we evaluated the appropriate series numerically, and the resulting real and imaginary curves were then simultaneously fit to equation 4.8 with $M_\infty = 1$, $M_0 = 0$. These fits provided the frequency domain parameters τ_{HN}, α_{HN} and β_{HN} from our time domain data. Figure 4-11 shows an example of this analysis for values $\beta_{KWW} = 0.4$, $\tau_{KWW} = 1\ \mu s$.

Since these two functions are not strict Fourier transforms of one another, different parts of the spectrum fit to differing degrees. In order to extract consistent values of τ_{HN}, α_{HN}, and β_{HN} from the KWW parameters, the transformed spectrum was centered at the experimental value of τ_{KWW}^{-1} and the domain of the transform was taken as 5 decades. Fits to the entire spectrum for the values of β_{KWW} observed routinely led to values of $\alpha_{HN} = 0.75 \pm 0.15$ and $\beta_{HN} = 0.45 \pm 0.1$. Since β_{KWW} was observed to vary little in the original KWW fits, it was no surprise that α_{HN} and β_{HN} behaved similarly. Thus, the utility of equation 4.9 is not limited to obtaining a characteristic relaxation time that may be compared with the analogous frequency domain values. It also may be used to provide a regime of valid α_{HN} and β_{HN} parameters in equation 4.8 that may be compared to values determined from acoustic

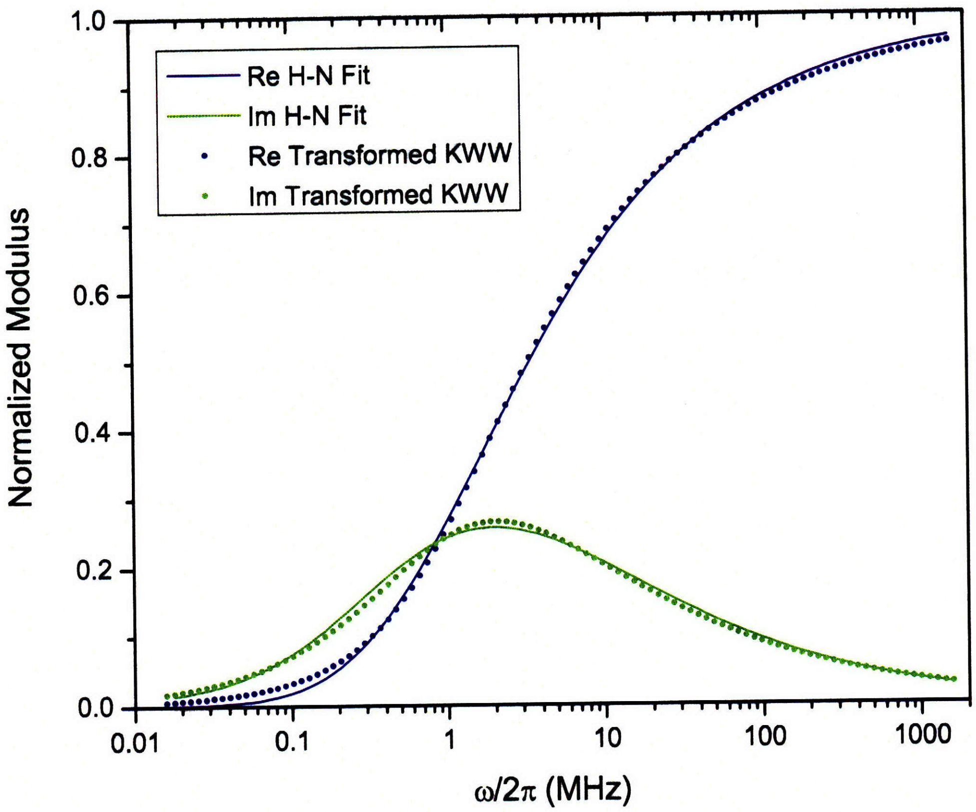

Figure 4-11: Comparison of transformed KWW function and its Havriliak Negami fit for $\beta_{KWW} = 0.4$ and τ_{KWW}=1 µs.

data in the same temperature range.

We believe that this procedure is more accurate (and more useful) than transforming the Havriliak-Negami fits into KWW parameters: as the structural relaxation modelled by the KWW equation represents the full long-time decay of the density-density correlator, it encapsulates the entirety of the alpha relaxation spectrum. In contrast, at the same temperatures that we observe relaxation in both the domains, we can only access this spectrum's high-frequency wing in our frequency domain. This is a consequence of the fact that we are able to observe the time-dependent thermal expansion from which the KWW parameters are derived when it occurs on slow time scales compared to the acoustic response at the same wavevector. As a result, our acoustic data provides information about the relaxation spectrum at higher frequencies than our time-dependent thermal expansion data. Even when the average relaxation time is in the middle of our acoustic window, our limit of two decades in acoustic frequency precludes the ability to accurately fit an acoustic spectrum without assumptions made for at least one of the fitting parameters.

In principle, fits to expression 4.8 may also be constrained by the limits of the elastic moduli, M_0 and M_∞. These may be obtained from the extrapolated results of the acoustic measurements, equations 4.2 and 4.3, respectively. However, as mentioned above, extrapolation of the value for c_∞ and c_0 far from the temperature ranges in which they were measured cannot be done reliably.

Thus, in fitting the acoustic results, we have adopted four different approaches with varying constraints, with a view of balancing the quality of the fits versus realistic bounds on the parameters. First, all parameters were allowed to vary in order to obtain a best fit whose only use (given the limited slice of the spectrum available) was for a visual comparison to the constrained fits.

In the second approach, the data were fit assuming that time-temperature superposition holds and that the spectral parameters derived from the KWW data are also applicable in the frequency domain. In these cases, we used $\alpha_{HN} = 0.75$ and $\beta_{HN} = 0.45$. The third approach was to fix the limiting moduli based on the linear extrapolations given above. Finally, the fourth method was to apply both sets of constraints, on the moduli and the exponents. If the constrained fit yielded results consistent with the transformed values of τ_{KWW} while still resulting in a low least squares error compared to the unconstrained fit, the fit was considered valid.

The results of fitting our longitudinal modulus data comparing constraints on the exponents with freely bounded fits are shown in figures 4-12 - 4-15. Qualitatively, we found that the fits with fixed exponents are consistent in quality with fits using freely varying parameters, although the latter are somewhat better for a few of the individual spectra, particularly for the lowest 3 temperatures studied (240 K - 244 K). Indeed, many of the unconstrained fits where the dissipative part of the susceptibility is in the middle of our frequency window yielded the same results as the constrained ones.

In both of these cases, we obtained the unrealistic value of the zero-frequency modulus being nearly equal to zero for the low-temperature regime, which is symp-

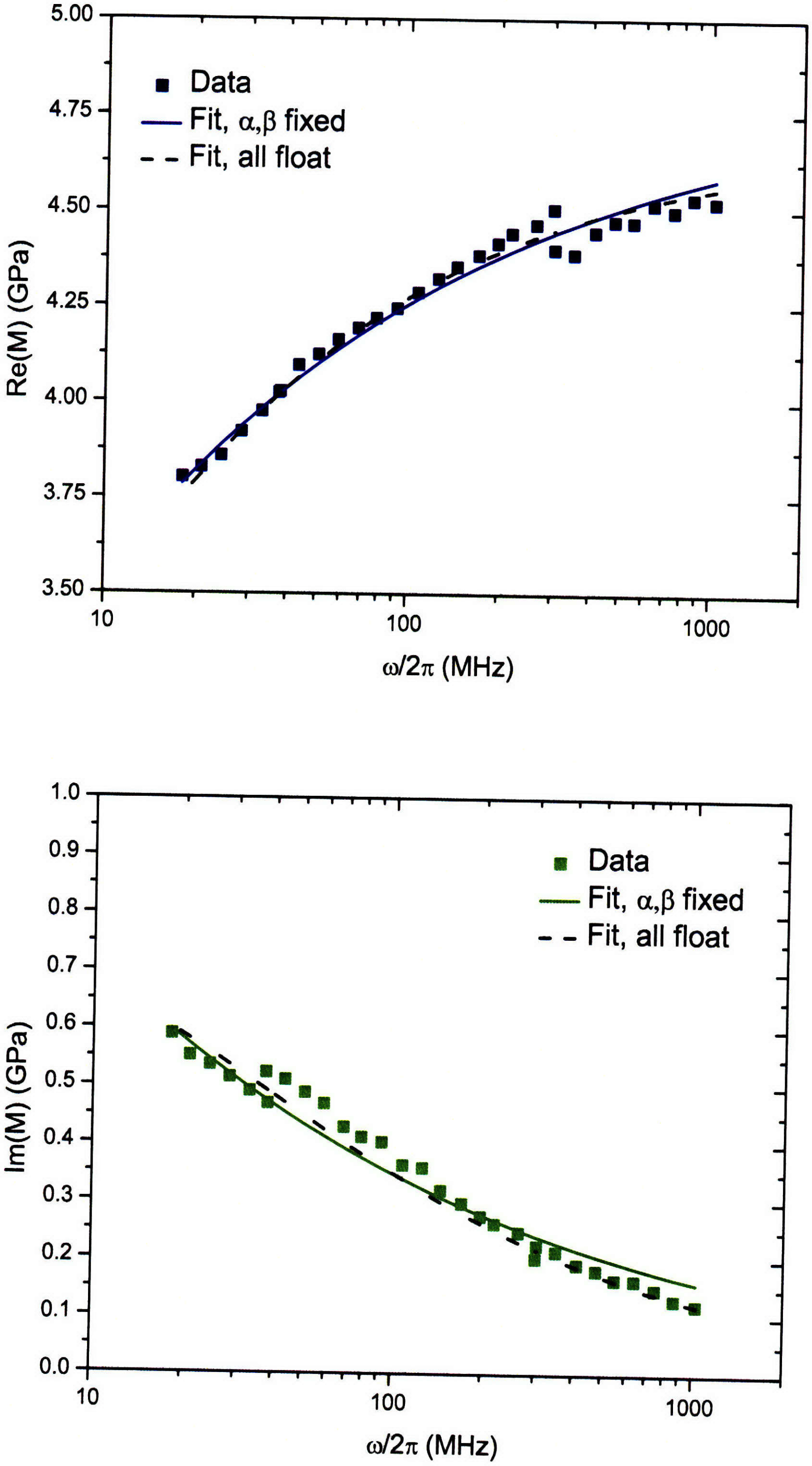

Figure 4-12: Longitudinal relaxation spectrum at 246K. The data are represented by points and the Havriliak-Negami fits by curves. The solid, colored line represents the fit when $\alpha_{HN} = 0.75$ and $\beta_{HN} = 0.45$, which gives $\tau_{HN} = 0.47 \pm 0.03$ µs. The dashed black line is from a free fit of all parameters. Here, this fit yields $\alpha_{HN} = 0.53 \pm 0.07$, $\beta_{HN} = 1 \pm 0.1$, and $\tau = 0.04 \pm 0.02$ µs.

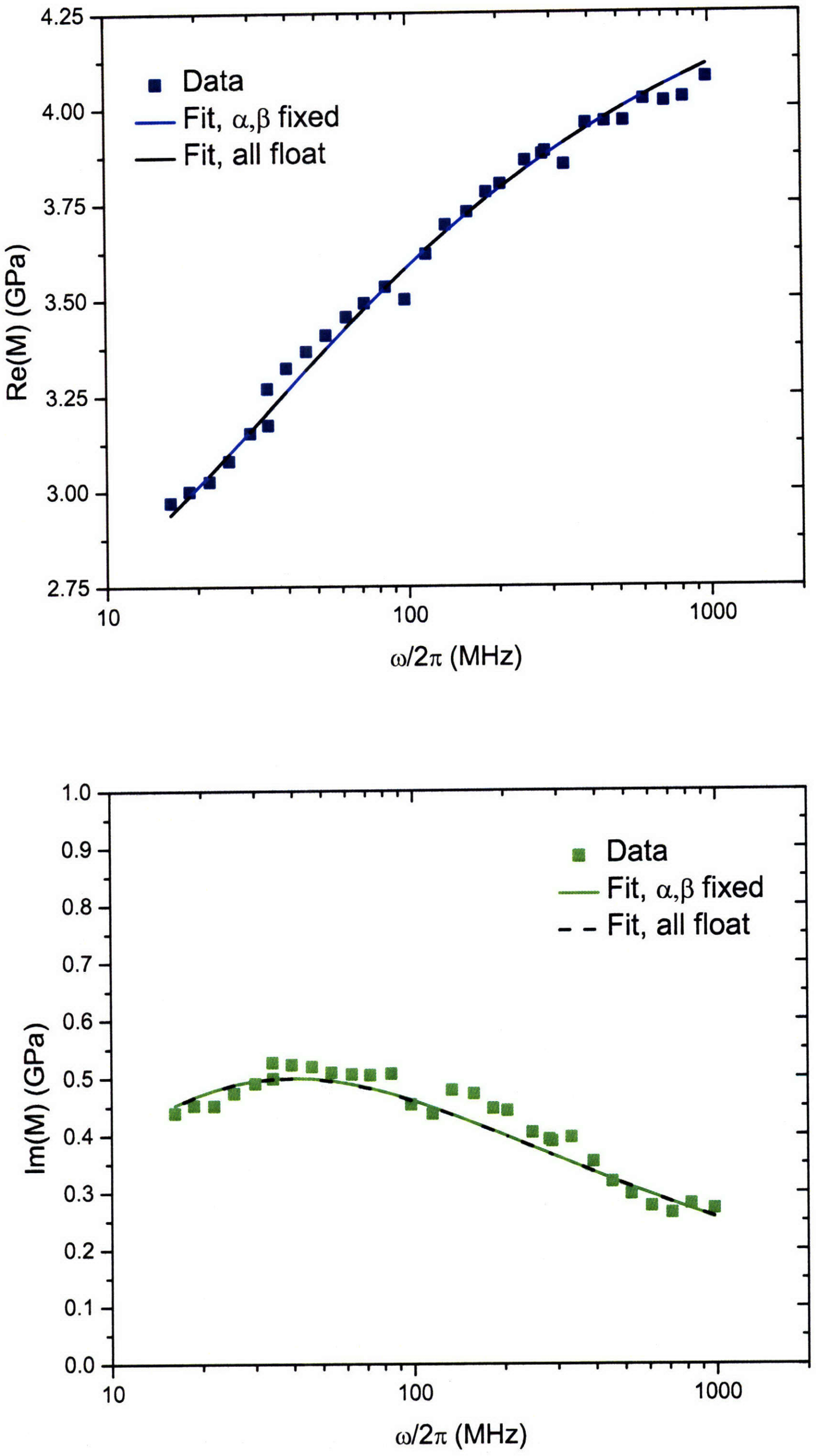

Figure 4-13: Longitudinal relaxation spectrum at 254K. The data are represented by points and the Havriliak-Negami fits by curves. The solid, colored line represents the fit when $\alpha_{HN} = 0.75$ and $\beta_{HN} = 0.45$, which gives $\tau_{HN} = 0.010 \pm 0.001$ µs. The dashed black line is from a free fit of all parameters. This fit yields $\alpha_{HN} = 0.76 \pm 0.05$, $\beta_{HN} = 0.44 \pm 0.08$, and $\tau = 0.011 \pm 0.005$ µs.

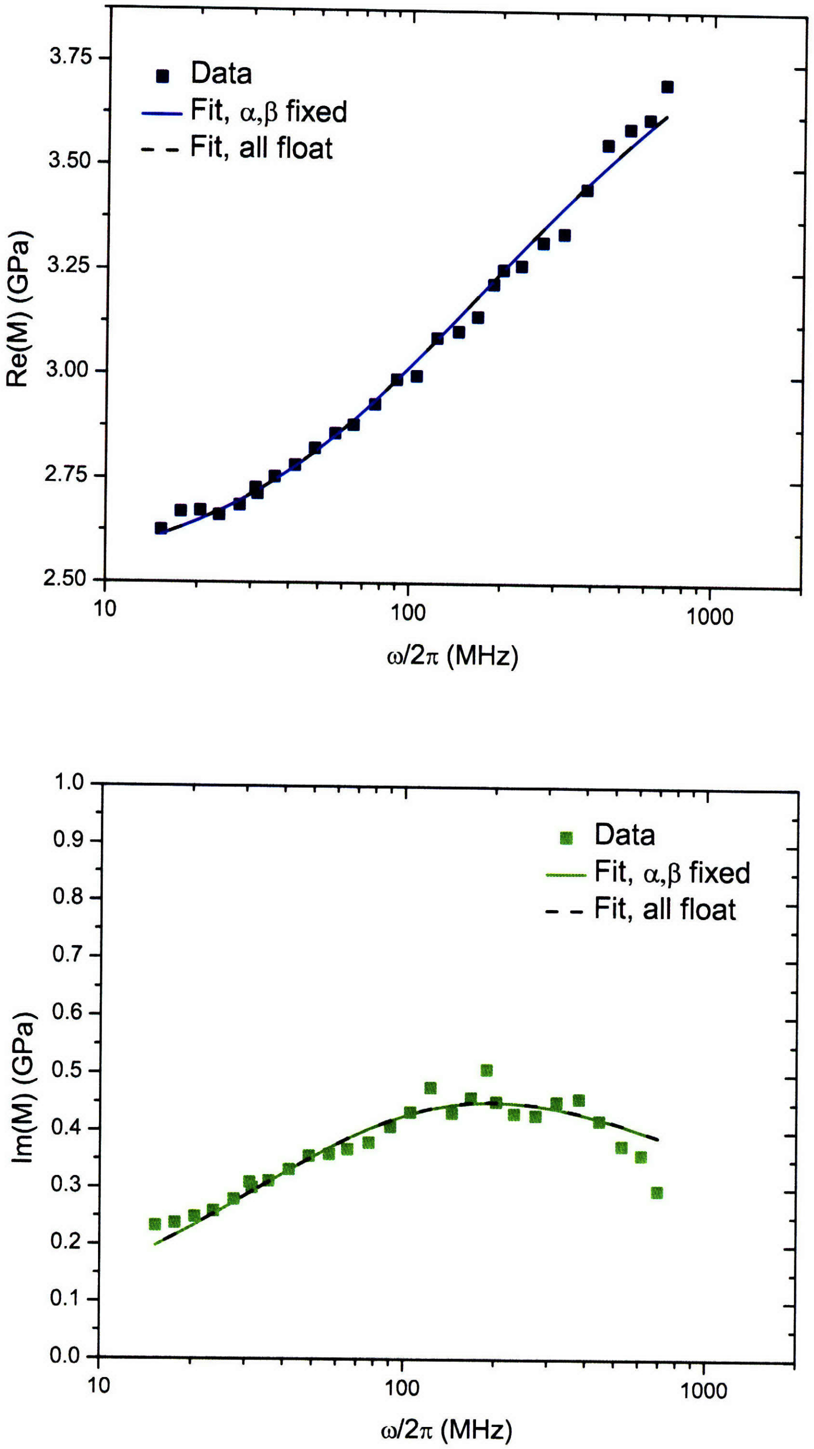

Figure 4-14: Longitudinal relaxation spectrum at 262K. The data are represented by points and the Havriliak-Negami fits by curves. The solid, colored line represents the fit when $\alpha_{HN} = 0.75$ and $\beta_{HN} = 0.45$, which gives $\tau_{HN} = 2.2 \ \pm 0.2$ ns. The dashed black line is from a free fit of all parameters. Here, this fit yields $\alpha_{HN} = 0.67 \ \pm 0.04$, $\beta_{HN} = 1 \ \pm 0.1$, and $\tau = 0.80 \ \pm 0.08$ ns.

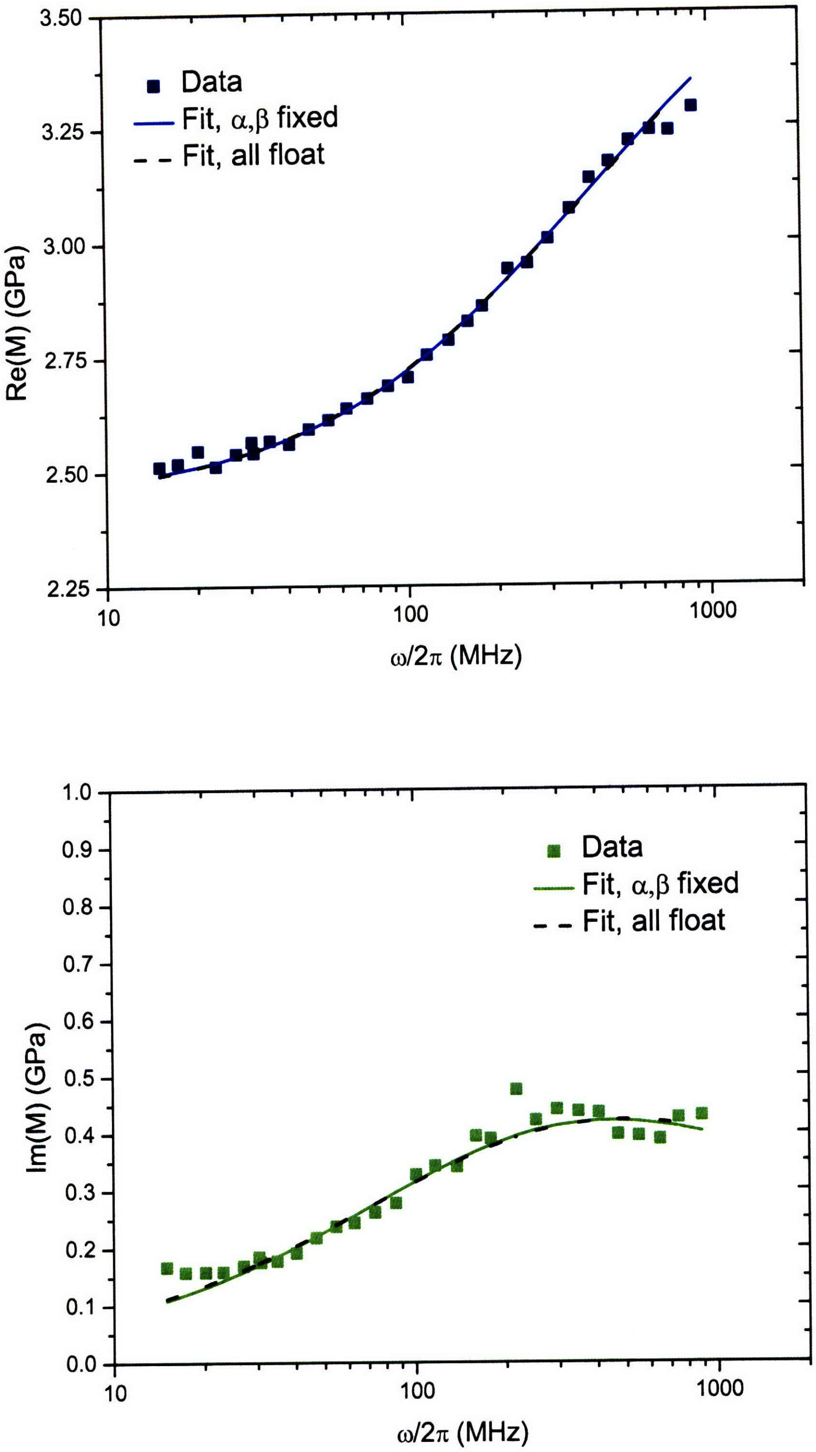

Figure 4-15: Longitudinal relaxation spectrum at 268K. The data are represented by points and the Havriliak-Negami fits by curves. The solid, colored line represents the fit when $\alpha_{HN} = 0.75$ and $\beta_{HN} = 0.45$, which gives $\tau_{HN} = 0.92 \pm 0.09$ ns. The dashed black line is from a free fit of all parameters. Here, this fit yields $\alpha_{HN} = 0.73 \pm 0.14$, $\beta_{HN} = 0.41 \pm 0.1$, and $\tau = 1.0 \pm 0.7$ ns.

tomatic of our acoustic frequency range being higher in frequency than the relaxation spectra determined mainly through thermal expansion data. Our dynamic range therefore did not include the center of the relaxation spectrum or the low-frequency limit at most temperatures. When we tried to fix the zero-frequency modulus using equation 4.2, we were not able to obtain good fits to the data for some of the lower temperature traces, and we observed significantly more scatter in the fitted values for all of the other parameters. Again, this is likely due to the fact that equation 4.2 is only applicable in the higher end of this temperature window and could not be extrapolated through the regime where we observe structural relaxation. Finally, we note that fixing M_0 and the exponents yielded even worse fits and more scatter in the fitted value of τ_{HN}. Indeed we only have direct knowledge of c_0 for $T > 270$ K and c_∞ for $T < 220$ K which is, unfortunately, outside of the range of interest for our acoustic spectra.

Our conclusion for the fits is as follows: KWW data show time temperature superposition via a temperature independent value for the exponent $\beta_{KWW} = 0.4$ in the regime 230 K - 248 K. Similarly, the best fits for the unconstrained variables reproduced the Havriliak-Negami values of $\alpha_{HN} = 0.75$ and $\beta_{HN} = 0.45$ for many temperatures in the range 252 K to 264 K, which corresponds to $\beta_{KWW} = 0.4$; those temperatures for which the free-fit spectral parameters were appreciably different did not have very different fits from when α_{HN} and β_{HN} were held fixed. Hence, we deduce that time-temperature superposition holds in this regime as well. For the regime 240 K to 250 K of the Havriliak-Negami fits, there was simply not enough spectral structure to contradict the KWW results, as the fits with α_{HN} and β_{HN} constrained by β_{KWW} were still consistent with the data.

Thus, we can conclude that time-temperature superposition holds for the range 230 K-268 K with parameters $\beta_{KWW} = 0.4$ or $\alpha_{HN} = 0.75$, $\beta_{HN} = 0.45$. This allows us to use our data shifted by the fitted values of τ_{HN} in order to obtain a master plot for the longitudinal acoustic modulus, as shown in figure 4-16. The data show remarkably good agreement with the master function. Of note is the lack of any anomalous behavior which may indicate the presence of a secondary relaxation

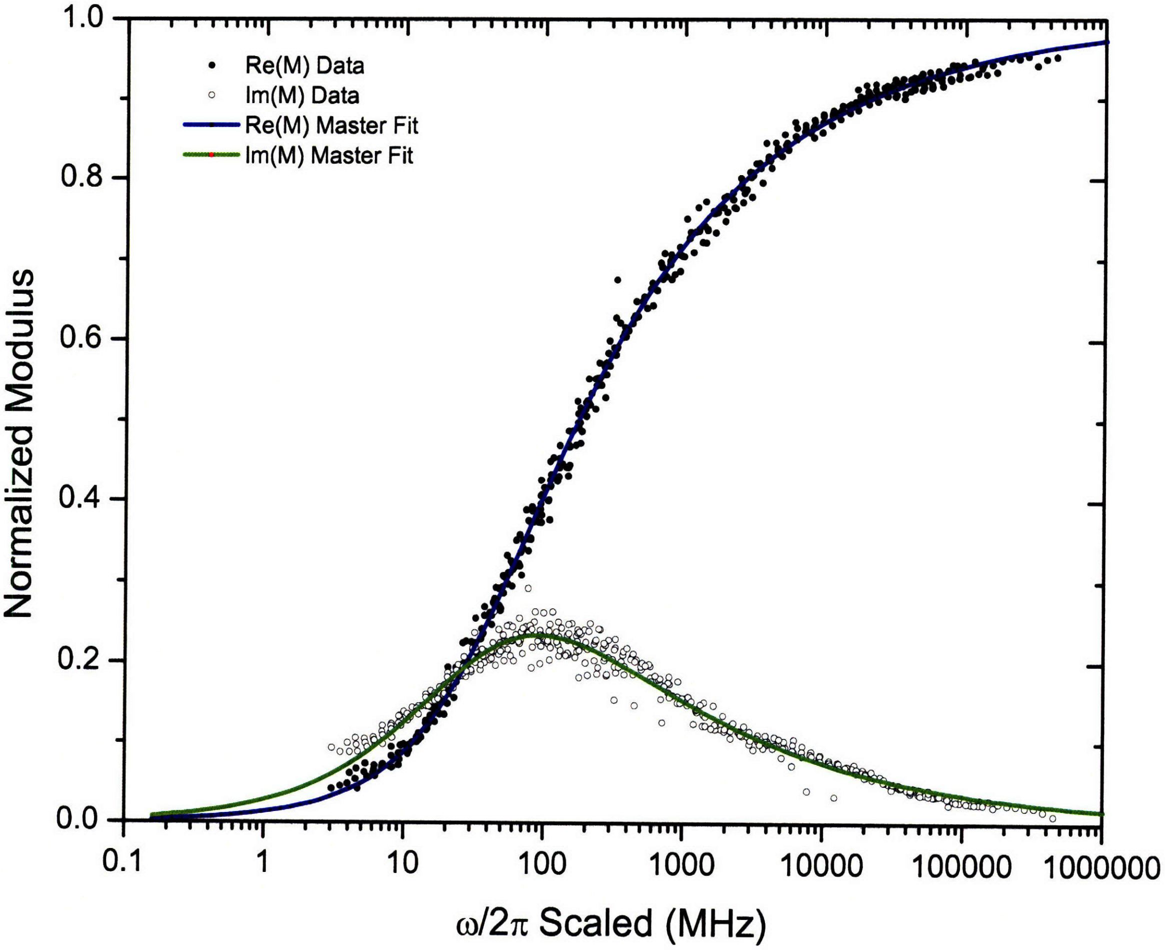

Figure 4-16: Master plot for DC704 longitudinal modulus showing the results of time-temperature superposition. The individual traces are scaled and shifted according to the fit values. Here, $\alpha = 0.75$ and $\beta = 0.45$ as determined from KWW fits to the time-dependent thermal expansion data and from Havriliak-Negami fits to acoustic data that included the peak of the loss modulus. Acoustic data that included the high-frequency wing of the spectrum but not the peak or low-frequency side could not be used to determine the fitting parameters α_{HN} and β_{HN} independently but were consistent with those values.

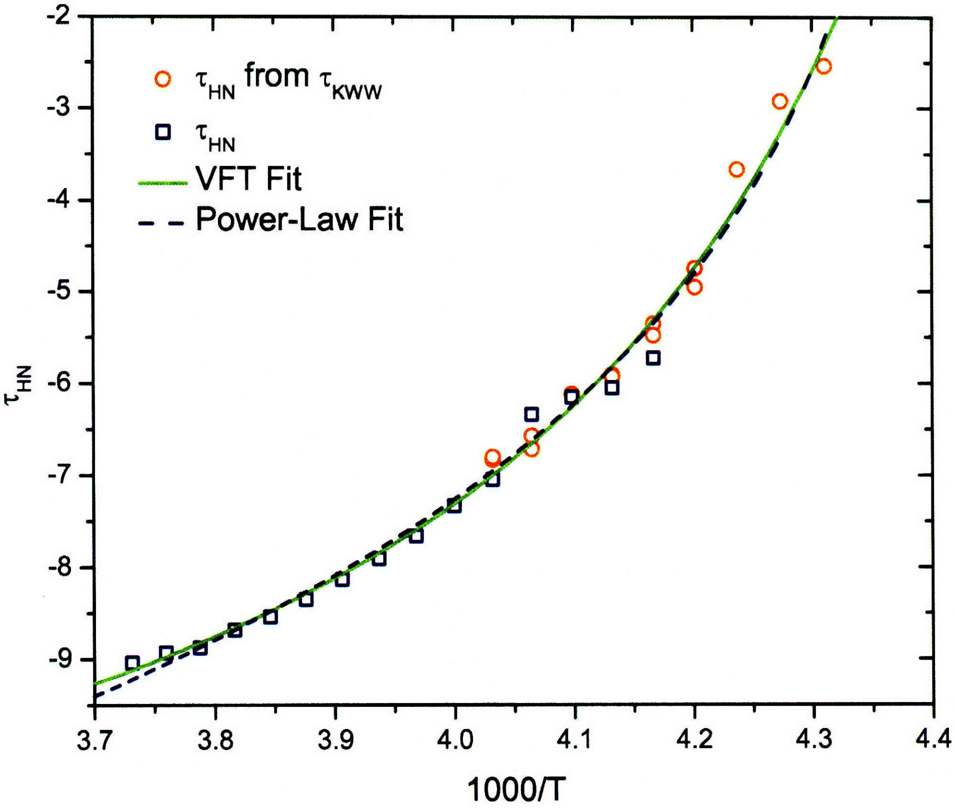

Figure 4-17: VFT and power law fit to relaxation time determined from both KWW fits and HN fits in DC704. Both forms provide good fits to the data over a wide range of temperatures and relaxation times. The VFT parameters for τ_{HN} are $\tau_0 = 100 \pm 200$ fs, $B = 500 \pm 100$ K, and $T_0 = 212 \pm 4$ K, and the power law parameters (discussed in terms of the mode-coupling theory in greater detail below) are $\gamma = 8 \pm 1$ and $T_c = 227 \pm 2$.

peak (the so-called Johari-Goldstein β-relaxation [75]). We note that there is slightly greater scatter in the fitted values of the imaginary part of the modulus near the peak. This is intrinsic to the measurement itself: in this regime, the acoustic damping rate is appreciably higher than in other areas. With fewer cycles to fit against, the spread in the fitted values becomes correspondingly larger.

Using the measured values for the average relaxation time obtained from both acoustic and time-domain structural relaxation measurements allows us to examine its evolution across several orders of magnitude in time. This behavior is plotted in figure 4-17, where rather good agreement is obtained for data taken in the two domains at a set of common temperatures; there is a slight difference that can be accounted for both in terms of fitting uncertainties, as well as the uncertainty associated with transforming KWW data into the frequency domain. We are able to attempt a VFT fit, which is also shown within figure 4-17. Fits to the entire set of τ_{HN} yields $\tau_0 = 100 \pm 200$ fs, $B = 500 \pm 100$ K, and $T_0 = 212 \pm 4$ K. Fits that only account for those values obtained by the Havrliak-Negami fits give $\tau_0 = 3 \pm 26$ fs, $B = 800 \pm 700$ K, and $T_0 = 200 \pm 30$ K.

The fitted parameters provided by the above analysis may also allow access to the full spectra for the mechanical relaxation of DC704 over a significant temperature range, and thus allow for a test of the growing length scale as predicted by [28] and outlined in chapter 2. Briefly, we require a derivative of the spectrum with respect to temperature

$$\chi_T(t) = \frac{\partial F(t)}{\partial T}, \tag{4.11}$$

which we can use to form a lower bound for the four-point correlator χ_4, which measures the degree of dynamic cooperativity in a relaxation process

$$\chi_4(t) \geq \frac{k_B}{c_P} T^2 \chi_T^2(t). \tag{4.12}$$

If the analysis is to be performed in the frequency domain, the compliance $J(\omega) = M^{-1}(\omega)$ must be calculated. However, a more straightforward approach may be to transform the modulus to the time-domain KWW form using the formalism of Hilfer [21, 22]. The temperature derivative in equation 4.11 can then be approximated by simply taking the difference between adjacent time-domain traces, using the fitted values instead of actual data in order to avoid experimental noise propagating with the results. Finally, measurements of the specific heat c_p are required for this analysis. These may be performed by differential scanning calorimetry (DSC); DSC data on DC704 from a scan performed every two degrees upon cooling from 280 K to 240 K is given in appendix B.

4.3.2 Mode-Coupling Analysis

In addition to the evolution of collective relaxation, the time domain data also provide access to the $q \to 0$ limit of the Debye-Waller factor through the relationship

$$f_{q\to 0} = \frac{B}{A+B} \tag{4.13}$$

where A is the magnitude of the thermal plus acoustic signals, and B is that of the structural relaxation contributions to the signal [7]. In figure 4-18 we have plotted $f_{q\to 0}$ for all of the wavevectors for which structural relaxation data were taken. We do not observe the predicted mode-coupling theory cusp from our data. We note that DC704 is not unique in this respect. Paolucci and Nelson observed no such feature in glycerol [76], nor did Torre and coworkers in their work on o-terphenyl [77], although a quantitative measure of non-ergodic behavior has been observed in o-terphenyl with neutron scattering [78, 79]. We also note that, to date, its presence in Impulsive Stimulated Scattering data has been verified in salol [57, 80] and CKN [81], the only other two liquids in which this feature has been sought after.

In order to explain the absence of the square-root cusp behavior in their data, Torre and coworkers offer that, for o-TP, neutron scattering measurements of the Debye-Waller factor taken in their $q \to 0$ limit would show a vanishingly small cusp. While this is likely to be the case for DC704, no such high-wavevector measurements have been taken by which to form a basis for comparison. In light of this, we would also like to recall the observation of Paolucci and Nelson that the average value of $f_{q\to 0}$ is already fairly high (i.e. > 0.6) while for CKN and salol, it is appreciably lower (~ 0.4). We note that the o-TP data of Torre data and our DC704 data share this feature with glycerol, as well. This may, albeit circumstantially, point to a common origin, such as the scenario presented in [77]. Paolucci and Nelson suggest reasons such as thermally assisted hopping events, or the fact that the sharp square root cusp is a feature of schematic MCT, whose predictions may be less valid for these liquids than for salol and CKN; the non-ergodicity feature in DC704 may be broader or more rounded than the sharp square-root cusp that is expected. At present, we can only

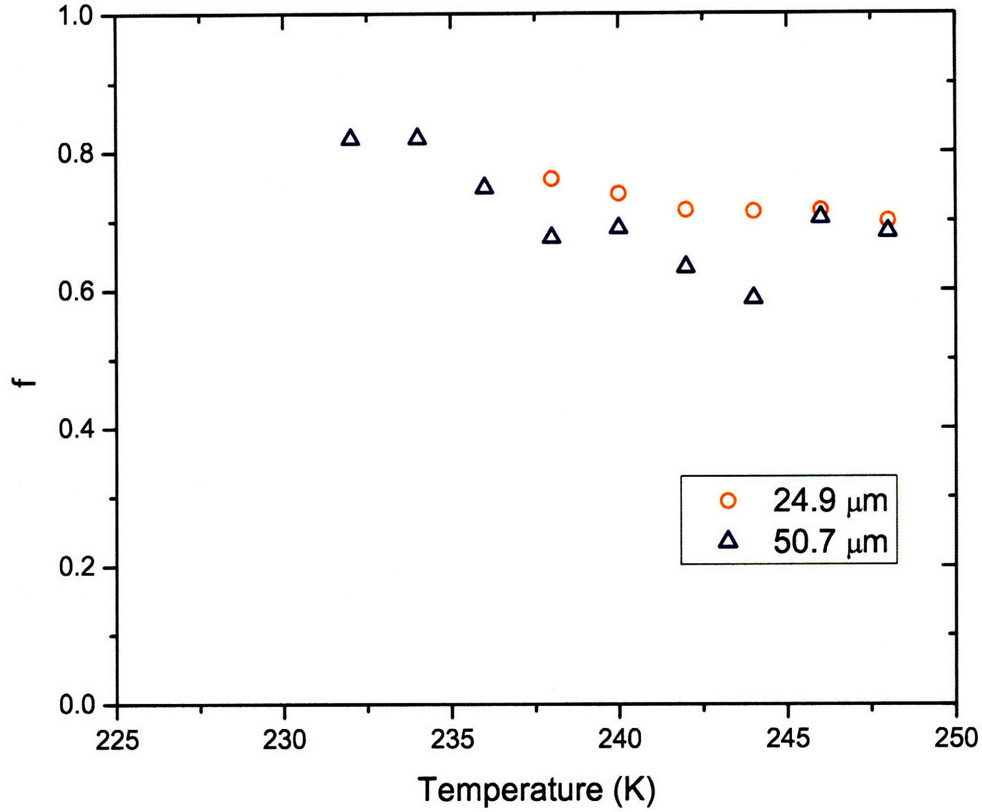

Figure 4-18: Calculated non-ergodicity parameter in DC704 from time-domain fits. We fail to observe any square-root cusp behavior as predicted by the mode-coupling theory.

conclude that further study is required to uncover the cause.

In principle, $f_{q\to 0}$ may also be obtained from the spectral fits to the acoustic data from the definition of the Debye-Waller factor as

$$f_{q\to 0} = 1 - \frac{c_0^2}{c_\infty^2}. \tag{4.14}$$

This underscores the necessity to extend our measurements across a broader range of temperatures and frequencies, a direction which is being actively pursued.

Testing the predicted power law behavior of the average relaxation time $\tau \sim (T - T_c)^{-\gamma}$ in equation 2.51 requires a measurement of the crossover temperature. Regrettably, without evidence of the square root cusp in the Debye-Waller factor, our only source of this behavior is examination of the characteristic relaxation time itself, which is shown in figures 4-5 from the KWW data and 4-17 from the combination of acoustic and time-domain data fit to the Havriliak-Negami function. The power-law behavior fits the data over a good range in the KWW data alone, yielding a value for $T_c = 227\ \pm 5$ K and $\gamma = 7\ \pm 3$. This value of T_c is reasonable, as it is about 10% higher than the accepted value for T_g. Fits to the entire measured spectrum, as shown in 4-17, are also quite good, yielding very similar parameters to the approach utilizing only the KWW information: $T_c = 227\ \pm 2$ K and $\gamma = 8\ \pm 1$. Both of these fits yield values for T_c which are lower than we were able to reliably study experimentally. While we may posit that the reason we did not see non-ergodicity in the Debye-Waller factor is that we simply could not go down far enough in temperature, this needs to be verified by further measurements.

The mode-coupling theory also makes predictions on the scaling behavior of the imaginary part of the modulus [82]. Notably, the low-frequency part of the α spectrum should fit to a frequency dependence of $M'' \sim \omega^1$, while the high frequency side of the α relaxation should be shown to scale as

$$M''(\omega) \sim \omega^{-b}. \tag{4.15}$$

The exponent in equation 4.15 is precisely the b exponent referred to in Chapter 2, equation 2.69. This implies that a determination of b from the high frequency piece of the α relaxation in tandem with measurements of the β relaxation to determine values for a in equations 2.67 and 2.73 should uniquely determine the critical behavior of DC704. In particular, these two exponents can then be used to obtain the power law exponent γ. Further work in the schematic model studied in [82] provides an estimate for the β_{KWW} parameter from these exponent parameters given by

$$\beta_{KWW} = -\frac{\log(2)}{\log(1-\lambda)}, \tag{4.16}$$

which is an assertion that should also be easily tested by this analysis.

The imaginary part of the modulus is plotted on a log-log scale in figure 4-19 in order to emphasize power-law behavior on both sides of the relaxation peak. Fitting the available portion of the low-frequency behavior, we recover the value 0.39 ±0.01. More data on this side of the maximum would be useful, but the available results cannot support the mode-coupling theoretical prediction.

From the high-frequency side of the peak, we are able to deduce a value of $b = 0.28 \pm 0.01$, which results in an exponent parameter $\lambda = 0.92$. Using the approximation, equation 4.16 for β_{KWW}, gives an estimate of $\beta_{KWW} = 0.29$, which is very close to the experimentally determined values centered around 0.4. Finally, we may use the values of γ and b to obtain a value for a from equation 2.73. Using the result for γ from the power law fit to the entire measured temperature range yields $a = 0.08$ which, then using equation 2.67 gives an exponent parameter $\lambda = 0.99$. This value is slightly higher than the value provided by b, but it is not far off. Without a direct measurement of the β relaxation regime it is impossible to confirm this result, but reasonable consistency among the exponent parameters motivates measurements of GHz frequency acoustic properties of DC704. Measurements of this type are presently underway.

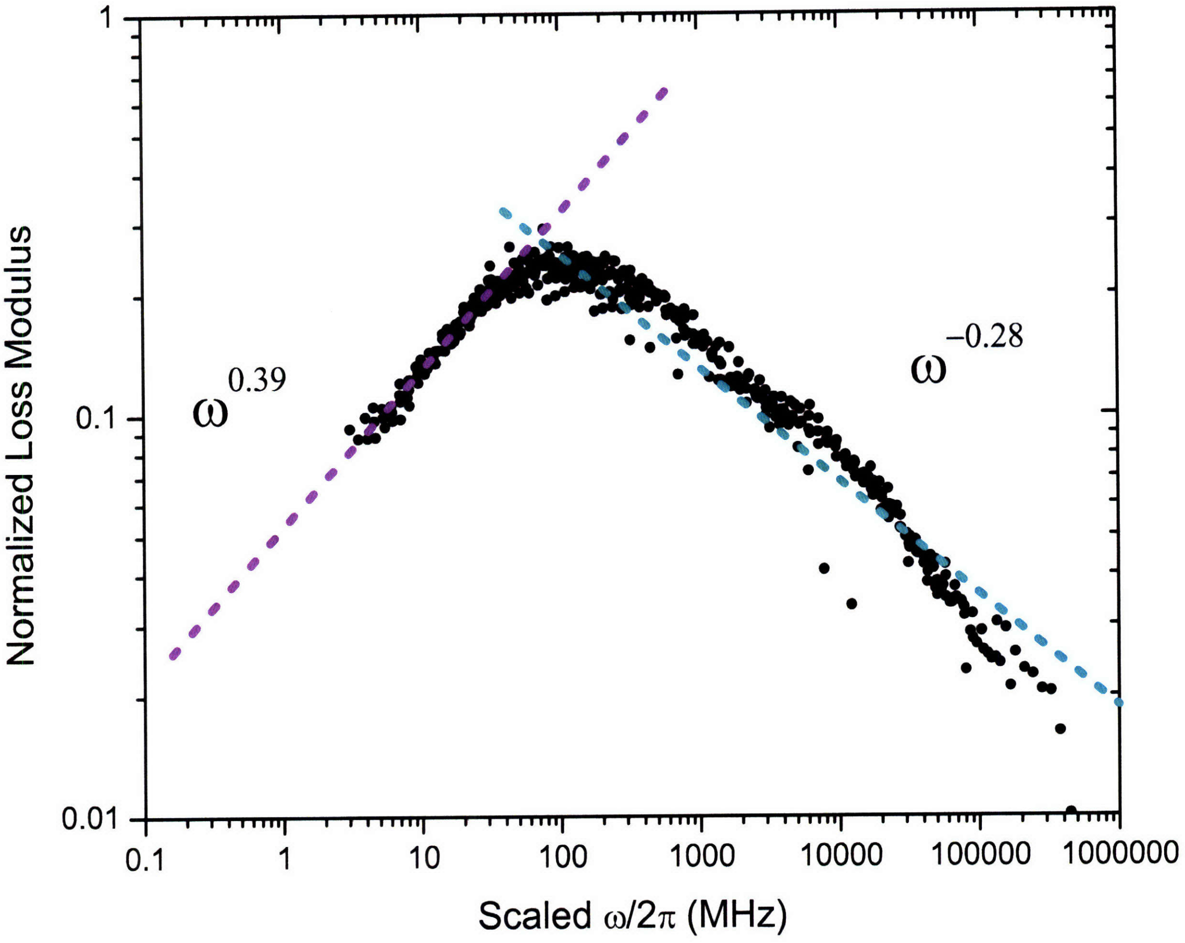

Figure 4-19: Log-log plot of loss modulus showing scaling behavior. The low frequency peak shows behavior that scales as $\omega^{0.39}$, which is anomalously low as compared to the predictions of the mode-coupling theory. This is due to the width parameter α_{HN} being less than 1. The high frequency shows behavior as $\omega^{-0.28}$, providing the mode-coupling exponent b.

4.3.3 Shear Acoustic Relaxation

Figures 4-20 shows representative shear wave data at 4.25 µm at a series of temperatures. At short times there is a spike in the signal due to the non-resonant electronic response to the pump pulses. Following this so-called hyperpolarizability spike are oscillations about zero due to counterpropagating shear waves which damp out over several acoustic cycles. In some of the warmer temperature traces, especially where the acoustic damping is stronger, we observe a gradual decay of the signal from an offset, which is due to the orientational relaxation described in section 3.2.2.

As mentioned in section 3.2.2, the data may be fit to the form

$$A\exp(-\Gamma_s t)\sin(\omega_s t+\phi)+B\exp(-\Gamma_R t)+C\delta(t) \tag{4.17}$$

which must be convolved with the instrument response function. Here, A is the acoustic amplitude, Γ_s is the shear damping rate and ω_s is the shear frequency. ϕ is a phase which accounts for the cosine term in equation 3.59 and only becomes important for temperatures where the damping is strong. In the next term, B is the optical Kerr effect signal, Γ_R is the orientational relaxation rate, and in the last term C is the strength of the hyperpolarizability spike. It is an over-simplification to model orientational relaxation with a single exponential [83], since complex relaxation dynamics can be observed in molecular orientational dynamics. However, the orientational contribution to our data was weak and the introduction of more parameters did not change the fits.

The fitting function is able to account for all features of the observed signal as is seen in the fits of figure 4-20. Analogous to the longitudinal case, using the information of the shear frequency and damping rate allows construction of a complex shear modulus $G^*(\omega)=G'(\omega)+iG''(\omega)$ according to

$$G'(\omega_s) = \rho\frac{\omega_s^2-\Gamma_s^2}{q^2} \tag{4.18}$$

$$G''(\omega_s) = \rho\frac{2\omega_s\Gamma_s}{q^2} \tag{4.19}$$

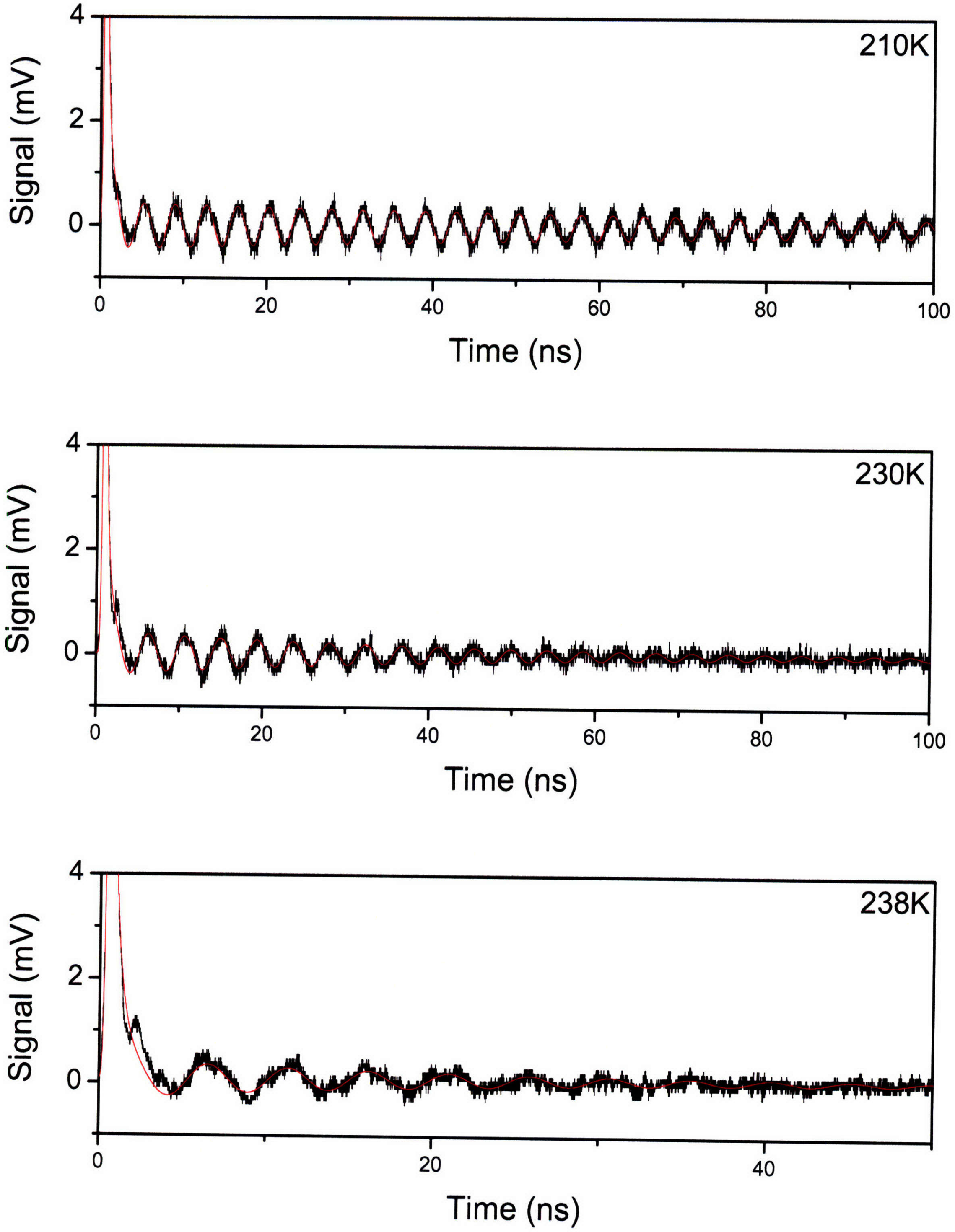

Figure 4-20: Shear waves in DC704 at 210 K, 230 K and 238 K at 4.20 µm grating spacing. The data are in black and the fits are in red. The data show excellent agreement with the fitting function, although a very weak signal is observed. Note that in (c), the time axis is zoomed in by a factor of two.

where the complex shear modulus can be modelled by a Havriliak-Negami spectrum of the form

$$G(\omega) = G_{\infty}\left(1 - \frac{1}{(1 + (i\omega\tau_s)^{\alpha})^{\beta}}\right) \tag{4.20}$$

which has the same form as equation 4.8 save that the zero frequency shear modulus of the supercooled liquid $G_0 = 0$ by definition.

Figures 4-21 and 4-22 show attempts at construction of a shear spectrum at 230 K and 238 K, respectively. The fits shown are supposing that the values for $\alpha_{HN} = 0.75$ and $\beta_{HN} = 0.45$ obtained from analysis of the longitudinal measurements apply to the shear spectrum as well. Fits allowing τ_s to vary yield values of the characteristic relaxation time for the shear degrees of freedom as $\tau_s = 3 \pm 1$ µs at 230 K and $\tau_s = 0.3 \pm 0.1$ µs at 238 K. When τ_s is constrained by the value from the longitudinal data, we are not able to construct a fit to the data as the curve for G'' is consistently low.

The fitted value for τ_s at 230 K is at least three orders of magnitude smaller than the longitudinal value, while the value at 238 K is two orders smaller, which may indicate that the shear degrees of freedom relax at a significantly faster rate than the longitudinal ones, and that their evolution with temperature is not as pronounced as in the longitudinal case. However, low signal levels, even at relatively high wavevector, preclude the development of a full shear modulus spectrum that spans a range much wider than a decade in frequency; the linear q dependence of the signal strength becomes prohibitive for this measurement, and we were typically unable to observe shear waves for wavelengths greater than 11 µm. Although our shear results are limited in scope, they are provocative because they suggest significant differences between longitudinal and shear relaxation dynamics in a supercooled liquid.

4.4 Conclusions

Longitudinal relaxation was measured in the glass former DC704 over a range of temperatures from 232 K to 268 K using Impulsive Stimulated Thermal Scattering. From 232 K to 248 K, the data were obtained from time-domain from fits of

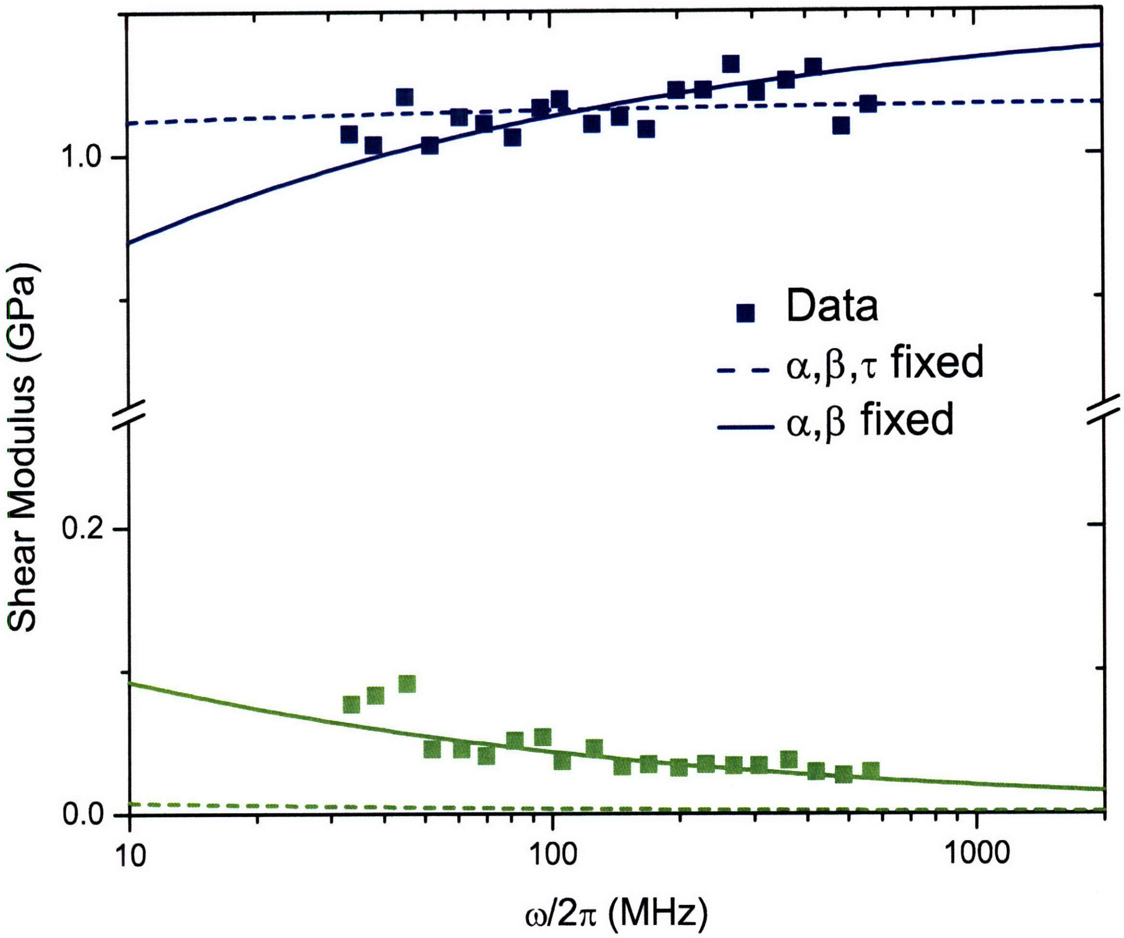

Figure 4-21: Shear relaxation spectrum at 230K. The data are represented by points and the different fits by curves. The data show considerable scatter due to the noise in the original data traces, as well as the low signal levels. We also note that the data are only available over slightly wider than one decade. These factors preclude a free fit to the data, but we are still able to perform a fit constraining the spectral exponents $\alpha_{HN} = 0.75$ and $\beta_{HN} = 0.45$ with the relaxation time τ_s both free and fixed by the longitudinal data. In the case where τ_s is fixed, the imaginary part is consistently below all the data points, while allowing it to vary produces a good fit with $\tau_s = 3 \pm 1$ µs.

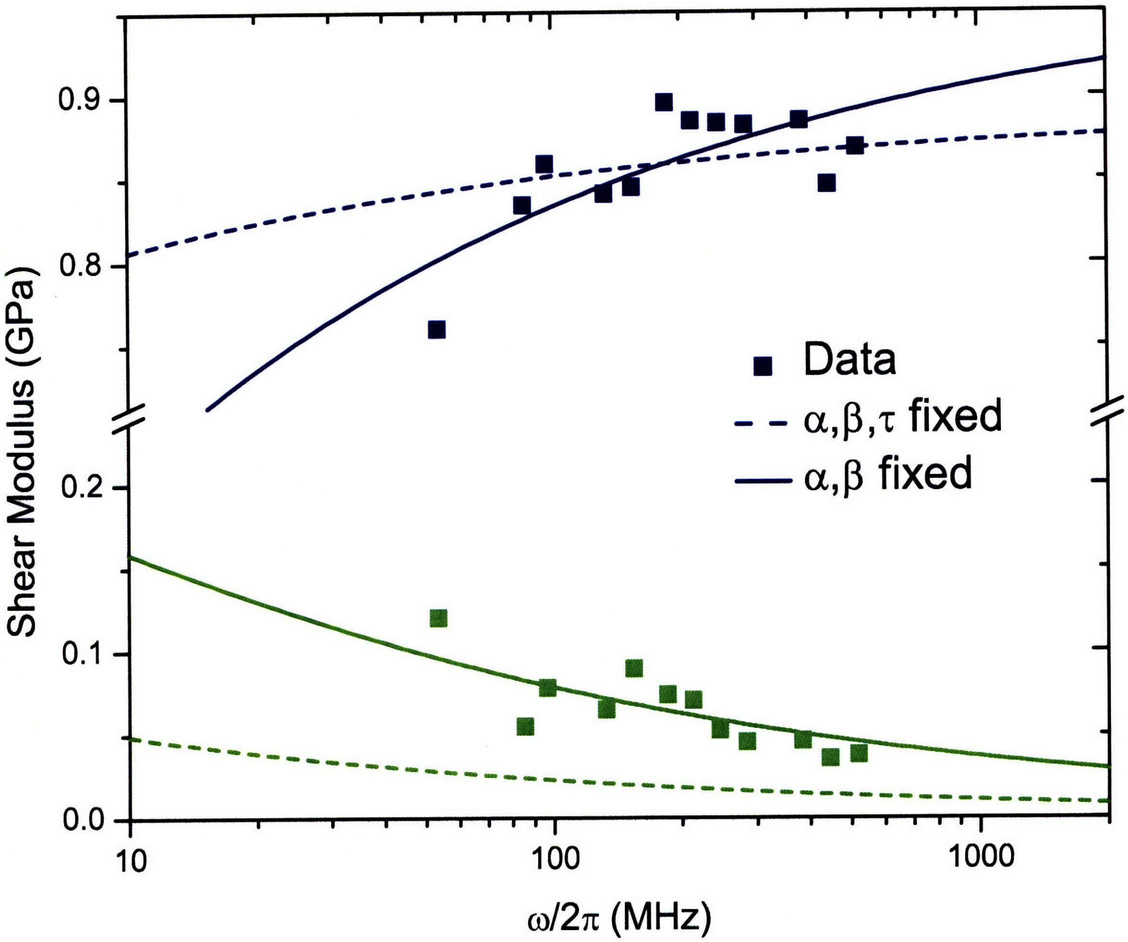

Figure 4-22: Shear relaxation spectrum at 238K. The data are represented by points and the fits by curves. The data show even more scatter than at 230 K. We also note that the data are only available over one decade. These factors preclude a free fit to the data, but we are still able to perform a fit constraining the spectral exponents $\alpha_{HN} = 0.75$ and $\beta_{HN} = 0.45$ with the relaxation time τ_s both free and fixed by the longitudinal data. In the case where τ_s is fixed, the imaginary part is consistently below all the data points, while allowing it to vary produces a good fit with $\tau_s = 0.3 \pm 0.1$ µs.

the KWW function to time-dependent thermal expansion signals, while a frequency-domain Havilriak-Negami functional form was fit to acoustic wave data recorded in the temperature range from 240 K to 268 K. Both sets of results were consistent with time-temperature superposition, with the KWW exponent value $\beta_{KWW} = 0.4$ and Havriliak-Negami parameters of $\alpha_{HN} = 0.75$, $\beta_{HN} = 0.45$.

The temperature-dependent characteristic relaxation times were successfully fit to both VFT and mode-coupling power-law expressions. An examination of the Debye-Waller factor was unable to find any evidence of the system following the trend in nonergodicity that is predicted by the mode-coupling theory. This outcome is consistent with ISTS studies of two other glass forming liquids (glycerol and o-terphenyl) and inconsistent with ISTS studies of yet another two liquids, salol and CKN. Unlike glycerol where it is speculated that hydrogen bonding may be responsible for this behavior, DC704 is incapable of forming hydrogen bonds, suggesting that the root of this behavior may be in the large value for the Debye-Waller factor at all temperatures, the only common trait between these three liquids. In the case of DC704, however, we may also speculate from the value of T_c derived from the relaxation time fits that we may not have been able to take data to low enough temperatures to observe the cusp in $f_{q \to 0}$.

Power-law fits to the wings of a master spectrum for alpha relaxation yielded the exponent $b = 0.28$ which yielded a value of the control parameter $\lambda = 0.92$. This in turn yielded a value of the KWW exponent $\beta_{KWW} = 0.3$ that was consistent with our experimental measurements. The value of b, in combination with the exponent $\gamma = 7.3$ derived from the power-law fit of relaxation times, also yields a prediction for the value of the power-law exponent $a = 0.1$ that characterizes the low-frequency wing of the beta-relaxation. This should be tested by future measurements of GHz-frequency acoustic properties. A power-law fit to the low-frequency side of the α relaxation spectrum yielded an exponent $0.39 \ll 1$, inconsistent with mode-coupling theoretical predictions.

Shear wave propagation was also observed in DC704 over a limited range of temperatures and wavevectors. An attempt at construction of a shear relaxation spectrum was precluded due to low signal levels and the resulting limited spectral range of about one decade. Preliminary results indicate that the characteristic shear relaxation time is several of orders of magnitude faster than the longitudinal one, although better data with a wider dynamic range and temperature range will be needed to verify this conclusion.

Further studies of DC704 will hinge on broadening the ranges of observation, examining both the longitudinal and shear degrees of freedom. The use of shorter optical wavelengths and larger-angle excitation geometries will widen the available extent of ISTS measurements. More efficient detection schemes with larger bandwidth will also aid these experiments. Finally, the study of glass forming liquids will profit immensely from the use of novel longitudinal and shear acoustic generation methods [72, 84]. Efforts in these directions are presently underway.

Chapter 5

Depolarized Impulsive Stimulated Scattering Study of triphenyl phosphite [1]

5.1 Introduction

The analysis of DC704 concluded with preliminary results on shear wave propagation and the construction of a shear modulus spectrum akin to the longitudinal spectrum. However, due to low shear signal levels in that liquid, our measurements were limited to a narrow range of frequencies. Building upon prior work [8, 9] on the fragile glass-former triphenyl phosphite (TPP), the experiments described below constitute an attempt at directly characterizing the shear acoustic spectrum in the regime from 10 MHz to 1 GHz. In this prior work, the shear modulus was measured over a narrow frequency range, comparable to our results from DC704 presented in the previous chapter. As in our case with DC704, the earlier results did not permit sufficient comparison between shear and longitudinal modulus spectra. In the present case, a more complete comparison is carried out and an assessment is made of whether the transverse current correlations that comprise the shear spectrum has sufficient

---

[1] Done collaboratively with Jeremy Johnson of MIT.

overlap with the density fluctuations of the longitudinal spectrum to yield identical behavior as predicted by MCT.

5.2 Experimental Methods

The experimental setups used in this study have already been described in chapter 3. Here, we used both the mirror-based and lens-based systems to be able to probe the largest possible range of wavevectors. In order to generate the polarization grating, we inserted $\lambda/2$ waveplates into each of the beams. These waveplates were held in precision rotation mounts to provide accurate alignment of the relative polarization of the V and H polarized beams. This set the upper limit on the grating spacing that could be achieved in our measurements – for longer wavelengths, the beams came close enough together to be clipped by the rotation mounts. In the lens-based system, this limit was at 6.56 µm, and for the mirror-based system, it was at 24.9 µm which was extended to 50.7 µm with proper imaging. Finally, as noted in chapter 3, we did not find it necessary to use Glan-Thompson polarizers to ensure a high degree of purity for the polarizations due to the amplification provided the shear wave by heterodyne detection relative to the homodyne longitudinal signal. In both setups, the signal was collected in a Cummings Electronics Laboratories model 3031-0003 detector and recorded by a Tektronix Model TDS-7404 oscilloscope. The shear signals were weak and required 10,000 averages, resulting in data acquisition times of a few minutes.

TPP at 97% nominal purity was purchased from Alfa Aesar and had both water and volatile impurities removed by heating under vacuum with the drying agent $MgSO_4$ immersed in the liquid. The sample was then transferred to a cell with movable windows [68] via filtering through a millipore 0.22 µm teflon filter. After loading, the cell was placed in a Janis ST-100-H cryostat where the temperature was measured with a Lakeshore model PT-102 platinum resistor immersed directly within the liquid, and monitored and controlled with a Lakeshore 331 temperature controller.

The grating spacings examined in this study were 2.33 µm, 3.65 µm, 6.70 µm, 7.61 µm, 9.14 µm, 10.2 µm, 11.7 µm, 13.7 µm, 15.7 µm, 18.3 µm, 21.3 µm, 24.9 µm,

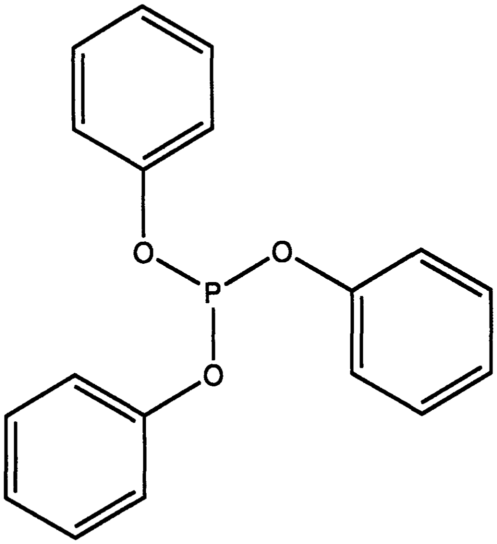

Figure 5-1: Chemical structure of triphenyl phosphite.

28.5 µm, 33.0 µm, 38.1 µm, 42.6 µm, and 50.7 µm, while data for 0.48 µm, 1.52 µm, 3.14 µm, and 4.55 µm grating spacings were taken from prior reported results [8, 9]. When the samples were cooled to the desired temperature, the cooling rate never exceeded 6 K/min, with 2 K/min being typical. Data were taken at fixed wavevector every 2 K from 220 K to 250 K upon warming as we found crystallization was less likely to occur upon warming than cooling. Only a few measurements could be taken without having to thermally cycle the liquid, as it invariably crystallized. We noticed that the tendency towards crystallization was particularly pronounced in the temperature range between 234 K and 242 K. After a few days of use, the sample was observed to develop a slightly cloudy yellowish hue, and so was replaced by a new one. The yellowish samples tended more readily towards photorefractive damage, as well as crystallization, than the original, clear samples. Comparison of the signals obtained from the degraded samples and fresh ones yielded the same frequency and damping rate values, indicating that uncertainties in either of these quantities were due mainly to noise in the data or to the variations in cooling rates, as described in the previous chapter.

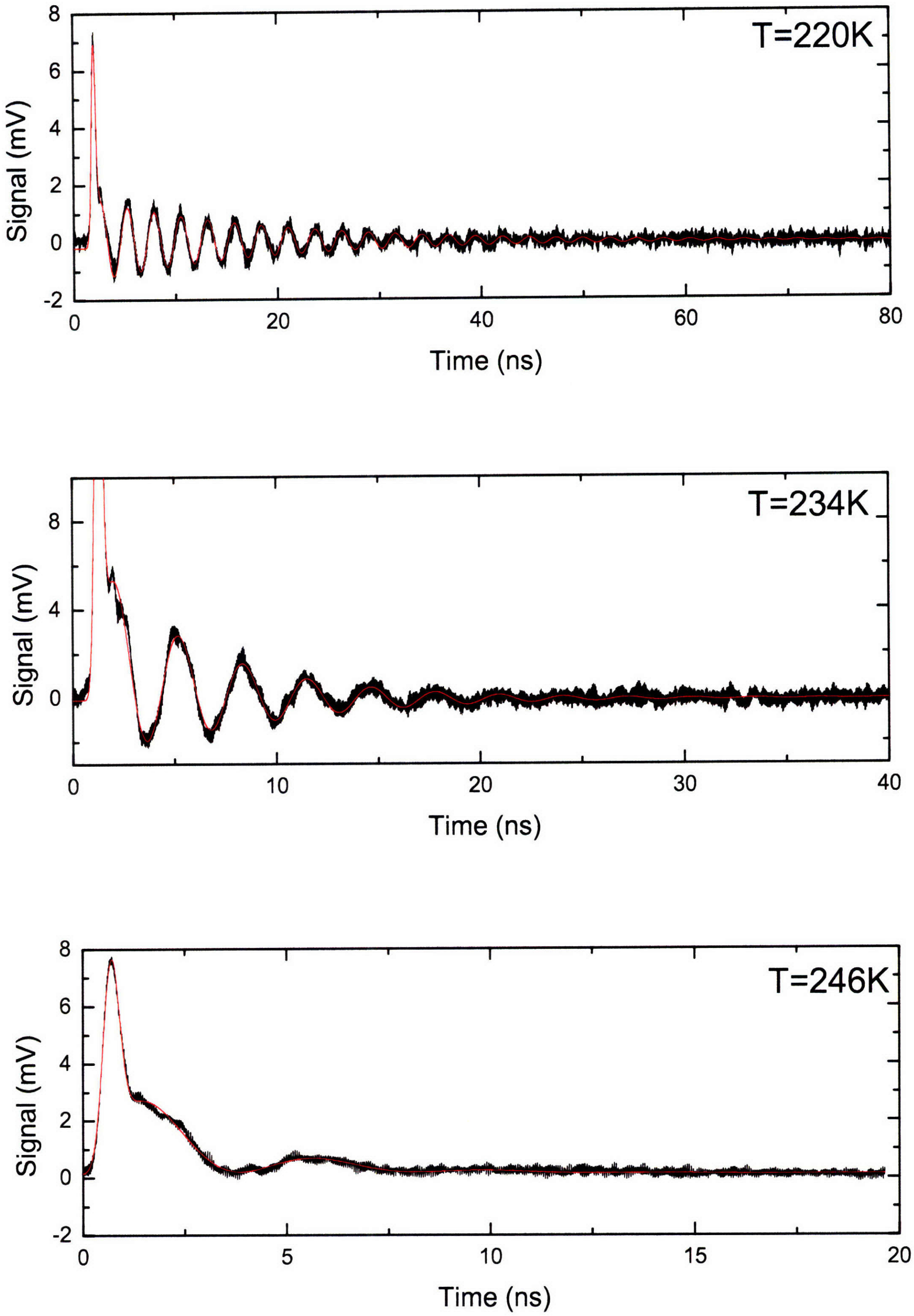

Figure 5-2: Shear waves in TPP at 2.33 µm grating spacing. The data are in black and the fits in red. As the temperature is increased, the acoustic wave becomes more heavily damped. At higher temperatures, we also note the presence of the orientational relaxation, which appears to skew the signal such that the oscillations do not occur about the zero baseline.

5.3 Results and Discussion

The results of several VHVH experiments performed at λ=2.33 µm grating spacing are shown in figure 5-2. There is an initial spike due to the non-resonant electronic response. Immediately following this hyperpolarizability peak are oscillations about the zero baseline from the counterpropagating shear waves. At a sample temperature of 220 K, these oscillations are seen to disappear on the scale of tens of nanoseconds due to acoustic damping. As the sample is warmed, the shear modulus is observed to soften and the damping increases dramatically with temperature. At sufficiently high temperatures, the shear wave becomes overdamped. We also note that at some temperatures, the signature of orientational relaxation is observed through a long diffusive mode which offsets the signal from zero baseline.

Another illustration of the influence of relaxation dynamics upon the signal may be obtained by examining data from a collection of wavevectors at a common temperature, as depicted in figure 5-3, where we provide data taken at 10.2 µm, 21.3 µm, and 44.2 µm grating spacings. Since the shear waves are driven electrostrictively, signals at larger grating spacings are observed to be weaker due to the linear q dependence of the excitation efficiency. We also observe that shear waves at lower frequencies are more heavily damped than their higher frequency counterparts as at these frequencies, the acoustic period is closer to the time scale of the characteristic relaxation time τ_s.

Time-domain signals were fit to the function

$$I(t) = A\exp(-\Gamma_s t)\sin(\omega_s t + \phi) + B\exp(-\Gamma_R t) + C\delta(t) \tag{5.1}$$

which was convolved with the instrument response function, modelled here by a Gaussian with duration 0.262 ns. This convolution was necessary to determine the true $t = 0$ for the experiment. Here, A is the acoustic amplitude, Γ_s is the shear damping rate and ω_s is the shear frequency. ϕ is a phase which accounts for the cosine term proportional relaxation strength and only becomes important for temperatures where the damping is strong. In the next term, B is the optical Kerr effect signal ampli-

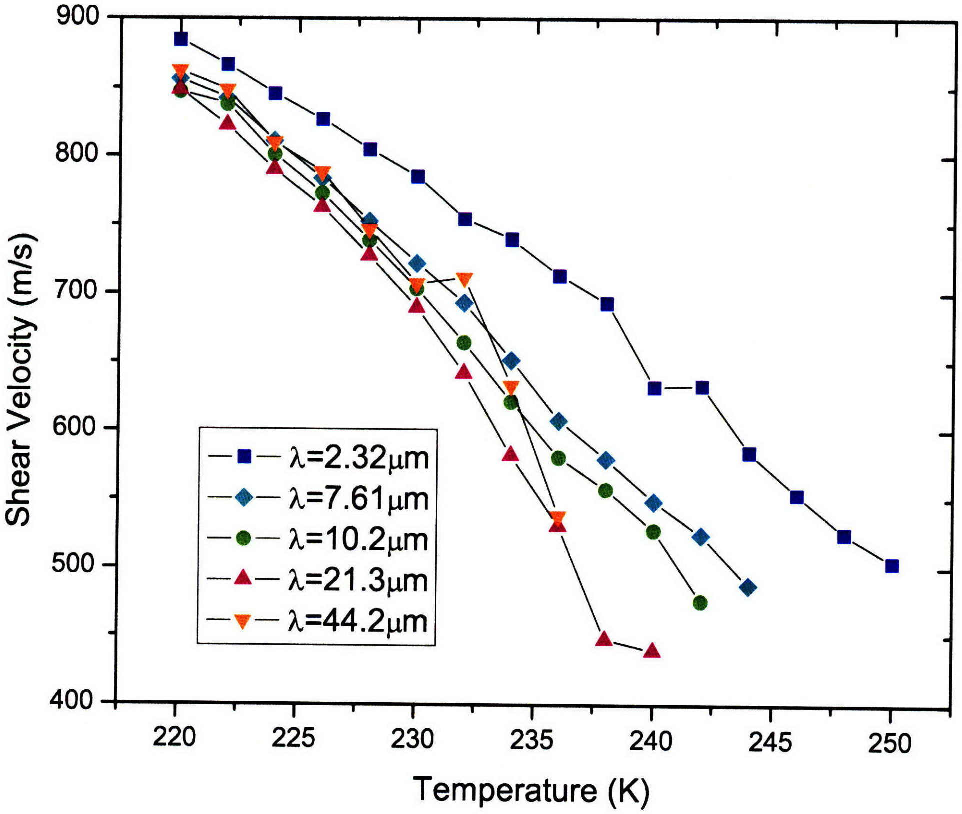

Figure 5-4: Shear speed of sound in TPP as a function of temperature for a variety of grating spacings. We note that the highest temperature for which we could observe shear waves increases with the decrease of grating spacing.

tude, Γ_R is the orientational relaxation rate, and in the last term C is the strength of the hyperpolarizability spike. As discussed in chapter 3, it is an over-simplification to model the orientational behavior by a single decaying exponential [83]. A more accurate description might be in terms of a KWW function, as is used for the longitudinal mechanical relaxation; however, since the orientational signal contributions are weak, we were still able to obtain excellent fits with fewer parameters using a single exponential.

The obtained values of the the shear acoustic velocity $c_s = \omega_s/q$ at a collection of wavevectors are shown in figure 5-4, while in figure 5-5 the scaled damping rates are shown. Two features of the data are immediately evident in these plots: first, we observe significant acoustic dispersion for the shear waves across all temperatures studied, and this dispersion increases dramatically as the temperature is raised. This is the hallmark of the structural relaxation dynamics we are characterizing in this temperature region. The second feature we note is that, as a result of the dispersion and the shear softening it represents, at each temperature above 240 K there is a wavelength beyond which we are unable to observe the shear wave in our measurements due to its increased damping and reduced signal strength. This wavelength is observed to increase with temperature.

From the fitted values for the shear frequency ω_s and the damping rate Γ_s, we may compute a value of the reactive and dissipative shear moduli from

$$G'(\omega_s) = \rho\frac{\omega_s^2 - \Gamma_s^2}{q^2} \tag{5.2}$$

$$G''(\omega_s) = \rho\frac{2\omega_s\Gamma_s}{q^2}. \tag{5.3}$$

In contrast with the longitudinal case, we have not been able to deduce a background damping term, as we were unable to get an accurate enough measure of the damping across a wide enough range of temperatures and wavevectors. Hence, the term Γ_s in the expressions above is simply the observed damping rate in equation 5.1. Since the shear waves become overdamped at high temperatures, it is likely that the damping rate at all temperatures are dominated by structural relaxation rather than back-

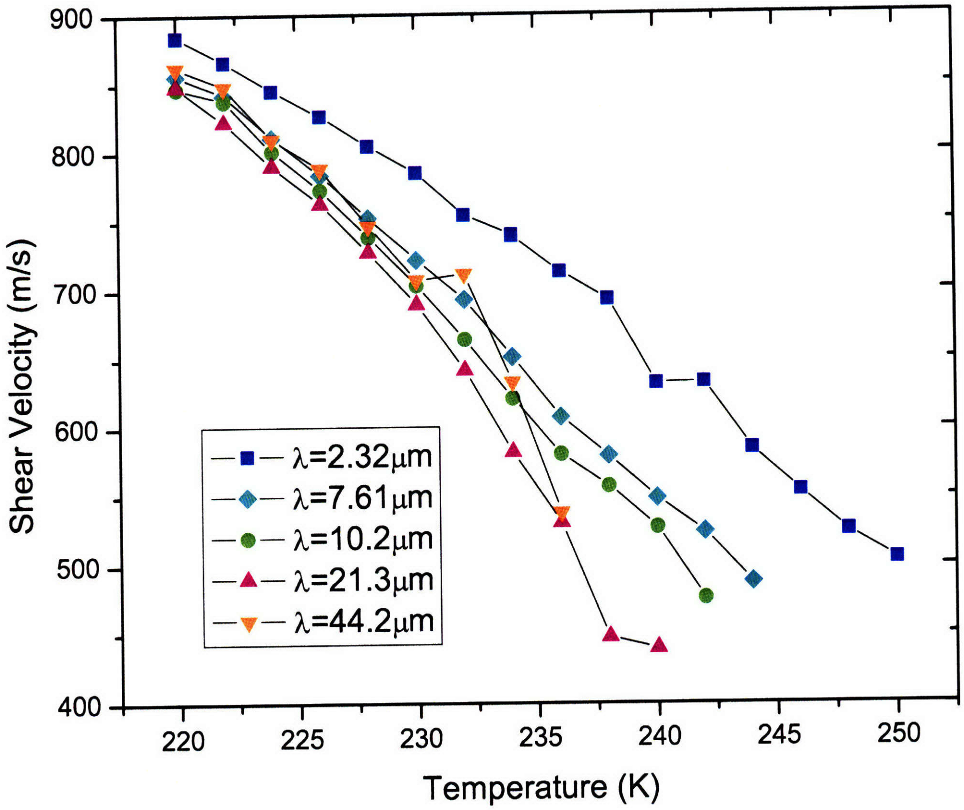

Figure 5-4: Shear speed of sound in TPP as a function of temperature for a variety of grating spacings. We note that the highest temperature for which we could observe shear waves increases with the decrease of grating spacing.

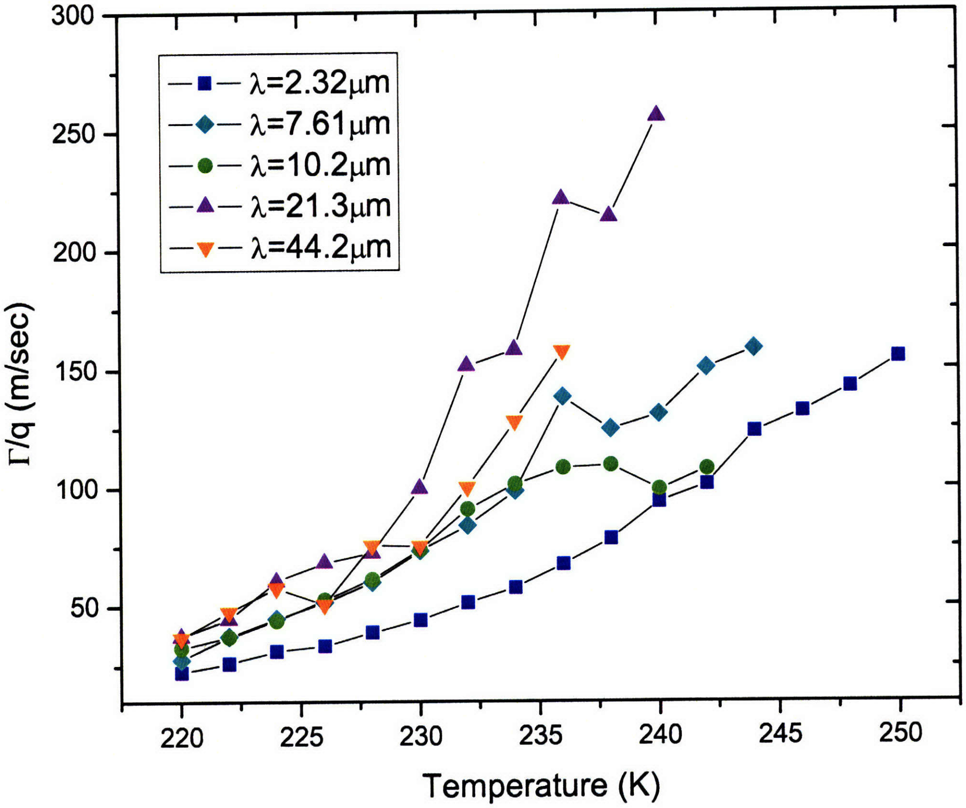

Figure 5-5: Scaled shear damping rate in TPP as a function of temperature for a variety of grating spacings. Longer wavelength acoustic waves have a higher scaled damping rate which increases with temperature.

ground viscous damping. The density values we obtained from data in reference [85] were fit to a quadratic as

$$\rho(T) = 1.507\ [\mathrm{g/cm^3}] - 1.3 \times 10^{-3}\ T\ [\mathrm{K}] + 6.8 \times 10^{-7}\ T^2\ [\mathrm{K^2}] \tag{5.4}$$

Figures 5-6 and 5-7 show plots of the real and imaginary parts of the shear modulus, respectively, as a function of temperature. These plots are for the same collection of wavevectors for which we have plotted the velocity and damping information. As in the plot of the velocity, we see the softening of the modulus at higher temperatures. The imaginary part shows generally monotonic behavior as a function of temperature as well, save for the 10.2 µm data, which shows a small decrease in the imaginary part at higher temperatures, a feature which is only weakly evident in the damping rate itself represented in figure 5-5. This is likely due to the period of our shear wave exceeding the characteristic relaxation time τ_s, permitting observation of a piece of the low-frequency side of the relaxation curve. We generally did not observe this trend at most wavevectors, as the shear wave signal often became either too weak or too strongly damped.

The moduli at each temperature were plotted as a function of frequency and then fit to the Havriliak-Negami relaxation function

$$G^*(\omega_s) = G_\infty \left(1 - \frac{1}{(1 + (i\omega_s\tau_s)^\alpha)^\beta}\right) \tag{5.5}$$

in order to extract the shear relaxation spectrum. We note that $G_0 = 0$ for all temperatures, by definition. As discussed in chapter 4, the Havriliak-Negami function has been chosen due to the fact that a transformation of the time-domain KWW parameters into the frequency domain is readily achieved with the two exponents α_{HN} and β_{HN}. This transformation into the frequency domain was done using the results of Hilfer [21, 22] as described in the previous chapter.

In fitting our spectral data, we adapted three different approaches with different constraints, with the aim of balancing the quality of the fits against how realistic the parameters we obtained were. In the first approach, we let all of the parameters vary.

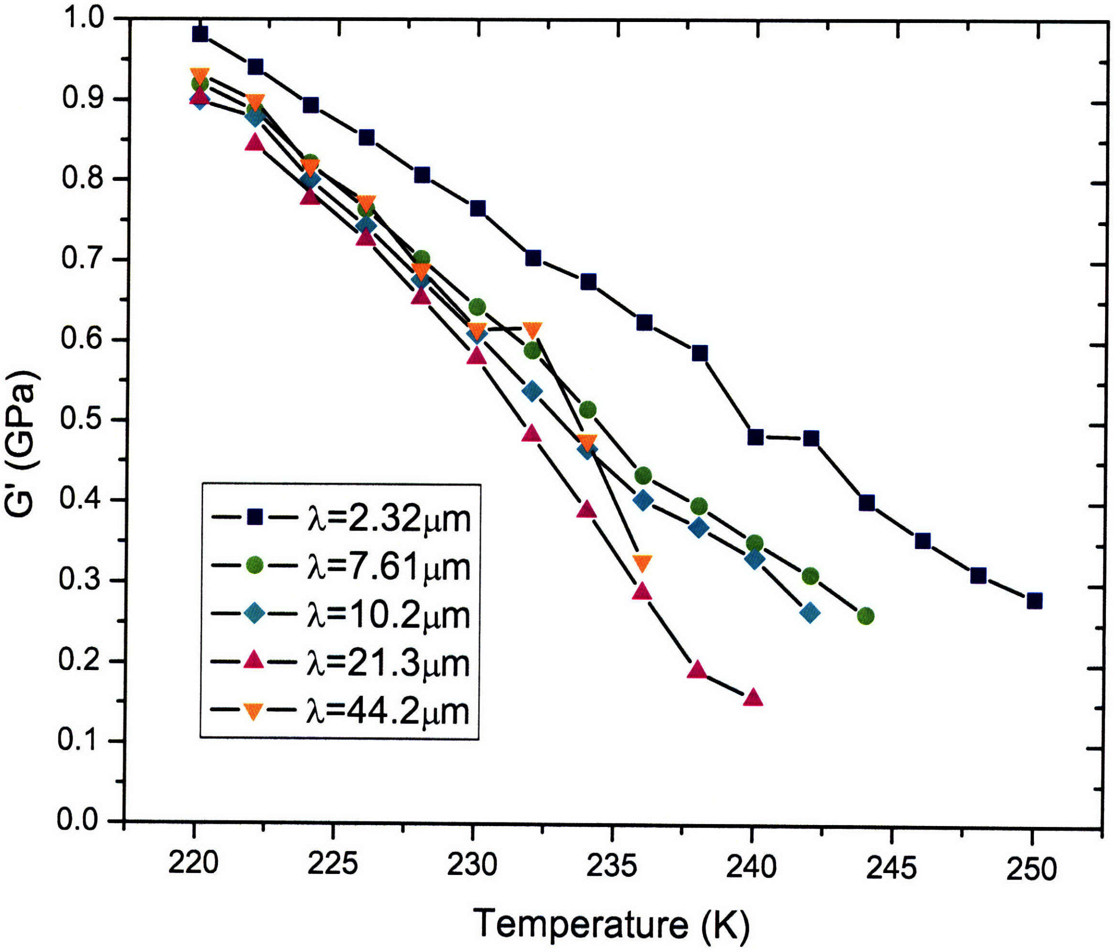

Figure 5-6: $G'(T)$ at a number of grating spacings. As the temperature is increased, the shear modulus is observed to soften considerably. Again, the highest temperature for which we could observe shear waves increases with the decrease of grating spacing.

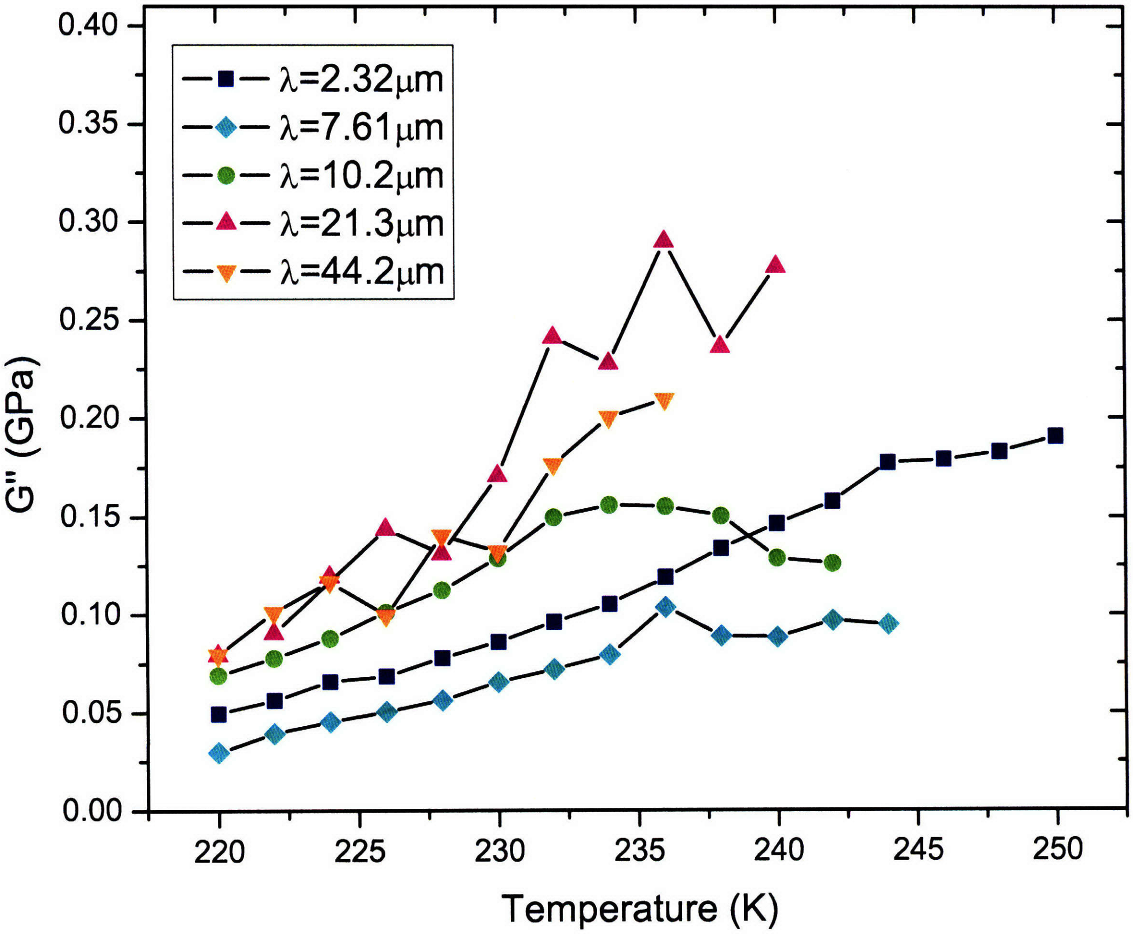

Figure 5-7: $G''(T)$ at a number of grating spacings. For most wavevectors examined in this study, we only observed a rise in the value of $G''(T)$ with temperature. At a handful of wavevectors, we were able to see the low-frequency side of the relaxation peak through, as is shown here for $2\pi/q = 10.2$ μm.

This was done in order to provide a visual guideline for the minimum least-squares uncertainties of the fitting routine relative to the ranges of physically plausible values for the fitting parameters.

The second approach relied heavily on the results of the analysis presented in [8, 9]. As we typically only saw the high-frequency side of the α relaxation peak, with a frequency range of two decades, it is likely that a free fit of the spectral parameters α_{HN} and β_{HN} would produce unreliable results. Hence, we chose to constrain these exponents with the transformed value for β_{KWW} supplied from polarized ISTS measurements of longitudinal acoustic waves and time-dependent thermal expansion reported previously in [8, 9]. Finally, the third method was to constrain not only α_{HN} and β_{HN}, but also the value of the relaxation time τ_s to its corresponding value for longitudinal relaxation, τ_l, obtained by transformation of KWW fits to previously reported polarized ISTS data into the frequency domain by the procedure described above.

Three representative plots of the complex shear modulus with their fits are shown in figures 5-8 - 5-10. As a first comparison, we see that the fit which is constrained for the three parameters α_{HN}, β_{HN}, τ_s does not fit the data. The fitted portion of $G'(\omega)$ is consistently high for all plots, and that of $G''(\omega)$ consistently low. This was true for all temperatures. Hence, we may draw the immediate conclusion that the shear spectrum of TPP that we observe does not share identical relaxation parameters with the previously published longitudinal spectrum. As mentioned above, we have not subtracted the background damping term, but it is unlikely that this is comparable in magnitude to the shear wave damping due to structural relaxation. Background damping was not subtracted from the previously reported longitudinal spectra [8, 9] that we are comparing our results to, but this could not account for poor agreement across the entire two-decade frequency range.

Over most of the temperature and wavevector ranges covered, the fits without constraints and with constraints on the HN exponents are consistent with each other within the uncertainties inferred from the scatter in the data. We note that the results from earlier work [8, 9] suggested a weak variation of the KWW exponent β_{KWW} with

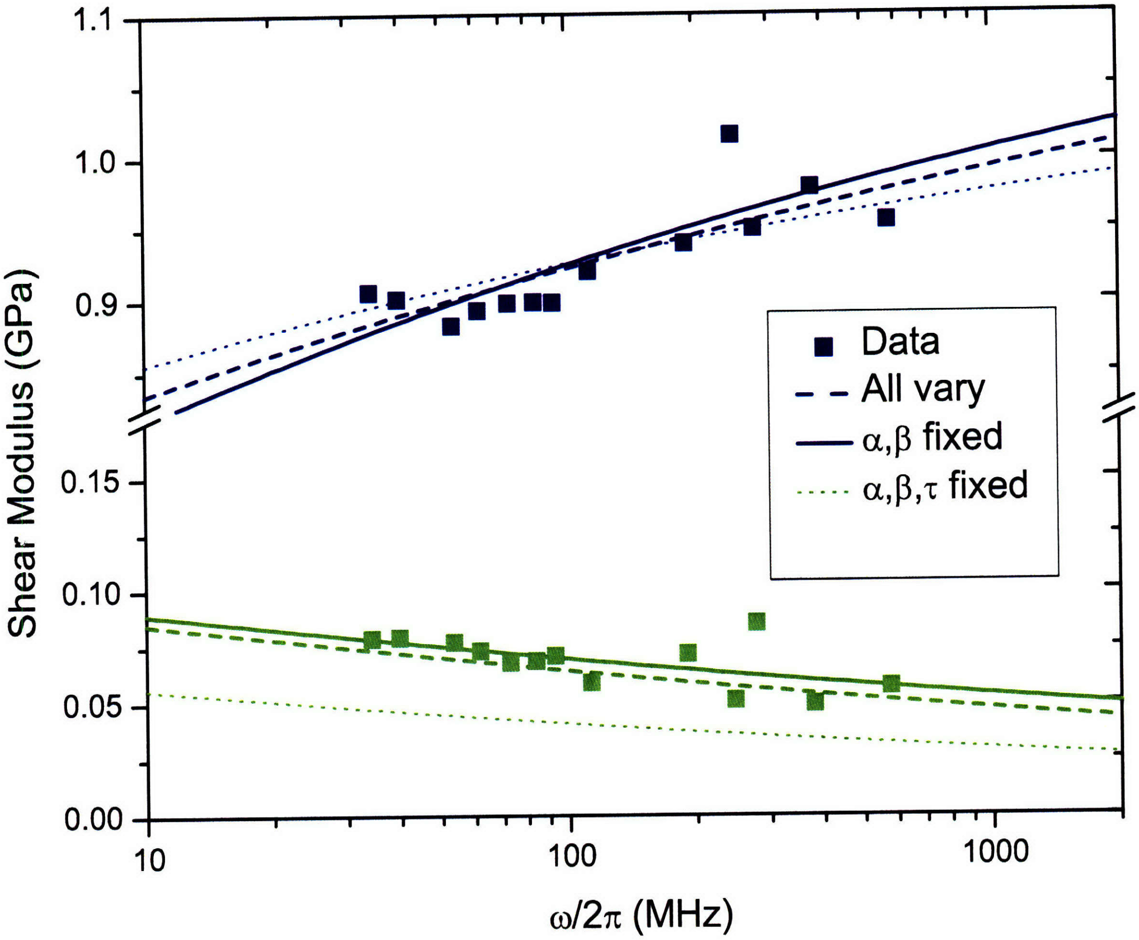

Figure 5-8: Shear acoustic spectrum of TPP at 220 K. The freely varying fits and the fits with α_{HN} and β_{HN} are nearly identical, while the fit constrained for all spectral parameters except G_∞ produces a poorer fit in the real part, and is consistently low in the imaginary part.

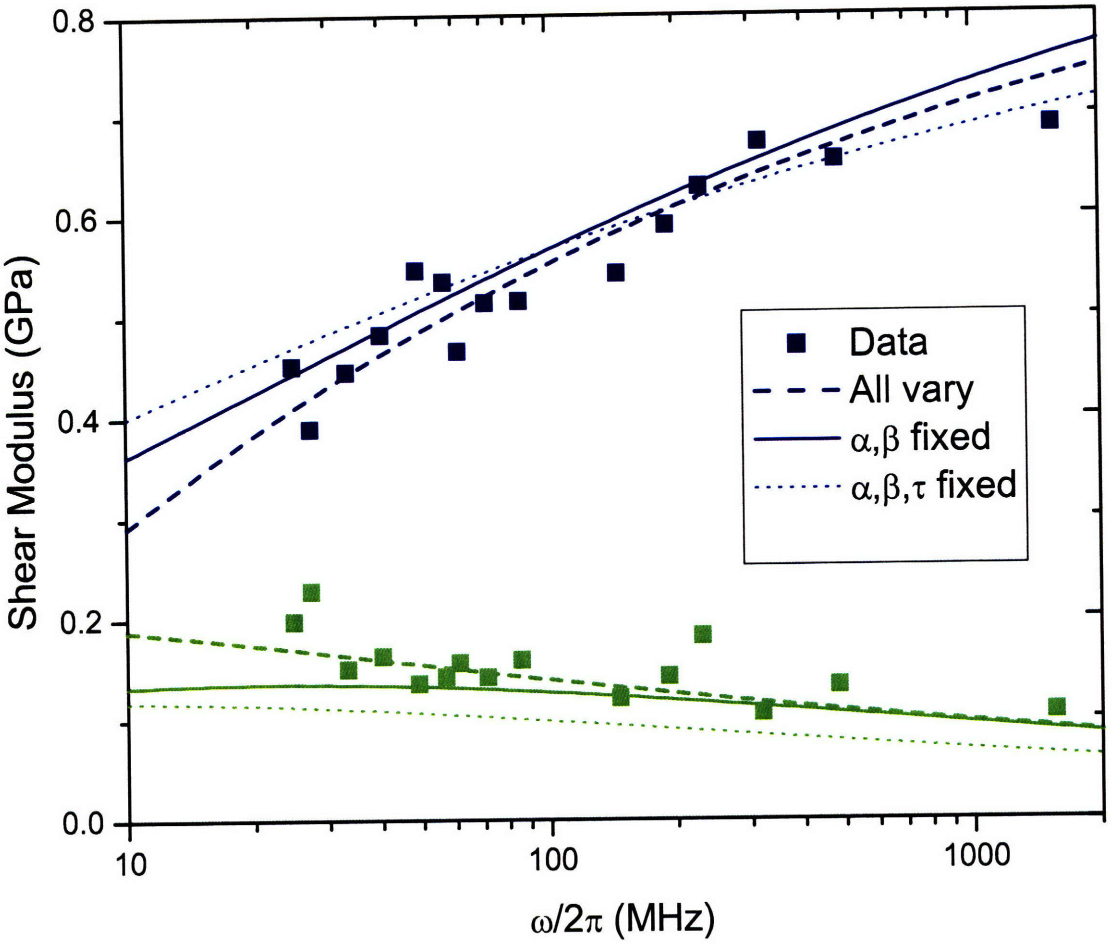

Figure 5-9: Shear acoustic spectrum of TPP at 234 K. Again, the freely varying fits and the fits with α_{HN} and β_{HN} are comparable. The fit with α_{HN}, β_{HN}, and τ_s fixed produces poorer agreement with the real part of the modulus consistently low values compared to the imaginary part.

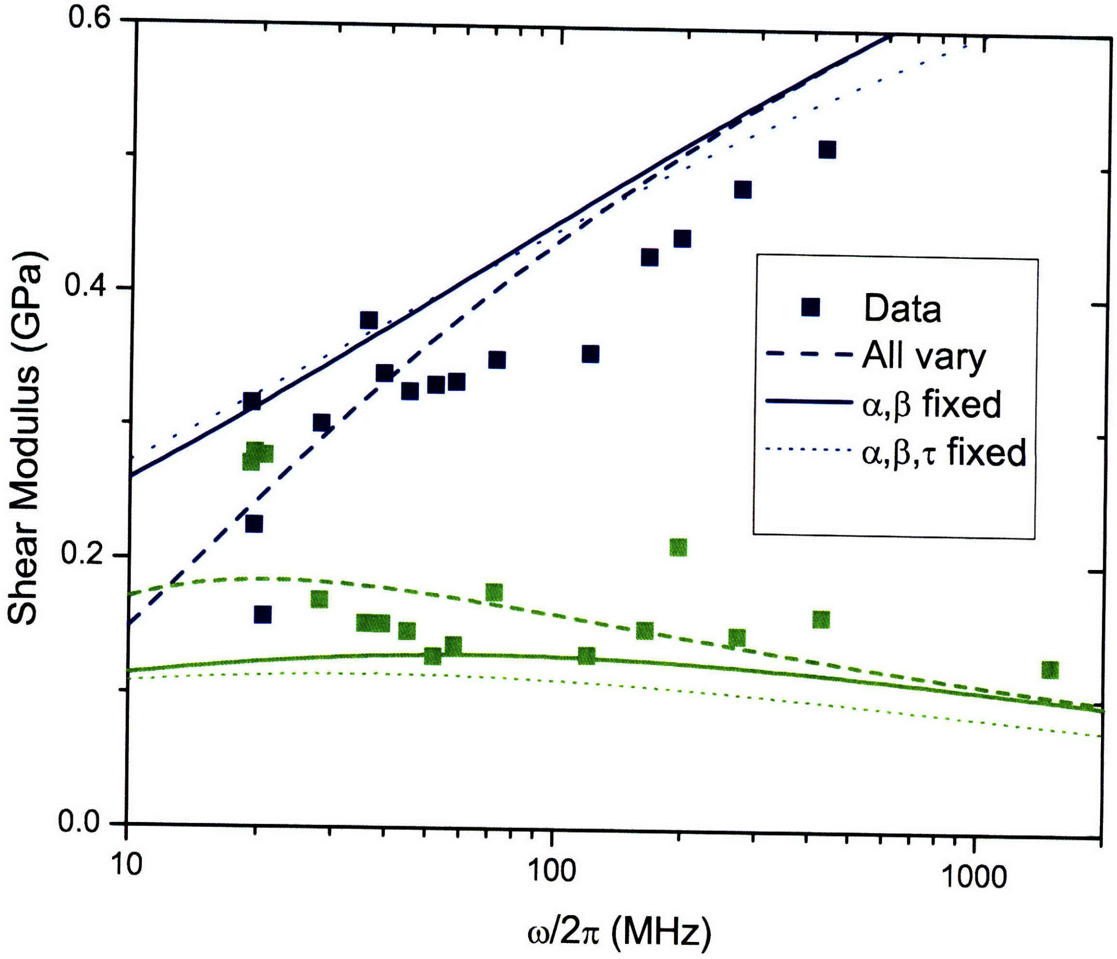

Figure 5-10: Shear acoustic spectrum of TPP at 240 K. Here, the freely varying fits and the fits with α_{HN} and β_{HN} differ considerably due to the scatter in the obtained values. The fit presented by the constraining α_{HN}, β_{HN}, and τ_s together also agrees poorly for the real part of the modulus, while it is again consistently low for the imaginary part.

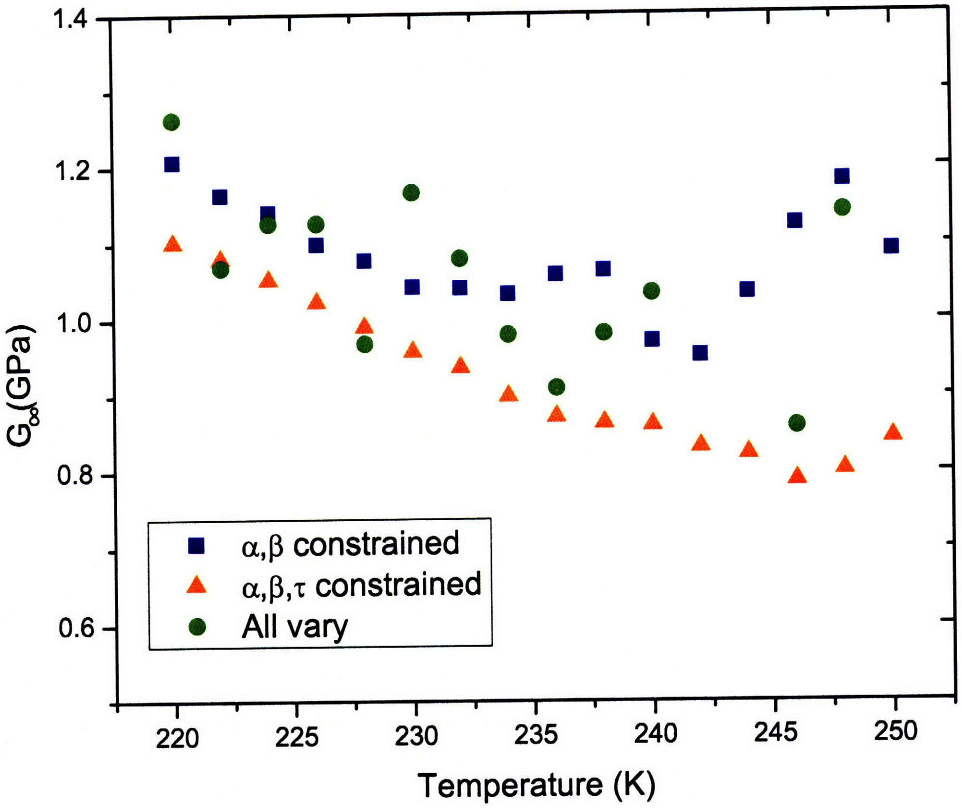

Figure 5-11: Values of $G_\infty(T)$ obtained from the various fitting approaches. The expected decrease of G_∞ with temperature is observed except (for fits with constrained values of the parameters α_{HN}, β_{HN}, and for unconstrained fits) at the highest temperatures at which the determination of G_∞ becomes unreliable.

temperature (a change of 0.15 over 30 K) which is within the uncertainty that can be deduced from the present results.

A plot of the fits of G_∞ as a function of temperature is shown in figure 5-11. Since the material is becoming less and less viscous with an increase in the temperature, we should expect G_∞ to decrease monotonically with T. We observe this behavior for all temperatures when the full set of parameters α_{HN}, β_{HN} and τ_s are constrained and for all but the highest temperatures when only the exponents are constrained or when no constraints are applied At the highest temperatures, our data are probing the low-frequency wing of the relaxation spectrum and so the high-frequency features, including the high-frequency limiting modulus value cannot be determined accurately.

Figure 5-12 presents τ_s as obtained from the various fitting approaches, where the values of τ_l to which some of the fits have been constrained are also shown. When

α_{HN} and β_{HN} are fixed by the longitudinal spectra, τ_s is consistently lower than τ_l by slightly less than an order of magnitude, although the two sets of values run parallel to each other over the entire temperature regime probed. The fit with freely varying parameters shows more scatter in τ_s, with significant deviation from the τ_l values at higher temperatures.

From this analysis, we conclude that the HN spectral parameters α_{HN} and β_{HN} from our shear acoustic wave data differ significantly, at least at the higher sample temperatures measured, from those obtained based on KWW fits to earlier polarized ISTS data [8, 9]. The differences between our results and the earlier results at some temperatures clearly exceed their combined uncertainties. We are hopeful that the shear frequency range can be extended significantly, but the two decades of frequencies that we have collected already are sufficient to indicate real differences in shear and longitudinal modulus spectra. In particular, the width of the shear spectra at higher temperatures appears to be greater than that of the longitudinal spectra. The characteristic relaxation times may also show systematic differences, but we do not believe we have sufficient data to reach a firm conclusion about this at present.

In figure 5-12, we present VFT fits to the temperature-dependent τ_s values derived from the different fitting approaches. The fit of the τ_s values obtained without constraints produced a value for $T_g = 218$ K and a fragility of $m = 73$, while the fit of the τ_s values obtained by constraining α_{HN} and β_{HN} also yields $T_g = 218$ K, with $m = 63$. The original VFT fit gives $T_g = 212$ K and $m = 161$. The literature value of T_g is generally accepted at around 202 K [86], while the fragility obtained in these measurements varies from $m = 100$ to $m = 120$.

Using the theoretical results of chapter 3 for the signal, we may attempt to deduce a lower length scale for shear wave propagation. Briefly, we recall that the observed frequency of the shear acoustic wave is given by

$$\omega_s = \sqrt{c_\infty^2 q^2 - \left(\frac{1}{2\tau_R}\right)^2}, \tag{5.6}$$

where c_∞ is the instantaneous shear velocity, q is the wavevector, and τ_R is the

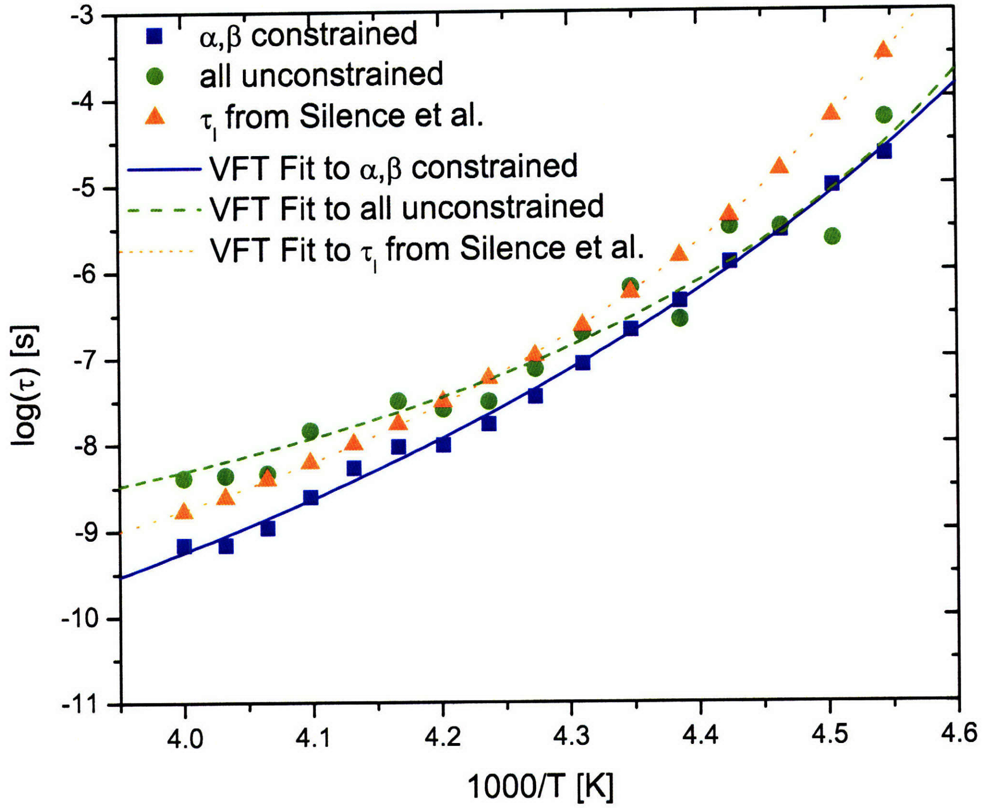

Figure 5-12: Characteristic relaxation time τ_s plotted versus temperature for both the constrained and unconstrained fits. The VFT fit of the original data yields $\tau_0 = 31 \pm 8$ fs, $B = 600 \pm 20$ K, and $T_0 = 191.4 \pm 0.6$ K. For α_{HN} and β_{HN} constrained we obtained $\tau_0 = 0.2 \pm 1$ ps, $B = 1200 \pm 600$ K, and $T_0 = 190 \pm 10$ K, while the unconstrained fit produced $\tau_0 = 2 \pm 20$ ns, $B = 400 \pm 600$ K, and $T_0 = 190 \pm 30$ K.

characteristic relaxation time of the liquid. This expression has been derived in a Debye model, and thus can be viewed as a simple approximation to the result with a more general relaxation spectrum. Assuming that the acoustic speed has gone to zero at finite wavevector, we set $\omega_s = 0$ and solve for the critical wavevector q_0

$$q_0 = \frac{1}{2c_\infty \tau_R}. \tag{5.7}$$

This analysis requires information on the value of G_∞, whose determination has not been entirely consistent by our measurements here, as mentioned above. In this light of this, we have chosen to substitute the values obtained by Brillouin scattering measurements [87] in a linear extrapolation to colder temperatures as

$$c_\infty = 2904.7 - 8.84T \text{ [K]} \tag{5.8}$$

This extrapolated values were consistently $\sim 8\%$ larger than the acoustic velocities measured in this study.

The results of this analysis are shown in figure 5-13 using both the constrained and unconstrained fits of the relaxation spectrum. As with the plot of the characteristic relaxation times, the constrained fits show a parallel evolution in temperature, while the unconstrained fits display more scatter, and appear to vary between the other two approaches.

We may attempt to understand our results in the mode-coupling framework of Das [44]. Briefly, when a calculation of a collection of hard spheres in a Percus-Yevick approximation is considered, the critical length scale $L_0 = 2\pi/q_0$ beyond which propagation of shear waves becomes overdamped obeys the power law

$$L_0 = \frac{A}{(\Delta - \Delta_c)^\delta} \tag{5.9}$$

where $A = 1$, $\delta = 1.2$, Δ represents the packing fraction, and Δ_c is a critical value beyond which shear wave propagation is allowed for all length scales.

In our study, we have instead chosen the scaled temperature T_g/T as the inde-

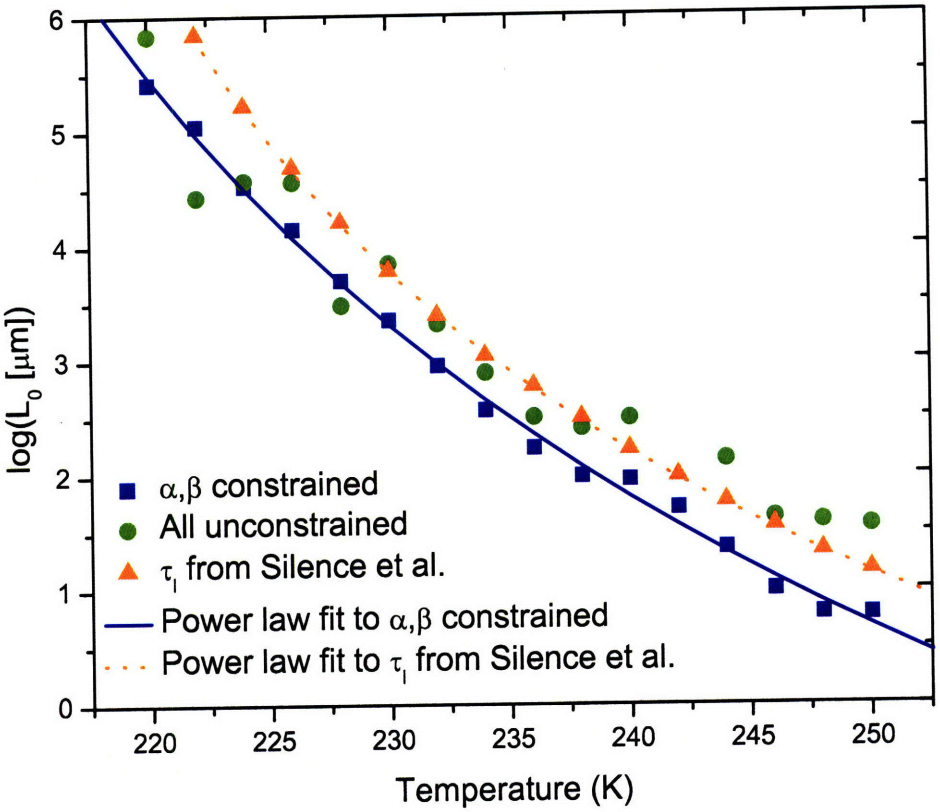

Figure 5-13: Computed value of length scale limit for shear wave propagation as a function of temperature. Fitting these results to a power law yields the values $\log(A) = -9 \pm 2$, $\delta = 15 \pm 5$, and a critical temperature of $T_c = 198$ K ± 9 K. From the $\tau_l(T)$ values, we obtain $\log(A) = -6.9 \pm 0.2$, $\delta = 9.9 \pm 0.3$, and $T_c = 210$ K ± 8 K.

pendent parameter. A power law fit to our data is shown in figure 5-13, where we are able to produce a good fit only if we let both A and the exponent δ vary. The critical temperature which yields a diverging length scale for shear wave propagation is $T_c = 198$ K ± 9 K for the fit with constrained exponents, and $T_c = 210$ K ± 8 K for the values of τ_l. Both values are close to the literature value for $T_g = 202$ K. We remark that the wavelength scales L_0 reached as this temperature is approached from above are several orders of magnitude larger than those corresponding to any diverging structural correlation length scale.

The value for the exponent that we have obtained, $\delta = 15 \pm 5$ from the constrained exponent fits and $\delta = 9.9 \pm 0.3$ from the values of $\tau_l(T)$, are significantly larger than the value of 1.2 suggested by eq. 5.9. We may explain this by the remarks made in [44], which state this value for the exponent is particular to the model studied, and is not expected to be a universal characteristic of the mode-coupling theory. A more detailed computation with a model and parameters more relevant to triphenyl phosphite may be able to explain the exponent we obtain here.

5.4 Conclusions

We have used depolarized Impulsive Stimulated Brillouin Scattering to measure shear acoustic waves in supercooled triphenyl phosphite from 220 K to 250 K. Using previously obtained results, we are able to examine a frequency regime from $\sim$ 10 MHz to almost 1 GHz. Our results indicate that the shear and longitudinal spectra do not share the same spectral parameters α_{HN} and β_{HN}.

Further work in the study of shear relaxation in triphenyl phosphite will center on expanding the dynamic range of the measurements. We also note that a comparison with dielectric data via the model of DiMarzio and Bishop [88] could also be performed if dielectric relaxation measurements at a similar combination of temperatures and frequencies were carried out. Research in these directions is presently underway.

Chapter 6

Elastic Perspectives of the Glass Transition[1]

6.1 Introduction

We present an Impulsive Stimulated Scattering (ISS) test of the "shoving model" of the glass transition and of the correlation between the fragility index and Poisson ratio of eight supercooled liquids. Samples of triphenyl phosphite, DC704 (tetramethyl tetraphenyl trisiloxane), m-fluoroaniline, $Ca(NO_3)_2 \cdot 4H_2O$, diethyl phthalate, propylene carbonate, m-toluidine, phenyl salicylate (salol), 2-benzylphenol, and Santovac 5 (5-phenyl 4-ether) were cooled to their respective glass transition temperatures and the elastic moduli directly measured at the highest accessible shear frequencies. The shear modulus was then measured every 2K as deeply as permitted into the liquid state for all liquids save propylene carbonate. Our results, in conjunction with dynamical relaxation data for these liquids obtained from the literature, lend credence to the notion that the dynamics of the glass transition are governed by the evolution of the shear modulus, but do not suggest a strong correlation between fragility and Poisson ratio.

---

[1] Done collaboratively with Jeremy Johnson of MIT

6.2 General Background

One of the foremost puzzles of the glass transition continues to be the origin of a glassformer's "fragility," which is a measure of the departure of its relaxation behavior from Arrhenius activated kinetics. Recent developments in the study of the glass transition aimed at addressing this mystery have centered around the relationship of the elastic properties of the glassy state to the fragility of the supercooled liquid [89].

Dyre and coworkers have proposed that the instantaneous shear modulus G_∞ controls the fragility [10, 90] as the activation energy at all temperatures is controlled by the energy cost associated with a non-compressional rearrangement of molecules via the "shoving aside" of their neighbors. As such a model of glassy systems views collective relaxation as a series of individual relaxation events between configurational minima, this perspective recalls landscape activated models [91] for the glass transition [92], and in recent years has been equated with them [93].

Building upon both the shoving model, which ties the shear modulus to the activation energy, and the empirical observation that the activation energy at T_g scales with the elastic moduli [94, 95], Novikov et al. [48, 96] have provided evidence that there exists a linear relationship between the ratio of the instantaneous elastic moduli of the glass and the fragility of the liquid:

$$m = 29(K_\infty/G_\infty - 0.41) \tag{6.1}$$

where K_∞ and G_∞ are the bulk and shear moduli, respectively and m the fragility index. While the form of this correlation is contested [97, 98, 99], that there exists a connection is less disputed.

At the core of both of these theoretical advancements is the shear elastic modulus. A brief survey of the literature reveals that its measurement in glass forming liquids is underdeveloped at frequencies in the high MHz and GHz regime, largely due to the small cross section of depolarized Brillouin scattering (BS) through which thermally excited shear acoustic phonons may be observed. This stumbling block can be partly overcome by the technique of Impulsive Stimulated Brillouin Scattering (ISBS) [100] performed in a depolarized geometry [8, 64] through which coherent shear acoustic phonons may be excited and probed. Until now, however, this technique has remained relatively unexploited in the study of glass forming liquids, also because of low signal levels. Here, we show that the implementation of diffractive optics and heterodyne detection make this measurement significantly more accessible.

With the aim of testing both of the aforementioned theoretical assertions, we have conducted depolarized ISBS on a collection of liquids, many of which are not included in the earlier theoretical and phenomenological developments [10, 48, 90, 96]. We also have examined longitudinal acoustic waves in polarized impulsive stimulated Brillouin and thermal scattering (polarized ISBS and ISTS respectively). The family of impulse stimulated scattering (ISS) methods is well suited to the study of longitudinal acoustics waves in supercooled liquids, shear waves have remained largely unexamined despite their obvious importance.

6.3 Theoretical Background

6.3.1 The Shoving Model

Conceptually, the shoving model predicts that the temperature dependence of the fragility arises solely from that of the instantaneous shear modulus G_∞. One arrives at this result via the core assumptions that the average relaxation time is dictated only by flow and that during a rearrangement as occurs during this flow event, the molecules do not rearrange at constant volume – the energy cost arising from the strongly anharmonic repulsive piece of the intermolecular potential renders this too costly. Rather, it is more energetically favorable for this rearrangement to occur with a change in volume as the molecules do work on their neighbors.

In analyzing the nature of this work, one first assumes that the molecular displacements are purely radial, i.e. the displacement vector $\mathbf{u}$ satisfies $\nabla \times \mathbf{u} = \mathbf{0}$. In such a case, it is possible to show that no compressional work is done on the surrounding medium; rather than a change in density, the neighboring molecules are simply "shoved" aside during flow. With no change in density, the energy required to make a local rearrangement of the liquid is due exclusively to the contribution from the shear elastic modulus. As these motions take place at very short length and time scales, they are necessarily due to the instantaneous modulus.

In the framework of the shoving model, this relaxation event is considered as an Arrhenius activated process and hence the average relaxation time τ depends on temperature as $\tau \sim \exp(\Delta E_r(T)/k_BT)$ where now the activation energy ΔE_r is explicitly temperature dependent. According to the arguments of the shoving model, this energy is entirely elastic, and hence, its temperature dependence derives exclusively from that of the instantaneous shear modulus G_∞. Thus, the average relaxation time is given as

$$\tau = \tau_0 exp\left(\frac{G_\infty V_c}{k_BT}\right). \tag{6.2}$$

Here, τ_0 is a high temperature relaxation time, typically on the order of picoseconds. V_c is a "characteristic" volume associated with the flow event and is given by

$$V_c = \frac{2}{3}\frac{\Delta V^2}{V} \tag{6.3}$$

where ΔV is the change in volume during the flow event and V is the volume of the flowing region before flow.

In practice, it is generally not possible to estimate the value of V_c. Rather, a more experimentally accessible coordinate is provided by examining the logarithm of the characteristic relaxation time τ versus a normalized argument of equation 6.2

$$X = \frac{G_\infty(T)T_g}{G_\infty(T_g)T}. \tag{6.4}$$

The variable X runs from 0 in the liquid state to 1 at T_g, for which we have used the definition of a relaxation time $\tau = 100$ s. In the high temperature liquid state limit, i.e. $X = 0$, we take τ to represent an attempt frequency, [71], so here we have assigned a value of $\tau = 10^{-15}$ s. Thus, for the shoving model to successfully map the average relaxation time to Arrhenius activated kinetics, in terms of X, we must observe

$$\log(\tau) = 17X - 15. \tag{6.5}$$

Inherent in the derivation of this model is the simplification that the geometry of the flowing region is perfectly spherical. This is a highly idealized case as more realistically, much less symmetric and also more varied geometries are involved in flow. Both of these issues preclude the assignment of a single activation energy to the dynamics of flow, and due to this lack of spherical symmetry, it is reasonable to expect that the bulk modulus will contribute to the activation energy, as well. While the issue of these dynamical heterogeneities in the shoving model is not addressed in the literature, it can be shown [101] that the upper bound for the contribution to relaxation from the longitudinal modulus can be set at 10%, even in the most asymmetric of flowing geometries.

6.3.2 Relationship between the fragility and K_∞/G_∞

We now review the arguments made by Novikov et al. in the derivation of equation 6.1. By construction, all glass-forming liquids, regardless of fragility, share two common points on the Angell plot: in the liquid state (defined by a viscosity of 10^{-3} P or relaxation time $\tau \sim 1$ ps), and at T_g. The derivative of such a viscosity curve is monotonically increasing with the scaled inverse temperature T_g/T, which implies that the higher the liquid's fragility, as determined by the definition

$$m = \left(\frac{d\log(\eta)}{dT}\right)_{T=T_g} \tag{6.6}$$

the shallower the slope of the viscosity curve in the liquid state.

To put this relationship in more quantitative terms, the authors first appeal to the observation that the temperature dependence of the viscosity in the region of the liquid state is linear on an Angell plot. Hence, the viscosity at high T is considered to follow the Arrhenius law $\eta \sim \exp(\Delta E_l/T)$, where a single activation energy ΔE_l has been assigned to the dynamics. As the derivative of the relaxation time with respect to scaled inverse temperature T_g/T is equal to $\Delta E_l/T_g$ in the liquid state, the authors argue that this is the proper combination of variables with which to correlate against fragility. The authors then proceed to fit experimental values of m versus $\Delta E_l/T_g$ to obtain

$$\frac{\Delta E_l}{T_g} = \frac{19.2^2 \ln 10}{m}. \tag{6.7}$$

Novikov et al. then recall other authors' arguments – all based on empirical grounds – that the transition temperature T_g correlates linearly with both the bulk K and shear modulus G of the glass [95, 102, 103, 104]. This idea leads them to posit that T_g is proportional to a linear combination of elastic constants

$$T_g \propto K_\infty + x G_\infty \tag{6.8}$$

where x is a fitted proportionality constant.

To link these two arguments, the authors first argue that $\Delta E \propto G_\infty$ from the shoving model, so they may substitute this into equation 6.7. The next step is to simply replace T_g in equation 6.7 by the right hand of equation 6.8 and solve for m. Fitting the results of several measurements of elastic parameters with fragilities to a straight line finally yields equation 6.1.

Johari and coworkers have debated that the linear form of this relationship is unjustified, and as an example, demonstrate that a quadratic dependence of m on the ratio K_∞/G_∞ fits the data as well as a linear one. They further call into question the ability to make a prediction at all due to the scatter in the plot. Novikov et al. have, to some extent, addressed the latter issue by showing that metallic glass formers cannot be considered alongside molecular ones due to the contribution to the elastic modulus made by the Fermi gas [105].

Nevertheless, Priya and Das have sought to put this correlation on sound theoretical ground by a first-principles treatment in terms of the mode-coupling theory studied for a system of hard spheres [46]. Briefly, the theory is extended to include slow modes associated with molecular constituents that have been frozen into their configurations in the glass. Using a scaled packing fraction as the analogy to temperature, the relaxation time (equivalently the fragility) in the model is correlated with the change in elastic moduli. When a specific value is picked for the upper wavevector cutoff of the density fluctuations considered in the theory, the behavior of the ratio K_∞/G_∞ as a function of m exhibits remarkable agreement with the results of [48].

6.4 Experimental Methods

6.4.1 Impulsive stimulated scattering: General considerations

Experimentally, the assertions are best tested with a technique that can simultaneously probe the longitudinal and shear modulus at a common, high frequency. While somewhat lower in frequency than Brillouin scattering, ISS holds the significant advantage that the scattered light arises from coherently generated phonons, rather than those that are thermally present, resulting in better signal to noise ratios and much quicker data acquisition times. Additionally, the data are recorded in the time domain, and avoid the problem of overlap of central peak phenomena with the dynamics of interest. Consequently, we are able to detect shear waves in a collection of liquids that have previously remained unstudied.

In a typical ISS experiment, conducted in a heterodyned four-wave mixing geometry, light from a pulsed laser is incident on a diffractive optical element, typically a binary phase mask (PM) pattern, and split into two parts (±1 diffraction orders; other orders are blocked) that are recombined at an angle θ as depicted in Fig. 6-1. The crossed excitation pulses excite an acoustic wave whose wavelength Λ and wavevector magnitude q are given by

$$\Lambda = \frac{\lambda}{2\sin\theta/2} \tag{6.9}$$

where λ is the excitation laser wavelength. Probe light (in the present case from a CW diode laser) is also incident on a phase mask pattern (the same one or another with the same spatial period) and split into two parts that are recombined at the

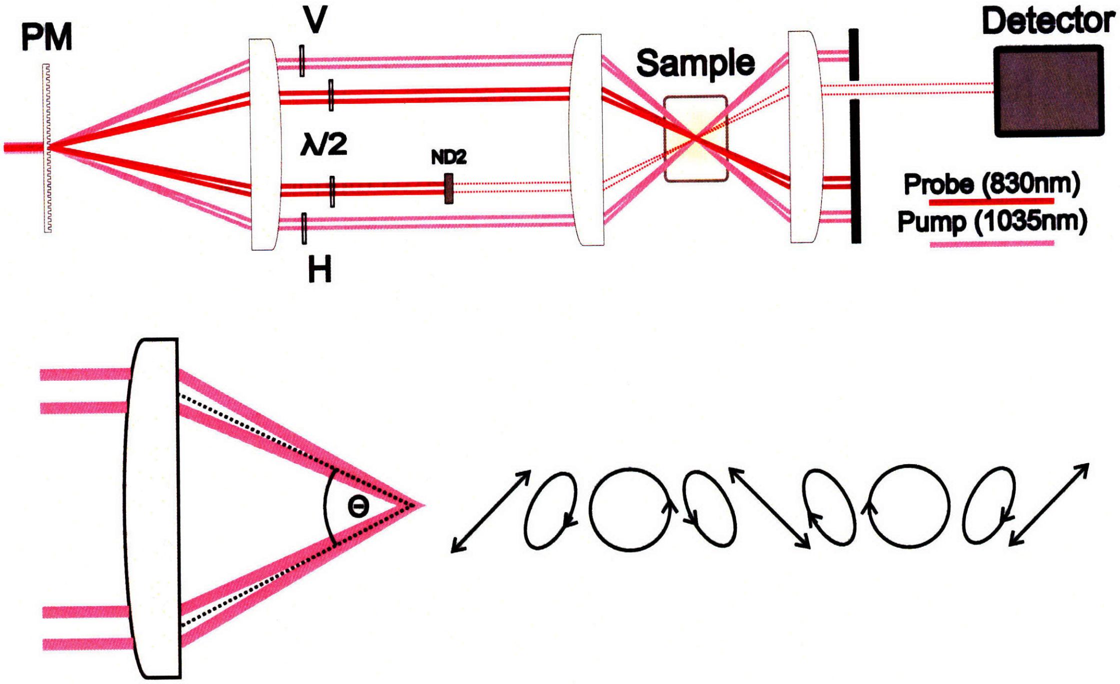

Figure 6-1: Schematic illustration of the ISS setup. Both the pump and probe beams are incident on the phase mask (PM) and their ±1 diffraction orders are recombined at the sample at an angle θ. In the case of a depolarized experiment, waveplates in the path of each of the four beams are used to create a polarization grating pattern in the sample plane as depicted.

sample to serve as probe and reference beams. The signal arises from diffraction of probe light off the acoustic wave and any other spatially periodic responses induced by the excitation pulses. The diffracted signal field is superposed with the reference field for heterodyned time-resolved detection of the signal, which typically shows damped acoustic oscillations from which the acoustic frequency and damping rate can be determined.

The polarizations of the beams in the present measurements are all vertical (V) or horizontal (H) relative to the scattering plane. We denote the polarizations of the excitation fields, probe field, and reference/signal field in that order, i.e. VHVH denotes V and H excitation, V probe, and H reference and signal polarizations while VVVV denotes all V polarizations. All the measurements reported herein were conducted with one of these two polarization combinations.

In a VVVV experiment, the action of the excitation pulses is twofold. First, depending upon the absorbance at the pump wavelength, a fraction of the light is absorbed into the sample and this energy is very rapidly converted into heat. Sudden thermal expansion launches counterpropagating acoustic waves with the acoustic period Λ. In addition to acoustic oscillations, the signal may also show slower, nonoscillatory density responses and thermal diffusion from which complex structural relaxation dynamics and thermal diffusivities may be determined [7]. This excitation mechanism is labelled Impulsive Stimulated Thermal Scattering (ISTS) and is the dominant mechanism in the VVVV measurements.

The second excitation channel arises from the electrostrictive work done on the liquid by the V-polarized excitations pulses. The electric field of the interference maxima both induces a polarization and does compressive work on the induced dipoles, resulting in impulsive excitations of counterpropagating longitudinal acoustic waves of wavelength Λ even in the absence of optical absorption. This excitation mechanism is impulsive stimulated Brillouin scattering (ISBS). As the force scales with the gradient of the field squared, the efficiency of the excitation scales as q. Therefore this mechanism becomes more important as the scattering wavevector is increased.

In a depolarized (VHVH) experiment, each of the pump arms carries a different polarization and the ensuing grating is described as an alternating polarization pattern, depicted in the Fig.6-1 inset. Here it is the regions of linear polarization that perform electrostrictive work, deforming the excited region in a fashion that drives counterpropagating shear acoustic waves. As described above, the ISBS driving force scales as q, so the signal from shear waves becomes markedly stronger as the wavevector is increased. In this case, the diffracted signal polarization is rotated 90° from that of the incident probe light, analogous to depolarized (VH) Brillouin scattering. The excitation pulses may also induce molecular orientational responses that can contribute to signal, analogous to depolarized quasielastic scattering [8, 83].

To our knowledge, until this work, neither diffractive optics nor heterodyne detection has been used in depolarized ISBS experiments. We have found that both of these experimental advances have been indispensable in our measurements.

6.4.2 Impulsive stimulated scattering: Experimental setup

The pump laser system used for these studies was an Yb:KWG High-Q FemtoRegen lasing at 1035 nm and producing pulses of 500 µJ at a repetition rate of 1 kHz. While a 300 fs compressed pulse width FWHM was typical, we bypassed the compressor to retrieve pulses directly from the regen that are 80 ps in duration in order to avoid sample damage at high peak powers, yet remain in the impulsive limit relative to the oscillation period. The excitations beams were focussed to a spot 2.5 mm in the grating dimension and 100 µm in the perpendicular dimension so that the acoustic waves would have many periods and the decay of signal would be due primarily to acoustic damping rather than propagation away from the excitations and probing region of the sample.

As a probe, we used a Sanyo DL8032-001 CW diode laser lasing at 830 nm with 150 mW power focused to a spot of 1 mm in the grating dimension by 50 µm in the perpendicular dimension. We also used a common phase mask optimized for diffraction into ±1 order at 800 nm for both pump and probe beams, and we utilized two-lens 2:1 imaging with Thorlabs' NIR achromats to recombine the beams at the sample. The local oscillator was attenuated by a factor of 10^{-3}. Approximately 30%

of the pump power was lost into zero order with this configuration, but the pump intensity still had to be routinely reduced significantly to avoid unwanted nonlinear effects. The signal was collected with a Cummings Electronics Labs Model 3031-0003 amplified photodiode with 3 GHz bandwidth and processed in a Tektronix TDS-7404 digitizing oscilloscope with a 4 GHz bandwidth. Signals from 10,000 repetitions of the measurement were averaged for each data trace, with total data acquisition times of a few minutes.

The acoustic wavelength was calibrated through ISTS measurements in ethylene glycol, for which the speed of sound is known to a high degree of accuracy [66]. The acoustic wavelength selected for each sample was between 1.75 μm and 4.67 μm, the choice dictated by the amount of signal the sample produced. While at higher acoustic wavevector q (i.e. shorter acoustic wavelength), the ISBS signal is greater due to the linear q-dependence of the excitation efficiency, this enhancement is offset by the reduced depth of overlap of the beams in the bulk liquid sample when they are crossed at a larger angle. The signal at large angles is also diminished somewhat due to imaging defects caused by working outside of the paraxial limit for the imaging optics. The wavevectors for shear and longitudinal acoustic wave measurements were selected to give frequencies that were as similar as possible.

Samples of triphenylphosphite (TPP), DC704 (tetramethyl tetraphenyl trisiloxane), m-fluoroaniline, m-toluidine, $Ca(NO_3)_2 \cdot 4H_2O$, diethyl phthalate, propylene carbonate, an 87% 2-benzylphenol (α-phenol o-cresol) 13% o-terphenyl mixture ($2BP_{87}/oTP_{13}$), and Santovac 5 (5-phenyl 4-ether) were obtained from Alfa Aesar. TPP, diethyl phthalate, salol, and the 2-benzylphenol mixture were heated under vacuum to remove volatile impurities, while DC704, propylene carbonate, m-toluidine, and m-fluoroaniline were mixed with anhydrous $MgSO_4$ to remove water. $Ca(NO_3)_2 \cdot 4H_2O$ was used directly without further processing other than heating to a melt in a sealed container. After filtering with a 0.2 μm millipore teflon filter, the samples were loaded into a teflon coated aluminum cell with movable windows and a factory calibrated Lakeshore PT-102 platinum resistor thermometer immersed in the liquid for temperature measurement; this cell is described in detail elsewhere [68]. The cell was then placed in a Janis coldfinger ST-100 cryostat and the temperature monitored and controlled with a Lakeshore 331 temperature controller.

The samples were cooled to T_g at a cooling rate that never exceeded 6 K/min, with 2 K/min the typical rate. Although the sample cell windows were designed to move in order to relieve the stresses due to contraction of the liquid upon cooling, diethyl phthalate and 2-benzylphenol were still observed to crack shortly after vitrification. In these cases, a clear spot of the sample was found and the measurement continued.

In the case of TPP, crystallization or clouding associated with the "glacial" phase [15] was observed occasionally. In such cases the sample was heated to melt and then cooled back down. Homodyne ISBS data from an earlier study of TPP [8, 9] (the only previous depolarized ISBS study of a glass-forming liquid, made possible by strong signal from this sample) were compared to the data recorded in the present study and were in agreement within experimental uncertainties at all common temperatures. Data from the earlier study were used for the analysis below since a slightly higher wavevector range was achieved.

Samples were equilibrated at T_g for 15 minutes before longitudinal and shear wave measurements were made. Then, the shear measurement was conducted upon warming every 2K until the sample either crystallized (as in the case of $Ca(NO_3)_2 \cdot 4H_2O$, $2BP_{87}/oTP_{13}$, salol, and diethyl phthalate) or the shear modulus disappeared. At each temperature, the sample equilibrated for roughly 15-30 minutes.

6.5 Results and Discussion

Fig. 6-2 shows representative VVVV data from diethyl phthalate collected with a 4.22 µm acoustic wavelength. Upon arrival of the pump laser pulses there is a nonresonant electronic response observed, followed by a modulation of the diffracted signal due to the counterpropagating longitudinal acoustic waves in the region of excitation. The oscillations are not centered around zero, but rather about a steady-state DC offset which is due to the induced thermal grating whose decay time ($\propto q^2$) is long compared that of the acoustic waves. The signal is fit in the time domain to a simple

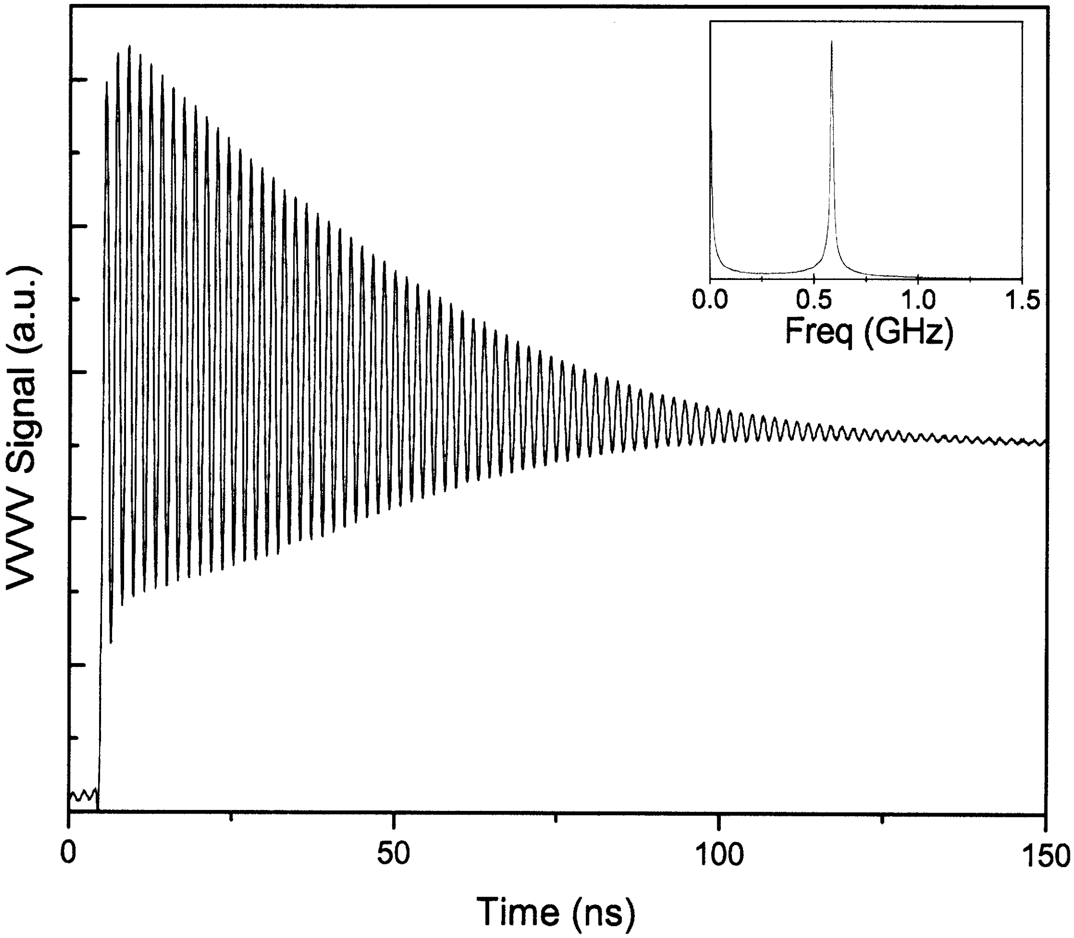

Figure 6-2: 4.22 μm longitudinal waves in diethyl phthalate at $T_g = 178$ K. The signal is offset from zero after the arrival of the laser pump pulses due to the thermal grating which diffuses on the order of 10 μs. The inset shows the Fourier transform of the signal on the GHz scale, revealing the acoustic frequency in a manner analogous to a Brillouin spectrum.

damped sine wave

$$I(t) = A\exp(-\Gamma t) + B\exp(-\gamma t)\cos(\omega t + \phi) \tag{6.10}$$

where A and B are thermal/orientational and acoustic amplitude coefficients, respectively, γ is the acoustic damping rate, ω is the acoustic angular frequency, and ϕ is a phase. The variable Γ was used to represent thermal decay in the case of longitudinal measurements and the decay of orientational relaxation in the case of shear measurements. The phase accounts for the ISTS and ISBS signals which are $\pi/2$ out of phase with one another and contribute to the overall signal in differing amounts. From the fit, we deduce the acoustic frequency and damping rate, and hence the complex Young's modulus M according to

$$M = M'(\omega) + iM''(\omega) \tag{6.11}$$

where the storage modulus is given by

$$M'(\omega) = \frac{\rho\,(\omega^2 - \gamma^2)}{q^2} \tag{6.12}$$

and the loss modulus by

$$M''(\omega) = \frac{2\rho\omega\gamma}{q^2} \tag{6.13}$$

.

The results of several VHVH experiments are shown in figures 6-3 and 6-4, and an example of evolution with temperature is provided by Fig. 6-5. There is an initial spike caused by the nonresonant electronic hyperpolarizability induced by the excitation pulses, followed by oscillations about baseline due to counterpropagating shear waves which disappear on the scale of hundreds of nanoseconds as a result of acoustic damping. With the exceptions of m-fluoroaniline and m-toluidine, there are no significant slow components of the signal resulting from either a thermal background or to structural relaxation dynamics. In these two liquids, the influence of the pump

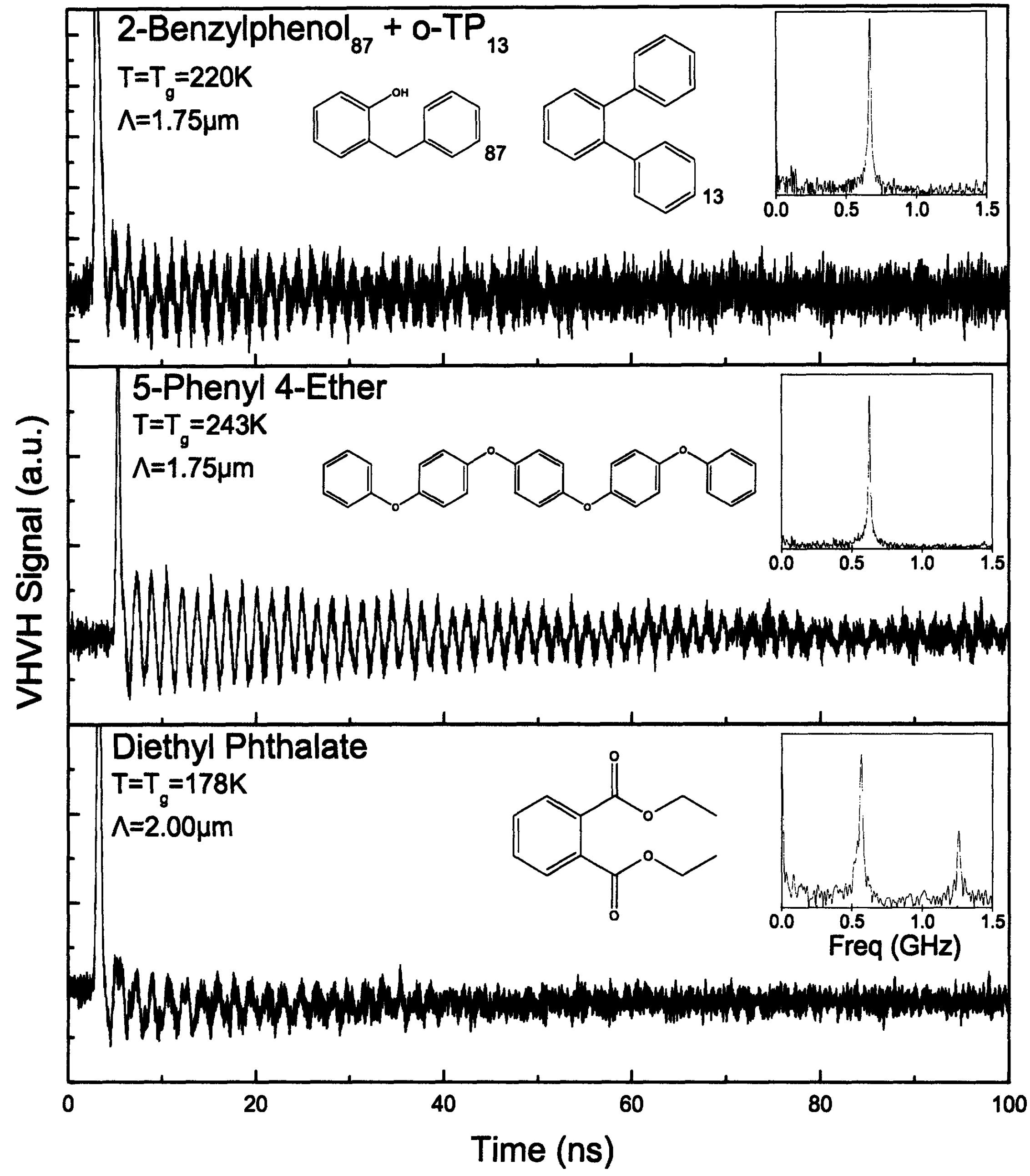

Figure 6-3: Shear waves in, and chemical structures for, $2BP_{87}/oTP_{13}$, 5-phenyl 4-ether, and diethyl phthalate at their literature glass transition temperatures T_g and transient grating spacing as given in Table 6.1 below. The vertical scale, though arbitrary, is the same for all liquids. The inset shows the Fourier spectrum on the GHz scale. The predominant peak is always due to shear waves, though in some cases (particularly in diethyl phthalate), longitudinal signal leaks through.

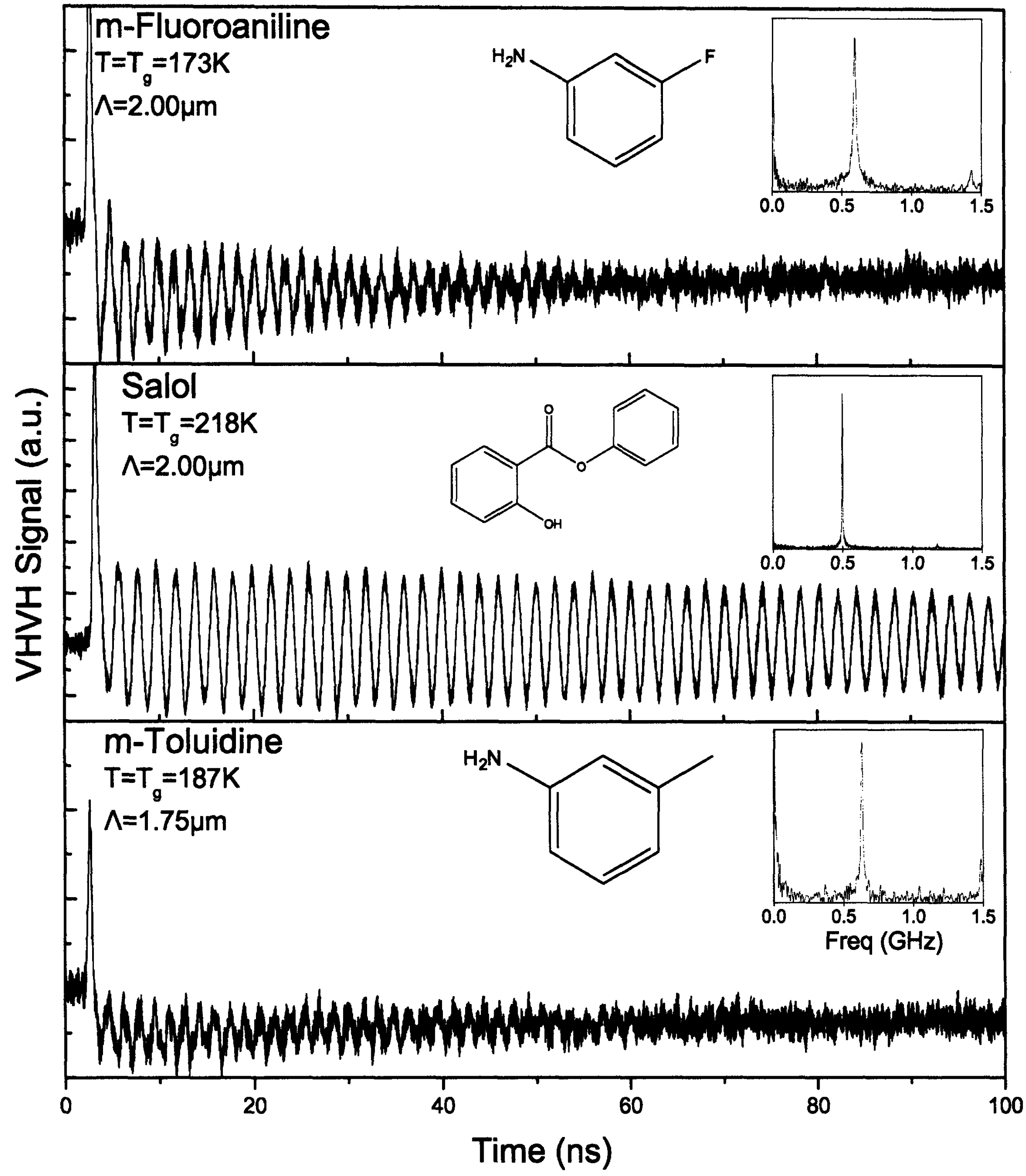

Figure 6-4: Shear waves in, and chemical structures for, m-fluroaniline, salol, and m-toluidine at their literature glass transition temperatures T_g and transient grating spacing as given in Table 6.1 below. The vertical scale, though arbitrary, is the same for all liquids except salol, for which it is scaled down by 2×. The inset shows the Fourier spectrum on the GHz scale. The predominant peak is always due to shear waves, though in some cases, longitudinal signal leaks through. The baseline offset seen in m-fluoroaniline and m-toluidine is due to absorption effects, as explained in the text.

pulses on the liquid caused a change in the transmitted profile of the probe laser. This observed change was manifest in the offset of the signal from zero, as well as the likelihood of cumulative nonlinear effects in the liquid. It did not, however, affect the observed shear frequency or damping rate. As all of these effect were strongly dependent upon pump intensity, the pump was attenuated as much as was possible while still maintaining good signal to noise ratios. Consequently, the sample was not observed to undergo any physical changes during measurement.

We point out that although the absolute scale of the signal is arbitrary, the relative scales of the VVVV and VHVH signals can be compared as all of the incident pulse intensities were comparible – the VVVV signal level was roughly 100× stronger than the VHVH signal. This is due to two reasons: first, the shear acoustic wave is driven entirely by electrostriction, as opposed to the longitudinal wave which benefits from the contribution from heating. Further, off-diagonal coefficients of the photoelasticity tensor are generally an order of magnitude weaker than the diagonal ones, implying that shear acoustic waves should be ~ 10 times weaker in amplitude than the corresponding electrostrictively generated longitudinal ones.

A test of the shoving model would normally require the correlation of the derived quantity X as described in equation 6.4 with the relaxation time at that temperature as deduced from either viscosity data or measurements of the evolution of the loss peak of shear relaxation. To the extent that these data are available in the literature, we have used them to compare with our results. However, motivated by the greater accessibility of dielectric relaxation data, as well as the theoretical proposal that dielectric and shear relaxation should be related [106, 107], we have also performed the analysis with respect to this form of relaxation, too.

Figs. 6-6 and 6-7 show the results of several shear wave measurements performed as deeply as permitted into the melt at the highest wavevector at which these measurements could be performed, and scaled according to equation 6.4. For each liquid, we have accounted for the thermal contraction during cooling with literature data of either measured densities [85, 108, 109, 110, 111, 112, 113, 114]. For all liquids save TPP and diethyl phthalate, this information was a simple linear expression which

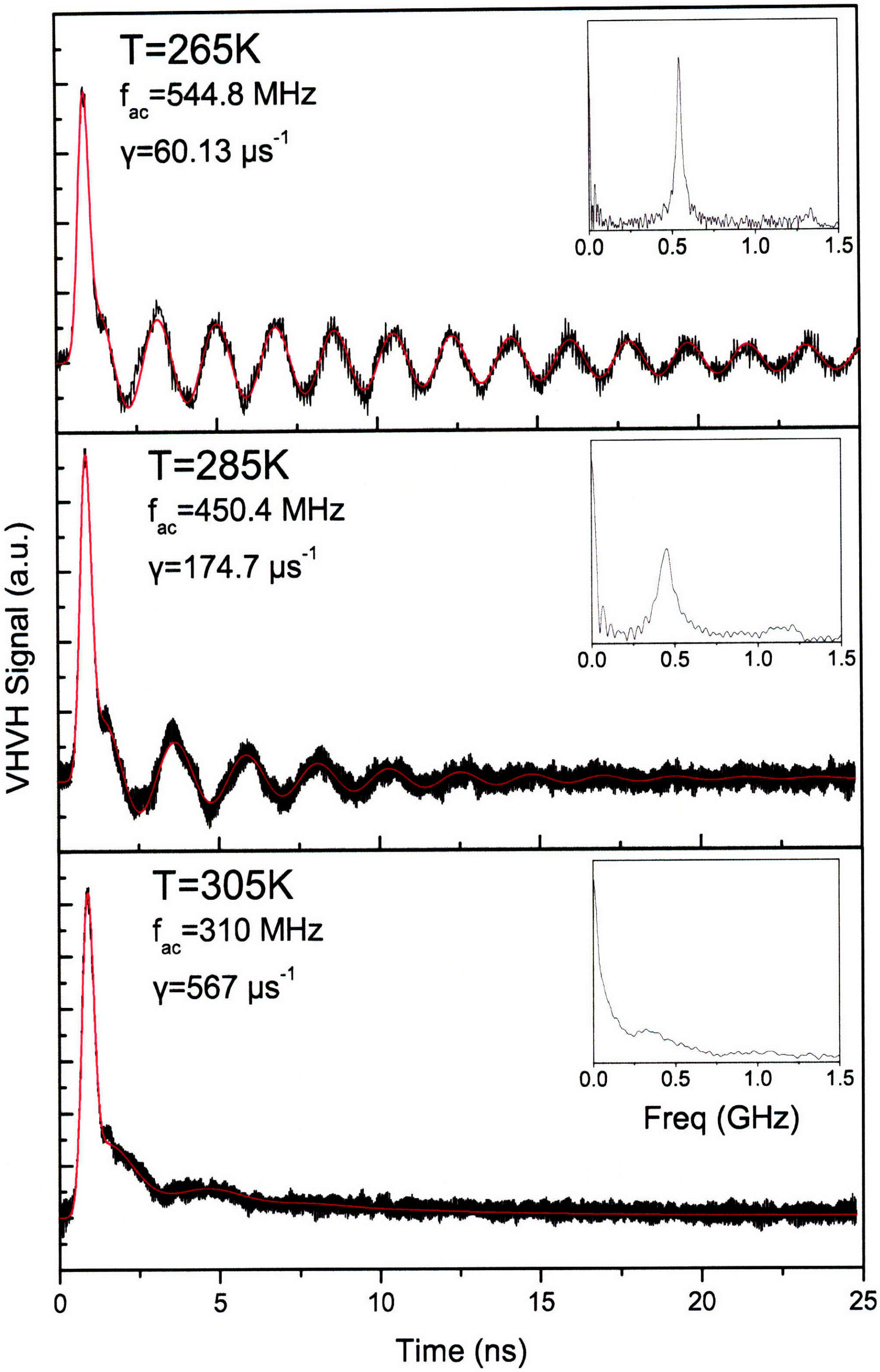

Figure 6-5: Shear waves in 5-phenyl 4-ether at three characteristic temperatures, displaying weakly damped, moderately damped, and strongly damped behavior respectively. Data are in black and the best fit is represented in red, which capture all features of the measured signal. Insets are Fourier transforms from the point forward of the non-resonant electronic response. Of note at T= 305 K is the long tail in the signal due to the decay of the slow orientational relaxation.

Table 6.1: Raw data used in comparison of the ratio K_∞/G_∞ to dynamic fragilities. All elastic parameters as listed were taken at the literature values of T_g. The temperature in parentheses is T_g as calculated for each liquid from the low temperature dielectric VFT fits given in the references. We have used the convention of a transition temperature defined by $\tau = 100$ s, used in the test of the shoving model. Fragilities m are literature values, while the adjacent values in parentheses denote those calculated from the VFT fits at the derived T_g, again from the dielectric relaxation data. m_{calc} was computed using eq. 6.1. The data for TPP are from [8].

Liquid designations are: (A) $2\mathrm{BP}_{87}/\mathrm{oTP}_{13}$; (B) 5-phenyl 4-ether; (C) $\mathrm{Ca(NO_3)_2 \cdot 4H_2O}$; (D) DC704; (E) diethyl phthalate; (F) m-fluoroaniline; (G) propylene carbonate; (H) salol; (I) m-toluidine; (J) triphenyl phosphite.
Grating spacings are: (1) 1.52 µm; (2) 1.75 µm; (3) 2.00 µm; (4) 2.35 µm; (5) 3.00 µm; (6) 3.65 µm; (7) 4.22 µm; (8) 4.87 µm.

Liquid	T_g(K)	ν_s(MHz)	v_s(m/sec)	ν_l(MHz)	v_l(m/sec)	m	m_{calc}
A	220	669^2	1171	611.2^7	2579	83 (84)	90
B	243 (236)	625.2^2	1094	666.8^6	2434	85 (65)	93
C	217 (212)	729.5^4	1714	750.3^8	3654	101 (79)	81
D	214	482.1^2	1133	486.4^8	2369	95	80
E	178	570.1^3	1140	593.6^7	2505	73 (62)	89
F	173 (172)	590^2	1033	584.3^7	2466	70 (127)	115
G	159.5	589^2	1031	618.1^7	2608	99	135
H	218	496.8^3	994	486.4^8	2369	73	114
I	187 (184)	620.2^2	1085	603.9^7	2548	78 (84)	109
J	208 (202)	640.7^1	974	785.5^5	2357	115 (98)	120

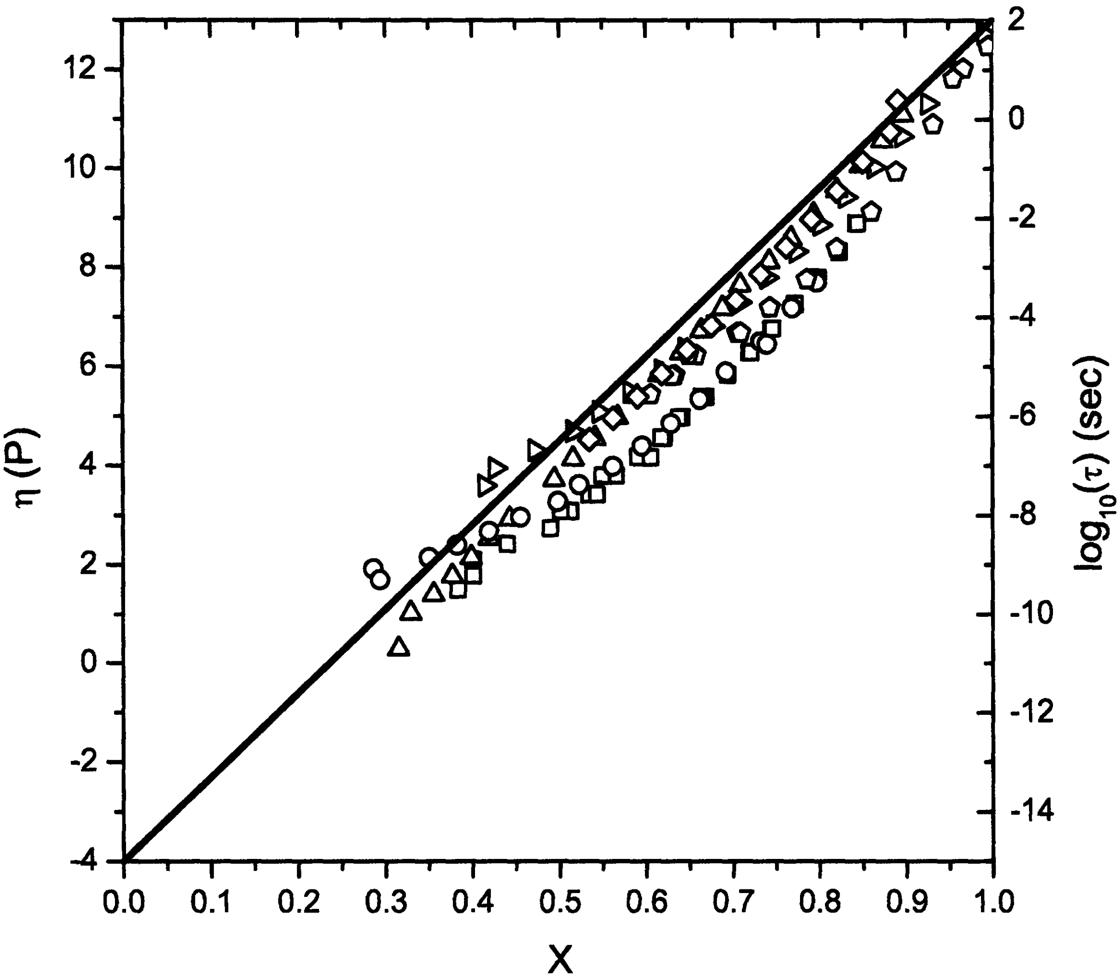

Figure 6-6: Test of the shoving model using mechanical relaxation data for the six liquids for which data were available: the 2-benzylphenol/o-TP mixture (□), 5-phenyl-4-ether (△), DC704 (▷), m-fluoroaniline (○), salol (◇), and m-toluidine (⬠). There are two scales, viscosity which only applies to 5-phenyl-4-ether, and average relaxation time, which is relevant for the rest. X is obtained from our measured values of $G_\infty(T)$ via equation 6.4, while $\tau(T)$ and $\eta(T)$ are from literature VFT mechanical relaxation fits. The straight line represents Arrhenius activated kinetics, which would be either $\log_{10}(\tau) = 17X - 15$ in terms of average relaxation time or $\log_{10}(\tau) = 17X - 4$ in the case of the viscosity.

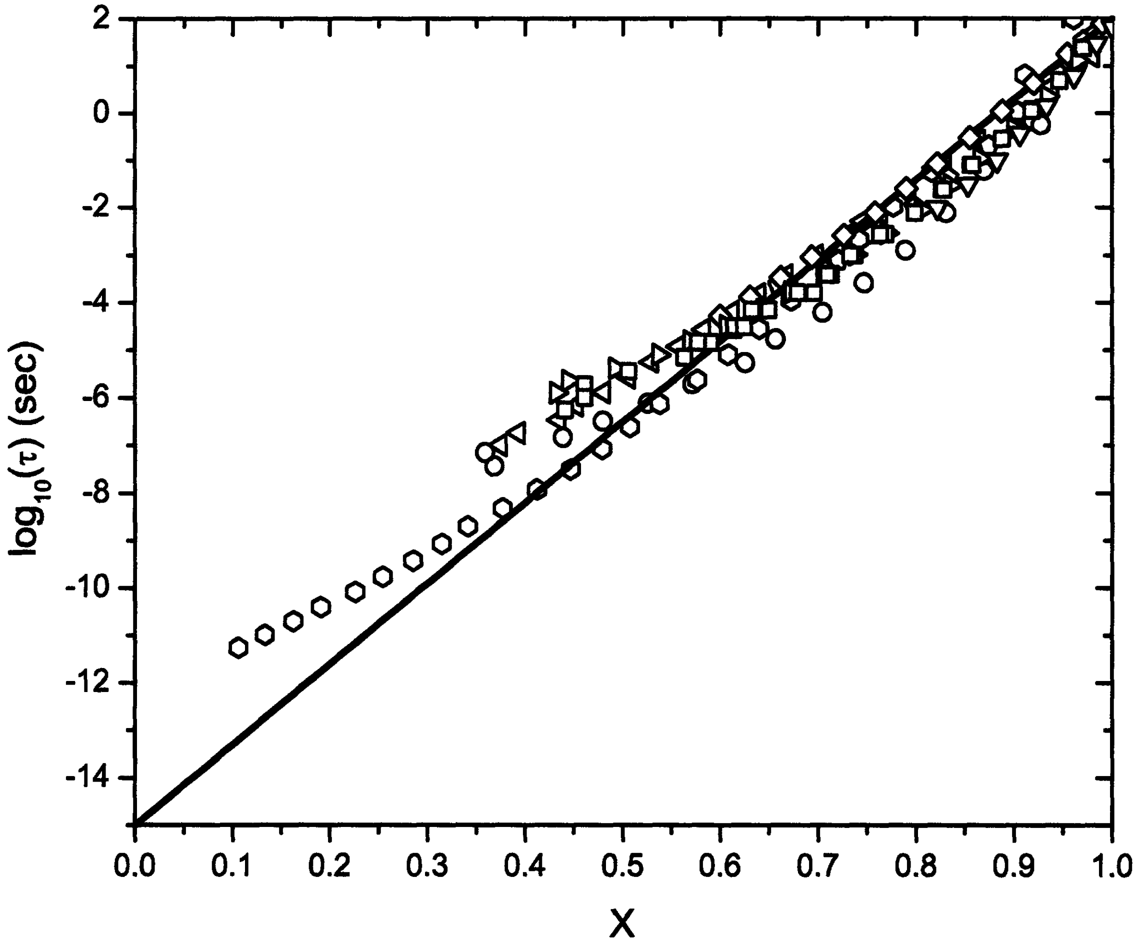

Figure 6-7: Test of the shoving model for 8 glass forming liquids using dielectric data: the 2-benzylphenol/o-TP mixture (□), $Ca(NO_3)_2 \cdot 4H_2O$ (▽), DC704 (▷), diethyl phthalate (◁), m-fluoroaniline (○), salol (◇), m-toluidine (⬠), and triphenyl phosphite (⬡). As before, X results from using this work's measured value of $G_\infty(T)$ in equation 6.4, and $\tau(T)$ comes from literature VFT fits of the average relaxation time measured in dielectric experiments. The straight line is a plot of $\log_{10}(\tau) = 17X - 15$, which represents Arrhenius activated kinetics.

prompted us, in cases where this information was not available, to assume linear contraction using the thermal expansion coefficient at room temperature [73, 74]. By comparing linear approximations to full forms for the density for TPP and diethyl phthalate, the uncertainty in the linear assumption was determined to be on the order of 5% .

To obtain the average relaxation time, we have used fits to the Vogel-Fulcher-Tammann (VFT) relationship

$$\tau = \tau_0 exp\left(\frac{B}{T - T_0}\right) \tag{6.14}$$

as obtained in the literature [86, 111, 114, 115, 116, 117, 118, 119, 120, 121, 122] for both dielectric and mechanical degrees of freedom. These VFT fits are also the source of our values of T_g, and in all cases, great care was taken to ensure that this form fit the data over the range of temperatures examined. As discussed above, if the predictions of the shoving model are borne out in practice, the points from the various liquids should fall on the straight line $\log_{10}(\tau) = 17X - 15$ indicating that the temperature dependence of the activation energy arises from that of the shear elastic modulus.

Most of the points from our measurements come close to resting upon a straight line in both cases, yet they still include some amount of non-Arrhenius activated behavior, especially in the glass formers m-fluoroaniline and triphenyl phosphite. To quantify the shoving model's departure from ideal, we have computed the root mean squared error Δ of the model from the observed behavior as

$$\Delta = \sqrt{\sum((17X_{obs} - 15) - \log_{10}(\tau))^2/N} \tag{6.15}$$

where X_{obs} is the observed value of X for the given liquid, τ is the observed relaxation time, and N is the number of points recorded.

The results of this analysis are presented in Fig. 6-8. Clearly, in the case of the dielectric measurements, the higher the degree of measured fragility, the greater the departure from the predictions of the shoving model. We have not observed the

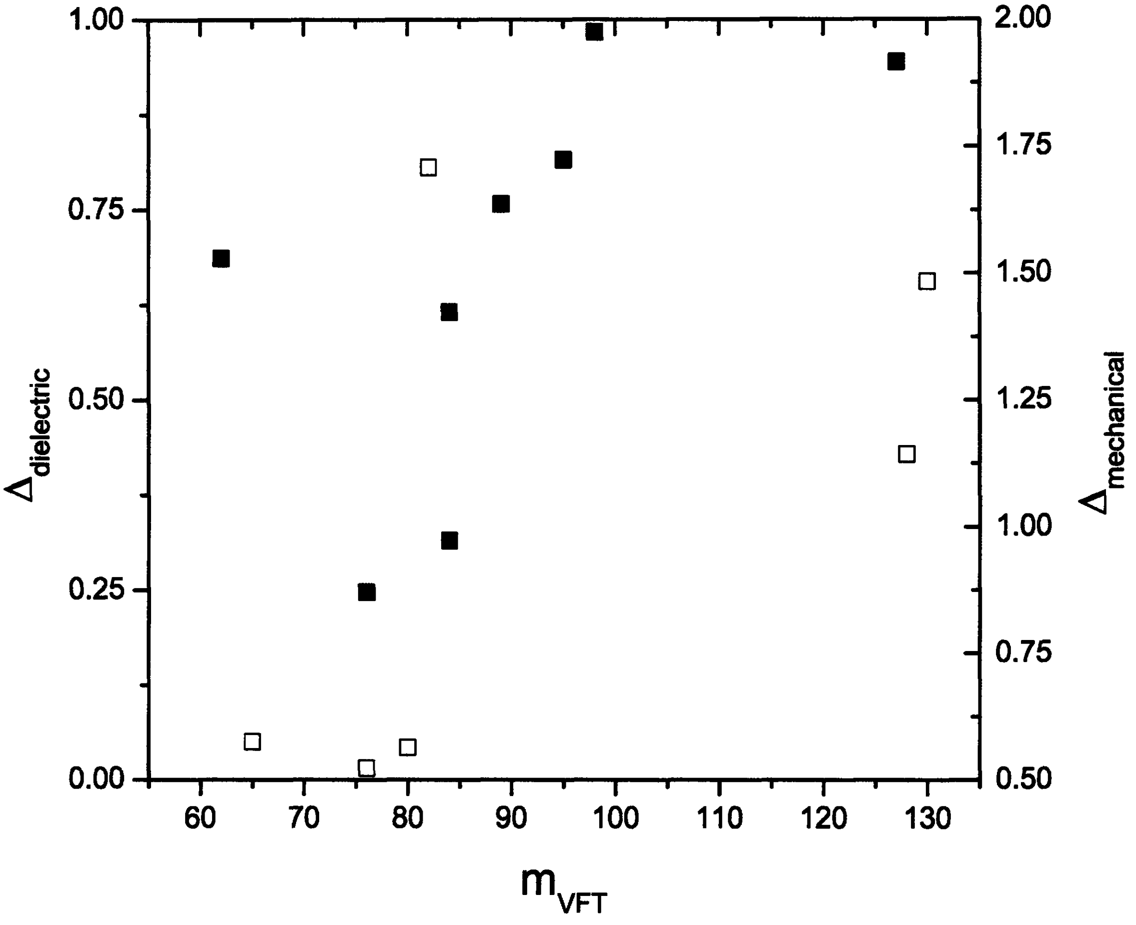

Figure 6-8: Correlation between deviation from the shoving model and fragility computed from VFT fits. The clear positive trend in the dielectric data suggests that the model does not fully encapsulate the dynamics of the glass transition as seen from dielectric relaxation. The inset shows the same plot for the mechanical data, for which no such correlation exists.

same trend in the departure of the shoving model from ideal for the mechanical data. Efforts in the past to link these two degrees of freedom [107, 123, 124] have found that qualitatively, there is physical grounds for a definite relationship, but making such a connection quantitative is tenuous at best. Therefore, we can only conclude that the model is progressively more in disagreement with dielectric measurements as the fragility increases.

With Fig. 6-9 we show a plot of the measured ratio $K_\infty/G_\infty - 4/3$ versus the fragility index m. Where possible, we have taken the temperature dependent average relaxation times and computed the fragility as

$$m = \left(\frac{d\log(\tau)}{dT}\right)_{T=T_g} \tag{6.16}$$

directly from the VFT literature fits. T_g was defined as a relaxation time of $\tau = 100$ s.

Our data show considerably more scatter than those used in [48], and we show the points used therein for comparison. Owing to the extremely good signal to noise ratio in both polarized and depolarized components of all of our measurements, we consider that any scatter due to measurement error arises from determination of the fragility – our uncertainties are in K_∞/G_∞ are computed to be ± 0.05 based on error propagation of the uncertainties in the grating period and acoustic frequencies. In an effort to remove the scatter in fragilities, the values for m used for this plot were all derived from the dielectric VFT fits used in the test of the shoving model. Here, too, the uncertainties are low. For the three VFT variables $\log_{10}(\tau_0)$, B, and T_0 as represented in the equation 6.14, typical errors were on the order of ± 3, ± 200, and ± 5 respectively.

We have also included salol and m-toluidine in our study to serve as points of comparison between our data and that used by Novikov et al. Our m-toluidine data yield the same shear acoustic velocity for the glassy state as [114] to within 1%, yet we obtain a slightly higher longitudinal velocity. As our results are almost two orders of magnitude higher in frequency, they may avoid secondary relaxation features that have been observed in m-toluidine [125] which may skew the acoustic results.

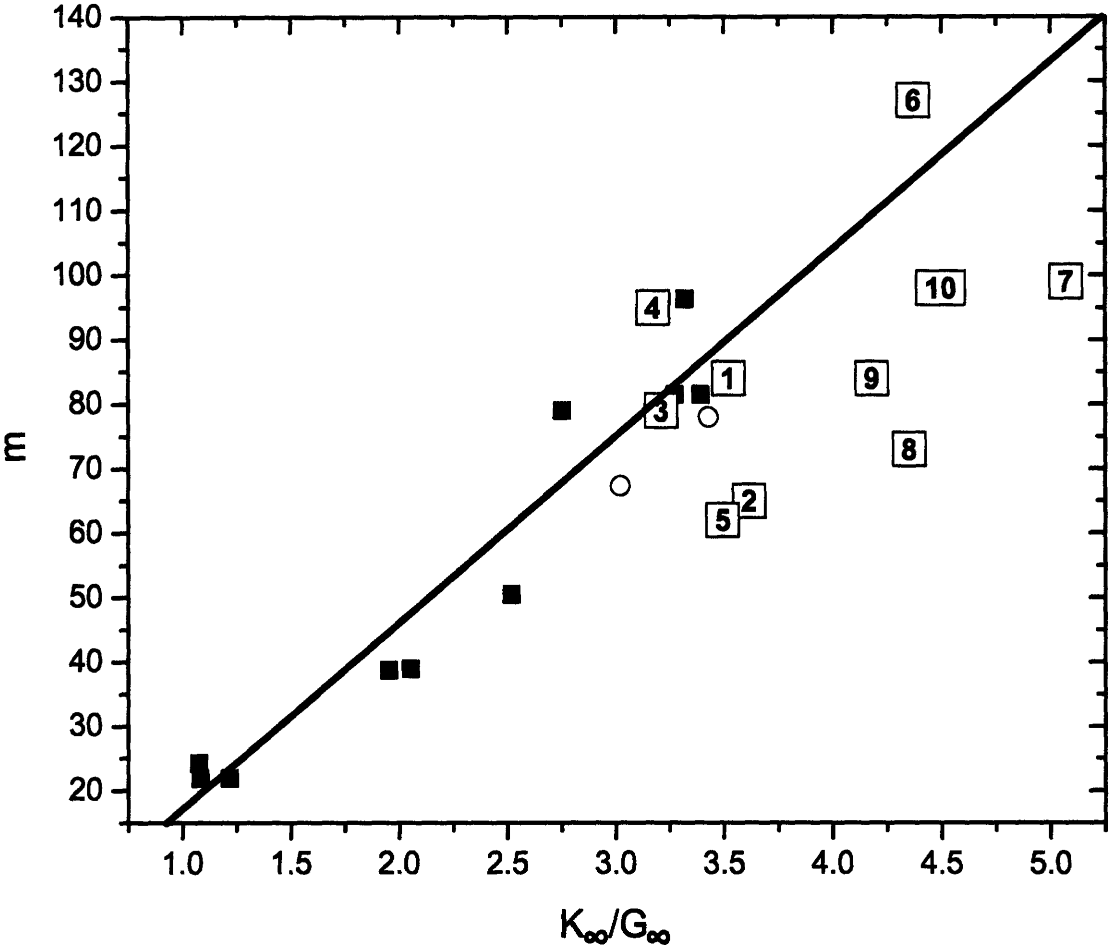

Figure 6-9: Plot of the fragility index m versus K_∞/G_∞ for a variety of glass forming systems. Those points denoted by ■ are from [48], while those depicted by numerals are from this work. The two points represented by ○ are liquids in common between this work and [48], specifically, from left to right, m-toluidine and salol. The numerals are: 1. $2BP_{87}/oTP_{13}$, 2. 5-phenyl 4-ether, 3. $Ca(NO_3)_2 \cdot 4H_2O$, 4. DC704, 5. diethyl phthalate, 6. m-fluoroaniline, 7. propylene carbonate, 8. salol, 9. m-toluidine, and 10. triphenyl phosphite. There is considerably more scatter in the measurements from this work. We consider this to be real, as the uncertainties in our values are much smaller than the scatter in the plot.

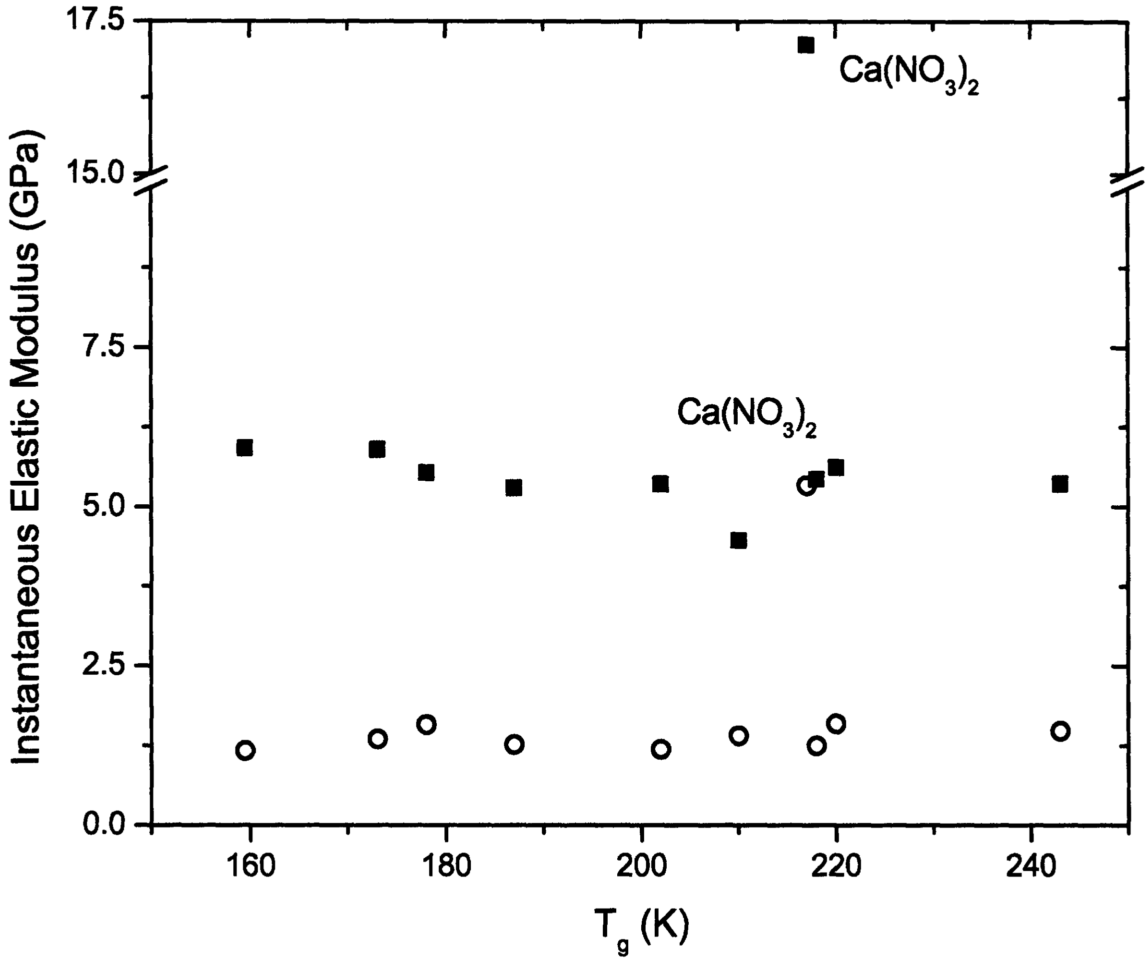

Figure 6-10: Plot of the instantaneous elastic moduli K_∞ (■) and G_∞ (○) for the glass formers studied here. There is no clear dependance of either of these quantities on T_g. Of note is the significant outlier posed by the sole ionic glass former $Ca(NO_3)_2 \cdot 4H_2O$, which is discussed briefly in the text.

Our salol data are in agreement with literature values used for the longitudinal wave [126], yet the shear velocity we observe is significantly lower than that used in [48]. Since our longitudinal and shear data were taken at the same time and temperature, and at very similar frequencies, we believe that this difference is much larger than the margin of error in our experiments.

A more direct test of the predictions of reference [48] would also involve testing the individual assertions underlying the derivation of equation 6.1. The most immediately available is the linear dependence of the instantaneous elastic moduli on the glass transition temperatures. A plot G_∞ and K_∞ vs T_g using our data is shown in Figure

6-10. It is clear that there is at best a weak linear dependence of both of these elastic properties on the glass transition temperature T_g. The most striking feature of the results is how similar all the modulus values are. A large departure from this trend is demonstrated by $Ca(NO_3)_2 \cdot 4H_2O$, a material that displays significantly stiffer elastic properties likely due to its higher density compared with the rest of the liquids under consideration.

Our efforts to enforce consistency and provide points of reference in the relationships used in Fig. 6-9 have only introduced more disagreement between the proposed relationship eq. 6.1 and the results based on our data. These problems are, in fact, exacerbated by using liquids already present in the original study. Hence, we cannot support the simple linear form suggested in [48] unless selective choices of both the fragility and acoustic velocities are made in the literature. We suggest that to examine the relationship in a more systematic fashion, further elastic results need to be compared with fragility results from mechanical relaxation experiments taken with the same samples and apparatus.

In terms of the theoretical work of Priya and Das, our results may indicate either that the choice of a single upper wavevector cutoff for density fluctuations is not justified across a broad selection of liquids or that the hard-sphere model on which the treatment is based is inadequate to describe all the liquids studied here.

6.6 Conclusions

We have performed a systematic investigation of the Poisson ratio of several glass forming liquids, and measured the evolution of the shear elastic modulus from T_g to as deeply as permitted into the melt. The shoving model of the glass transition is generally supported by our data when used in conjunction with literature data on average relaxation times in glass forming liquids. We find that the deviations from the model describing the non-Arrhenius dependence of the relaxation time on temperature increase with the fragility of the liquid for dielectric degrees of freedom, suggesting that other degrees of freedom besides G_∞ are fundamental to the transition. No such behavior is observed for the mechanical degrees of freedom.

We observe a considerable amount of scatter in the plot of m vs. K_∞/G_∞ beyond what was originally present in [48]. It is still unclear if the source of this scatter is from measurements of m by the variety of methods utilized, or if the correlation is more fundamentally called into question. We suggest that to remove this scatter, more consistent fragility measurements could be used in tandem with the above reported elastic parameters.

Our studies have been primarily focused on aromatic compounds, both van der Waals and hydrogen bonded. A more complete test of the correlations of these parameters would involve the study of ionic systems and also studies of network glass formers at high temperature.

The experimental data reported here show the capability for determination of both shear and longitudinal acoustic properties of glass-forming liquids in the MHz frequency range. Complementary methods have been developed to permit study of GHz frequency acoustic responsed [72]. This opens up the possibility of determination of the mechanical relaxation spectrum across all of these frequencies. Work towards this objective is underway.

The author would like to thank Tina Hecksher for useful discussions and Joshua Lessing for assistance with sample preparation. This work was supported in part by NSF grants CHE-0616939 and DMR-0414895.

Chapter 7

Further Applications of Impulsive Stimulated Scattering

7.1 Introduction

Impulsive Stimulated Thermal Scattering finds a variety of uses outside of the realm of supercooled liquids. Here we will briefly review the other applications of this technique as it has recently advanced the understanding of a variety of different systems, and we will provide an outlook of how these methods and results can impact the study of glass forming liquids.

7.2 Studying Liquids Under Shock Loading[1]

7.2.1 Introduction

Here, we will discuss a novel application of the Impulsive Stimulated Scattering technique in the study of simple liquids, where the mechanical properties of a liquid are examined in the "shocked" state. The term "shock loading" is used to refer to a unique state of stress and temperature imposed on a sample by the passage of a mechanical shock front through it. The shock front can be generated in a number of ways,

---

[1] Done collaboratively with Dr. Naoki Hemmi, Dr. Michael Winey, and Prof. Yogendra Gupta of Washington State University

ranging from mechanical impact of a projectile, to ablation of a layer attached to the sample by a high powered laser [127] to the highly exotic plasma Z-pinch approach implemented as Sandia National Laboratory's Z-machine [128]. In the present study, we concern ourselves with the"plate impact" experiment, defined by the imposition of a uniaxial strain by mechanical impact.

Depending upon the velocity of the projectile and the mechanical impedances of both target and impactor, one can use the Rankine-Hugoniot equations, which express conservation of mass, momentum, and energy

$$\begin{aligned} \rho_0 D &= \rho_1(D - u_1) \\ p_1 &= \rho_0 D u_1 \\ e_0 - e_1 &= \frac{1}{2} p_1(\rho_0^{-1} - \rho_1^{-1}), \end{aligned} \tag{7.1}$$

in tandem with an externally supplied equation of state for the material to deduce its final thermodynamic state [129]. Here, ρ is the density, D is the speed of the shock front, u is the local particle velocity, p is the pressure, e is the internal energy, and the initial and final states are represented by the subscripts 0 and 1, respectively (the sample is also assumed to be at rest and under negligible pressure prior to the shock). The portion of the phase diagram reached in this manner is generally inaccessible by other means, due to the unique combination of density, stress, and temperature.

The equations in 7.1 represent a set of three equations in five unknowns implying that experimental determination of two of these variables permits a complete description of the sample in the shocked state. Therefore, the traditional study of shocked materials involves the mapping of the "Hugoniot" curve, which is the locus of end states of a liquid upon a series of shock experiments; this curve may be represented in the two-dimensional space of any pair of the variables from 7.1. The most conveniently measured variables are the particle velocity u, which is a measure of the velocity of the shocked material in the wake of the shock front, and the shock wave's speed, D. Single shot measurement of the former is elegantly performed by the use of the VISAR interferometric technique [130], while determination of the latter proceeds by recording the time from impact to observation of the shock on the back end. Given the Hugoniot curves of samples of interest, it is possible to deduce the pressure given an initial projectile speed.

7.2.2 Experiment and Results

The setup used for this experiment differs from the ISTS experiments described previously due to the destructive nature of the measurement. The sample sits at the end of a 44'-long gun, and the shock excitation is created by the impact of a 4"-diameter, 12'-long, hollow barrel of aluminum. This ballistic projectile is normally incident on a sample at velocities ranging anywhere from 400m/sec to 2.5km/sec. Since the sample is destroyed by the impact, it is important that the experiment be carried out in a single shot, in contrast to the rest of the results presented in this thesis, where the data are the results of thousands of averaged traces. It is also not possible to position the detector on the far side of the sample; instead the signal is reflected by a mirror that forms part of the sample cell, and transmitted back through the original imaging optics to a pick-off mirror that relays the signal and reference fields to the detector. Great care is also taken to ensure that the impact between projectile and target is completely planar, typical tolerances being on the order of 1-2 milliradians; larger amounts of "tilt" will cause the beam to walk off of the detector upon impact and ruin the measurement.

The laser is run in an external-trigger mode, where the seeding of the amplifier occurs upon the impact of the projectile on a trigger pin extended a predetermined distance from the target. The offset of this pin is set by the speed of the projectile, the build-up time of the amplifier, and the delivery time of the amplified pulse to the sample. Triggering of the detection electronics is achieved by a photodiode monitoring the output of the laser. Timing performed in this manner is generally accurate to within 10 ns.

Benzene was selected as the target liquid due to its large ISTS signal levels, ease of loading (i.e. low viscosity), and wealth of prior knowledge of its shocked and static high-pressure properties [132]. Further, the question of whether or not benzene

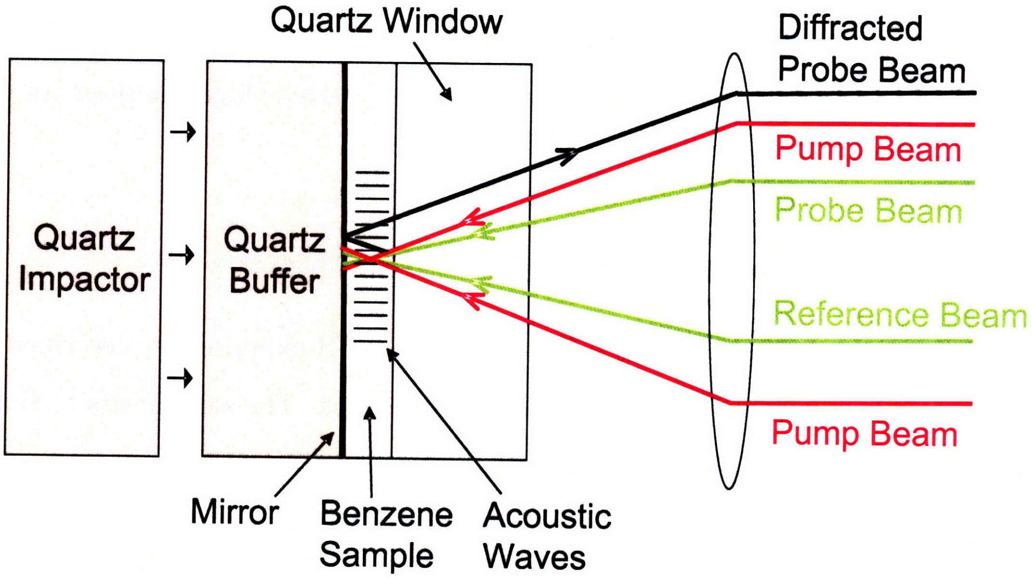

Figure 7-1: Schematic illustration of setup used in single-shot shock-ISTS experiments. The projectile is incident from the left, precluding the placement of optics on that side of the sample. A mirror incorporated as part of the sample cell serves to return the beams to the same side from which they are delivered. Figure from [131].

crystallizes under shock has been approached by a number of different authors [133, 134] in differing fashions, and a definitive answer based on hard evidence is lacking. A method which directly probes the mechanical properties could resolve this issue.

Examples of the signal from such an experiment is shown in figure 7-2. The data show an excellent signal-to-noise ratio that permits easy analysis. There is an initial jump of the signal which we attribute to changes in alignment from passage of the shock front through the mirror. As the shock front progresses through the benzene, there is a growing in of signal at a higher frequency, which is that of the shocked liquid. The spectral content of this trace is shown in figure 7-3, where a shift by nearly a factor of two is shown. It is worthy of mention that another measurement at a lower pressure indicates a shift by a number that is not close to a factor of the original frequency, indicating that this change in frequency is not due to the appearance of a homodyne signal component; homodyne signal would be at exactly twice the frequency.

Experiments of this kind were performed at two pressures: 0.42 GPa and 0.85 GPa, whose values were determined from benzene's Hugoniot curve in the manner described above. The measurements were redone a number of times in order to ensure repeatability. The experiment could not be performed at higher pressures, as in these cases the silver mirror on the sample cell would peel off of the front window resulting in the disappearance of the signal. Unfortunately, this precluded looking for a phase transition that has been reported to occur at ~ 2.5 GPa [134]. Nevertheless, we were able to compare our results with those taken at static high pressure where benzene crystallizes at 0.7 GPa. For the static high pressure measurements, liquid benzene was loaded into the cell and the pressure repeatedly cycled in order to "grow" a single crystal. ISTS measurements were then conducted in order to form a basis of comparison with the shock measurements.

This comparison is shown in figure 7-4. There is a clear difference between the shock and static high pressure results. The nearly factor of two difference between the speeds of sound in the two states is not attributable to the modest increase in temperature that the benzene undergoes as a result of shock loading. We can conclude from this that the benzene is not crystallizing at these shock pressures. Due to the comparatively low speed of sound at this pressure, and the absence of any marked change in damping behavior, we may simply deduce that, in addition to not crystallizing, the liquid has also not vitrified at these modest pressures.

7.2.3 Future Directions

The potentials for single-shot ISTS spectroscopy in the study of glass-forming liquids are myriad. In the process of initiating a shock in a liquid is the pressure equivalent of rapid thermal quenching – therefore, these measurements may form a method by which to study structurally arrested liquids that would otherwise crystallize under conditions of slowly increased pressure. Additionally, the theoretical description of glass-forming liquids under both linear [135] and nonlinear [136] externally imposed stresses and strains is in a nascent stage that lacks experimental verification. Further studies of this kind will be able to provide much needed input.

This work was supported by ONR MURI Awards N00014-01-1-0802 and ONR

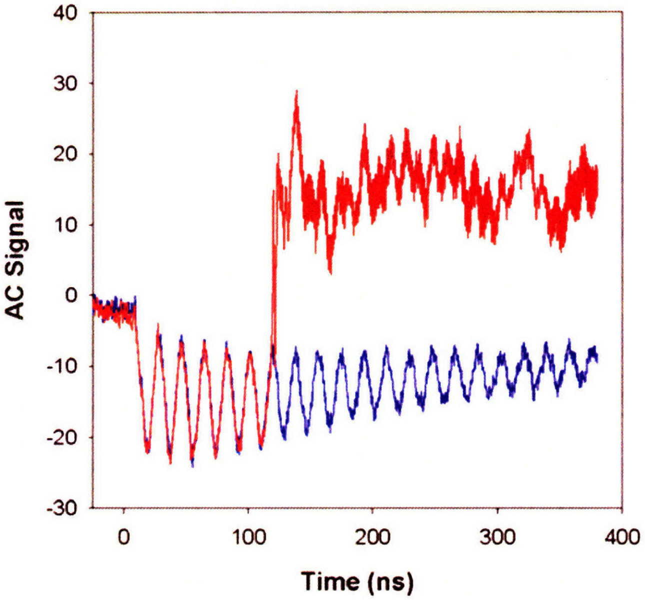

(a) Acoustic waves in benzene under shock loading at 0.42 GPa.

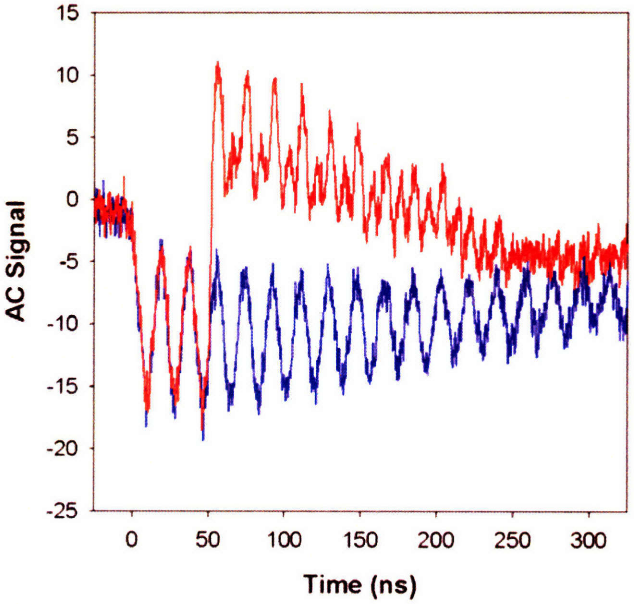

(b) Acoustic waves in benzene under shock loading at 0.85 GPa.

Figure 7-2: Acoustic waves in benzene under shock loading. The blue trace is from the unshocked sample, and the red trace is the one taken during a shock experiment. After the arrival of the impactor, there is a jump in the signal, likely due to a change in alignment. The liquid gradually shifts from unshocked to shocked as the shock front progresses through the sample. This is made evident by the diminishing of the original signal frequency and the growing in of the shocked signal frequency. Figure from [131].

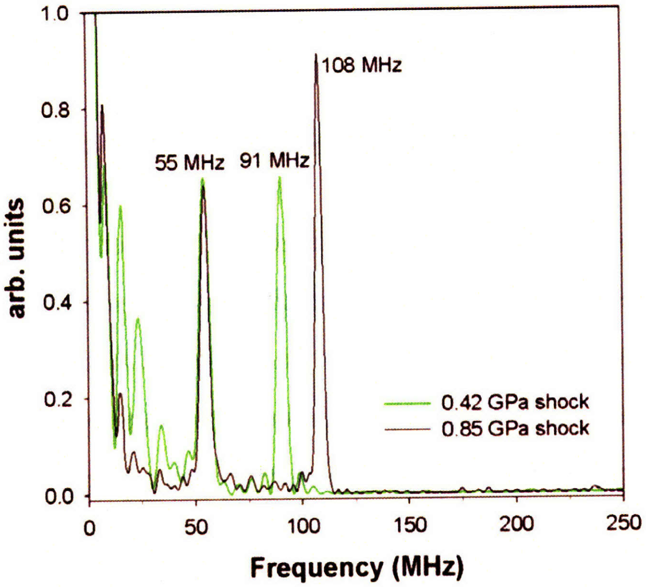

Figure 7-3: Fourier transform of signal from shocked benzene at 0.42 GPa and 0.85 GPa. In both instances, there are two distinct frequencies that appear in the shock experiment. The lower is due to the signal at ambient conditions, while the higher one is in the shocked state. Figure from [131].

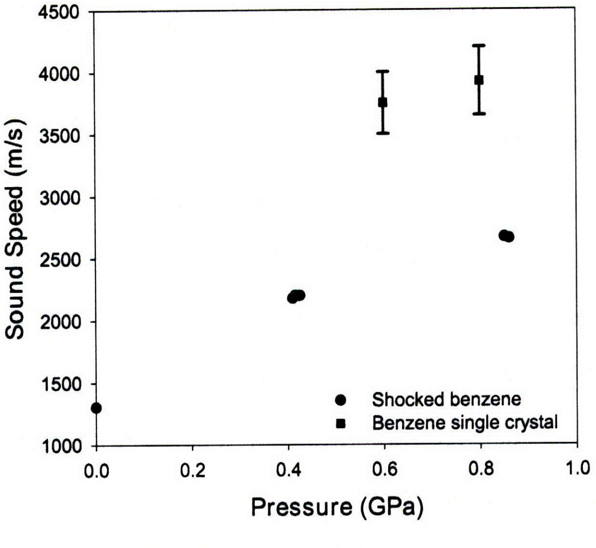

Figure 7-4: Acoustic velocities in benzene under static high pressure and shock loading for various pressures. The shock results are denoted by (•) and the static high pressure by (■). The brackets around the static high-pressure results denote the range of longitudinal sound speeds observed in the benzene single crystal. There is a clear discrepancy between the two different sets of data, indicating that, at the pressures reached here, the benzene did not crystallize or vitrify on the time scale of the measurement. Figure from [131].

MURI N00014-06-1-0459.

7.3 Characterizing Transport in Nanofluids [2]

The study of liquid-solid composites has gained recent attention for both fundamental and practical reasons [137, 138]. Apart from the relative ease of conducting numerical "experiments" on hard-sphere colloid solutions, these systems are deserving of study in their own right; many of the same phenomena that take place in simple glass forming liquids are also manifest in colloids, where the controlling parameter is the volume fraction ϕ instead of the temperature or pressure. Indeed, many of the predictions of even the Idealized Mode-Coupling Theory agree with dynamic light scattering measurements performed on colloids [139, 140]. The execution of Impulsive Stimulated Scattering studies on colloidal suspensions may thus be seen as a "proof of principle" for its application in testing theoretical predictions of MCT for these samples.

The experiments conducted here were centered on studying other aspects of these systems, in particular their thermal conductivity and both longitudinal and shear viscosities. Theoretical modelling of the shear viscosity of colloids as a function of volume fraction has been conducted extensively from a microscopic perspective [141]. At present, the best available method for predicting thermal transport of colloidal solutions is based on the effective medium theory work of Hamilton and Crosser [142]. This theory greatly underestimates their thermal conductivities, and this theoretical shortcoming is readily accepted in the present-day literature [143, 144]. Further complication arises from the fact that different measurements of thermal transport in these systems have produced inconsisten results.

Our choice of colloidal system is a simple liquid doped with nanometer-scale inclusions, i.e. a "nanofluid." For the studies conducted here, we have used alumina (Al_2O_3) nanoparticles, shown in figure 7-5, stabilized by the surfactant surbitan monolurate in host liquids of either decane or isoparaffinic polyalphaolefin (PAO). Both acoustic and thermal ISTS measurements were conducted on concentrations

---

[2] Done collaboratively with Jeremy Johnson, Aaron Schmidt, and Dr. Matteo Chiesa.

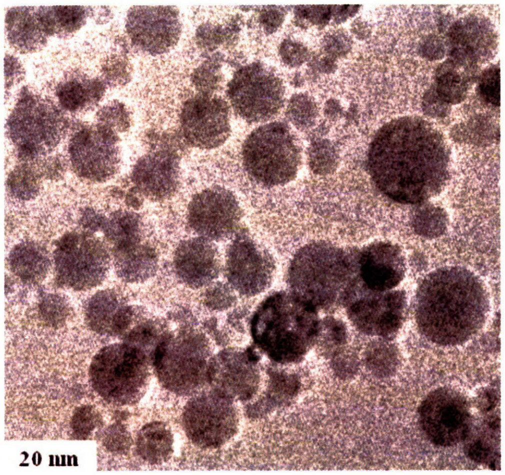

Figure 7-5: TEM image of alumina nanoparticles. From [145].

ranging from 0.15% volume fraction to a maximum of 1% volume fraction in both of these liquids. Higher volume fractions could not be studied, as the alumina nanoparticles are poorly index matched with the base fluids; bulk quantities of the suspension are opaque, even at the lowest concentrations used. To overcome this difficulty, we used a 200 µm thick cuvette for all the measurements and utilized the achromatic lens-based setup described in chapter 3. The grating spacings used here were between 2 µm and 6 µm, which is much smaller than the sample thickness. This preserves the one-dimensional nature of the measurement while allowing enough light through to enable adequate signal levels.

7.3.1 Thermal Conductivity Measurements

The primary interest in this portion of the study was to provide a consistency check between the "hotwire" technique [146] and measurements of the thermal diffusivity performed by Impulsive Stimulated Scattering. Two methods differing so much in execution likely do not share common sources of systematic error, suggesting that agreement between them would provide a strong indication of reliability.

In the hotwire method, the liquid is contained in a cylindrical pipe 19 mm in diameter and 190 mm in length. Within this pipe, a 150 mm long, 25 µm diameter platinum wire is connected to two copper electrodes. The wire is coated with a

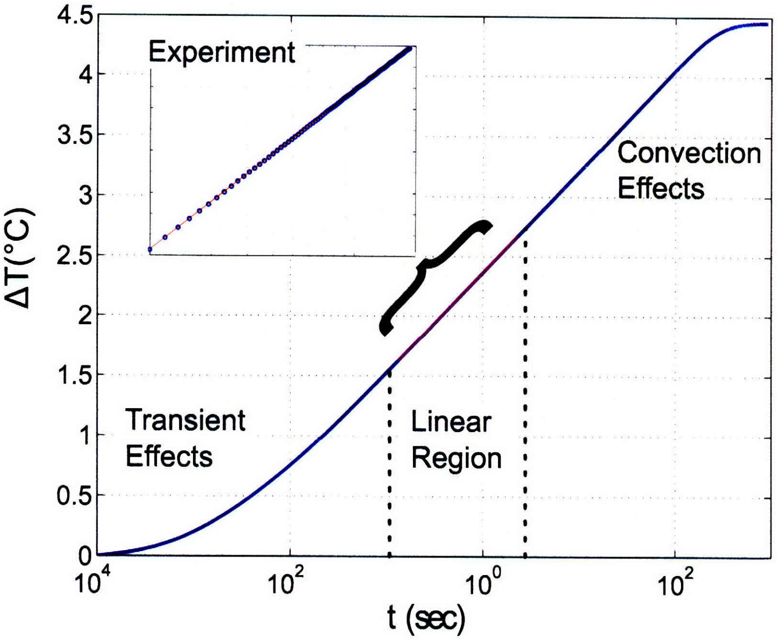

Figure 7-6: Simulation of the increase in temperature measured in a hotwire measurement. The inset shows actual data, taken between 0.1 and 2 seconds. From [145].

1.5 µm thick layer of isonel to provide electrical, but not thermal, isolation from the surrounding liquid. A current is passed through the the wire and the liquid is warmed via Joule heating. The thermal conductivity of the sample k_{nf} can then be directly determined through

$$k_{nf} = \frac{Q}{4\pi L \frac{dT}{d\ln t}} \tag{7.2}$$

where Q is the power dissipated, L is the length of the wire, T is its temperature (derived from accurate measurement of its resistance), and t the elapsed time. An example of both simulation and experimental data of this kind of experiment is shown in figure 7-6. In practice, data between 0.1 and 1 seconds is used; before 0.1 s, the data suffer from transient effects of thermal capacitance, and after 100 s, convection effects are manifest.

As described in chapter 3, ISTS data at long times show an exponential decay of the induced thermal grating, given by $\exp(-t/\tau_{th})$. Here, τ_{th} is a thermal relaxation time expressed in terms of the thermal diffusivity D_{th} and the grating wavevector q as

$\tau_{th}^{-1} = q^2 D_{th}$. In contrast to the hotwire technique, ISTS does not provide direct access to the thermal conductivity k which must be determined through the relationship

$$D_{th} = \frac{k}{\rho c_p} \tag{7.3}$$

where ρ is the density, c_p is the heat capacity, q is the grating wavevector, and the product ρc_p is known as the volumetric heat capacity. For ρc_p, we have used an effective value given by $(\rho c_p)_{nf} = \phi(\rho c_p)_{particle} + (1-\phi)(\rho c_p)_{fluid}$, where ϕ is the volume fraction of the nanoparticles; the heat capacities and densities of the individual constituents used here were taken from accepted literature values [147].

In principle, it is possible to determine the thermal diffusivity from a single transient grating experiment. However, in order to reduce experimental uncertainty in the measured value, we have chosen to make a series of measurements as a function of grating wavevector for each base fluid and volume fraction combination. The results of several measurements of the thermal decay time τ_{th} are plotted as a function of q^{-2} and the slope of this line provides a more accurate measurement of the inverse thermal diffusivity D_{th}. An example of this analysis is provided in figure 7-7.

The results for the thermal conductivity of the nanofluid k_{nf} at various volume fractions can then be compared with that of the base fluid k_f. The Hamilton-Crosser prediction for k_{nf} is expressed in terms of the ratio of these quantities by

$$\frac{k_{nf}}{k_f} = \frac{k_p + 2k_f - 2\phi(k_f - k_p)}{k_p + 2k_f + \phi(k_f - k_p)} \tag{7.4}$$

where k_p is the thermal conductivity of the nanoparticle.

In figures 7-8 and 7-9 we show the plots of experimentally determined values of k_{nf}/k_f from both techniques, as well as the predictions of the Hamilton-Crosser model. From analysis of our results, two important observations that can be made. First is that the hotwire and transient grating techniques appear to be quite consistent with one another, although we observe a slightly larger discrepancy at higher volume fraction. This is likely attributable to greater opacity at these larger values of ϕ – with less light getting through the sample, the ISTS signal-to-noise ratio was significantly

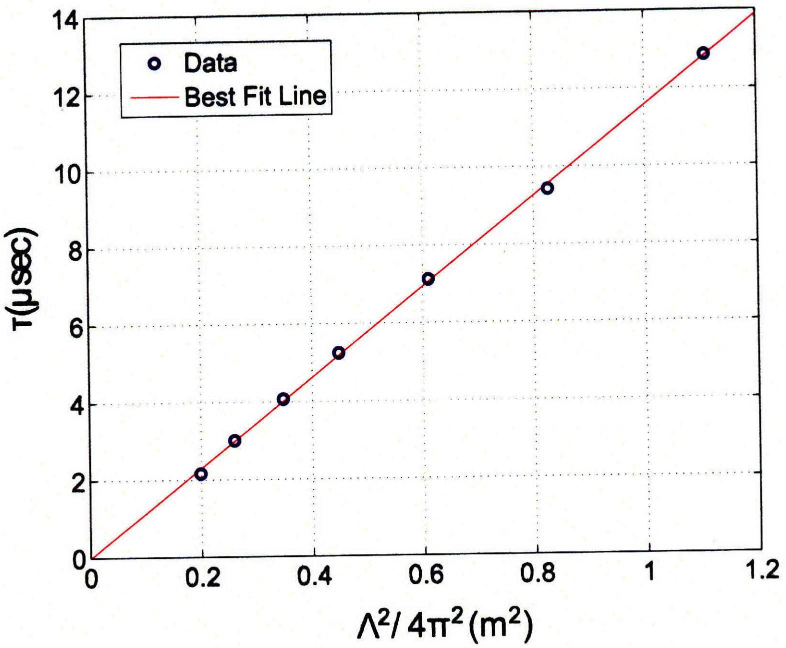

Figure 7-7: Plot of thermal diffusion time versus inverse grating wavevector squared. From [145].

decreased, which led to greater uncertainties in the values for k_{nf}.

The second observation is that both the transient grating and hotwire techniques show a marked enhancement of the thermal conductivity of the nanofluid beyond the predictions of the Hamilton-Crosser model. In the case of decane the relative thermal conductivity is 3.3 times greater than that predicted by the effective medium model, while for PAO the enhancement is by a factor of 1.6. Thus, transient grating spectroscopy has not only verified the enhancement of thermal transport in nanofluids, but has also provided accurate numerical values for the extent of this enhancement.

7.3.2 Longitudinal Viscosity Measurements

In prior chapters, we have used the measurements of the acoustic damping rate as a probe of the mechanical loss spectrum of the liquid being studied. As noted in chapter 3, however, structural relaxation is not the sole contributor to acoustic damping: equation (3.23) also bears contributions from the frequency independent viscosity,

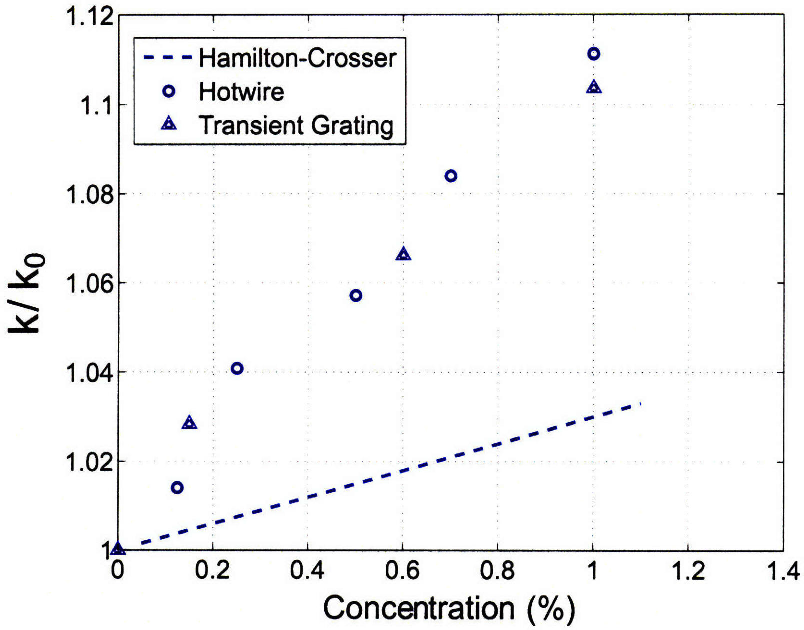

Figure 7-8: Relative thermal conductivity versus concentration in decane measured by transient grating and hotwire techniques. Both the hotwire and transient grating measurements show an enhancement of the conductivity relative to the Hamilton-Crosser theory. Results from the two methods are in good agreement. From [145].

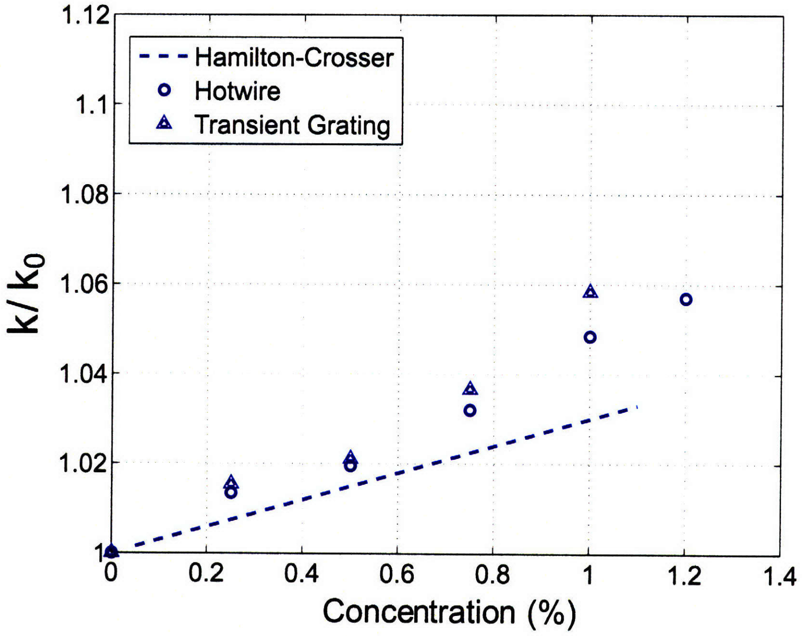

Figure 7-9: Relative thermal conductivity versus concentration in PAO measured by transient grating and hotwire techniques. Here, too, the hotwire and transient grating techniques show an enhancement of the conductivity relative to the Hamilton-Crosser theory. From [145].

as well as thermal diffusion. As before, the contribution to the damping from thermal diffusion is negligible since the nanosecond acoustic oscillation periods accessed through ISTS are much too fast for significant thermal diffusion to occur across the micron acoustic wavelengths. Since we may choose to operate in a temperature regime where the structural relaxation dynamics are far from our acoustic frequency regime, we are left with the frictional contribution to the damping: $\Gamma = \frac{1}{2}q^2\nu_L$. Here, ν_L is the "longitudinal" viscosity, which is defined by $\nu_L = \frac{4}{3}\eta + \kappa$, η being the shear viscosity and κ the bulk viscosity.[3] This quantity, in conjunction with a separate shear viscosity measurement, would thus be able to provide full information of the effects of nanoparticles on frictional damping in liquids.

While a number of acoustic measurements on colloids have been made [148, 149], in contrast with the present work, those systems of study have consisted of larger volume fractions and particle sizes than the ones presented here. Few measurements of the viscosity of such systems have been performed [150, 151, 152, 153], and even then, these have centered around the shear viscosity rather than the longitudinal viscosity accessible by the ISS technique.

Experimentally, we have proceeded by measuring the acoustic response of the liquid in tandem with the above thermal measurements, using the same samples, grating spacings and setup as described above and in previous chapters. The acoustic signals were fit to the form

$$A\exp(-t/\tau)\cos(\omega t + \phi) + B\exp(-t/\tau_{th}) \tag{7.5}$$

where A and B are amplitude parameters, τ is the acoustic decay time, and τ_{th} is the thermal decay time. ω is the acoustic frequency from which the acoustic velocity may be obtained, while ϕ a phase which results from a combination of ISTS and ISBS contributions to the signal.

---

[3] A careful reader of this thesis will note that the expression for the acoustic damping was derived using a hydrodynamic model, whereas with a colloidal suspension such an assumption may not be valid. We believe that the hydrodynamic approximation is still valid due to the fact that the average particle size is, on average, 2 orders of magnitude smaller than the shortest acoustic wavelengths accessed here. Further interpretation of the results are performed with a hydrodynamic model.

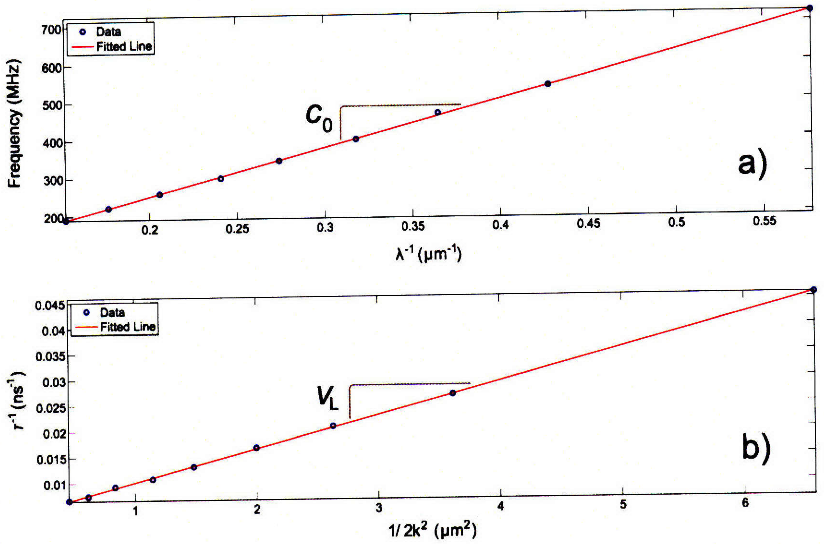

Figure 7-10: a) Plot of frequency vs. wavevector from which the isentropic sound speed can be derived. b) Plot of the damping rate vs. wavevector squared for 0.5%Al_2O_3. The slope of this line yields the longitudinal viscosity ν_L. From [154].

To obtain reliable measurements of the longitudinal viscosity, we applied the same rationale as was used for determining the thermal diffusivity: experiments were conducted at several grating spacings and the damping rate was plotted versus the quantity $1/2q^2$. The slope of this line gives the required result. This was also the approach taken for acoustic velocity measurements, where the slope of the line of the frequency versus the inverse wavelength provides the value of interest. Data from ISTS experiments on 0.5% Al_2O_3 in decane are shown in figure 7-10.

Measurement of the shear viscosity was performed at zero frequency using a commercial TA Instruments model AR-G2 controlled-stress rheometer. These results are shown in figure 7-11, along with the predictions of the Einstein model [155, 156]

$$\frac{\eta_{nf}}{\eta_f} = 1 + 2.5\phi, \tag{7.6}$$

which under-predicts the increase in shear viscosity with volume fraction. A more accurate prediction proposed by Prasher et al. [157] is given by $\eta_{nf}/\eta_f = 1 + 10\phi$, as shown within the figure.

A summary of all viscosity measurements for the base fluids is shown in table 7.1.

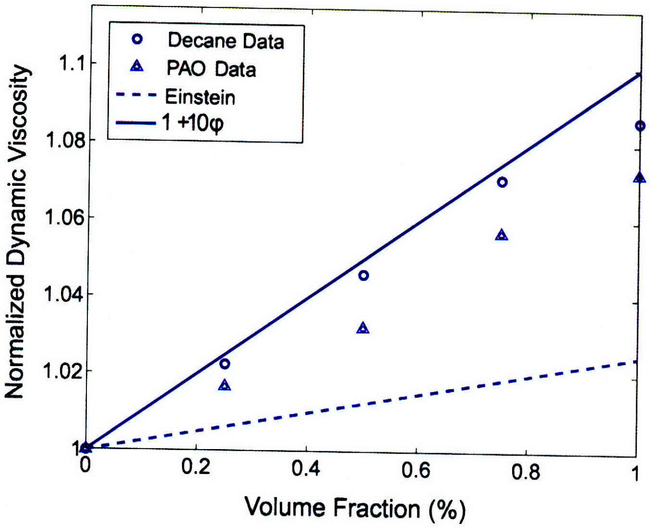

Figure 7-11: Zero-frequency viscosities for the liquids studied here. The values are significantly higher than the predictions of the Einstein model, while the expression proposed in [157] comes much closer. From [154].

Table 7.1: Measured Properties of Base Fluids. From [154]

Fluid	β $(\mathrm{Pa}^{-1}) \times 10^{-9}$	η $(\mathrm{Pa} \cdot \mathrm{s}) \times 10^{-3}$	ν_L $(\mathrm{Pa} \cdot \mathrm{s}) \times 10^{-3}$
Decane + Surf.	0.41	0.85	4.10
PAO + Surf.	0.74	30.0	32.3

The tabulated results can be used to derive the bulk viscosity $\kappa = \nu_L - \frac{4}{3}\eta$; the value for $\kappa = 2.54^{-3}$ Pa · s in decane is in good agreement with a previously measured value [158], while that obtained for PAO is found to be negative. At present, we do not have a definitive explanation for this anomaly; PAO is a multi-component oil and it is possible that mechanical relaxation processes that are active at low frequency are not present at MHz ISS acoustic frequencies. Other evidence, discussed below, points to a spuriously high value for the shear viscosity.

In the further analysis of our data, we have assumed that the attenuation of the acoustic wave is governed by the linear sum of the viscous decay of the base fluid $\nu_{L,bf}$ and a contribution due to the presence of the nanoparticles

$$\tau^{-1} = \frac{1}{2}q^2\nu_{L,bf} + \tau_{part}^{-1}, \tag{7.7}$$

allowing us to deduce the influence of the nanoparticles by subtracting away the portion due to the base fluid.

Such an approach allows a direct test of the model developed by Harker and Temple [159], which supplies an experimental prediction for the quantity τ_{part} from other easily obtainable experimental values. Here, the problem is approached by solving the hydrodynamic equations using conservation of momentum and mass between the base fluid and nanoparticles. We simply state here the result that the decay rate due to the nanoparticles is given by $\tau_{part}^{-1} = c \times \mathrm{Im}(q)$ where c is the speed of sound and

$$q^2 = \omega^2[(1-\phi)\beta] \times \frac{\rho_f[\rho_s(1-\phi+\phi S)+\rho_f S(1-\phi)]}{\rho_s(1-\phi)^2+\rho_f[S+\phi(1-\phi)]} \tag{7.8}$$

is the complex wavevector. In the above equation, ω is the measured angular frequency, ϕ is the volume fraction, β is the compressibility of the fluid, ρ_s is the density of the solid nanoparticles and ρ_f is the density of the base fluid. The quantity S is given by

$$S = \frac{1}{2}\left(\frac{1+2\phi}{1-\phi}+\frac{9\delta}{4a}\right)+i\frac{9}{4}\left(\frac{\delta}{a}+\frac{\delta^2}{a^2}\right) \tag{7.9}$$

with a the average particle radius and $\delta = \sqrt{2\eta/\omega\rho_f}$.

Expression 7.8 can be considered as defining a longitudinal viscosity due to the nanoparticles, $\tau_{part}^{-1} = 1/2q^2\nu_{L,part}$, meaning that using equation 7.7 we may write $\nu_L/\nu_{L,bf} = 1+\nu_{L,part}$. Thus, the predictions of the Harker-Temple model as a function of the volume fraction can be tested by plotting the experimentally determined ratio $\nu_L/\nu_{L,bf}$ for each sample using the measured shear viscosity. This is done in figure 7-12 for the different liquids studied here, where good agreement is found for the decane system. The same is not true for the PAO-based nanofluids, where the Harker-Temple model grossly under-predicts the longitudinal viscosity; as discussed above, the shear viscosity measured at DC frequencies appears to be spuriously high. This notion is supported by the fact that, when a lower value for the shear viscosity is inserted in the relation 7.8, much closer agreement between the Harker-Temple model and experimental data is obtained.

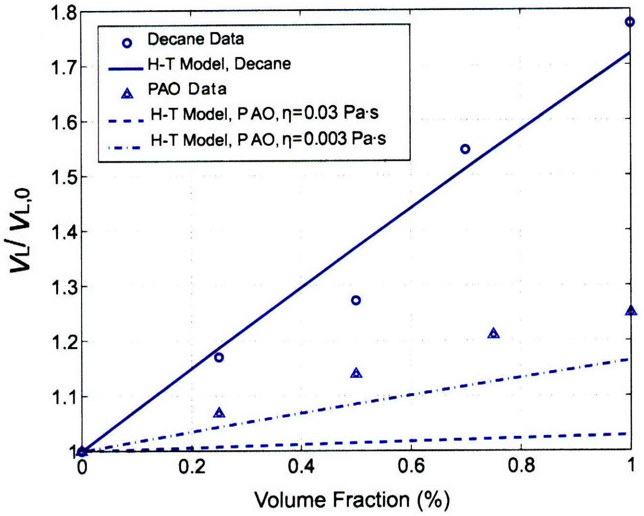

Figure 7-12: Bulk viscosity for volume fractions from 0.25% to 1.0%. There is fairly good agreement between experiment and the Harker Temple model for decane, but not for the PAO system. From [154].

7.3.3 Conclusion and Future Directions

The measurements described above clearly demonstrate the capabilities of ISTS as a viable technique for probing the transport quantities of colloidal systems. With ISTS, we have confirmed the anomalously high thermal conductivity displayed by nanofluids, and also determined their longitudinal viscosities. Future research may be centered on improved fundamental understanding of structural relaxation dynamics in colloidal solutions, including comparison to phenomenological models, numerical simulations, and mode-coupling theoretical predictions. This may require access to higher volume fractions. Although in this study it was not possible to conduct transient grating measurements at values greater than 1% due to the sample's opacity at the probe wavelength, possible solutions may be to seek base fluids and nanoparticles that are better index-matched to one another or to perform the experiment with longer wavelength light.

This work was supported in part by NSF grants CHE-0616939 and DMR-0414895.

7.4 Elastic Properties of Thin Film Multilayers [4]

One of the greatest successes for Impulsive Stiumlated Thermal Scattering has been its use in the characterization of multilayer thin films, in particular in the private sector, where an automated instrument has been developed that uses ISTS to generate surface acoustic waves (SAWs) in a multilayer thin film deposited atop a thick substrate. In these measurements, the excitation beams are crossed on the surface of the sample being characterized, creating a grating. As in the case of bulk liquids, the light is absorbed and its energy is rapidly thermalized, forming a modulation in temperature which in turn causes sudden thermal expansion, launching acoustic waves. Since this thermal expansion occurs at the surface, the resulting deformation is uninhibited in the perpendicular direction, and in addition to expanding against neighboring regions, the acoustic wave also bows outward in the transverse dimension. Being a combination of longitudinal and shear deformations, the surface acoustic wave thus encodes information about both the shear and longitudinal elastic properties of the material in which it is generated.

When the SAW is generated in a film whose thickness is of the same order as the wavelength of the acoustic wave, propagation takes place as an acoustic waveguide mode and is not only influenced by the elastic properties of film and substrate, but also by the film thickness. Characterization then proceeds by scanning the wavevector and building up an acoustic dispersion curve. Fits of this curve to well developed models [160] provide a non-invasive and highly accurate measurement of film thicknesses and elastic parameters. Among the systems most commonly studied in this manner are polymers , which share a lot of the phenomenology and relaxation behavior observed in glass forming liquids, and thin metallic films important in industry[161]. In general, multiple acoustic waveguide modes may be generated within a single layer or a multilayer structure. The theoretical understanding of SAWs generated in ISTS measurements on thin film multilayers has been worked out by Rogers, Duggal, et al. [160, 162] and a complete treatment is found therein.

---

[4] Done collaboratively with Gagan Saini and Dr. Thomas Pezeril

In general, SAW propagation is not only governed by the elastic properties of the substrate and deposited layers, but also by the same quantities in a semi-infinite adjacent medium. Depending upon the proper confluence of acoustic impedance between the substrate and adjoining medium, the elastic energy may even be confined to a bound-state interface wave, known as a Scholte wave [163], whose single-mode propagation is sensitive to the shear modulus of this adjacent material. In practice, this may be a glass-forming liquid. This approach has recently been exploited by Glorieux and coworkers [164], avoiding the experimental pitfalls in direct shear wave generation, specifically the need for a large polarizability anisotropy, as well as those associated with the linear q dependence of excitation efficiency. The main drawback of this method is the necessity to deconvolve the liquid's shear properties from the single Scholte oscillation frequency observed.

Experimentally, the application of ISTS to thin-film samples differs little in execution from the prior results presented in this thesis. Since the samples tend to be reflective, the measurement must be conducted in a folded geometry similar to the one described for shock measurements in section 7.2. In conducting these experiments, we have also found it convenient to excite the sample with ultraviolet light (specifically the fourth harmonic of the laser at 257 nm), where the absorption is greater, and to probe with 532 nm light. As there are no achromats available for this combination of wavelengths, we used reflective optics instead of lenses.

In the experiments conducted here, the samples of interest were a layer of PMMA deposited on a silicon wafer, a distribution of TiO_2 nanoparticles on a silicon wafer, and a multilayer system of alternating layers of these two materials as depicted in figure 7-13, bottom inset. The goal of this study was to determine the elastic properties of the composite system based upon an understanding of the individual constituent layers.

Figure 7-13 shows ISTS data from the multilayer structure, along with a TEM image of the sample. The data and their Fourier transform clearly reveal two prominent waveguide modes (and one weaker mode) beating against each other.

ISTS measurements were conducted at several different wavevectors, and acous-

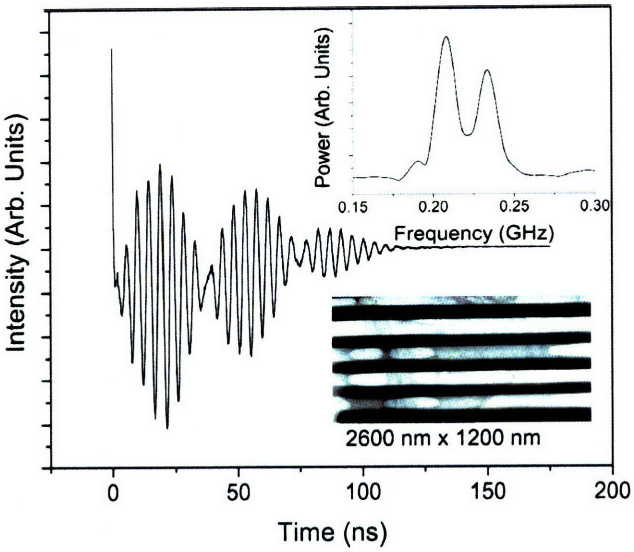

Figure 7-13: Surface acoustic waves in a PMMA – TiO_2 multilayer system, whose TEM image is presented in the lower inset. A Fourier transformation of the time domain signal is shown in upper inset and clearly shows the two frequencies which contribute to the signal. From [165].

tic dispersion curves were constructed for the two modes that contribute strongly to signals from the multicomponent system (see figure 7-14). From the fit to the dispersion curves, the effective density and elastic constant values of the composite were extracted. Multilayer organic-inorganic hybrid structures of the sort studied here are of interest for impact mitigation applications. The figures in Fig. 7-14 show that at the higher wavevectors examined, the group velocity of the lower-frequency mode is extremely low. This suggests a strategy for impcat and shock mitigation in which acoustic energy is split among waveguide modes with substantially different group velocities, spreading the energy out in the propagation direction and strongly reducing peak amplitudes to preventing or reducing shock formation and other nonlinear responses.

This work was supported by the United States Army through the Institute for Soldier Nanotechnologies, under Contract DAAD-19-02-D-0002 with the United States Army Research Office.

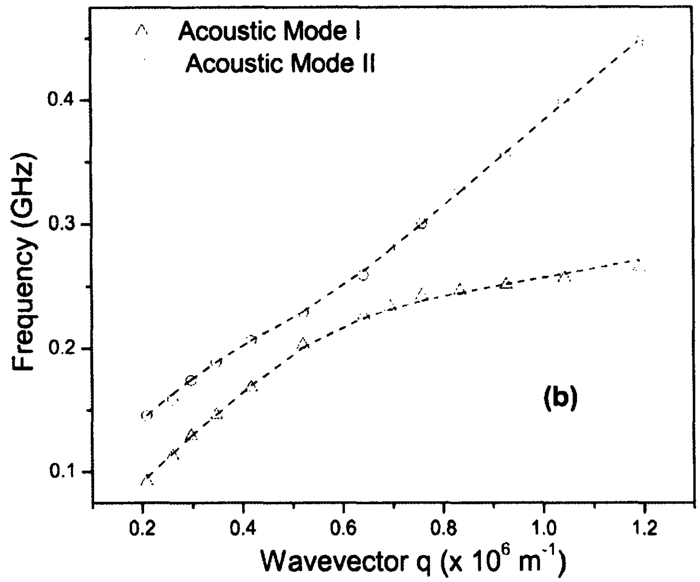

Figure 7-14: Acoustic dispersion curves in the multilayer system. Note the avoided crossing which indicates coupling between the acoustic waveguide modes. From [165].

7.5 Impulsive Stimulated Scattering at Higher Wavevector [5]

All of the experiments described above occur at $q \approx 0$. Measurements in this regime profit from easier analysis in the context of hydrodynamics, yet often fall outside the regime of much of the contemporary theoretical and computational work on liquids and other materials. Many new phenomena become apparent with acoustic wavelengths comparable to the length scales of $g(r)$, the two-particle distribution function. Atomistic computer simulations also are often limited to nanosecond timescales and nanometer length scales [16]. The need for shorter length and time scale measurements becomes even more conspicuous when confronting the issues of dynamical heterogeneities and correlated length scales in supercooled liquids.

To this end, acoustic measurements that reach towards the edge of the Brillouin zone become increasingly important. Traditionally, incoherent neutron [36] and inelastic X-ray scattering [37] have been the only ways to achieve the required wavevectors, presenting experimental challenges that reach beyond the need to bring samples

---

[5] Done collaboratively with Dr. Raanan Tobey of the Kapteyn-Murnane group at JILA.

to – and acquire time at – nuclear reactors and synchrotron facilities.

A few approaches that enable experimentalists to make these measurements on laser tables rather than at large-scale facilities have emerged in recent years. One that shows particular promise, which we simply reference [72], uses tunable pulse trains to measure narrowband longitudinal or shear acoustic waves at frequencies from 3 GHz to 300 GHz.

Another method that we shall briefly review here takes advantage of the recent advances in the field of high harmonic generation [166, 167]. In such experiments, an intense, short pulse of 800 nm laser light from a Ti:sapphire laser is focused into a gas jet. Multiphoton processes lead to the ejection of a frequency comb of the odd harmonics of the fundamental (even harmonics are symmetry forbidden), ranging from the 3^{rd} harmonic all the way up to the 35^{th} or higher. In principle, this light may then be used to perform many of the same experiments done in the visible regime, including transient grating measurements.

While a pure EUV-pump EUV-probe transient grating experiment has yet to be performed, great progress has been made towards this capability through a collaborative effort with the Kapteyn-Murnane group at JILA. Figure 7-15 presents the ISTS setup used in these experiments, which differs substantially from setups used in this thesis first in the way that probe light is generated and detected, and also in the back/front pump/probe geometry used.

Figure 7-16 shows data from surface acoustic waves in a thin nickel film on a silicon substrate recorded with this system. Although the probe light was derived from the 29^{th} harmonic of the amplified laser output, the data still show excellent signal to noise. The data provided from this experiment were analyzed in a similar manner as described above in section 7.4 to provide accurate measurement of the thickness of Nickel films. This analysis is displayed in figure 7-17, where the results are provided to a high degree of accuracy.

The significant advantage posed by use of such high frequency light, beyond the ability to probe smaller scale and faster dynamics, is its much greater sensitivity; diffraction efficiencies at these wavelengths are up to 700 times higher than at fun-

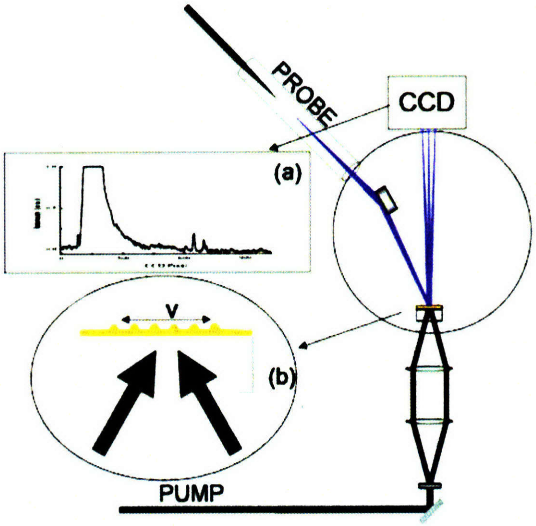

Figure 7-15: High wavevector EUV setup. The acoustic wave is generated in the thin film using either the fundamental, second or third harmonic of a Ti:sapphire laser and amplifier system. Probing is done from the other side using the 30 nm HHG output. The diffracted EUV light at a given temporal delay is then is collected on a CCD camera. Inset (a) shows a typical CCD output at maximum signal levels, and (b) provides a detail of the excited sample. Figure from [168].

damental [168]. While inadequate laser fluences may limit the intensity required to excite the sample, efforts to optimize the levels of HHG may lead to such experiments being routinely employable. This would advance the study of not only thin films, but also glass-forming liquids.

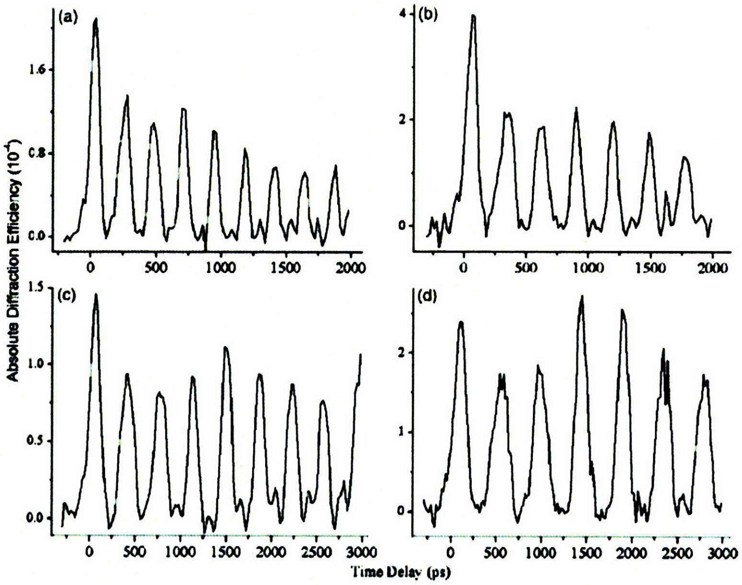

Figure 7-16: Data from a nickel/silicon sample recorded using the high wavevector EUV setup with four different acoustic wavelengths. The y-axis is the total diffracted light and the x-axis is the delay of the probe pulse with respect to the pump. The data correspond to grating spacings of a) 750 nm, b) 940 nm, c) 1.2 µm, and d) 1.5 µm. Figure from [168].

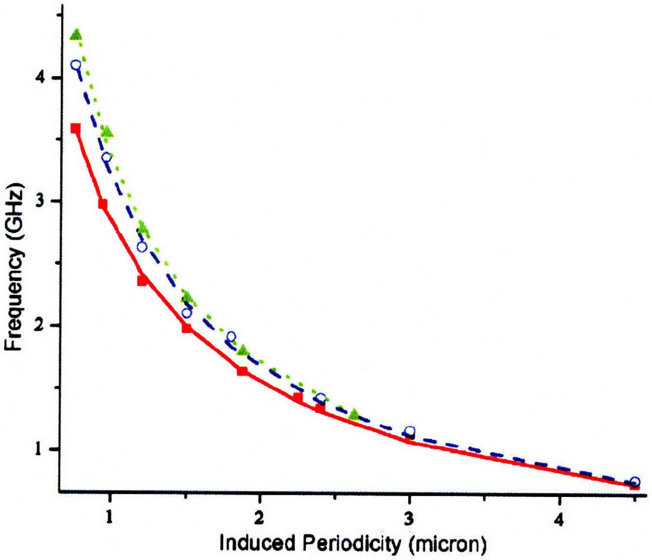

Figure 7-17: Nickel dispersion curves. The symbols denote the experimental data and the lines provide a fit to the acoustic dispersion curve. The filled squares with solid line correspond to a film thickness of 75 nm, the open circles with dashed line to a thickness of 29 nm, and the triangles with dotted line to a thickness of 12.5 nm. From [168].

Chapter 8

Conclusions and Future Directions for Research

In this thesis, we have used Impulsive Stimulated Scattering to characterize longitudinal and shear acoustic waves, time-dependent thermal expansion, and thermal diffusion in glass-forming materials. The results have been used for empirical characterization of structural relaxation dynamics and for testing of mode-coupling theoretical predictions. They also have been used to test models that relate the fragility of a supercooled liquid to the mechanical properties of the corresponding glass.

The longitudinal modulus spectrum of the glass forming liquid tetramethyl tetraphenyl trisiloxane (DC704) was characterized based on measurements of acoustic waves in the regime from 10 MHz to 1 GHz, and was fit by the Havriliak-Negami function. Direct time-domain measurements of nonexponential structural relaxation dynamics in time-dependent thermal expansion were conducted on nanosecond and microsecond time scales, and the results were fit by the KWW function. Comparison between the results showed that they were largely consistent in overlapping frequency ranges and that they could be combined reliably to provide longitudinal modulus spectra that covered about 5 decades in frequencies from roughly 10 kHz to 1 GHz. Time-temperature superposition of the spectra at different sample temperatures was observed to obtain the the high-frequency α relaxation exponent b. Relating it with the observed power-law behavior of the characteristic relaxation time given by γ, we were able to predict a value for the low frequency β relaxation exponent a. We also applied a mode-coupling analysis to our data and did not see evidence for a square-root cusp in our measurements of the Debye-Waller factor.

Initial results also showed the ability to generate and probe coherent shear waves in DC704, with the preliminary result that the shear degrees of freedom either do not share the same spectral exponents as, or relax at a significantly faster rate than the longitudinal spectrum. This conclusion can only be made firm with a separate, full characterization of the spectrum, which at present was not possible.

A more full characterization could be performed on the glass former triphenyl phosphite, where we have built upon prior measurements in order to build a shear relaxation spectrum spanning nearly two decades in frequency. Using this information, we were able to measure the evolution of the characteristic shear relaxation time with temperature. Our results indicate that it does not follow that of the longitudinal relaxation time for the temperatures in which we could observe it.

We have also been able to use this information to test for a growing length scale required for shear wave propagation. Motivated by the arguments of [44] derived in the idealized mode-coupling theory for hard spheres, we have fit the length scale to a power law, from which we obtain an unusually high exponent of 15. We also observe critical behavior in the temperature dependence of the longest wavelength for underdamped shear wave propagation. The critical temperature is almost identical to the glass transition temperature and the centimeter wavelength scales reached as this temperature is approached from above are much too large to be meaningful in terms of any diverging structural correlation length scale.

Our test of the "shoving" model of the glass transition [10, 90] on nine separate glass forming liquids supports its view that the non-Arrhenius evolution of relaxation time with temperature is governed by the temperature dependence of the instantaneous shear modulus. Nevertheless, these same measurements called into question other arguments which derive from this model and link the fragility of the supercooled liquid state to the elastic parameters of the corresponding glass [48, 96].

Finally, we demonstrated the versatility of the Impulsive Stimulated Scattering technique in its ability to examine systems under shock on a single-shot basis, as means to determine transport quantities in nanofluids, and as a method by which to derive mechanical properties of thin film multilayers.

8.1 Further Directions

To date, broadband shear measurements utilizing ISS methods have only been performed on TPP. In chapter 6, we showed that the shear behavior of a variety of liquids may be studied with this technique. A particularly good candidate is 5-phenyl 4-ether, which showed excellent shear signal and never crystallized. Although we were not able to do so, prior work on salol indicated that it was possible to prepare this liquid in a stable form that avoids crystallization [57]. It, too, has shown excellent depolarized ISBS signal, and thus warrants future study. Salol carries the advantage of being well studied by other researchers and so it may facilitate comparisons between ISBS results and those of other spectroscopies, in particular dielectric relaxation.

Studies of the glass transition have most commonly been performed using temperature as the control variable, yet a very fundamental question remains in the study of these liquids: what are the separate roles of the change in density and the change in kinetic energy when the system is cooled? The answer to this question may be approached by using pressure as a control variable in addition to temperature. There has been a recent burgeoning in this field led by the work of Paluch [169, 170], as well as Casalini and Roland [171, 172], among others. In [171, 172] it is proposed that a thermodynamic scaling of the characteristic relaxation time in terms of the density and temperature

$$\tau(T,V) = \tau_0 \exp\left(\frac{C}{TV^\gamma}\right) \tag{8.1}$$

where C and τ_0 are system constants, and γ is an exponent which measures the degree of anharmonicity of intermolecular interactions. Plotting the characteristic relaxation time τ versus $1000/TV^\gamma$ was shown to permit data superposition onto a single plot for all liquids examined in this fashion. However, verification of this relationship has only been performed with dielectric measurements, and not with mechanical spectroscopy.

The workhorse of the high pressure community is the Diamond Anvil Cell (DAC) [173]. ISTS measurements have already been conducted in DACs on liquids [131, 174], and on inorganic single crystals [175]. ISTS measurements of supercooled liquids in DACs are just getting under way.

8.2 Experimental Improvements

Measurements on the same liquids performed by ultrasonic transducers, impulsive stimulated scattering, and picosecond ultrasonics present the novel opportunity to create acoustic spectra whose bandwidths may rival that of dielectric spectroscopy. This will enable thorough tests of α and β relaxation behavior and the connections between them as predicted by mode-coupling theory from the point of view of density fluctuations, which are the natural variables of the theory.

To this end, experiments conducted at common frequencies can eliminate sources of systematic differences between the different experimental methods. Extensions to lower wavevector are unnecessary, as broadband transducer measurements are already available in a range that overlaps with the lower end of the ISTS bandwidth. Thus, attention should be focussed on increasing the upper-frequency limit of the measurements.

It has already been suggested [176] that novel geometries involving prisms may be used to increase the effective numerical aperture of the imaging system [177]. If successful, this would push measurements toward significantly higher frequencies. Additionally, taking advantage of the linear dependence of electrostriction on wavevector q implies that IR excitation light may be superseded by higher laser harmonics, due to the linear dependence of grating wavelength on pump wavelength, the sole caveat being that the laser light must not induce photochemistry on the sample. For example, unpublished test data at 1.1 µm grating spacing were taken with 514 nm excitation and probed with a 532 nm CW laser. The data yielded excellent signal-to-noise for a variety of liquids, producing signals up to 1.5 GHz in the simple liquid state.

CW probing may still be used in these configurations, as higher harmonics of diode pumped CW lasers can be employed so as to reduce the imaging restrictions on the setup. The electronic bandwidth needed to probe such higher frequencies is also available in the correspondingly higher range; some optical detectors can reach up to 20 GHz, and digitization electronics can match these frequencies. Amplification can be performed by a separate microwave amplifier or for lower electronic noise, a cooled microwave amplifier.

The measurements of the shear modulus presented here constituted an improvement over previous efforts [8, 9], although there is much room for growth. As in the case of longitudinal measurements, there is a distinct need for larger bandwidths as mentioned above and, in particular for shear wave experiments, higher signal levels in order to reduce scatter in measured moduli.

The pump laser is likely not a source of improvement. The major step that made many of these experiments possible was to bypass the compressor, which yielded more light and a lower peak power due to the output of 60 ps pulses. A separate stretcher may be built outside of the laser[1], but little more can be done to decrease the peak power significantly without pushing the pulse duration outside of the impulsive limit.

Perhaps the easiest improvement that can be made on the experiments is to increase the probe power. As mentioned in chapter 3, the choice of probe laser is a balance between optical (in the form of imaging), electronic (in the form of photodiode sensitivity), and physical (in the form of diffraction efficiency) constraints. The ideal probe source for CW measurements is a high powered, single-mode laser that can be easily gated, and whose wavelength is close to that of the pump.

For the probe wavelength of 830 nm used here, at present the highest available power for single transverse mode output is 200 mW. However, the recent advent of tapered amplifier diodes provides for the single-mode operation desirable for an optical experiment with output powers in the single watt range that rival their multimode counterparts. Diode lasers also have the advantage of being easily electronically gated to the duration of the acoustic signal, which can limit the amount of heating the sample experiences from the probe.

---

[1] The stretcher within can not and should not be adjusted!

Another means of increasing the probe power would be to use a different diffractive optic for the pump and probe. In the present experimental configuration, almost half the probe light is simply thrown away by attenuating the local oscillator with an ND 3 or ND 4 filter. The probe's phase mask could be blazed, rather than binary, so that probe light is preferentially diffracted into one order. Invariably, there will be light present at other orders; the light in the local oscillator will still have to attenuated, although by a much weaker filter.

It was discovered that even the modest local oscillator levels used here almost began to saturate the bias of the amplification circuit used. A reduction of the level of light simply leads to lower signal, while an increase in the bias amounts to more noise. The source of the noise is likely not the dark current of the avalanche photodiode employed in the detector, but more likely from the amplification electronics. The most effective means of overcoming this problem would be to employ a Peltier cooled (or cryogenically cooled, if necessary) amplifier circuit.

With such improvements, the detection for the experiment may be adequately sensitive to turn the shear wave measurements from the difficult experiment we found it to be into one as routine, and fruitful, as the longitudinal measurements.

The work in this thesis was supported by ONR MURI awards N00014-01-1-0802 and N00014-06-1-0459, and NSF grants CHE-0616939 and DMR-0414895.

Appendix A

Notes on the High Q FemtoRegen

A.1 The Oscillator

The laser used for these experiments is a High Q FemtoRegen regeneratively amplified system based on an Yb:KGW gain medium and lasing anywhere from 1030 nm to 1040 nm depending upon the selected wavelength of the oscillator. The oscillator is in a factory-sealed box which cannot by opened by the user due to the Semiconducting Saturable Absorbing Mirror (SESAM), which must be kept in cleanroom conditions. The function of the SESAM is to passively mode-lock the system. It also doubles as a cavity end-mirror.

The oscillator has five knobs accessible from the outside for tuning and alignment. Two are for directing the laser on the SESAM (labelled SAH and SAV), and two others for aligning the other end mirror of the cavity (CAH and CAV). These should only be touched by a High Q technician except in the direst of circumstances. There is a fifth, unlabelled knob which controls a filter responsible for tuning the wavelength of the oscillator cavity. Adjustment of this knob can effectively increase the seeding efficiency of the amplifier. This is strongly discouraged, as safe operation of the system depends upon reliable operation of the oscillator, as described below. Consequently, the wavelength has been adjusted to optimize for reliability and not output power of the laser.

Pumping is accomplished by user-replaceable laser didoes integrated into the main oscillator housing. The diodes must be pumped by no less than 4.5 A of current. The current may be turned up to 5.0 A, but not beyond this limit unless cleared by a High Q technician. After a lifetime of 10000 hours, these diodes will have to be replaced.

The oscillator runs at a 78 MHz repetition rate and is monitored by a photodiode which detects leakage from one of the end mirrors. The output of this photodiode is the SMA connector labelled "PD Seed," which is on the back of the laser. PD Seed serves as the clock for the Pulse Delay Generator (PDG), but also as a means by which to monitor the workings of the oscillator. When the system is properly mode-locked, the output will be a train of pulses that register between 50 mV to 200 mV on the oscilloscope.

The main failure mode of the oscillator is a self Q-switched output, usually indicating either insufficient diode pumping or a damaged optical element in the cavity. Its main signature will be extremely unstable triggering of the oscilloscope, and a modulated rise in the monitored pulse train that behaves erratically. *Do not attempt to operate the amplifier while the oscillator is self Q-switching as this will cause it to fail!* Thus, it is highly recommended that when turning on the system, the oscillator output should be observed to be stable before proceeding to turn on the amplifier.

In the event that such oscillator failure occurs, the safest solution is to turn the system off and contact a High Q technician. However, other steps which may solve the problem are:

1. Check that the chiller is on and operating properly, and that the temperature is stabilized. If the oscillator is not at the correct temperature it may self Q-switch.

2. Increase the current to the pump diodes in increments of 0.1 A. Self Q-switching can be an unstable mode of operation due to insufficient pumping of the gain medium. The current to the diodes may safely be increased to up to 5.0 A.

3. Slowly shift the wavelength of the oscillator. The oscillator will come into mode-lock when the wavelength is selected for stable operation. Note: *Before proceeding, mark the starting position of this knob!*

4. If it is suspected that the SESAM crystal is burned, it is possible to move the spot off of this damaged position by slowly adjusting the SAH and SAM knobs. *Again, before proceeding, mark the starting position of these knobs!* Turning these mirrors too far may cause the oscillator to stop lasing altogether. Additionally, the beam pointing from the oscillator cavity will change slightly, and this may require that the seeding of the amplifier be reoptimized by a High Q technician.

If these steps don't fix the oscillator, the problem is likely very serious (such as a burned gain crystal) and needs to be attended to by the technician.

A.2 Timing Electronics

The PDG down-counts the oscillator pulse train by a factor set by a user-controllable program running on a PC, and in this manner sets the repetition rate of the laser. This program is not straightforward to use. If the PDG has been powered down since it was last operated, it will have to be activated using the program "`PDG1 neu.exe`." When doing this, the first button pressed should be "Get State." After that, one must then check the "Pulse Enable" box and the "internal trigger" box. *At this point, it may be necessary to click directly on the labels Div(27), Div(15), SP2, SP1, SP4, SP3, Latch1, and Latch2 to get the PDG to start working properly!* These labels are actually toggles. After this has been done, or if the PDG has not been powered down since its last use, the program `PDG120.EXE` may then be used to adjust the timing of the Pockels cell, as described below.

It is essential that the PDG register an amplitude of over 50 mV in order to operate stably and safely trigger the Pockels Cell gating the amplifier. The divide-by marker ("Divisor" in the program `PDG120.EXE`), can be set at any value which operates the laser from a repetition rate of 500 Hz all the way up to 100 kHz. Note that this is division of 78 MHz by Divisor. The lower limit of this range is set by the fact that if the pulse duration is too low, too much gain can build up in the amplifier gain medium before it is extracted by a pulse. This highly amplified pulse can damage optical components in the amplifier. Hence, on turning down the repetition rate, the current to the amplifier pump diodes should be decreased first. The upper limit of the repetition rate range is set by the operating speed of the Pockels cell, as well as the excited state lifetime of the gain medium. Finally, we remark that over this broad range of repetition rates, the average power of the laser generally decreases anywhere from 10-20% as the repetition rate is increased.

During normal operation, the oscillator is continually seeding the amplifier. Both admittance of one of these pulses into the amplifier cavity, as well as retrieval of it, are controlled by the same intracavity Pockels cell. The window of the amplifier next to the Pockels cell is in fact a $\lambda/4$ waveplate. If an oscillator pulse makes two visits to this optic, its polarization is rotated by 90° and it is subsequently ejected by the thin film polarizer. During pulse amplification, a voltage is applied to the Pockels cell which causes it, too, to function as a $\lambda/4$ retarder. The combined effect leaves the polarization of the incident pulse untouched. In this case, it is reflected by the TFP, and continuously makes round-trips in the cavity until it is ejected at the user-specified time when the voltage on the Pockels cell is released. Meanwhile, other oscillator pulses continue to pass through the amplifier and to the experiment.

The gating of the Pockels cell is tuned via `PDG120.EXE`. Fine adjustment is given for the "on" and "off" triggering of the amplifier in units of 0.15 ns. Coarse operation for the "off" designation is provided in units of amplifier cavity round-trip times. This can be accomplished through intracavity monitoring of the amplifier via the "PD Int" SMA output and extracavity monitoring via the "PD Ext" SMA output. The maximum output power of the laser is achieved when the gain medium is observed to saturate. The output of the amplifier cavity should also be monitored at a point after the laser's output. The fluence is high enough the unfocussed reflection off a glass slide onto a photodiode will suffice.

The Pockels cell is powered by a control box which sits on the rack near the laser. On the front of this box is a knob which provides fine control over the Pockels cell voltage. Pre and post pulses can be eliminated by a combination of proper timing of all of these elements: the Pockels cell voltage primarily corrects for pre-pulses, while adjustment of the Pockels cell timing, the $\lambda/4$ waveplate, and the angle of the Pockels cell can correct for post-pulses. Voltage adjustments require no special precautions, though optimization of the $\lambda/4$ waveplate should only be done while the amplifier diodes are run at a significantly reduced amperage – this is so that excessive gain does not build up in the cavity which may damage amplifier components. Physical adjustment of the Pockels cell is inadvisable, as small adjustments can cause the amplifier to stop lasing. This should only be attempted by a High Q technician.

A.3 The Stretcher, Compressor, and Amplifier

Before entering the amplifier, the oscillator seed pulses are stretched by a folded-geometry grating stretcher. The blazed 1800 grooves/mm gold gratings used in both stretching, and later in recompression, are *extremely* fragile and should not be touched under any circumstances. They also cannot be cleaned. Over time, they will degrade in quality, becoming cloudy and will have to be replaced.

The degree of compression can be adjusted via movement of an internal roof mirror. Adjustment of this mirror is accomplished via a servo motor attached to the amplifier diode power supply. Optimal compression has been measured via an autocorrelator at FWHM of 250 fs. Pulse durations as long as 10 ps can be achieved this way. Longer pulses are available only if the compressor is bypassed altogether. The stretcher and compressor cannot be adjusted by the experimentalist, as this may change the seeding of the amplifier or the ejection of the pulse from the laser.

As of the writing of this thesis, adjustment of the servo driving the roof mirror causes the amplifier power supply to cut power to the amplifier diodes. The power will also be cut off randomly if the cable connecting the amplifier power supply to the servo motor is even in place at all. Leaving the connecting cable unplugged temporarily resolves this issue.

The amplifier is pumped by a bank of laser diodes powered externally. Adjustment of the current to the amplifier diodes is an effective way of controlling the output power of the laser. There is no lower limit to this current, although an upper limit of 40.0 A is suggested by the manufacturer.

When working directly with *any* of the laser diodes, it is absolutely necessary to be grounded via a wrist bracelet to ground. It is also necessary to ground the amplifier pump diodes by shorting the inputs to one another by a single power cable when the amplifier diodes are unplugged. These precautions are taken to prevent failure due to electrostatic discharge. No such shorting precautions need be taken for the oscillator diode bank, though it is still recommended.

The main failure mode of the amplifier has historically been burning of the thin-film polarizer, and less commonly, the amplifier crystal. In either case, the result is that the amplifier will stop lasing or produce a weak TEM_{11} output. The mechanism has been determined to arise from faulty timing by the PDG: if the PDG is mistimed, too much gain in the amplifier cavity will build up while there is no pulse to remove it. Then, the PDG will trap the pulse in the cavity for too long, extracting all of the energy from the gain medium. The resulting pulse carries so much energy that it will cause damage to the optical elements. This timing usually arises from the oscillator self Q-switching. Damage to the amplifier's optics may also occur if the stretched seeding bandwidth is clipped.

Finally, the amplifier gain crystal is housed in a copper mount that is cooled by a Peltier element. The setpoint and temperature of the Peltier cooler can be monitored by the banana cable outputs on the back of the amplifier's thermoelectric cooler controller, TEC AMP. If the element is working properly, the two numbers should match well when the system is turned on. The thermal contact between these two components has failed in the past. The distinguishing characteristic of this failure is a gradually decreasing amplifier output power with time (on the scale of minutes). This may be confirmed by noticing that the Peltier element's voltage drifts from the setpoint over time after the amplifier has been turned on. As alignment of the amplifier cavity is difficult, this problem may only be approached by a High Q technician.

Appendix B

Raw Data for DC704 used in Chapter 4

Below are the longitudinal spectral data for DC704. Grating spacings with $*$ before them are provided for completeness but were not used in construction of the spectra due to systematic errors which led to unrealistic fits.

B.1 Time-Dependent Thermal Expansion Data

Table B.1: τ_{KWW} and β_{KWW} for DC704

Λ (µm)	T (K)	τ_{KWW} (µs)	β_{KWW} [-]
24.9	238	3.21	0.32
24.9	240	0.864	0.38
24.9	242	0.401	0.43
24.9	244	0.191	0.44
24.9	246	0.100	0.47
24.9	248	0.0644	0.5
50.8	232	779	0.40
50.8	234	260	0.33
50.8	236	40.8	0.31
50.8	238	2.42	0.33
50.8	240	0.667	0.28
50.8	242	0.397	0.44
50.8	244	0.121	0.63
50.8	246	0.0474	0.37
50.8	248	0.0411	0.40

B.2 Frequencies and Damping Rates Used in Construction of Modulus Spectra

Table B.2: T=240 K

Λ (µm)	$\omega/2\pi$ (MHz)	Γ (1/µs)
1.97	1061	139
2.33	894.9	121
2.68	772.6	107
3.14	663.4	84.7
3.65	571.4	71.9
4.20	496.1	60.0
4.85	428.6	52.5
5.66	366.8	47.6
6.56	316.3	40.5
6.70	309.0	34.0
7.62	273.1	29.3
9.14	227.0	24.6
10.2	204.3	23.0
11.7	177.1	22.7
13.7	150.7	18.9
15.7	131.2	17.8
18.3	112.7	16.6
21.3	96.40	14.9
24.9	82.38	13.4
28.5	72.07	12.6
33.0	61.96	12.1
38.1	53.82	10.9
44.2	46.38	10.7
49.8	40.48	9.23
50.8	40.24	10.1
56.9	35.36	8.42
65.9	30.35	7.75
76.0	26.25	7.27
88.0	22.55	6.68
101	19.59	6.30

Table B.3: T=242 K

Λ (µm)	$\omega/2\pi$ (MHz)	Γ (1/µs)
$*$1.97	1052	146
$*$2.33	885.2	129
$*$2.68	767.0	112
$*$3.14	654.1	93.7
$*$3.65	563.7	82.6
$*$4.20	488.1	72.4
$*$5.66	361.4	56.8
$*$6.56	311.7	46.2
6.70	308.0	43.6
7.62	270.5	40.0
9.14	225.1	38.1
10.2	201.4	32.8
11.7	175.7	31.5
13.7	149.3	27.1
15.7	129.8	27.4
18.3	111.5	25.9
21.3	95.51	21.6
24.9	81.64	20.0
$*$28.4	68.98	20.0
$*$33.0	59.43	17.3
$*$38.1	51.45	15.7
$*$44.2	44.09	12.5
$*$49.8	39.70	10.9
$*$50.8	38.25	13.1
$*$56.9	34.61	9.92
$*$65.9	29.75	8.86
$*$76.0	25.68	8.15
$*$88.0	22.09	7.33
$*$101	19.20	6.68

Table B.4: T=244 K

Λ (µm)	$\omega/2\pi$ (MHz)	Γ (1/µs)
1.97	1041	178.5
2.33	877.9	145.6
2.68	761.5	118.7
3.14	648.4	103.5
3.65	559.0	89.9
4.20	484.9	76.3
4.85	419.0	69.3
5.66	357.8	63.7
6.56	308.0	54.4
6.70	305.0	46.1
7.62	267.7	40.9
9.14	222.9	38.3
10.2	200.2	34.8
11.7	173.4	33.1
13.7	147.1	30.8
15.7	127.8	29.0
18.3	109.8	26.6
21.3	93.91	23.7
24.5	80.19	21.7
28.4	70.04	19.6
33.0	60.30	18.2
38.1	52.07	16.6
44.2	44.74	15.5
49.8	39.05	12.7
50.8	38.86	14.5
56.9	33.92	11.9
65.9	29.14	10.6
76.0	25.13	9.65
88.0	21.61	8.94
101	18.70	8.12

Table B.5: T=246 K

Λ (µm)	$\omega/2\pi$ (MHz)	Γ (1/µs)
1.97	1029	196
2.33	870.4	156
2.68	751.7	137
3.14	643.0	116
3.65	551.8	95.9
4.20	479.0	84.9
4.85	413.3	73.8
5.66	352.3	66.9
6.56	304.1	58.3
6.70	301.3	51.8
7.62	264.0	53.1
9.14	219.4	45.5
10.2	196.9	42.5
11.7	170.6	39.3
13.7	144.8	35.5
15.7	125.7	34.3
18.3	107.8	29.8
21.3	92.00	28.2
24.9	78.62	24.6
28.5	68.59	22.5
33.0	58.90	21.1
38.1	50.81	19.1
44.2	43.66	17.2
49.8	38.18	14.0
50.8	37.66	15.4
56.9	33.20	12.9
65.9	28.41	11.7
76.0	24.43	10.6
88.0	20.98	9.50
101	18.20	8.84

Table B.6: T=248 K

Λ (μm)	$\omega/2\pi$ (MHz)	Γ (1/μs)
1.71	1182	233
1.97	1012	227
2.33	855.2	190
2.68	740.9	146
3.14	632.3	132
3.65	543.5	116
4.20	471.3	102
4.85	407.5	94.7
5.66	348.4	83.2
6.56	299.8	73.0
6.70	296.0	66.6
7.62	259.6	62.3
9.14	215.0	56.5
10.2	193.6	50.3
11.7	167.7	45.8
13.7	142.3	40.8
15.7	123.5	38.1
18.3	105.9	32.6
21.3	90.30	30.4
24.9	76.92	26.9
28.5	67.03	24.3
33.0	57.52	22.0
38.1	49.61	19.9
44.2	42.48	17.6
49.8	37.40	16.6
50.8	36.82	16.1
56.9	32.34	14.8
65.9	27.69	12.9
76.0	23.89	11.4
88.0	20.39	10.1
101	17.66	9.06

Table B.7: T=250 K

Λ (μm)	$\omega/2\pi$ (MHz)	Γ (1/μs)
1.70	1171	231
2.65	745.6	126
3.44	577.0	124
4.06	486.4	112
4.67	421.4	105
5.46	360.4	87.9
6.37	306.1	73.0
6.70	286.8	74.2
7.61	252.9	70.2
9.13	210.2	56.2
10.2	189.2	53.6
11.7	163.2	47.3
13.7	138.1	41.6
15.7	120.3	40.8
18.3	103.1	37.1
21.3	87.78	32.5
24.9	74.92	30.2
28.5	65.46	28.1
33.0	56.02	25.4
38.0	48.21	23.4
44.2	41.14	21.8
49.8	36.35	21.5
50.7	35.61	19.4
56.9	31.50	15.5
65.9	26.91	10.9
76.0	23.12	8.39
88.0	19.77	6.51
101	17.18	4.63

Table B.8: T=252 K

Λ (µm)	$\omega/2\pi$ (MHz)	Γ (1/µs)
1.97	994.8	306
2.33	836.8	237
2.68	721.3	194
3.14	617.4	163
3.65	527.3	144
4.20	456.8	132
4.85	393.3	121
5.66	336.0	110
6.56	288.5	96.1
6.70	287.0	84.1
7.62	252.0	75.8
9.13	209.2	68.2
10.2	186.1	62.6
11.7	161.4	62.0
13.7	137.1	51.5
15.7	118.5	49.0
18.3	101.2	42.2
21.3	86.04	37.9
24.9	73.33	32.1
28.5	63.89	28.6
33.0	54.61	26.3
38.1	47.09	23.4
44.2	40.17	20.0
49.8	35.33	17.4
50.8	34.98	18.5
56.9	30.60	15.1
65.9	26.20	13.0
76.0	22.47	11.1
88.0	19.23	9.44
101	16.63	8.04

Table B.9: T=254 K

Λ (µm)	$\omega/2\pi$ (MHz)	Γ (1/µs)
1.97	980.3	318
2.33	822.9	260
2.68	712.3	207
3.14	608.5	175
3.65	521.3	155
4.20	452.3	138
4.85	391.3	128
5.66	331.2	120
6.56	286.8	100
6.70	280.6	98.6
7.62	246.4	88.3
9.14	203.7	79.5
10.2	182.8	71.8
11.7	157.9	65.7
13.7	133.9	56.6
15.7	115.4	45.4
18.3	97.80	40.9
21.3	84.28	38.7
24.7	71.80	33.1
28.5	62.51	29.1
33.0	53.49	25.3
38.1	46.08	22.5
44.2	39.47	19.6
49.8	34.24	16.9
50.8	34.07	17.3
56.9	29.87	14.6
65.9	25.43	12.3
76.0	21.85	10.2
88.0	18.75	8.89
101	16.23	7.54

Table B.10: T=256 K

Λ (µm)	$\omega/2\pi$ (MHz)	Γ (1/µs)
1.97	969.9	300
2.33	811.3	279
2.68	701.0	238
3.14	597.6	200
3.65	512.5	171
4.20	444.5	153
4.85	382.9	139
5.66	326.6	124
6.56	280.8	109
6.70	274.9	106
7.62	240.8	99.5
9.14	199.4	82.6
10.2	178.4	77.3
11.7	154.1	70.8
13.7	130.9	61.9
15.7	112.4	51.6
18.3	96.89	46.6
21.3	82.02	39.3
24.9	70.50	36.2
28.5	60.99	31.8
33.0	52.06	26.4
38.1	45.12	22.2
44.2	38.42	18.6
49.8	33.65	15.4
50.8	33.22	15.7
56.9	29.04	13.3
65.9	24.93	11.1
76.0	21.36	9.15
88.0	18.39	7.79
101	15.99	6.58

Table B.11: T=258 K

Λ (µm)	$\omega/2\pi$ (MHz)	Γ (1/µs)
1.97	958.1	349
2.33	803.4	290
2.68	696.5	239
3.14	589.6	220
4.85	378.1	145
4.20	439.6	163
5.66	323.2	134
6.56	277.3	117
6.70	271.5	115
7.62	237.7	103
9.14	196.0	89.7
10.2	175.3	80.8
11.7	151.4	72.3
13.7	128.0	62.1
15.7	110.7	53.7
18.3	94.47	45.0
21.3	80.05	38.3
24.9	68.25	31.7
28.5	59.46	27.7
33.0	50.98	23.7
38.1	43.68	19.7
44.2	37.60	17.0
49.8	32.74	15.3
50.8	32.55	13.8
56.9	28.48	12.8
65.9	24.42	10.7
76.0	21.03	8.51
88.0	18.04	6.95
101	15.65	5.90

Table B.12: T=260 K

Λ (µm)	$\omega/2\pi$ (MHz)	Γ (1/µs)
1.70	1102	373
2.65	696.4	229
3.44	533.1	208
4.06	449.2	181
4.67	386.0	178
5.46	327.1	150
6.37	278.6	116
6.70	264.5	112
7.61	228.9	95.4
9.13	190.6	87.5
10.2	169.0	79.7
11.7	146.7	66.7
13.7	124.3	60.2
15.7	106.7	51.2
18.3	91.44	42.1
21.3	78.33	34.1
24.9	66.80	30.4
28.5	58.07	23.8
33.0	49.59	24.4
38.1	42.91	16.4
44.2	36.59	13.9
49.8	32.15	12.3
50.8	31.91	12.7
56.9	27.89	9.89
65.9	24.02	8.29
76.0	20.66	6.76
88.0	17.80	5.78
101	15.49	4.84

Table B.13: T=262 K

Λ (µm)	$\omega/2\pi$ (MHz)	Γ (1/µs)
2.65	694.9	240
2.97	613.1	243
3.44	527.7	212
4.06	444.9	192
4.67	381.1	179
5.46	320.9	151
6.37	274.1	122
7.44	232.7	104
8.52	202.9	94.6
9.14	188.3	98.5
10.2	167.3	80.9
11.7	144.6	66.4
13.7	123.0	61.8
15.7	105.5	49.6
18.3	90.66	40.1
21.3	76.92	32.3
24.9	65.36	26.9
28.5	56.99	23.0
33.0	48.78	19.7
38.1	41.96	16.0
44.2	35.98	13.0
49.8	31.70	11.2
50.8	31.15	11.3
56.9	27.60	9.17
65.9	23.66	7.35
76.0	20.55	6.09
88.0	17.70	5.00
101	15.27	4.30

Table B.14: T=264 K

Λ (µm)	$\omega/2\pi$ (MHz)	Γ (1/µs)
1.71	1095	563
1.97	922.0	445
2.33	769.8	359
2.68	665.6	299
3.14	562.5	255
3.65	481.5	218
4.20	415.8	199
4.85	357.3	171
5.66	304.2	145
6.56	260.6	129
6.70	257.3	152
7.62	225.0	117
9.14	184.0	95.2
10.2	163.9	75.7
11.7	142.0	62.8
13.7	120.4	54.5
15.7	103.9	46.8
18.3	88.94	38.2
21.3	75.49	28.5
24.9	64.32	23.2
28.5	56.10	19.7
33.0	48.02	17.7
38.1	41.31	13.6
44.2	35.47	11.2
49.8	31.29	9.84
50.8	30.75	8.98
56.9	27.28	7.81
65.9	23.49	6.31
76.0	20.31	5.14
88.0	17.51	4.34
101	15.19	3.82

Table B.15: T=266 K

Λ (µm)	$\omega/2\pi$ (MHz)	Γ (1/µs)
*1.90	909.1	465
*2.20	755.1	360
*2.65	652.8	301
*2.97	555.2	261
*3.44	475.9	225
*4.06	411.0	201
*4.67	353.2	173
*5.46	299.7	144
*6.37	256.4	127
6.70	249.6	116
7.62	219.8	94.3
9.14	181.4	89.4
10.2	160.9	72.6
11.7	139.4	61.1
13.7	117.8	54.4
15.7	102.1	45.0
18.3	86.73	33.0
21.3	73.80	26.4
24.9	63.04	21.3
28.5	54.97	17.9
33.0	47.11	14.7
38.1	40.61	11.8
44.2	34.84	10.5
49.8	31.05	8.17
50.8	30.28	7.69
56.9	27.05	6.69
65.9	23.26	5.44
76.0	20.21	4.54
88.0	17.38	3.83
101	15.02	3.42

Table B.16: T=268 K

Λ (µm)	$\omega/2\pi$ (MHz)	Γ (1/µs)
1.97	885.7	484
2.33	742.6	393
2.68	643.6	307
3.14	547.5	258
3.65	469.0	219
4.20	404.9	202
4.85	346.8	174
5.66	294.4	150
6.56	251.5	123
7.62	216.4	117
9.14	177.7	81.4
10.2	159.0	73.9
11.7	137.2	56.0
13.7	116.2	47.7
15.7	100.3	39.9
18.3	86.02	29.3
21.3	73.35	23.6
24.9	62.61	18.9
28.5	54.52	16.1
33.0	46.78	12.8
38.1	40.28	9.76
44.2	34.77	7.76
49.8	30.71	6.84
50.8	30.24	7.00
56.9	26.86	5.75
65.9	23.02	4.68
76.0	20.09	4.00
88.0	17.22	3.45
101	14.96	3.17

B.3 Differential Scanning Calorimetry Data

T (K)	c_p (mJ/K)
240.0	2.6102
240.1	3.1218
240.2	2.4911
240.3	2.4149
240.4	3.3593
240.5	5.0192
240.6	5.8023
240.7	7.0529
240.8	8.1438
241.0	9.1694
241.5	10.2724
242.0	11.1201
242.5	11.9863
243.0	12.4167
243.5	12.6266
244.0	12.8145
244.5	12.9882
245.0	13.0744
246.0	13.1370
247.0	13.1471
248.0	13.1557
249.0	13.1745
250.0	13.1984
251.0	13.2194

T (K)	c_p (mJ/K)
252.0	13.2358
253.0	13.2443
254.0	13.2593
255.0	13.2714
256.0	13.2721
257.0	13.2642
258.0	13.2516
259.0	13.2395
260.0	13.2336
261.0	13.2258
262.0	13.1782
263.0	13.1568
264.0	13.1388
265.0	13.1279
266.0	13.1103
267.0	13.0931
268.0	13.0812
269.0	13.0698
270.0	13.0607
271.0	13.0433
272.0	13.0313
273.0	13.0303
274.0	13.0188

Appendix C

Raw Data for TPP used in Chapter 5

Below are listed the data used in shear spectral fits for TPP. Grating spacings preceded by $*$ are provided for completeness but were not used in construction of the spectra because of systematic errors in their collection which led to unrealistic spectral fits. Data at $\Lambda = 0.48$ µm, 1.52 µm, 3.14 µm, and 4.55 µm are from [66].

Table C.1: T=220 K

Λ (µm)	$\omega/2\pi$ (MHz)	Γ (1/µs)
1.52	574.3	107
2.33	379.6	60.2
3.14	277.4	78.0
3.65	246.9	38.9
4.55	190.3	45.6
7.62	112.5	22.7
9.14	92.72	23.0
10.2	83.40	20.1
11.7	72.45	17.2
13.7	61.61	15.9
15.7	53.34	14.7
21.3	39.77	11.0
24.9	34.19	9.36
∗28.5	32.35	5.95
∗33.0	27.78	7.48
∗38.1	24.12	6.04
∗44.2	20.21	5.41
∗50.7	17.14	4.22

Table C.2: T=222 K

Λ (µm)	$\omega/2\pi$ (MHz)	Γ (1/µs)
1.52	563.2	128
2.33	372.0	70.0
3.14	269.7	38.0
3.65	241.8	40.1
4.55	183.5	48.3
7.62	110.7	30.7
9.14	91.69	26.5
10.2	82.51	23.0
11.7	71.27	21.3
13.7	60.46	19.0
15.7	52.25	16.0
18.3	45.11	15.1
21.3	38.54	13.1
24.9	33.17	9.36
∗28.5	31.35	8.79
∗33.0	27.31	6.49
∗38.1	23.31	7.55
∗44.2	19.88	7.01
∗50.7	16.57	5.30

Table C.3: T=224 K

Λ (μm)	$\omega/2\pi$ (MHz)	Γ (1/μs)
1.52	551.3	153
2.33	362.9	83.8
3.14	265.9	98.0
3.65	232.3	50.6
4.55	179.3	52.5
7.62	106.6	36.9
10.2	78.88	27.1
11.7	68.26	26.8
13.7	59.34	22.6
15.7	52.39	15.3
18.3	43.75	14.7
21.3	37.04	17.8
24.9	32.10	12.2
*28.5	30.39	9.02
*33.0	26.57	9.59
*38.1	22.71	9.06
*44.2	18.99	8.50
*50.7	16.01	5.69

Table C.4: T=226 K

Λ (μm)	$\omega/2\pi$ (MHz)	Γ (1/μs)
0.48	1710	537
1.52	535.5	169
2.33	355.0	89.7
3.14	261.1	138
3.65	222.4	69.2
4.55	172.7	70.4
7.62	103.0	42.4
9.14	85.04	35.5
10.2	78.88	27.1
11.7	65.89	31.7
13.7	57.43	25.1
15.7	51.15	18.1
18.3	42.20	19.2
21.3	35.75	20.1
24.9	30.59	14.8
*33.0	25.66	9.19
*38.1	21.64	10.4
*44.2	18.48	7.45
*50.7	15.16	9.28

Table C.5: T=228 K

Λ (µm)	$\omega/2\pi$ (MHz)	Γ (1/µs)
0.48	1654	602
1.52	523.0	194
2.33	345.6	105
3.14	253.8	124
3.65	224.3	68.5
4.55	167.0	91.1
7.62	98.94	49.4
9.14	81.86	39.0
10.2	72.61	40.5
11.7	63.61	36.1
13.7	54.82	28.1
15.7	47.33	23.6
18.3	40.11	23.9
21.3	35.92	22.1
24.9	29.35	20.4
$*$28.5	27.97	15.0
$*$33.0	24.61	12.4
$*$38.1	21.25	11.0
$*$44.2	17.50	11.1
$*$50.7	14.42	10.8

Table C.6: T=230 K

Λ (µm)	$\omega/2\pi$ (MHz)	Γ (1/µs)
0.48	1644	681
1.52	511.2	219
2.33	337.1	119
3.14	241.7	166
3.65	207.8	90.9
4.55	160.4	98.0
7.62	94.90	60.3
9.14	78.47	46.0
10.2	69.25	45.6
11.7	61.99	39.1
13.7	52.34	31.1
15.7	44.67	32.1
18.3	38.11	26.6
21.3	34.09	21.3
24.9	28.32	17.3
$*$28.5	26.38	19.5
$*$33.0	23.58	14.9
$*$38.1	20.03	12.8
$*$44.2	16.57	11.1
$*$50.7	14.02	11.8

Table C.7: T=232 K

Λ (µm)	$\omega/2\pi$ (MHz)	Γ (1/µs)
0.48	1621	720
1.52	496.7	256
2.33	323.9	138
3.14	237.3	174
3.65	199.6	122
4.55	153.4	116
7.62	91.10	69.1
9.14	74.79	52.2
10.2	65.38	56.1
11.7	58.53	43.5
13.7	51.46	33.0
15.7	42.57	34.8
18.3	36.59	30.2
21.3	32.32	29.3
24.9	26.55	28.2
$*$28.5	24.40	25.2
$*$33.0	23.08	17.6
$*$38.1	18.06	18.8
$*$44.2	16.67	14.7
$*$50.7	13.01	18.0

Table C.8: T=234 K

Λ (µm)	$\omega/2\pi$ (MHz)	Γ (1/µs)
0.48	1556	746
1.52	480.3	302
2.33	317.4	155
3.14	229.0	204
3.65	190.5	142
4.55	146.2	101
7.62	85.64	81.2
9.14	71.11	60.4
10.2	61.17	62.6
11.7	56.66	46.7
13.7	48.78	37.5
15.7	40.18	41.4
18.3	33.23	34.3
21.3	27.28	46.4
24.9	24.81	32.6
$*$28.5	23.11	27.4
$*$33.0	21.32	27.0
$*$38.1	17.49	29.7
$*$44.2	14.83	18.8
$*$50.7	12.38	11.6

Table C.9: T=236 K

Λ (µm)	$\omega/2\pi$ (MHz)	Γ (1/µs)
0.48	1563	772
1.52	462.5	339
2.33	306.1	182
3.14	220.1	234
3.65	183.0	158
4.55	139.3	110
7.62	79.87	114
9.14	66.26	65.3
10.2	57.14	66.8
11.7	53.47	53.4
13.7	45.77	41.3
15.7	37.54	44.8
18.3	31.01	43.9
21.3	24.86	65.0
24.9	22.88	54.3
∗28.5	23.00	36.2
∗33.0	20.54	28.0
∗44.2	12.60	23.2
∗50.7	12.21	22.5

Table C.10: T=238 K

Λ (µm)	$\omega/2\pi$ (MHz)	Γ (1/µs)
0.48	1554	942
1.52	443.4	376
2.33	297.5	211
3.14	210.2	262
3.65	175.0	166
4.55	131.9	119
7.62	76.14	103
9.14	62.40	68.5
10.2	54.87	67.5
11.7	49.33	62.1
13.7	43.02	45.1
15.7	33.89	48.1
21.3	20.98	62.8
24.9	21.04	69.9
∗28.5	20.38	50.8
∗33.0	15.26	68.5
∗50.7	10.65	33.0

Table C.11: T=240 K

Λ (µm)	$\omega/2\pi$ (MHz)	Γ (1/µs)
0.48	1500	929
1.52	428.9	413
2.33	271.4	253
3.14	196.2	280
3.65	164.3	175
4.55	120.0	134
7.62	72.09	108
9.14	58.06	72.1
10.2	51.92	61.2
11.7	45.03	61.0
13.7	39.17	52.8
15.7	35.88	43.8
18.3	27.99	46.1
21.3	20.59	75.3
24.9	19.55	58.8
28.5	19.15	44.5

Table C.12: T=242 K

Λ (µm)	$\omega/2\pi$ (MHz)	Γ (1/µs)
0.48	1463	1100
1.52	411.8	455
2.33	271.7	273
3.14	172.6	256
3.65	155.5	184
7.62	68.88	124
9.14	52.16	79.7
10.2	46.86	66.5
11.7	42.61	63.8
13.7	35.28	62.5
18.3	24.35	45.9

Table C.13: T=244 K

Λ (µm)	$\omega/2\pi$ (MHz)	Γ (1/µs)
0.48	1423	1113
1.52	392.8	504
2.33	250.9	378
3.14	165.9	320
3.65	146.3	173
7.62	64.08	131
9.14	44.54	109
10.2	35.45	164
11.7	36.56	79.1
13.7	33.03	41.1
15.7	27.03	88.5

Table C.14: T=246 K

Λ (µm)	$\omega/2\pi$ (MHz)	Γ (1/µs)
0.48	1381	1283
1.52	375.0	554
2.33	237.6	355
3.14	160.5	304
9.14	38.69	204
10.2	23.66	300
11.7	31.50	99.9
15.7	24.81	98.8

Table C.15: T=248 K

Λ (μm)	$\omega/2\pi$ (MHz)	Γ (1/μs)
0.48	1346	1427
1.52	351.3	641
2.33	225.3	383
3.14	136.6	400
9.14	37.16	197
10.2	22.02	304
11.7	26.75	158
15.7	21.04	110

Table C.16: T=250 K

Λ (μm)	$\omega/2\pi$ (MHz)	Γ (1/μs)
0.48	1304	1728
1.52	331.6	703
2.33	216.3	416
3.14	145.5	382

Appendix D

Raw Data used in Chapter 6

Below are tabulated the data for the shear frequency $\omega/2\pi$ and damping rate Γ used in the analysis in chapter 6.

Table D.1: $2BP_{87}/oTP_{13}$, Λ =1.75 µm

T (K)	$\omega/2\pi$ (MHz)	Γ (1/µs)
220	669.5	31.9
222	661.7	33.4
224	655.6	35.2
226	648.1	42.7
228	639.9	45.6
230	631.0	57.2
232	621.6	56.2
236	602.1	68.4
238	592.4	80.4
240	582.4	105
242	572.1	117
244	559.5	118
246	544.2	137
248	537.2	164
250	516.4	170
252	508.9	206
254	489.7	199
256	471.4	230

Table D.2: 5-phenyl 4-ether, Λ =1.75 µm

T (K)	$\omega/2\pi$ (MHz)	Γ (1/µs)
243	625.2	24.6
245	619.8	26.0
247	613.7	28.0
249	606.4	31.8
251	599.2	32.0
253	592.0	33.4
255	584.8	36.9
259	568.3	47.6
261	560.2	46.2
263	552.4	56.0
265	543.8	60.4
267	534.8	63.7
269	526.7	68.2
271	517.2	76.8
273	507.5	90.9
275	496.8	106
279	477.1	120
281	466.8	130
283	456.7	151
285	447.5	165
289	425.9	209
293	422.1	294
297	385.0	384
301	364.2	593
305	311.7	915

Table D.3: $Ca(NO_3)_2 \cdot 4H_2O$, Λ =2.35 µm

T (K)	$\omega/2\pi$ (MHz)	Γ (1/µs)
213	743.7	27.6
215	737.8	27.9
217	730.8	31.7
219	723.0	35.9
221	713.8	48.3
223	707.0	37.6

Table D.4: DC704 K, Λ =2.35 µm

T (K)	$\omega/2\pi$ (MHz)	Γ (1/µs)
210	482.1	25.9
212	476.3	27.2
216	466.1	26.2
214	469.2	28.3
218	459.4	28.8
220	454.3	29.4
222	447.7	32.8
224	447.6	32.9
226	434.0	40.7
228	426.7	46.3
230	418.9	56.3
232	408.7	77.0
234	399.4	96.6
236	391.9	90.3
238	382.5	107
240	372.2	109
242	363.4	146
244	356.5	169
246	339.3	249
248	336.6	438
250	333.7	623

Table D.5: diethyl phthalate, Λ =2.00 µm

T (K)	$\omega/2\pi$ (MHz)	Γ (1/µs)
178	568.1	54.8
180	562.0	59.1
182	557.5	43.3
184	549.0	42.6
186	540.5	46.5
188	532.9	45.5
190	525.5	42.3
192	517.8	44.1
194	509.4	49.4
196	501.2	47.6
198	493.7	48.7
200	485.6	50.6
202	476.9	53.0
204	469.2	56.0
206	461.3	55.4
208	451.5	60.1
210	442.8	64.6
212	434.5	75.9
214	423.0	90.3
216	412.2	97.3
220	390.5	106
222	382.9	129
224	376.0	143
226	364.3	137

Table D.6: m-fluroaniline, Λ =1.75 µm

T (K)	$\omega/2\pi$ (MHz)	Γ (1/µs)
173	589.7	44.2
175	579.8	46.1
177	568.2	48.0
179	556.8	52.8
181	544.0	63.6
183	532.2	69.6
185	517.0	91.0
187	499.0	112
189	485.1	134
191	474.4	195
195	456.3	337
197	460.0	280

Table D.7: salol, Λ =2.00 µm

T (K)	$\omega/2\pi$ (MHz)	Γ (1/µs)
218	497.5	5.45
220	497.8	5.44
222	491.5	5.42
224	484.7	7.66
226	478.5	8.23
228	471.9	8.67
230	465.1	9.73
230	465.2	9.10
232	458.4	10.4
234	451.1	12.8
236	443.7	15.3
238	435.9	18.2
240	427.8	21.2
242	419.4	27.8
244	410.7	36.3

Table D.8: m-toluidine, Λ =1.75 µm

T (K)	$\omega/2\pi$ (MHz)	Γ (1/µs)
185	630.6	23.6
187	622.2	26.7
189	613.8	32.2
191	603.2	37.0
193	592.2	39.9
195	583.4	49.0
197	573.6	57.8
199	562.5	60.4
201	543.1	113.1
203	534.0	87.8

Appendix E

VFT Parameters Used in Chapter 6

Here we present the VFT data used for testing the shoving model, deriving the value of T_g used in the analysis, and deriving the value of m used in the analysis. Except where noted, all liquids were presented in the form

$$\tau = \exp A + \frac{B}{T - T_0}. \tag{E.1}$$

m-toluidine was represented by a base-10 form of this equation, i.e.

$$\tau = 10^{A+B/(T-T_0)}. \tag{E.2}$$

The mechanical relaxation data for 5-phenyl 4-ether were fit to a simple exponential of the form

$$\eta = B \exp(\frac{\Delta h^*}{RT}) \tag{E.3}$$

where B= 6.8×10^{-53} P, $\Delta h^* = 70322 \frac{\text{cal}}{\text{mol}}$, R is the ideal gas constant, and T is the temperature [111].

Dielectric relaxation data for salol were represented in the form [117]

$$\log_{10}(\tau_R) = A + B/\left(T - T_0 + \left((T - T_0)^2 + CT\right)^{1/2}\right) \tag{E.4}$$

where A=-2.157, B=123 K, C=3.984 K, and $T_0 = 261.2$.

Table E.1: VFT parameters used in chapter 6. Liquid designations are: (A) $2BP_{87}/oTP_{13}$; (B) Pure 2-benzylphenol; (C) $Ca(NO_3)_2 \cdot 4H_2O$; (D) DC704; (E) diethyl phthalate; (F) m-fluoroaniline; (G) m-toluidine; (H) triphenyl phosphite.

Liquid	$\log_{10}(A)$	B	T_0	T_g derived	m derived	Method	Ref
A	-17.4	988	169.4	220	84	Dielectric	[118]
B	-16.5	2221	134.5	210	82	Mechanical	[122]
C	-43	2300	160	212	79	Dielectric	[116]
D	-14.6	619	176.5	214	95	Dielectric	[70, 71]
D	-26.8	988	135.7	211	80	Mechanical	[70, 71]
E	-21.2	3552	111	178	62	Dielectric	[115]
F	-14.7	870	149	172	127	Dielectric	[120]
F	-15.8	909	140	162	130	Mechanical	[121]
G	-19.2	981	138	184	84	Dielectric	[119]
G	-13.3	755.2	161.5	184	128	Mechanical	[178]
H	-26.4	3837	143.7	202	98	Dielectric	[86]

Appendix F

Haikus on the Glass Transition

Go, boson peak! Run!
My laser can not see you;
Are you really there?

Happy beta peak,
You hide all your mysteries
at high omega.

Alpha processes,
your spectrum is as wide as
Mount Fuji in spring.

Salol is fragile.
Crystallization sets in
Our data are crap.

Warm, 'tis the spring hare;
Now cold, slow as the tortoise:
Flow is arrested.

Cunning like the fox
and stealthy like the ninja
shear waves elude me.

The pulse is too short.
My signal disappears like
fog burns off at dawn.

Words, once my servants,
Now reign as cruel masters.
Writing theses sucks.

Bibliography

[1] Alan Macfarlane and Gerry Martin. *Glass: A World History.* University of Chicago Press, 2002.

[2] J. C. Dyre. Solidity of viscous liquids. iv. density fluctuations. *Physical Review E*, 74(2), 2006. Part 1.

[3] W. Kauzmann. The nature of the glassy state and the behavior of liquids at low temperatures. *Chemical Reviews*, 43:219–256, 1948.

[4] E. A. Gibbs, J. H. DiMarzio. Nature of the glass transition and the glassy state. *Journal of Chemical Physics*, 28 373:383, 1958.

[5] J. H. Adam, G. Gibbs. On the temperature dependence of cooperative relaxation properties in glass-forming liquids. *Journal of Chemical Physics*, 43:139–146, 1965.

[6] Ludger Santen and Werner Krauth. Absence of thermodynamic phase transition in a model glass former. *Nature*, 405(6786):550–551, 2000.

[7] Y. W. Yang and K. A. Nelson. Impulsive stimulated light-scattering from glass-forming liquids .1. generalized hydrodynamics approach. *Journal of Chemical Physics*, 103(18):7722–7731, 1995.

[8] S. M. Silence, A. R. Duggal, L. Dhar, and K. A. Nelson. Structural and orientational relaxation in supercooled liquid triphenylphosphite. *Journal of Chemical Physics*, 96(7):5448–5459, 1992.

[9] S. M. Silence, S. R. Goates, and K. A. Nelson. Impulsive stimulated scattering study of the structural relaxation dynamics of liquid triphenylphosphite. *Journal of Non-Crystalline Solids*, 131, 1991.

[10] J. C. Dyre, N. B. Olsen, and T. Christensen. Local elastic expansion model for viscous-flow activation energies of glass-forming molecular liquids. *Physical Review B*, 53(5):2171–2174, 1996.

[11] M. D. Ediger, C. A. Angell, and S. R. Nagel. Supercooled liquids and glasses. *Journal of Physical Chemistry*, 100(31):13200–13212, 1996.

[12] H. Tanaka, R. Kurita, and K. I. Murata. Kinetics and control of liquid-liquid transition. In *Complex Systems*, volume 982 of *Aip Conference Proceedings*, pages 24–33. 2008.

[13] H. W. Sheng, H. Z. Liu, Y. Q. Cheng, J. Wen, P. L. Lee, W. K. Luo, S. D. Shastri, and E. Ma. Polyamorphismin ametallic glass. *Nature Materials*, 6(3):192–197, 2007.

[14] K. Winkel, M. S. Elsaesser, E. Mayer, and T. Loerting. Water polyamorphism: Reversibility and (dis)continuity. *Journal of Chemical Physics*, 128(4), 2008.

[15] A. Hedoux, Y. Guinet, P. Derollez, O. Hernandez, R. Lefort, and M. Descamps. A contribution to the understanding of the polyamorphism situation in triphenyl phosphite. *Physical Chemistry Chemical Physics*, 6(12):3192–3199, 2004.

[16] Kurt Binder and Walter Kob. *Glassy Materials and Disordered Solids – An Introduction to Theiry Statistical Mechanics.* World Scientific Publishing Co. Pte. Ltd., 2005.

[17] P. Lunkenheimer, U. Schneider, R. Brand, and A. Loid. Glassy dynamics. *Contemporary Physics*, 41(1):15 – 36, 2000.

[18] U. Schneider, P. Lunkenheimer, R. Brand, and A. Loidl. Dielectric and far-infrared spectroscopy of glycerol. *Journal of Non-Crystalline Solids*, 235-237:173–179, 1998.

[19] S. Havriliak and S. Negami. A complex plane representation of dielectric and mechanical relaxation processes in some polymers. *Polymer*, 8(4):161, 1967.

[20] D. Caprion and H. R. Schober. Structure and relaxation in liquid and amorphous selenium. *Phys. Rev. B*, 62(6):3709–3716, Aug 2000.

[21] R. Hilfer. H-function representations for stretched exponential relaxation and non-debye susceptibilities in glassy systems. *Physical Review E*, 65(6), 2002.

[22] R. Hilfer. Analytical representations for relaxation functions of glasses. *Journal of Non-Crystalline Solids*, 305(1-3):122–126, 2002.

[23] R. Richert. Homogeneous dispersion of dielectric responses in a simple glass. *Journal of Non-Crystalline Solids*, 172:209–213, 1994. Part 1.

[24] C. A. Angell, K. L. Ngai, G. B. McKenna, P. F. McMillan, and S. W. Martin. Relaxation in glassforming liquids and amorphous solids. *Journal of Applied Physics*, 88(6):3113–3157, 2000.

[25] R. Bohmer, K. L. Ngai, C. A. Angell, and D. J. Plazek. Nonexponential relaxations in strong and fragile glass formers. *Journal of Chemical Physics*, 99(5):4201–4209, 1993.

[26] C. A. Angell. Formation of glasses from liquids and biopolymers. *Science*, 267(5206):1924–1935, 1995.

[27] D. I. Goldman and H. L. Swinney. Signatures of glass formation in a fluidized bed of hard spheres. *Physical Review Letters*, 96(14), 2006.

[28] L. Berthier, G. Biroli, J. P. Bouchaud, L. Cipelletti, D. El Masri, D. L'Hote, F. Ladieu, and M. Pierno. Direct experimental evidence of a growing length scale accompanying the glass transition. *Science*, 310(5755):1797–1800, 2005.

[29] J. L. Lebowitz, J. K. Percus, and L. Verlet. *Physical Review*, 153:250, 1967.

[30] C. Dalle-Ferrier, C. Thibierge, C. Alba-Simionesco, L. Berthier, G. Biroli, J. P. Bouchaud, F. Ladieu, D. L'Hote, and G. Tarjus. Spatial correlations in the dynamics of glassforming liquids: Experimental determination of their temperature dependence. *Physical Review E*, 76(4), 2007. Part 1.

[31] H. Mori. *Progress in Theoretical Physics*, 33:423, 1965.

[32] H. Mori. *Progress in Theoretical Physics*, 34:399, 1965.

[33] Robert Zwanzig. *Nonequilibrium Statistical Mechanics.* Oxford University Press, 2001.

[34] Bruce J. Berne and Robert Pecora. *Dynamic Light Scattering.* Dover Publications, Inc., 2000.

[35] Jean-Pierre Hansen and Ian R. McDonald. *Theory of Simple Liquids, 3rd ed.* Elsevier, 2006.

[36] R. N. Sinclair. Inelastic neutron-scattering from amorphous solids. *Journal of Non-Crystalline Solids*, 76(1):61–78, 1985.

[37] E. Burkel. Phonon spectroscopy by inelastic x-ray scattering. *Reports on Progress in Physics*, 63(2):171–232, 2000.

[38] D. R. Reichman and P. Charbonneau. Mode-coupling theory. *Journal of Statistical Mechanics-Theory and Experiment*, 2005.

[39] K. Kawasaki. *Ann. Phys. N.Y.*, 61:1, 1970.

[40] U. Bengtzelius, W. Goetze, and A. Sjolander. *J. Phys*, C17:5915.

[41] M. Fuchs, W. Gotze, and A. Latz. Some comments on the alpha-relaxation dynamics of supercooled cakno3. *Chemical Physics*, 149(1-2):185–196, 1990.

[42] M. Fuchs, W. Götze, and M. R. Mayr. Asymptotic laws for tagged-particle motion in glassy systems. *Phys. Rev. E*, 58(3):3384–3399, Sep 1998.

[43] Peter Mayer, Kunimasa Miyazaki, and David R. Reichman. Cooperativity beyond caging: Generalized mode-coupling theory. *Physical Review Letters*, 97(9):095702, 2006.

[44] R. Ahluwalia and S. P. Das. Growing length scale related to the solidlike behavior in a supercooled liquid. *Physical Review E*, 57(5):5771–5774, 1998. Part B.

[45] S. P. Das. Elastic behavior in a supercooled liquid: Analysis of viscoelasticity using an extended mode coupling model. *Physical Review E*, 62(2):1670–1673, 2000. Part A.

[46] M. Priya and S. P. Das. Fragility and elastic behavior of a supercooled liquid. *Physical Review E*, 76(6), 2007.

[47] S. Srivastava, U. Harbola, and S. P. Das. Anomalous stretching in a simple glass-forming liquid. *Physical Review E*, 65(5), 2002. Part 1.

[48] V. N. Novikov and A. P. Sokolov. Poisson's ratio and the fragility of glass-forming liquids. *Nature*, 431(7011):961–963, 2004.

[49] A. Brodin, M. Frank, S. Wiebel, G. Q. Shen, J. Wuttke, and H. Z. Cummins. Brillouin-scattering study of propylene carbonate: An evaluation of phenomenological and mode coupling analyses. *Physical Review E*, 65(5), 2002. Part 1.

[50] A. Aouadi, C. Dreyfus, M. Massot, R. M. Pick, T. Berger, W. Steffen, A. Patkowski, and C. Alba-Simionesco. Light scattering study of the liquid-glass transition of meta-toluidine. *Journal of Chemical Physics*, 112(22):9860–9873, 2000.

[51] P. Lunkenheimer, L. C. Pardo, M. Koehler, and A. Loidl. Broadband dielectric spectroscopy on benzophenone: alpha relaxation, beta relaxation, and mode coupling theory. *Physical Review E*, 77(3), 2008. Part 1.

[52] D. Fioretto, M. Mattarelli, C. Masciovecchio, G. Monaco, G. Ruocco, and F. Sette. Cusp-like temperature behavior of the nonergodicity factor in polybutadiene revealed by a joint light and x-ray brillouin scattering investigation. *Physical Review B*, 65(22), 2002.

[53] S. M. Chathoth and A. Podlesnyak. Fast and slow dynamics in pr60ni10cu20al10 melts as seen by neutron scattering. *Journal of Applied Physics*, 103(1), 2008.

[54] E. Rossler and W. Schnauss. Beta-process of supercooled ortho-terphenyl - a comparison of dielectrical and nmr data guided by mode-coupling theory. *Chemical Physics Letters*, 170(4):315–320, 1990.

[55] W. Paul, D. Bedrov, and G. D. Smith. Glass transition in 1,4-polybutadiene: Mode-coupling theory analysis of molecular dynamics simulations using a chemically realistic model. *Physical Review E*, 74(2), 2006. Part 1.

[56] W. Gotze. Recent tests of the mode-coupling theory for glassy dynamics. *Journal of Physics-Condensed Matter*, 11(10A):A1–A45, 1999.

[57] Y. W. Yang and K. A. Nelson. Impulsive stimulated light scattered from glass-forming liquids .2. salol relaxation dynamics, nonergodicity parameter, and testing of mode-coupling theory. *Journal of Chemical Physics*, 103(18):7732–7739, 1995.

[58] L. Comez, S. Corezzi, G. Monaco, R. Verbeni, and D. Fioretto. Non-ergodicity in a locally ordered fragile glass former. *Journal of Non-Crystalline Solids*, 352(42-49):4531–4535, 2006. Sp. Iss. SI.

[59] D. Engberg, L. Borjesson, J. Swenson, L. M. Torell, W. S. Howells, and A. Wannberg. The liquid-glass transition in a strong network glass former investigated by neutron scattering. *Europhysics Letters*, 47(2):213–219, 1999.

[60] N. Gedik, J. Orenstein, R. X. Liang, D. A. Bonn, and W. N. Hardy. Diffusion of nonequilibrium quasi-particles in a cuprate superconductor. *Science*, 300(5624):1410–1412, 2003.

[61] D. R. Lutz, Keith A. Nelson, C. R. Gochanour, and M. D. Fayer. Electronic excited state energy transfer, trapping by dimers and fluorescence quenching in concentrated dye solutions: Picosecond transient grating exp. *Chemical Physics*, 58(3):325–334, 1981.

[62] Thomas P. Dougherty, Gary P. Wiederrecht, and Keith A. Nelson. Impulsive stimulated raman scattering experiments in the polariton regime. *J. Opt. Soc. Am. B*, 9(12):2179, 1992.

[63] C. H. Wang. Depolarized rayleigh-brillouin scattering of shear-waves and molecular-reorientation in a viscoelastic liquid. *Molecular Physics*, 41(3):541–565, 1980.

[64] K. A. Nelson. Stimulated brillouin-scattering and optical-excitation of coherent shear-waves. *Journal of Applied Physics*, 53(9):6060–6063, 1982.

[65] Jean Pierre Boon and Sidney Yip. *Molecular Hydrodynamics.* Dover Publications, Inc., 1991.

[66] Scott Silence. PhD thesis, Massachusetts Institute of Technology, 1991.

[67] C. Glorieux, K. A. Nelson, G. Hinze, and M. D. Fayer. Thermal, structural, and orientational relaxation of supercooled salol studied by polarization-dependent impulsive stimulated scattering. *Journal of Chemical Physics*, 116(8):3384–3395, 2002.

[68] I. C. Halalay and K. A. Nelson. *Review of Scientific Instruments*, 61(11):3623–3624, 1990.

[69] Bo Jakobsen, Kristine Niss, and Niels Boye Olsen. Dielectric and shear mechanical alpha and beta relaxations in seven glass-forming liquids. *The Journal of Chemical Physics*, 123(23):234511, 2005.

[70] Tina Hecksher and Niels Boye Olsen. Private communication, 2007.

[71] Jeppe C. Dyre. Private Communication, 2007.

[72] J. D. Choi, T. Feurer, M. Yamaguchi, B. Paxton, and K. A. Nelson. Generation of ultrahigh-frequency tunable acoustic waves. *Applied Physics Letters*, 87(8), 2005.

[73] R. H. Orcutt. Interlot density variation of a siloxane manometer fluid. *Journal of Vacuum Science and Technology*, 10(4):506–506, 1973.

[74] K. F. Poulter and P. J. Nash. Interferometric oil micromanometer. *Journal of Physics E-Scientific Instruments*, 12(10):931–936, 1979.

[75] K. L. Ngai. Dynamic and thermodynamic properties of glass-forming substances. *Journal of Non-Crystalline Solids*, 275(1-2):7–51, 2000.

[76] D. M. Paolucci and K. A. Nelson. Impulsive stimulated thermal scattering study of structural relaxation in supercooled glycerol. *Journal of Chemical Physics*, 112(15):6725–6732, 2000.

[77] R. Torre, A. Taschin, and M. Sampoli. Acoustic and relaxation processes in supercooled orthoterphenyl by optical-heterodyne transient grating experiment. *Physical Review E*, 6406(6), 2001. Part 1.

[78] A. Tolle, H. Schober, J. Wuttke, and F. Fujara. Coherent dynamic structure factor of orthoterphenyl around the mode coupling crossover temperature t-c. *Physical Review E*, 56(1):809–815, 1997. Part B.

[79] E. Bartsch, F. Fujara, B. Geil, M. Kiebel, W. Petry, W. Schnauss, H. Sillescu, and J. Wuttke. Signatures of the glass-transition in a van-der-waals liquid seen by neutrons and nmr. *Physica A*, 201(1-3):223–236, 1993.

[80] Y. W. Yang and K. A. Nelson. T-c of the mode-coupling theory evaluated from impulsive stimulated light-scattering on salol. *Physical Review Letters*, 74(24):4883–4886, 1995.

[81] Y. W. Yang and K. A. Nelson. Impulsive stimulated thermal scattering study of alpha relaxation dynamics and the debye-waller factor anomaly in ca0.4k0.6(no3)(1.4). *Journal of Chemical Physics*, 104(14):5429–5436, 1996.

[82] W. Gotze and L. Sjogren. Scaling properties in supercooled liquids near the glass-transition. *Journal of Physics C-Solid State Physics*, 21(18):3407–3421, 1988.

[83] G. Hinze, D. D. Brace, S. D. Gottke, and M. D. Fayer. A detailed test of mode-coupling theory on all time scales: Time domain studies of structural relaxation in a supercooled liquid. *Journal of Chemical Physics*, 113(9):3723–3733, 2000.

[84] T. Pezeril, P. Ruello, S. Gougeon, N. Chigarev, D. Mounier, J. M. Breteau, P. Picart, and V. Gusev. Generation and detection of plane coherent shear picosecond acoustic pulses by lasers: Experiment and theory. *Physical Review B*, 75(17), 2007.

[85] M. L. Ferrer, C. Lawrence, B. G. Demirjian, D. Kivelson, C. Alba-Simionesco, and G. Tarjus. Supercooled liquids and the glass transition: Temperature as the control variable. *Journal of Chemical Physics*, 109(18):8010–8015, 1998.

[86] M. Mizukami, K. Kobashi, M. Hanaya, and M. Oguni. Presence of two freezing-in processes concerning alpha-glass transition in the new liquid phase of triphenyl phosphite and its consistency with"cluster structure" and "intracluster rearrangement for alpha process" models. *Journal of Physical Chemistry B*, 103(20):4078–4088, 1999.

[87] P. J. Chappell and D. Kivelson. A comprehensive light-scattering study of a liquid composed of symmetric top molecules. *Journal of Chemical Physics*, 76(4):1742–1753, 1982.

[88] E. A. Dimarzio and M. Bishop. Connection between macroscopic electric and mechanical susceptibilities. *Journal of Chemical Physics*, 60(10):3802–3811, 1974.

[89] T. Scopigno, G. Ruocco, F. Sette, and G. Monaco. Is the fragility of a liquid embedded in the properties of its glass? *Science*, 302(5646):849–852, 2003.

[90] J. C. Dyre. Source of non-arrhenius average relaxation time in glass-forming liquids. *Journal of Non-Crystalline Solids*, 235:142–149, 1998.

[91] R. W. Hall and P. G. Wolynes. The aperiodic crystal picture and free-energy barriers in glasses. *Journal of Chemical Physics*, 86(5):2943–2948, 1987.

[92] U. Buchenau. Mechanical relaxation in glasses and at the glass transition. *Physical Review B*, 63(10):13, 2001.

[93] J. C. Dyre and N. B. Olsen. Landscape equivalent of the shoving model. *Physical Review E*, 69:042501, 2004.

[94] W. H. Wang, P. Wen, D. Q. Zhao, M. X. Pan, and R. J. Wang. Relationship between glass transition temperature and debye temperature in bulk metallic glasses. *Journal of Materials Research*, 18(12):2747–2751, 2003.

[95] D. S. Sanditov, S. Sh. Sangadhiev, and G. V. Kozlov. *Glass Physical Chemistry*, 24:539, 1998.

[96] V. N. Novikov, Y. Ding, and A. P. Sokolov. Correlation of fragility of supercooled liquids with elastic properties of glasses. *Physical Review E*, 71(6):12, 2005.

[97] S. N. Yannopoulos and G. P. Johari. Glass behaviour - poisson's ratio and liquid's fragility. *Nature*, 442(7102):E7–E8, 2006.

[98] G. P. Johari. On poisson's ratio of glass and liquid vitrification characteristics. *Philosophical Magazine*, 86(11):1567–1579, 2006.

[99] V. N. Novikov and A. P. Sokolov. Correlation of fragility and poisson's ratio: Difference between metallic and nonmetallic glass formers. *Physical Review B*, 74(6):7, 2006.

[100] K. A. Nelson, R. J. D. Miller, D. R. Lutz, and M. D. Fayer. Optical-generation of tunable ultrasonic-waves. *Journal of Applied Physics*, 53(2):1144–1149, 1982.

[101] N. B. Olsen, T. Christensen, and J. C. Dyre. Time-temperature superposition in viscous liquids. *Physical Review Letters*, 86(7):1271–1274, 2001.

[102] S. V. Nemilov. *Thermodynamic and Kinetic Aspects of the Vitreous State.* CRC Press, Boca Raton, 1995.

[103] A. Heuer and H. W. Spiess. *Journal of Non-Crystalline Solids*, 176:294, 1994.

[104] M. Pietralla, P. Mayr, and K. Weishaupt. *Journal of Non-Crystalline Solids*, 195:199, 1996.

[105] V. N. Novikov and A. P. Sokolov. Correlation of fragility and poisson's ratio: Difference between metallic and nonmetallic glass formers. *Physical Review B*, 74(6), 2006.

[106] U. Buchenau, M. Ohl, and A. Wischnewski. A new interpretation of dielectric data in molecular glass formers. *Journal of Chemical Physics*, 124(9):6, 2006.

[107] A. Gemant. *Trans. Fraday Soc.*, 31:1582, 1935.

[108] G. D. Enright and B. P. Stoicheff. Light-scattering from shear modes in liquid salol. *Journal of Chemical Physics*, 64(9):3658–3665, 1976.

[109] E. Eckstein, J. Qian, R. Hentschke, T. Thurn-Albrecht, W. Steffen, and E. W. Fischer. X-ray scattering study and molecular simulation of glass forming liquids: Propylene carbonate and salol. *Journal of Chemical Physics*, 113(11):4751–4762, 2000.

[110] S. K. Jain. Density and partial equivalent volumes of hydrated melts - tetrahydrates of calcium nitrate, cadmium nitrate, and their mixtures with lithium, sodium, and potassium-nitrate. *Journal of Chemical and Engineering Data*, 18(4):397–399, 1973.

[111] C. T. Moynihan, P. B. Macedo, C. J. Montrose, P. K. Gupta, M. A. Debolt, J. F. Dill, B. E. Dom, P. W. Drake, A. J. Easteal, P. B. Elterman, R. P. Moeller,

H. Sasabe, and J. A. Wilder. Structural relaxation in vitreous materials. *Annals of the New York Academy of Sciences*, 279(OCT15):15–35, 1976.

[112] L. DeLorenzi, M. Fermeglia, and G. Torriano. Density, refractive index, and kinematic viscosity of diesters and triesters. *Journal of Chemical and Engineering Data*, 42(5):919–923, 1997.

[113] M. Cutroni, P. Migliardo, A. Piccolo, and C. Alba-Simionesco. The dynamic glass-transition of a fragile molecular liquid in the megahertz domain. *Journal of Physics-Condensed Matter*, 6(28):5283–5293, 1994.

[114] M. Cutroni and A. Mandanici. *Journal of Chemical Physics*, 114(16):7124–7129, 2001.

[115] Aleksandra Drozd-Rzoska and Sylwester J. Rzoska. Derivative-based analysis for temperature and pressure evolution of dielectric relaxation times in vitrifying liquids. *Physical Review E*, 73(4):041502, 2006.

[116] D. R. Macfarlane and D. K. Y. Wong. Conductivity and dielectric-relaxation in calcium nitrate tetrahydrate and sodium thiosulfate pentahydrate near t_g. *Journal of Physical Chemistry*, 89(26):5849–5855, 1985.

[117] H. P. Zhang, A. Brodin, H. C. Barshilia, G. Q. Shen, H. Z. Cummins, and R. M. Pick. Brillouin scattering study of salol: Exploring the effects of rotation-translation coupling. *Physical Review E*, 70(1), 2004. Part 1.

[118] P. K. Dixon, L. Wu, S. R. Nagel, B. D. Williams, and J. P. Carini. Scaling in the relaxation of supercooled liquids. *Physical Review Letters*, 65(9):1108–1111, 1990.

[119] A. Mandanici, R. Richert, M. Cutroni, X. F. Shi, S. A. Hutcheson, and G. B. McKenna. Relaxational features of supercooled and glassy m-toluidine. *Journal of Non-Crystalline Solids*, 352(42-49):4729–4734, 2006. Sp. Iss. SI.

[120] M. Cutroni, A. Mandanici, and A. Piccolo. The dielectric-relaxation behavior of m-fluoroaniline above the glass-transition. *Journal of Physics-Condensed Matter*, 7(34):6781–6788, 1995.

[121] M. Cutroni, P. Migliardo, A. Piccolo, and C. Alba-Simionesco. The dynamic glass-transition of a fragile molecular liquid in the megahertz domain. *Journal of Physics-Condensed Matter*, 6(28):5283–5293, 1994.

[122] W. T. Laughlin and D. R. Uhlmann. Viscous flow in simple organic liquids. *J. Phys. Chem.*, 76(16):2317–2325, 1972.

[123] K. Niss, B. Jakobsen, and N. B. Olsen. Dielectric and shear mechanical relaxations in glass-forming liquids: A test of the gemant-dimarzio-bishop model. *Journal of Chemical Physics*, 123(23):8, 2005.

[124] B. Jakobsen, K. Niss, and N. B. Olsen. Dielectric and shear mechanical alpha and beta relaxations in seven glass-forming liquids. *Journal of Chemical Physics*, 123(23):9, 2005.

[125] A. Mandanici, M. Cutroni, and R. Richert. Dynamics of glassy and liquid m-toluidine investigated by high-resolution dielectric spectroscopy. *Journal of Chemical Physics*, 122(8), 2005.

[126] G. Li, W. M. Du, A. Sakai, and H. Z. Cummins. Light-scattering investigation of alpha-relaxation and beta-relaxation near the liquid-glass transition of the molecular glass salol. *Physical Review A*, 46(6):3343–3356, 1992.

[127] B. A. Remington, G. Bazan, J. Belak, E. Bringa, M. Caturla, J. D. Colvin, M. J. Edwards, S. G. Glendinning, D. S. Ivanov, B. Kad, D. H. Kalantar, M. Kumar, B. F. Lasinski, K. T. Lorenz, J. M. McNaney, D. D. Meyerhofer, M. A. Meyers, S. M. Pollaine, D. Rowley, M. Schneider, J. S. Stolken, J. S. Wark, S. V. Weber, W. G. Wolfer, B. Yaakobi, and L. V. Zhigilei. Materials science under extreme conditions of pressure and strain rate. *Metallurgical and Materials Transactions a-Physical Metallurgy and Materials Science*, 35A(9):2587–2607, 2004.

[128] R. B. Spielman and J. S. De Groot. Z pinches - a historical view. *Laser and Particle Beams*, 19(4):509–525, 2001.

[129] Yogendra M. Gupta. Physics 592 Class Notes, 2002.

[130] C. F. McMillan, D. R. Goosman, N. L. Parker, L. L. Steinmetz, H. H. Chau, T. Huen, R. K. Whipkey, and S. J. Perry. Velocimetry of fast surfaces using fabry-perot interferometry. *Review of Scientific Instruments*, 59(1):1–21, 1988.

[131] N. Hemmi, D. H. Torchinsky, K. A. Zimmerman, J. M. Winey, K. A. Nelson, and Y. M. Gupta. Photoacoustic measurements to determine acoustic velocities in shocked condensed materials: Application to liquid benzene. *Applied Physics Letters*. In Press.

[132] L. Ciabini, F. A. Gorelli, M. Santoro, R. Bini, V. Schettino, and M. Mezouar. High-pressure and high-temperature equation of state and phase diagram of solid benzene. *Physical Review B*, 72(9), 2005.

[133] S. Root and Y. M. Gupta. Optical spectroscopy and imaging of liquid benzene multiply shocked to 13 gpa. *Chemical Physics Letters*, 442(4-6):293–297, 2007.

[134] A. Matsuda, K. Kondo, and K. G. Nakamura. Nanosecond rapid freezing of liquid benzene under shock compression studied by time-resolved coherent anti-stokes raman spectroscopy. *Journal of Chemical Physics*, 124(5), 2006.

[135] K. Miyazaki, D. R. Reichman, and R. Yamamoto. Supercooled liquids under shear: Theory and simulation. *Physical Review E*, 70(1), 2004. Part 1.

[136] K. Miyazaki, H. M. Wyss, D. A. Weitz, and D. R. Reichman. Nonlinear viscoelasticity of metastable complex fluids. *Europhysics Letters*, 75(6):915–921, 2006.

[137] M. E. Cates. Arrest and flow of colloidal glasses. *Annales Henri Poincare*, 4:S647–S661, 2003. Suppl. 2.

[138] F. Sciortino and P. Tartaglia. Glassy colloidal systems. *Advances in Physics*, 54(6-7):471–524, 2005.

[139] W. van Megen, T. C. Mortensen, S. R. Williams, and J. Müller. Measurement of the self-intermediate scattering function of suspensions of hard spherical particles near the glass transition. *Phys. Rev. E*, 58(5):6073–6085, Nov 1998.

[140] W. van Megen and S. M. Underwood. Glass transition in colloidal hard spheres: Measurement and mode-coupling-theory analysis of the coherent intermediate scattering function. *Phys. Rev. E*, 49(5):4206–4220, May 1994.

[141] Erica J. Saltzman and Kenneth S. Schweizer. Transport coefficients in glassy colloidal fluids. *The Journal of Chemical Physics*, 119(2):1197–1203, 2003.

[142] R. L. Hamilton and O. K. Crosser. Thermal conductivity of heterogeneous two-component systems. *Industrial & Engineering Chemistry Fundamentals*, 1(3):187–191, 1962.

[143] Pawel Keblinski, Jeffrey A. Eastman, and David G. Cahill. Nanofluids for thermal transport. *Materials Today*, 8(6):36–44, 2005.

[144] J. A. Eastman, S. R. Phillpot, S. U. S. Choi, and P. Keblinski. Thermal transport in nanofluids. *Annual Review of Materials Research*, 34:219–246, 2004.

[145] A. Schmidt, M. Chiesa, D. H. Torchinsky, J. A. Johnson, K. A. Nelson, and G. Chen. Thermal conductivity of nanoparticle suspensions in insulating media measured with a transient optical grating and a hotwire. *Journal of Applied Physics*. In Press.

[146] Y. Nagasaka and A. Nagashima. Absolute measurement of the thermal-conductivity of electrically conducting liquids by the transient hot-wire method. *Journal of Physics E-Scientific Instruments*, 14(12):1435–1440, 1981.

[147] David R. Lide, editor. *CRC Handbook on Chemistry and Physics, 88th Edition.*

[148] M L Mather R E Challis, M J W Povey and A K Holmes. Ultrasound techniques for characterizing colloidal dispersions. *Reports on Progress in Physics*, 68(7):1541–1637, 2005.

[149] R. E. Challis, J. S. Tebbutt, and A. K. Holmes. Equivalence between three scattering formulations for ultrasonic wave propagation in particulate mixtures. *Journal of Physics D-Applied Physics*, 31(24):3481–3497, 1998.

[150] R. Prasher, D. Song, J. L. Wang, and P. Phelan. Measurements of nanofluid viscosity and its implications for thermal applications. *Applied Physics Letters*, 89(13), 2006.

[151] B. C. Pak and Y. I. Cho. Hydrodynamic and heat transfer study of dispersed fluids with submicron metallic oxide particles. *Experimental Heat Transfer*, 11(2):151–170, 1998.

[152] H. S. Chen, Y. L. Ding, and C. Q. Tan. Rheological behaviour of nanofluids. *New Journal of Physics*, 9, 2007.

[153] S. K. Das, N. Putra, P. Thiesen, and W. Roetzel. Temperature dependence of thermal conductivity enhancement for nanofluids. *Journal of Heat Transfer-Transactions of the Asme*, 125(4):567–574, 2003.

[154] A. Schmidt, M. Chiesa, D. H. Torchinsky, J. A. Johnson, A. Boustani, K. A. Nelson, G.H. McKinley, and G. Chen. Shear and longitudinal viscosity of nanoparticle suspensions in insulating media. *Applied Physics Letters.* In Review.

[155] A. Einstein. *Ann. Physik*, 19:289, 1906.

[156] A. Einstein. *Ann. Physik*, 34:591, 1911.

[157] R. Prasher, D. Song, J. L. Wang, and P. Phelan. Measurements of nanofluid viscosity and its implications for thermal applications. *Applied Physics Letters*, 89(13):133108, 2006.

[158] M. G. Sceats and J. M. Dawes. On the viscoelastic properties of normal-alkane liquids. *Journal of Chemical Physics*, 83(3):1298–1304, 1985.

[159] A H Harker and J A G Temple. Velocity and attenuation of ultrasound in suspensions of particles in fluids. *Journal of Physics D: Applied Physics*, 21(11):1576–1588, 1988.

[160] A. R. Duggal, J. A. Rogers, and K. A. Nelson. Real-time optical characterization of surface acoustic modes of polyimide thin-film coatings. *Journal of Applied Physics*, 72(7):2823–2839, 1992.

[161] J. A. Rogers, A. A. Maznev, M. J. Banet, and K. A. Nelson. Optical generation and characterization of acoustic waves in thin films: Fundamentals and applications. *Annual Review of Materials Science*, 30:117–157, 2000.

[162] John A. Rogers. PhD thesis, Massachusetts Institute of Technology, 1995.

[163] V. Gusev, C. Desmet, W. Lauriks, C. Glorieux, and J. Thoen. Theory of scholte, leaky rayleigh, and lateral wave excitation via the laser-induced thermoelastic effect. *Journal of the Acoustical Society of America*, 100(3):1514–1528, 1996.

[164] C. Glorieux, K. Van de Rostyne, J. Goossens, G. Shkerdin, W. Lauriks, and K. A. Nelson. Shear properties of glycerol by interface wave laser ultrasonics. *Journal of Applied Physics*, 99(1), 2006.

[165] G. Saini, T. Pezeril, D. H. Torchinsky, J. Yoon, S. E. Kooi, E. L. Thomas, and K. A. Nelson. Pulsed laser characterization of multicomponent polymer acoustic and mechanical properties in the sub-ghz regime. *Journal of Materials Research*, 22(3):719–723, 2007.

[166] T. Brabec and F. Krausz. Intense few-cycle laser fields: Frontiers of nonlinear optics. *Reviews of Modern Physics*, 72(2):545–591, 2000.

[167] J. G. Eden. High-order harmonic generation and other intense optical field-matter interactions: review of recent experimental and theoretical advances. *Progress in Quantum Electronics*, 28(3-4):197–246, 2004.

[168] R. I. Tobey, M. E. Siemens, M. M. Murnane, H. C. Kapteyn, D. H. Torchinsky, and K. A. Nelson. Transient grating measurement of surface acoustic waves in thin metal films with extreme ultraviolet radiation. *Applied Physics Letters*, 89(9):091108, 2006.

[169] M. Paluch, K. Grzybowska, and A. Grzybowski. Effect of high pressure on the relaxation dynamics of glass-forming liquids. *Journal of Physics-Condensed Matter*, 19(20), 2007.

[170] A. Patkowski, M. Paluch, and H. Kriegs. Dynamic light scattering studies of supercooled phenylphthalein-dimethylether dynamics under high pressure. *Journal of Chemical Physics*, 117(5):2192–2198, 2002.

[171] R. Casalini, U. Mohanty, and C. M. Roland. Thermodynamic interpretation of the scaling of the dynamics of supercooled liquids. *Journal of Chemical Physics*, 125(1), 2006.

[172] R. Casalini and C. M. Roland. Scaling of the supercooled dynamics and its relation to the pressure dependences of the dynamic crossover and the fragility of glass formers. *Physical Review B*, 71(1), 2005.

[173] M. I. Eremets. *High Pressure Experimental Methods.* Oxford Science Publications, 1996.

[174] J. M. Brown, L. J. Slutsky, K. A. Nelson, and L. T. Cheng. Velocity of sound and equations of state for methanol and ethanol in a diamond-anvil cell. *Science*, 241(4861):65–67, 1988.

[175] J. M. Brown, L. J. Slutsky, K. A. Nelson, and L. T. Cheng. Single-crystal elastic-constants for san carlos peridot - an application of impulsive stimulated scattering. *Journal of Geophysical Research-Solid Earth and Planets*, 94(B7):9485–9492, 1989.

[176] Keith A. Nelson. Private communication, 2007.

[177] J.A. Hoffnagle, W.D. Hinsberg, M. Sanchez, and Houle F.A. Liquid immersion deep-ultraviolet interferometric lithography. *J. Vac. Sci. Tech. B*, 17:3306–3309, 1999.

[178] A. Mandanici, X. F. Shi, G. B. McKenna, and M. Cutroni. Slow dynamics of supercooled m-toluidine investigated by mechanical spectroscopy. *Journal of Chemical Physics*, 122(11), 2005.